Coherent fibre-optic link: applications in Time and Frequency metrology, Geodesy, Radio Astronomy and Seismology



Doctoral Dissertation
Doctoral Program in Metrology (31.th cycle)

Coherent fibre-optic link: applications in Time and Frequency metrology, Geodesy, Radio Astronomy and Seismology

Anna Tampellini

* * * * * *

Supervisor
Dr. Davide Calonico

Doctoral Examination Committee:
Dr. Paul-Eric Pottie, Referee, LNE-SYRTE, Observatoire de Paris
Dr. Mario Siciliani de Cumis, Referee, Agenzia Spazale Italiana

Politecnico di Torino
June 12, 2019

I hereby declare that, the contents and organisation of this dissertation constitute my own original work and does not compromise in any way the rights of third parties, including those relating to the security of personal data.

. . . . . .

Anna Tampellini

Turin, June 12, 2019

Summary

Optical fibre links for frequency dissemination are a key tool for Time and Frequency metrology and for the future redefinition of the SI second. They are based on the transmission of an ultrastable laser, whose frequency is referenced to an atomic clock at the National Metrology Institute (NMI) where it is generated, along standard telecom fibres. The fibre length variations due to temperature, acoustic and seismic noise deteriorate the stability of the signal by introducing phase noise on the optical carrier and thus need to be compensated for. Various techniques have been proposed to this task; at the highest performances, the frequency of an optical carrier can be delivered through thousands of kilometres with uncertainty at the 10^{-19} level, i.e. 5 orders of magnitude better than satellite techniques. This enables to disseminate atomic clocks of new generation at their intrinsic level of uncertainty. A fibre-based network of NMIs has been developed in Europe and is continuously growing, for the remote comparison of atomic clocks and frequency standards validation. More recently, fibre-based transfer of optical frequencies started to be exploited for other scientific purposes. In Italy a fibre link of almost 2000 km has been developed, connecting the Istituto Nazionale di Ricerca Metrologica (INRIM), the Italian NMI, to the National Institute for Astrophysics (INAF) and the Space Geodesy Center (CGS) of the Italian Space Agency (ASI) for experiments of Very Long Baseline Interferometry (VLBI) for geodesy and radio astronomy, the European Laboratory of Non-Linear Spectroscopy (LENS) and the National Institute of Optics (INO) for experiments of high precision spectroscopy on cold atoms and molecules. A connection to the French border has also been developed, in view of a connection to the European fibre network.

The first part is focused on the technical implementation and characterization of the Italian link, connecting the INAF radio telescopes, in central Italy, to CGS in southern Italy, for a total length of 1204 km. In order to simultaneously provide multiple laboratories of the country with an ultrastable signal and to cope with the attenuation across the whole network, a cascaded link has been developed. The full network has been divided in five spans, each provided with an ultrastable laser, phase-locked to the incoming light, and independent noise cancellation electronics. A further technical aspect addressed in this thesis is the implementation of the optical two-way noise cancellation scheme. It is an alternative to the Doppler

scheme for remote comparisons of frequency standards, which is more immune to optical attenuation and build-up of phase noise. In this thesis I describe for the first time the results we obtained with such technique in a real field, with independent setups for data processing, and address the most critical aspects. I show that this technique allows remote clocks comparisons at the 10^{-19} level of uncertainty.
Finally, I report on the phase noise characterization of submarine fibres, performed on two 200 km fibre links connecting Malta to Sicily. This measurement campaign has been performed in collaboration with the University of Malta and the National Physical Laboratory (NPL). We found that the phase noise on submarine fibres is orders of magnitude lower than on terrestrial fibres of the same length, which is interesting in view of future transcontinental comparisons of atomic clocks.

The second section of the thesis is dedicated to some applications of the fibre-based dissemination of frequency standards. The first is in radio astronomy, in particular, in Very Long Baseline Interferometry (VLBI). This technique is based on the simultaneous observation of an object in the sky with many telescopes on the Earth: by correlating the data of each telescope, the resolution is improved by orders of magnitude with respect to a single antenna observation. One of the limiting factors is the frequency instability of the local frequency reference. If two telescopes share the same reference, its uncertainty contribution becomes negligible in the final correlation. In this thesis I describe the implementation and characterization of a fibre link that disseminates a common frequency reference to two radio telescopes managed by INAF and ASI as well as the results of the preliminary tests in preparation to the first common-clock experiment.
Another application of optical fibre links is in relativistic geodesy. I describe a proof-of-principle experiment of chronometric levelling, jointly performed by INRIM, NPL and the Physikalisch-Technische Bundesantalt (PTB). An optical clock has been transported to the Laboratoire Souterrain de Modane (LSM) at the French border, 1000 m higher than Torino, and compared to the INRM primary frequency standard through a 150 km fibre link. By measuring the relativistic redshift between the two clocks, the difference of the gravity potential between the two locations is retrieved and compared with the results of traditional gravimetry techniques. This thesis reports the realization of the fibre link, its characterization and the results of the chronometric levelling experiment.
The last application exploits optical fibre as sensors of seismic noise. This thesis describes the first demonstration of earthquakes detection using optical fibres and coherent interferometry techniques, performed in collaboration with NPL, the British Geological Survey and the University of Malta. We predict the possibility of detecting earthquakes with ultra long-haul transoceanic fibres installed for telecom purposes. This would enable to reveal small seismic events generated on the bottom of the oceans which remain currently undetected due to the high costs of operation of seismic sensors in a submarine environment.

Acknowledgements

Grazie...

A Davide che mi ha guidato e motivato sempre.
A Cecilia per l'attenzione e la presenza costanti.
Ai miei colleghi dell'INRIM Alberto, Claudio, Elio, Filippo, Giovanni, Marco, Marco, Pierre e Salvatore per i suggerimenti e l'aiuto.
Ai miei colleghi dottorandi Benjamin, Carolina, Filippo, Gianmaria, Hai Xiao, Martina, Matteo, Michele, Piero e Stefano per il supporto e la condivisione.

Vorrei inoltre ringraziare...

I colleghi dell'INAF Claudio Bortolotti, Giuseppe Maccaferri, Monia Negusini, Federico Perini, Roberto Ricci e Mauro Roma per gli esperimenti di VLBI.
André Xuereb per gli esperimenti a Malta.
Giuseppe Marra per gli espermenti di sismologia.
Topix e in particolare Matteo Frittelli e Alessando Galardini per il supporto tecnico.

Funding: This work has been funded by the European Metrology Program for Innovation and Research (EMPIR) project 15SIB05 OFTEN. This project has received funding from the EMPIR programme co-financed by the Participating States and from the European Union's Horizon 2020 research and innovation programme.

Contents

List of Tables

List of Figures

Introduction

Over the millennia, a large number of methods has been realized for timekeeping, ranging from the observation of the apparent motion of sun and stars across the sky to the invention of mechanical devices such as pendulums and water clocks. As a common feature, they all depend on periodic natural phenomena with regular period of oscillation. Timekeeping is nothing more than counting these oscillations to mark the passage of time. Up to 1960, the second has been defined as a fraction (1/86400) of the mean solar day. As the human ability of measuring this unit of time improved, it became clear that the Earth's period of rotation is not constant and that this definition was not longer satisfactory.

Atomic standards

Already in 1870, J.C.Maxwell suggested that the definition of fundamental units was based on atomic properties, since atoms are eternal, unalterable and perfectly identical.
The first practical realization of a frequency standard based on caesium atoms was produced in 1955 at the National Physical Laboratory (NPL) by Louis Essen and Jack Parry [1]. That device was used at intervals of few days for the calibration of a quartz clock. Essen and Parry demonstrated that transitions between discrete energy levels in well-isolated caesium atoms could provide a much more stable frequency reference than any other astronomical phenomenon.
For this reason, in 1967 the General Conference on Weights and Measures (CGPM) redefined the second as *"the duration of 9 192 631 770 periods of the radiation corresponding to the transition between the two hyperfine levels of the ground state of the caesium-133 atom"* [2]. Since then, great efforts have been made to improve the performances of Cs atomic clocks. Current Cs clocks [3, 4] rely on laser cooled atoms, are based on the so-called fountain scheme [5] and are probed through the Ramsey interrogation scheme [6].
In November 2018 the 26$^{\text{th}}$ CGPM approved a resolution to revise the definitions of the units of the International System [7]. Since May 2019, the SI units is defined on the basis of seven physical constants, thus inherently stable, marking the end of the physical artefacts [8]. The definition of the second remains unchanged,

since it is already based on a physical constant, namely the Cs atomic transition. Nevertheless, from May the definition is reworded: *"The second, symbol s, is the SI unit of time. It is defined by taking the fixed numerical value of the caesium frequency $\Delta\nu_{Cs}$, the unperturbed ground-state hyperfine transition frequency of the caesium 133 atom, to be 9 192 631 770 when expressed in the unit* Hz*, which is equal to* s^{-1}*."*.

To quantify the clock performances, distinction is made between two types of uncertainty evaluations.

Type A: *"method of evaluation of uncertainty by the statistical analysis of series of observations."* [9]. It is commonly referred to as stability: it quantifies the dispersion of the frequency around the mean value over the measurement time. It is evaluated using the Allan deviation (or two-samples deviation) [10, 11]. This estimator enables to distinguish among the different noise processes that typically affect oscillators.

Type B: *"method of evaluation of uncertainty by means other than the statistical analysis of series of observations."* [9], also called accuracy: it quantifies the capability of reproducing the unperturbed atomic transition. All the environmental effects which perturb it (e.g. the Doppler Effect due to their motion, the electric and magnetic fields...) are controlled and evaluated in order to produce an uncertainty budget of the clock.

The basic formulation of fractional frequency instability for an atomic clock can be expressed as [12]:

$$\sigma(\tau) = \frac{\Delta\nu}{\nu}\sqrt{\frac{T_c}{\tau N}}, \tag{1}$$

where $\Delta\nu$ is the transition linewidth and ν is the transition frequency, T_c is the clock cycle time, τ is the integration time and N is the number of atoms detected in each cycle. The best Cs atomic clocks today achieve the 10^{-16} level of uncertainty with cryogenic fountains [4]. Nevertheless, they may now be at the limit of their accuracy capability. On the contrary a new generation of clocks based on optical atomic transitions is emerging, which enables lower uncertainty at the level of 10^{-18} thanks to the higher operating frequencies. Diverse atomic transitions have been investigated to date. Two approaches have been followed: optical clocks based on single trapped ions of Yb^+ [13], Sr^+ [14], Al^+ [15, 16], Hg^+ [17], and optical clocks using many neutral atoms of Sr [18, 19], Yb [20–22], Hg [23], trapped in an optical lattice.

Besides being promising candidates for a future redefinition of the second [24] and for clocks in space [25], optical clocks are powerful tools for other precision experiments, such as tests of fundamental physics [26–29], based on the precise measurement of the frequency clock transition.

Dissemination techniques

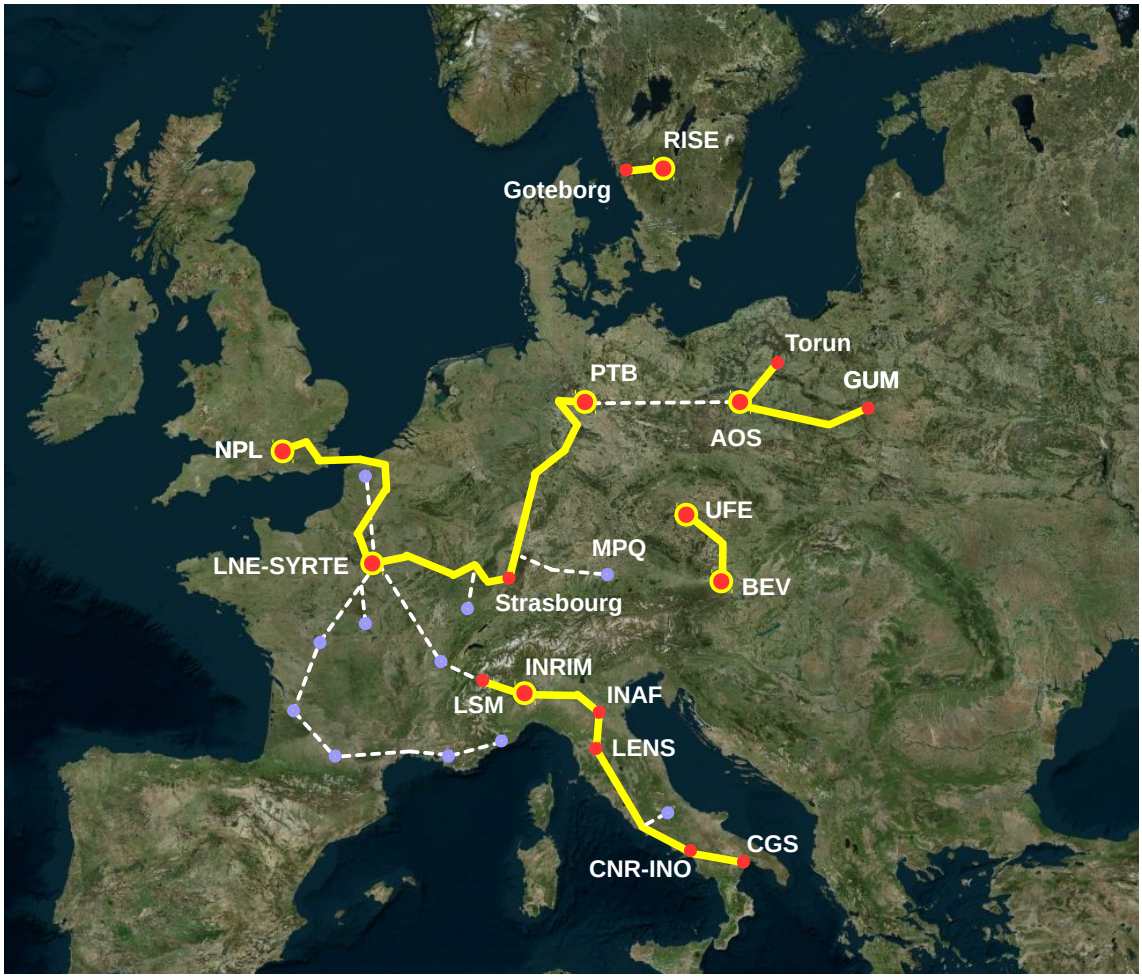

Figure 1: Yellow line: operating links. INRIM-INAF-LENS [30, 31], INRIM-LSM [32], LNE-SYRTE-PTB [33], LNE-SYRTE-NPL [34], Torun-AOS-GUM [35], SP-Goteborg [36], UFE-BEV [37]. White dashed lines: links under development within the OFTEN project.

With the improvements in clocks accuracy, it emerges the need of dissemination techniques capable of transferring the optical standards at their level of accuracy. The ultimate frequency stability of the dissemination techniques based on satellites, which nowadays represent the most reliable transmission method, is still four orders of magnitude lower than the relative accuracy exhibited by the optical clocks of new generation.

In the last 20 years novel techniques based on phase-stabilized optical fibres have been proposed for the dissemination of optical frequencies, microwaves and time references [38]. They rely on the infrastructure of optical fibres developed for telecommunication purposes. Remarkable results have been demonstrated: the ultimate

contribution of dissemination on the stability of the transmitted reference over thousands of kilometres is below 10^{-18} [30].
During the last twenty years fibre links have been developed worldwide: USA [39], Japan [40, 41], China [42], Australia [43, 44]. The realization of a network for metrological dissemination in Europe started in 2012 in the frame of the NEAT-FT project (2012-2015) [45], connecting National Metrology Institutes (NMIs), together with other research facilities and companies (fig. 1). It is now being extended within the European Metrology Programme for Innovation and Research (EMPIR) project "Optical Frequency Transfer-a European Network" (OFTEN) [46]: the overall objective is to enable fast on-demand clock comparisons and frequency dissemination by optical fibre between European NMIs, to enable large scale scientific projects and to pave the way for dissemination to industry. Within the project, the first metrological comparisons of Cs fountains [47] and optical clocks [33, 34] between remote laboratories were performed, limited by the clock uncertainties.
Beside the metrological purpose, several other applications within the field of research benefit from time and frequency references beyond the capabilities of GPS disciplined local oscillators. Among them: fundamental science, e.g. tests of special relativity [34], relativistic geodesy [32, 48], and experimental physics, e.g. for high precision spectroscopy [49, 50], Very-Long-Baseline-Interferometry (VLBI) for geodesy and radio astronomy [31, 51, 52]. Frequency dissemination over fibre is also motivated by experiments carried out in research facilities outside the range of satellite signals. Prominent examples are the large particle accelerator at CERN [53] and the array of detectors of KM3NeT neutrino telescopes [54].

Fibre link applications

A fibre link with total length of almost 2000 km has been developed in Italy since 2014 [30]. A first backbone, 1700 km long, connects INRIM to Matera using fibres which are provided by the Consortium GARR, the Italian national research and education network. A second backbone, established between INRIM and the Laboratoire Souterrain de Modane (LSM) at the French border, with length ~ 150 km, is provided by the Consortium TOP-IX, that manages an Internet-Exchange infrastructure in the north-west of Italy.
The Italian link connects INRIM to other Italian research facilities and will be extended to join the European network during 2019. The research activities where fibre-based frequency dissemination is used are described below.

Very Long Baseline Interferometry (VLBI). VLBI is an interferometric technique introduced in the late '60s for space-geodetic experiments. It relies on the simultaneous observation of a radio source by an array of radiotelescopes on Earth. By correlating the data acquired by each antenna, the resolution of the

observation is improved with respect to a single telescope observation. In a first approximation, the improvement can be quantified by the factor of $\frac{D}{d}$ [55], where d is the aperture of the single telescope and D is the baseline, i.e. the geometric distance between two antennas.
VLBI is a powerful tool for radio astronomy: the observation of compact radio sources and the spectroscopy of the interstellar medium provide very precise coordinates of extragalactic radio sources. On the other hand, in geodesy applications the radio sources of the International Celestial Reference Frame (ICRF) can be used, which is a fixed frame for geodesy. In this case, the observable becomes the delay between the arrival times of the radio signals at the different antennas. This depends on the array geometry and on the optical path of the atmosphere. Monitoring the variations of the time delay enables dynamic modelling of Earth surface and of the atmosphere. These data are complimentary to satellite-based measurement and are a key tool to understand the behaviour of our planet, especially in relation to the challenges of climate changes.
The frequency instability of the reference employed by the radio telescope for the data sampling and processing is one of the main limiting factors in the ultimate resolution of the observation. In [31, 51, 52] is investigated the frequency dissemination as an alternative to local frequency standards. In addition, if the same reference is provided to two antennas, a common-clock observation can be performed, which is expected to allow full rejection of the uncertainty of the atomic clocks.
INRIM is investigating this in collaboration with the National Institute for Astrophysics (INAF) and the Space Geodesy Center (CGS) of the Italian Space Agency (ASI). The two radiotelescopes of the VLBI Italian Network are connected to INRIM via fibre link. The first is a 32-m parabolic dish located in Medicina, near Bologna, managed by INAF. It cooperates to the European VLBI Network (EVN) and to the International VLBI Service for Geodesy and Astrometry (IVS) and is currently used both for single-dish and VLBI observations. The second radiotelescope is a 20-m dish in Matera managed by ASI and is employed for geodetic VLBI observations. The first common-clock VLBI observation performed providing both radio telescopes with a common frequency reference via fibre link was performed in the frame of the "Metrology for Geodesy and Space" (MetGeSp) project, founded by the Italian Ministry of Research and Education (MIUR) through Progetti Premiali.

High resolution spectroscopy. High precision spectroscopy is based on the measurement of the transition frequencies of cold atoms and molecules. Ultracold quantum gases allow the coherent control on the electronic and nuclear degrees of freedom of the atoms. This enables the realization of quantum simulations of a large number of fundamental effects which cannot be studied in their natural physical state. On the other hand, high precision spectroscopy on cold molecules,

thanks to the complex internal molecular structure and symmetry and to the strong intramolecular fields, is the most promising platform for tests of fundamental symmetries and for measurements of fundamental constants and their possible variation in time.
To interrogate the narrow atomic transitions, the probe laser source must feature high frequency stability and an absolute frequency traceability against the primary frequency standard. Moreover, the typical duration of a spectroscopy session is in the range of hours, with repeated scans, which imposes the requirement of high stability on the long term. Frequency dissemination via fibre link allows the SI-traceability of atomic and molecular spectroscopic measurements with improved metrological performance with respect to GPS-based dissemination [49, 50].
Experiments on Bose-Einstein condensates and Fermi gases are performed in Italy at the European Laboratory of Non-Linear Spectroscopy (LENS) in Sesto Fiorentino, Firenze. High resolution spectroscopy on an ultracold gas of ^{173}Yb was performed exploiting the 642 km fibre link connecting INRIM to LENS. In a first class of experiments [50], absolute spectroscopy was performed with an accuracy improved by two orders of magnitude. In a second class, the link-disseminated light was used as a tool to increase the robustness of a quantum simulation experiment with cold atoms, in particular to ensure reproducibility of results and reduce the typical duration of an experimental session [56]. Recently, on the same fibre infrastructure, mid-IR spectroscopy has been performed on high-excited CO molecules at LENS [57].The metrological chain required in this case includes nonlinear frequency conversion processes and scanning of broad frequency ranges. The fibre-disseminated frequency signal is used as reference to the conversion chain, allowing to reach the intrinsic uncertainty of the disseminated clock with short interaction times. More spectroscopy experiments will be performed on cold acetylene molecules with buffer gas beam cooling, exploiting the recent connection between INRIM and the National Institute of Optics (INO) of the National Research Council (CNR).

Chronometric geodesy. The main target of physical geodesy is to model and monitor the geometry and the rotation of Earth and identify the equipotential surface in its gravity field, which coincides with the undisturbed mean sea level extended continuously through the continents. This is currently done via terrestrial gravity measurements for short distances, employing gravimeters or spirit levelling, while for distances longer than 1000 km satellite measurements are performed. Combining these techniques an accuracy at the decimetre level is obtained.
On the other hand, it is known that the frequency of a clock at rest varies from different sites as a result of the gravitational red-shift. By comparing two clocks, located in different places, a direct measurement of the difference of gravity potential between the two sites can be retrieved. Chronometric geodesy is the use of clocks to investigate gravity equipotential surfaces and it has been introduced for the first time in the early 80' by Vermeer and Bjerhammar [58, 59].

The comparison of the best optical clocks of new generation via fibre link allows to achieve their intrinsic level of accuracy, i.e. $\sim 10^{-18}$. This fractional uncertainty allows to resolve a geopotential difference corresponding to ~ 1 cm on Earth. The first chronometric geodesy experiments have been already performed, pushed by the rapid development of optical clocks [33, 48, 60].
A joined experiment between INRIM, the Physikalisch-Technische Bundesanstalt (PTB) and the National Physical Laboratory (NPL) has been performed in 2016 within the European Metrology Research Programme (EMRP) project "International Timescales with Optical Clocks" (ITOC) [32]. A portable optical Sr clock was located at the Laboratoire Souterrain de Modane (LSM), which is a subterranean particle physics laboratory, in the middle of the Fréjus tunnel on the French Alps. It is located 1000 m higher than Torino and connected to INRIM via a 147 km fibre link. This allowed the comparison between the portable optical clock and the INRIM Cs fountain for a proof-of-principle experiment of chronometric levelling.

Seismology. The study of ocean-floor seismic activity is crucial for understanding the dynamic behaviour of the Earth's interior. The detection of earthquakes is currently performed by a network of seismic stations placed on the Earth's surface. Due to the high costs of underwater monitoring, only a small number of seismometers is deployed on the oceans floor and over geographically limited areas [61]. Alternative sensing techniques, like distributed acoustic sensing with optical fibres, enable a coverage of less than 100 km from the coast [62]. Therefore, earthquakes of small magnitude generated on the bottom of the oceans remain largely undetected. The frequency dissemination techniques over fibre which are developed for metrological purposes can be exploited for the detection of seismic events of various magnitude and distance [63]. They are based on an interferometric scheme which is sensible to changes at the femtosecond level in the propagation delay of an ultrastable laser travelling along the fibre, thus enabling the detection of environmentally-induced perturbations at the micrometres scale.
This technique is particularly interesting if applied to submarine fibres: we observed the environmental noise acting on a submarine cable to be orders of magnitude lower than on terrestrial cables of the same length [64]. Thanks to this lower noise floor, the proposed technique can be extended over thousands of kilometres, exploiting the existing extensive submarine fibre infrastructure that covers more than 1 million of kilometres on the bottom of the oceans. This could provide a cost-effective complement to ocean bottom seismometers for real-time detection of underwater earthquakes.

Thesis overview

This thesis describes the work I performed between 2015 and 2018 in the laboratories of the Quantum Metrology and Nanotechnology division of the Istituto Nazionale di Ricerca Metrologica (INRIM) in Turin. It reports on the extension of the Italian fibre backbone for optical carrier dissemination. More than 2000 km of fibre are now under operation in Italy for metrological purposes, allowing novel experiments in geodesy, radio astronomy and seismology.
Chapter 1 reports an overview of the main metrological dissemination techniques with an in-depth analysis of fibre dissemination. The main techniques developed to achieve a stable dissemination over long-haul and ultra long-haul fibre links are revised. Particular attention i devoted to the "Doppler-noise" cancellation technique and to the "two-way" technique, which have been implemented on the Italian backbone.
The first part of chapter 2 describes on the link infrastructure between INRIM and the National Institute for Astrophysics (INAF) in Medicina near Bologna as well as the realization and the first characterization of the link extension from INAF towards the Italian Space Agency (ASI) in Matera. The second part of the chapter reports on the improvements aimed at increasing the uptimes of the optical link between INRIM and INAF (7 days of uninterrupted operation have been achieved); this allowed its exploitation in radio astronomical observation instead of the local clock.
Chapter 3 describes the optical two-way transmission, realized for the first time on a real testbed of 294 km in Italy. Particular attention is devoted to the analysis of the effects introduced by time delays between the acquisition systems.
In chapter 4 the measurements of the noise figure of submarine fibres are described. This feature is of particular interest in view of intercontinental clock comparisons over fibre. A prediction of the noise contribution expected in a fibre-based comparison of atomic clocks on an intercontinental scale is also reported. The measurement was performed on a temporary 200 km link between Italy and Malta in collaboration with the University of Malta and NPL.
Chapter 5 describes three non metrological applications of the fibre-based frequency dissemination. The first application is VLBI, in collaboration with the radiotelescopes of INAF (Medicina) and ASI (Matera). Here the preliminary tests are presented in preparation of the first common-clock VLBI observation. The second experiment is the proof-of-principle test of chronometric levelling, performed in collaboration with PTB and NPL, with the aim of demonstrating that atomic clocks can be used as probes for gravitational potential. Here is described the implementation and characterization of the 147-km-long fibre link used to perform the remote comparison of atomic clocks between INRIM and LSM on the French Alps. The third experiment exploits the long-haul deployed optical fibres as sensing tools. This experiment was performed in collaboration with NPL, the British Geological

Survey and the University of Malta, with the aim of demonstrating the capability of detecting earthquakes by means of optical fibres and optical interferometry techniques.

Chapter 1

Fibre links for frequency dissemination

1.1 Time and Frequency transfer

Since the first experiments with atomic clocks, a parallel research has been initiated, aimed at developing efficient techniques for the dissemination of time and frequency standards and for the comparison of remote clocks. Beside the development of portable clocks, whose capabilities have been demonstrated in the last few years [32, 65], the greatest efforts have been put in the research of dissemination techniques based on the transfer of electromagnetic waves.
In the propagation of an electromagnetic wave through a transmission channel any fluctuation of the path length between two remote sites results in a Doppler shift on the frequency of the transmitted signal, which deteriorates its phase and the stability. By consequence, the crucial point of dissemination is to develop a technique capable of compensating for the additional noise contribution introduced by the transmission channel.
During the years a variety of techniques has been demonstrated to be appropriate; a first approach is to distribute the desired frequency in the microwave domain making use of satellites, while in most recent years the attention has been moved to the optical domain exploiting optical fibres.

1.1.1 Microwave links

The first techniques which were developed for frequency dissemination are based on transferring signals in the microwave domain through the air, making use of both Global Navigation Satellite System (GNSS) and geostationary satellites [66]. Although the noise contribution induced by these techniques exceeds by orders of magnitude the intrinsic accuracy of the best optical clocks of new generation, they still remain the only method where fibre links are not available, such as transoceanic

baselines. To date, satellites are the most robust and reliable tools for remote clocks synchronization and dissemination; clock comparisons performed with satellites of the Global Navigation Satellite System (GNSS) and with the Two-Way Satellite Time and Frequency Transfer (TWSTFT) are used by the BIPM for the calculation of the international atomic timescale [67].

The **GNSS-based** techniques exploit satellite constellations of 18-30 medium Earth Orbit satellites belonging to the United States' Global Positioning System (GPS), the Russia's GLONASS or the China's BEIDOU; since 2016 the European satellites of GALILEO are under operation and they will be full in service in 2019. Each satellite transmits two signals in the L band at about 1.2 GHz or 1.5 GHz to the ground, modulated with the Pulse Per Second (PPS) generated by the on-board clocks (Cs and Rb) and encoded with a pseudo-random code at a chip rate of about 1 MChip/s. At the receiver the signal is demodulated and corrections for the delay introduced by the transmission path, i.e. ionosphere, troposphere and geometry, are applied. In the early 80's the Common-View (CV) technique was developed for ground clock comparisons. It consists in two or more ground stations measuring time signals from the same satellite; by comparing and subtracting these measurements the uncertainty contribution of the on-board clock is cancelled. This technique is adequate for distances up to 10 000 km, if the receivers are too far apart the differences in the delays become non-negligible or the receivers cannot connect to the same physical transmitter. With the All-in-View method, the signals from all the satellites are traced back to a common time reference, allowing common-view comparisons, realized with respect to this timescale, even between stations that receive time signals from different physical satellites. A further improvement has been made with the Precise Point Positioning (PPP) algorithm, which exploits both the time code and the phase of the carrier transmitted by the satellite oscillator as observables. Since the carrier has a much shorter period than the code, this results in an improvement of the measurement resolution. Its latest development led to the IntegerPPP (IPPP) algorithm, which achieves 10^{-16} level after five days [68], limited by the instrumental calibration uncertainties.

An alternative technique introduced in the 80's is the **Two-Way Satellite Time and Frequency Transfer (TWSTFT)**. It is based on geostationary satellites, involving signals in the Ku-band, modulated with the PPS generated by the local timescale and encoded at 2.5 MChip/s. In this case, the signals travel both ways, using the satellite between the two terrestrial clocks just as a repeater. Assuming the reciprocity of the path in the two directions, the information about the delay is estimated from the difference between the local and received signals and applied as correction. After data post-processing, a time accuracy higher than 10^{-15} is achieved after one day measurement [69]. Differently from the GNSS-based techniques, this technique does not support casual or unplanned message exchanges,

both end stations must agree in advance on the format of the data transmission as well as on the schedule.

For the generation of timiescales, caesium and rubidium clocks are routinely used; nevertheless, the first measurements derived from optical clocks have been recently included for the TAI calculation (Sr standard of the Laboratoire national de métrologie et d'essais - Système de Références Temps-Espace, LNE-SYRTE, in circular T of March 2017).
The secondary optical standards exhibit relative uncertainties at the 10^{-18} level after few hours of measurements while the contribution of the microwave links routinely operated is on the order of 10^{-15} after one day averaging, which is clearly not enough to sustain the remote comparison of the optical clocks at their intrinsic levels of accuracy.
To explore the ultimate performances of satellite techniques, especially to compare optical clocks, in 2015, a coordinated programme of clock comparisons has been carried out within the "International Timescales with Optical Clocks" (ITOC) project of the European Metrology Research Programme (EMRP), involving both primary and optical standards of four National Metrology Institutes (NMIs), *"...to validate the performance levels of the optical clocks, to anchor their frequencies as well as possible to the current definition of the second, and to establish the leading contenders for a redefinition of the second..."* [70]. The comparison has been performed exploiting a broadband TWSTFT [71] and the IPPP, which both enabled the most extensive comparison of optical clocks ever performed achieving link uncertainties in the low parts in 10^{-16} range after one day averaging [72].

More microwave links are under development for the **Atomic Clock Ensamble in Space (ACES)** mission, which is an international metrological space mission led by the European Space Agency (ESA) in collaboration with the French Space Agency [73]. Within ACES, a number of time and frequency comparisons will be performed exploiting the Cs clock and the space hydrogen maser placed on board the ISS. Time and frequency comparisons between the on-board time scale and the time scales on the ground will be performed by dual-frequency, four-channel microwave links. The time signal will be encoded with a pseudo-random noise code that modulates the carrier at 100 Mchip/s. In addition, tests of General Relativity will be performed exploiting the on-board atomic clocks.
The noise cancellation is based on a two-way transmission between the ISS and nine ground terminals, especially designed to reduce the instrumental uncertainty, which is usually the limiting factor. The propagation delay cancels at first order when combining the up-link and down-link measurements. Further corrections are applied considering a model for the signal propagation, which takes into account atmospheric and instrumental delays. Thanks to all these features, comparisons of distant ground clocks at the 10^{-17} level are expected.

1.1.2 Optical links

In 1994 the first frequency transfer method in the optical domain has been proposed [74]. It was based on the transmission of an ultrastable laser source through the air. The noise accumulated along the path is cancelled through an interferometric scheme: part of the light travels the transmission path in a round-trip and is interfered with the local one. This enables the detection of the path noise and subsequent cancellation. The technique has been adopted in fibre transmission instead of air in 2003 by Je et al. [38]. The optical structure of the fibre ensures the signal to be confined into the fibre path. Moreover, it guarantees a better isolation from external electromagnetic interferences and lower losses in comparison to electrical cables. Since then, fibre-based techniques have been widely investigated within the metrology community and nowadays they are considered a viable alternative to the satellite techniques, for the dissemination of optical frequency standards.
The technique relies on the telecom fibre network commonly employed for internet traffic, whose signals are located in the C-band (1530-1565 nm) and in the L-band (1565-1610 nm), which correspond to the low-loss window of the fibre. It is compatible with the Dense Wavelength Division Multiplexing (DWDM) technology [75]: a single wavelength channel of the International Telecommunication Union (ITU) grid is required for the metrological dissemination while the remaining channels can be used for data transmission without any interference. In a DWDM architecture, optical add/drop multiplexers (OADM) are employed, which allow to inject or extract one single channel from the DWDM flux with a low insertion loss. The ITU channel 44, centred at 1542,14 nm, is conventionally adopted in Europe for metrological purposes. This approach is also referred to as "dark channel" architecture, whereas, if the fibre is fully dedicated to metrological dissemination, it is called "dark fibre" architecture.
The users of this infrastructures are diverse, thus different dissemination techniques have been developed to meet each user's need; the principal techniques for frequency dissemination exploiting optical links are revised below.

Optical carrier transfer. It is a coherent technique aimed at providing remote users with ultrastable frequency references in the optical domain. It relies on the transmission of continuous wavelength (CW) lasers in C or L band through the fibre. Since the laser signal must be used as absolute frequency reference, its frequency is measured or phase-locked to a frequency standard. An optical comb [76] is used to bridge the gap between the two spectral domains (see section 1.2.4).
The fibre is exposed to environmental noise sources which affect the optical carrier phase by introducing undesired phase fluctuations. These deteriorate the frequency stability of the signal. This noise can be partially compensated for following an interferometric scheme: part of the delivered signal is sent from the remote side of the link back to the original laboratory. The round-trip signal is compared to the

original one; this enables the detection of the accumulated fibre noise, exploiting the reciprocity of phase perturbation for counter propagating signals. The noise compensation is achieved by acting on the frequency of an acousto-optic modulator or by varying the length of the fibre through a piezo stretcher.
To avoid the noise of the laser to dominate the fibre noise at detection, the coherence length of the laser source has to be much longer than the link length. This is obtained by using narrow linewidth lasers, e.g. by frequency-locking the laser to a high-finesse Fabry-Pérot cavity using the Pound-Drever-Hall technique [77], which enables to achieve laser linewidths below 10 Hz.
Active noise compensation enables to transfer the frequency reference of optical standards over more than 1000 km with a noise contribution at the low 10^{-19} level after few hours measurements [30, 41, 78, 79].
An alternative technique, based on the passive rejection of the fibre noise, exploits a two-way scheme. It requires two ultrastable lasers, one at each end of the fibre; they are sent along the fibre in counter propagating directions and at each end of the fibre the local laser is compared to the remote one. By post-processing the data acquired at the two far ends, the fibre noise can be rejected retrieving the difference between the frequency standards to be compared. To this day, this technique has been implemented on testbeds of few hundreds of kilometres, demonstrating a residual phase noise of few parts in 10^{-19} after few hours [80, 81]. Its performances over longer fibre links still need to be demonstrated.
Both techniques are described in detail in section 1.2.

RF frequency transfer. The dissemination of RF signals is typically performed through an amplitude modulation of the optical carrier, using either sinusoidal or square waveforms, with an RF or microwave reference. At the remote end the modulated signal is detected with a fast photodiode.
Several RF frequency dissemination systems operate around 100 MHz. However, since the noise accumulated by the signal while travelling the fibre is proportional to the frequency of the signal itself, the dissemination of a microwave allows a better signal to noise ratio at detection, and hence a better compensation. On the other hand, the upper and lower modulation side bands suffer more from the chromatic dispersion of the fibre, which in turn causes parasitic phase and amplitude modulation of the microwave. In practice, a compromise between maximizing the operating frequency and reducing dispersion-induced instability has to be found.
The noise contribution introduced by the fibre can be actively compensated with a scheme based on the compensation between the local and the round trip-signal; differently from the carrier transfer, the correction is applied mechanically by changing the physical length of the fibre through a piezo stretcher. The transmission of a frequency of 10 GHz has been demonstrated on an urban loop of 86 km, showing an ultimate stability below 10^{-18} after one day integration time [44, 82]. A different approach employs electronic delay lines as actuators for the noise compensation. A

version of this system is also commercially available (ELSTAB). A long-haul implementation of this technique has been performed on a 615 km link, transferring 10 MHz and 100 MHz, reaching the 10^{-17} level after 10^5 s [35, 83, 84].
A quite different method is the based on phase conjugators. It exploits a probe signal, extracted from the main signal, to sense the phase fluctuations introduced by the fibre. This phase signal is then fed with opposite sign to the RF phase-modulation stage, to pre-distort the main signal and compensate for the link phase noise. Although based on a rather simple scheme, it exhibits some complications, such as leakage signals in mixers and long-term drifts of the electronics, that generate parasitic phase shifts. This technique has been demonstrated on a link of 150 km distributing an RF signal at 80 MHz, reaching the 10^{-17} level in 10^4 s [43, 85–90].

Frequency comb transfer. This technique has been pioneered with the aim of combining the transfer of optical carrier and RF. It is based on the dissemination of a mode-locked laser, which is composed by a periodic train of short pulses and hence an optical comb in the frequency domain. The optical carrier dissemination is achieved by transferring a single comb mode, while the RF dissemination can be performed, by detecting the repetition rate of the transmitted comb, i.e. the frequency spacing between consecutive comb modes, which is usually in the range of hundreds of megahertz. The fibre noise cancellation is based on an active scheme similar to those illustrated before; in this case the correction is retrieved by the comparisons of the local and round-trip repetition rate; fibre stretchers and temperature-controlled spools are used as actuators. To recompress the pulses of the mode-locked laser which are broadened due to the chromatic dispersion induced by the fibre, a dispersion compensating fibre module can be used [91]. The mode frequencies have been transferred on few kilometres of fibre with a fractional accuracy of few parts of 10^{-18} [92] over 7.7 km of fibre. The microwave transfer has been demonstrated with a residual stability of few parts in 10^{-17} on the long term over a 86-km-long fibre link [91].

Free-space optical transfer. It is based on the transmission of a mode-locked laser through the open air. Differently from fibre-based techniques, transmission across the air allows more flexible connections, not limited by fibre availability between fixed sites. On the other hand, free-space transmission poses several issues due to atmospheric turbulence which lead to strong phase noise and signal intermittence, limiting the time duration of measurements. The comparison of optical oscillators has been demonstrated over a free space path of 4 km, where two mode locked lasers have been compared according to an optical two-way scheme, derived from the two-way satellite technique. Atmospheric turbulences also lead to signal losses at random times and with random durations. These are overcome by combining both the information of the pulses carrier phase and envelope, allowing

to extend the coherence of the signal across the fades reaching the 10^{-19} level of stability at 1000 s [93].

1.2 Optical carrier dissemination

In the following sections the main schemes commonly adopted for optical carrier transfer are revised as well as the principal techniques to compensate fibre noise. The realization of reliable and robust techniques capable of serving many users at a time and covering continental distances is essential in view of building a routinely running service for research and industry.

1.2.1 Noise sources

Before describing in detail the principal techniques developed for phase-noise cancellation, it is useful to recall the main noise sources that deteriorate the stability of the optical carrier travelling along the fibre cable.
Temperature variations, e.g. diurnal and seasonal temperature cycles, generate slow path fluctuations by changing the refractive index and the length of the fibre. A typical room-temperature value of the thermo-optic coefficient is $\alpha_n = 1.06 \times 10^{-5}\,^{\circ}\mathrm{C}^{-1}$ [94]. The thermal expansion coefficient is $\alpha_\Lambda = 5.6 \times 10^{-7}\,^{\circ}\mathrm{C}^{-1}$, about 20 times lower [95]. Generally aerial fibres display the largest phase fluctuations, whereas buried fibre cables show a higher isolation from environment thanks to the surrounding soil [96–98].
At shorter time scales, path length variations are induced by environmental acoustic vibrations. Mechanical stresses exerted on the fibre cause its torsion, deformation and elongation, proportional to the amplitude of the perturbation force (Hooke's law). The greatest amount of mechanical stress is usually generated by traffic and building vibrations, thus fibres buried next to highways and railways [30], while aerial cables are affected by wind induced oscillations [99].

1.2.2 Noise cancellation techniques

In the following section the two commonly used noise cancellation schemes are described. As already mentioned, for the noise cancellation to be effective, the phase noise acquired by the carrier must be reciprocal in the two directions. In case of optical fibres, this condition is fulfilled if the infrastructure allows signal propagation in both directions on the same fibre (in the following, this scheme will be referred to as "bidirectional fibres").

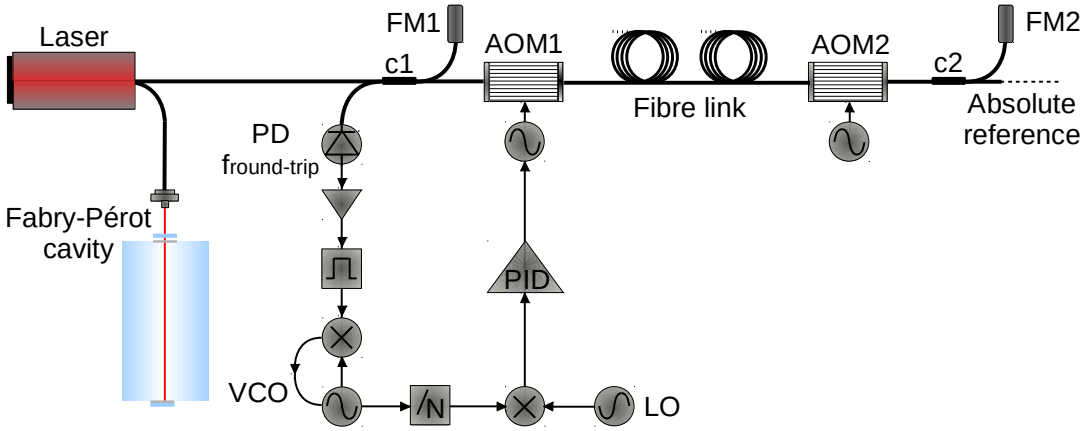

Figure 1.1: Optical and electronic setup for the Doppler-noise cancellation scheme. The laser source is frequency-stabilized against a Fabry-Pérot cavity and launched in the fibre. c_1 and c_2 are the couplers for the local and remote interferometers. AOM_1 is the local acousto-optic modulator that serves as actuator for the noise compensation, AOM_2 is the remote acousto-optic modulator. FM_1 and FM_2 are the local and remote Faraday mirrors. $f_{\text{round-trip}}$ is the beat note between local and round-trip signal, detected with a photodiode (PD), tracked with a voltage-controlled oscillator (VCO) and divided by a factor N. It is phase-compared through a mixer to a local oscillator (LO), the error signal is processed with a PID and the correction is fed to AOM_1.

Doppler-noise cancellation scheme

The Doppler-noise cancellation technique is based on the suppression of the round-trip noise exploiting a phase-locked loop (PLL). Fig. 1.1 outlines the basic components of the experimental setup. In the local laboratory a CW laser is frequency-locked to a Fabry-Pérot cavity, generating an ultrastable light source with high coherence length. The laser frequency depends on the ITU channel chosen for the dissemination, thus $\sim 1542\,\text{nm}$ for channel 44.
Part of this light source is launched into the link, passing through an acousto-optic modulator (AOM_1), while part is split off (c_1) and kept as local reference. At the remote end a part of the signal is extracted (c_2), and used as an absolute reference, while the reminder is retroreflected to generate the round-trip signal. The remote AOM_2 is introduced to distinguish the round-trip signal from the stray backreflections along the fibre. The round-trip signal is affected by the fibre noise acting in the two directions. At the local end, it is heterodyned with the local reference on a photodiode to extract this information. The beat note signal is at frequency $f_{\text{round-trip}} = 2\,(AOM_1 + AOM_2)$. The effects of chromatic dispersion on the one-way signal are negligible, being the linewidth of the laser source below 10 Hz. Nevertheless, because of the frequency offset introduced between the two propagating directions, the counter propagating signals experience different velocities. A compromise has to be chosen between clear distinction of the signal from stray reflections and minimization of the impairments due to the dependence of the

refractive index on the optical frequency. The driving frequency of the AOMs is usually kept below 100 MHz.
Both at the remote and at the local end, the light is reflected by means of a Faraday mirror (FM_1 and FM_2), which consists in an optically active material that rotates the polarization by 45°, followed by a mirror. As a result, the polarization plane of the signal passing twice in the device is rotated by 90°, ensuring that the PMD generated by the intrinsically induced birefringence of the fibre and by the environmental noise is compensated after the round-trip. As a consequence, the polarization states of the local and the round-trip signal, that heterodyne at the local end ($f_{\text{round-trip}}$), are aligned. Therefore, the amplitude of the RF beat note collected on the photodiode (PD) does not suffer from signal fading due to polarization rotations.
$f_{\text{round-trip}}$ contains the information about the noise of the fibre. It is generally characterized by a poor signal-to-noise ratio (SNR), due to the power attenuation induced by the fibre, and by a significant amplitude noise, introduced by amplifiers used to recover the optical losses (see section 1.2.3). A voltage-controlled oscillator (VCO) is therefore used as clean-up oscillator, the tracking bandwidth must be carefully tuned to avoid the occurrence of cycle-slip events. The phase error is retrieved by sending the VCO output to a double-balanced mixer in quadrature condition, with a stable RF reference as local oscillator (LO). Since the mixer has a limited dynamic, the beat note is prescaled, choosing the dividing factor (N) to ensure that the phase fluctuations do not exceed π. Other solutions with higher dynamic can be employed, such as phase-frequency detectors or digital devices.
The phase error is then integrated and a correction is fed as frequency modulation to the RF driving AOM_1. Other configurations exploit piezoelectric fibre stretchers as actuators for the PLL. However, they have a finite dynamic range, in contrast to AOMs, for which it is practically unlimited. In addition, the birefringence induced by stretching the fibre adds a significant contribution to the PMD.

The loop gain of the PLL can be described with a simple proportional-integral model (although in some cases a more elaborated servo scheme is adopted to ensure a better noise rejection at low frequencies) [39]

$$G(s) = \frac{1}{N} G_0 F(s) \frac{K}{s} \left(1 + e^{-2s\tau}\right), \tag{1.1}$$

where N is the diving factor, G_0 and K are the proportional and the integrative gain respectively and $F(s)$ is the loop filter gain. $\tau = \frac{nL}{c}$ is the one-way time travel and n, L and c are the refractive index, the link length and the speed of light in vacuum. The $1 + e^{-2s\tau}$ term accounts for the fact that the correction is applied twice: once in the forward pass, and another in the backward pass, with a 2τ delay between the two actuations. The delay introduced by the round-trip sets the ultimate limit to the loop bandwidth.

The noise of the phase-locked round-trip can be calculated as [100]:

$$S_{\text{fibre,RT,LOCKED}}(s) = \left|\frac{1}{1+G(s)}\right|^2 S_{\text{fibre,RT}}(s), \tag{1.2}$$

where the round-trip noise of the free running fibre $S_{\text{fibre,RT}}(s) \simeq 4S_{\text{fibre}}(s)$; this holds for Fourier frequencies $f \ll \frac{1}{\tau}$ where the noise in the two directions of propagations is highly correlated.
The open-loop gain G is constrained by stability requirements. Assuming that the knee of the proportional-integral Bode plot occurs at low frequencies, the gain argument can be written as:

$$\arg\left[G(i2\pi f)\right] = -\left(\frac{\pi}{2} + 2\pi f\tau\right). \tag{1.3}$$

It is straightforward to see that it achieves π, i.e. the feedback turns positive, at $f_{\text{c}} = \frac{1}{4\tau}$, where one would expect strong oscillations. In practice this effect is mitigated because the modulus $|G(i2\pi f)| \propto \cos(2\pi f\tau)$ nulls at exactly the same frequency, thus the gain can be increased such that its unit magnitude occurs at frequencies higher than f_{c}, obtaining a better noise rejection at low frequencies at the cost of a servo bump at f_{c}. To give an idea of a typical correction bandwidth, we consider a link length of $L = 100\,\text{km}$ and $\frac{c}{n} = 2\times10^8\,\text{m/s}$ the light speed into the optical fibre; thus $\tau = 0.5\,\text{ms}$ and $f_{\text{c}} = 500\,\text{Hz}$.
With such a control loop, a "perfect" compensation of the round-trip noise can be implemented; however, the main interest is on the noise cancellation at the remote end of the fibre after a one-way travel. Let us consider the round-trip noise in the time domain $\delta\phi_{\text{fibre,RT}}$, being $\delta\phi_z$ the phase perturbation of the signal, at distance z from the local end of the fibre [101]:

$$\delta\phi_{\text{fibre,RT}}(t) = \delta\phi_z\left(t - \frac{nz}{c}\right) + \delta\phi_z\left(t - 2\tau + \frac{nz}{c}\right), \tag{1.4}$$

which for 2τ and $\frac{nz}{c} \ll t$ can be expressed as:

$$\delta\phi_{\text{fibre,RT}}(t) \sim 2\delta\phi_z(t) - 2\tau\delta\phi'_z(t), \tag{1.5}$$

where $\delta\phi'_z = \frac{\mathrm{d}\phi_z}{\mathrm{d}t}$. In case of a "perfect" PLL, the correction ϕ_{c} applied to the AOM leads to:

$$\delta\phi_{\text{fibre,RT}}(t) - \left[\phi_{\text{c}}(t) + \phi_{\text{c}}(t-2\tau)\right] = 0. \tag{1.6}$$

Again expanding ϕ_{c} for $\tau \ll t$ and substituting eq. (1.5) in eq. (1.6) one obtains:

$$\phi_{\text{c}}(t) \sim \delta\phi_z(t). \tag{1.7}$$

According to this relation, the phase perturbation on the one-way signal becomes:

$$\delta\phi_z\left(t - \tau + \frac{nz}{c}\right) - \phi_{\text{c}}(t-\tau) \sim \left(\frac{nz}{c}\right)\delta\phi'_z(t), \tag{1.8}$$

which does not vanish, unless in case of a steady state or at $z = 0$. From the above formula, it is straightforward to understand that, even with an optimized control loop, the full compensation of the noise at the remote end is not achievable. This effect is intrinsic to the fact that the round-trip signal, which is phase-stabilized, and the fibre output are located in spatially separated positions.
The Power Spectral Density (PSD) of a phase noise $\phi(t)$ is calculated as the Fourier transform of its autocorrelation function. The autocorrelation function of $\phi(t)$ is defined as [102]:

$$R(\mathrm{T}) = \int_{-\infty}^{\infty} \phi^*(t)\,\phi(t+\mathrm{T})\,dt \tag{1.9}$$

and it holds if $R(\mathrm{T})$ does not depend on t, i.e. for a stationary noise, which is the case of the fibre phase noise. According to the Wiener-Khinchin theorem, the PSD is [102]:

$$S_\phi(f) = \int_{-\infty}^{\infty} R(\mathrm{T})\,e^{-i2\pi f \mathrm{T}} d\mathrm{T}. \tag{1.10}$$

To calculate the PSD of the residual one-way fibre noise it is required to apply eq. (1.9) and (1.10) on eq. (1.8) and to integrate over the fibre length. It can be shown [39] that, under the assumption of $G \to \infty$, which is met for low frequencies, the closed loop one-way noise is:

$$S_{\text{fibre,LOCKED}}(f) = a\,(2\pi f \tau)^2\, S_{\text{fibre}}(f)\,, \tag{1.11}$$

where $a = \frac{1}{3}$, when the fibre-induced noise is uncorrelated with position. Considering that the noise of a free running fibre can be generally expressed as $S_{\text{fibre}}(f) \sim \frac{h}{f^2}$ up to a certain cut off frequency $f \sim 1\,\text{kHz}$, the residual noise after compensation is expected to be white phase noise within the correction bandwidth. For higher Fourier frequencies the noise can be rejected by applying a proper digital filter on the acquired data [103].
This is the fundamental limit for the cancellation, set by the delay-unsuppressed noise when bidirectional fibres are employed. In practice this is not always possible. Telecom transmission is usually based on a pair of adjacent fibres, one for each direction and optical isolators are employed to clean up the signals from backreflections. Hence, to achieve the bidirectional propagation, some modifications on the telecom infrastructure are required which are not always feasible, including the removal of the isolators all along the fibre and the installation of dedicated optical amplifiers (see section 1.2.3). Eq. (1.11) refers to the case of bidirectional fibres, which is the preferred configuration for metrological purposes. In case of an unidirectional infrastructure, the telecom transmission scheme is employed, thus the round-trip signal is generated over a pair of adjacent fibres. The noise cancellation level depends on the degree of correlation between the fibres, which in turn depends on the cables insulation and environment. These may change significantly from one testbed to another; an estimation of the level of correlation between adjacent buried fibres and consequent noise rejection can be found in chapter 4.

More effects may limit the coherence of the transmitted signal.
A first contribution is introduced by the out-of-loop fibre paths in the local and remote arms of the interferometers. They include the local branch dedicated to the reflection of the local reference (FM_1), as well as the fibre patch at the remote end, that serves for the distribution of the delivered signal in the remote laboratory. Their length variations are uncontrolled and thus introduce a noise contribution $S_{\mathrm{Int}}(f) \sim \frac{1}{f^2}$. In order to keep the interferometers noise below the delay-unsuppressed noise floor:

$$S_{\mathrm{Int}}(f) < \frac{1}{3}(2\pi f\tau)^2 S_{\mathrm{fibre}}(f), \tag{1.12}$$

they are usually placed in specifically designed isolated enclosures. An accurate study of the effect of thermal fluctuations on uncompensated fibre branches can be found in [104].
In addition, the noise contribution of the light source, $S_{\mathrm{Laser}}(f)$, has to be accounted for. A loss of coherence over the round-trip prevents from distinguishing the laser from the fibre noise, affecting the error signal. The self-heterodyne contribution of the laser to the round-trip phase noise is [39]:

$$S_{\text{self-het}}(f) = (4\pi f\tau)^2 S_{\mathrm{Laser}}(f). \tag{1.13}$$

To ensure the laser contribution to be negligible with respect to the fibre noise, the following condition is required:

$$S_{\mathrm{Laser}}(f) < \frac{1}{3} S_{\mathrm{fibre}}(f). \tag{1.14}$$

This relation is easily satisfied if the laser is frequency-locked to an ultrastable cavity. Although the cavity length is usually stabilized with a temperature control, a residual frequency drift d is observed on the laser signal. This in turn adds an uncertainty contribution to the accuracy of the delivered signal of $d\tau$, that increases proportionally to the link length. For example, a drift of 0.1 Hz/s on a link of 200 km ($\tau = 1$ ms), originates a frequency offset at the level of $\sim 5 \times 10^{-19}$. To remove the long-term drift, the light source can be frequency-locked to a frequency standard through an optical comb.
A further contribution may rise from the phase noise of the RF signals, $S_{\mathrm{RF}}(f)$, employed both to drive the AOMs and as local oscillator for the mixer. The noise contribution of the AOM references is additive to the fibre noise, thus it needs to be kept:

$$S_{\mathrm{RF,AOM}}(f) < S_{\mathrm{fibre}}(f). \tag{1.15}$$

For the noise of the LO, it has to be taken into account that $f_{\text{round-trip}}$ is divided by a factor of N before being fed to the phase detector. Hence, in this case, the request is more strict:

$$S_{\mathrm{RF,LO}}(f) < \frac{1}{3}(2\pi f\tau)^2 \frac{S_{\mathrm{fibre}}(f)}{N^2}. \tag{1.16}$$

Both conditions are met if all the RF signals are locked to a common 10 MHz reference, possibly synthesized from a Hydrogen Maser.
Frequency dissemination over single-span fibre links of more than one thousand of kilometres has been demonstrated, showing an ultimate relative contribution at the 10^{-19} level [30, 41, 78, 79].
Nevertheless, one has to consider that as the length of the fibre span increases, the noise of the free running fibre is generally expected to grow as [101]:

$$S_{\text{fibre}}(f, L) \propto L, \tag{1.17}$$

while the cancellation bandwidth is reduced as $f_c = \frac{c}{4nL}$, such that the level of the residual noise floor increases as:

$$S_{\text{fibre,LOCKED}}(f, L) \propto L^3. \tag{1.18}$$

The fibre link can be divided into multiple spans, independently stabilized, to ensure a satisfactory noise rejection even in case of ultra-long fibre links [78, 105]. This solution is described in detail in section 1.2.3.
An alternative technique to improve the noise cancellation beyond the limit set by delay-unsuppressed noise has been proposed in [106]. It is based on a subtraction algorithm between the signal delivered at the remote end of the link and the round-trip signal. It enables a 6 dB improvement on the noise rejection; this approach is based on data post-processing, which prevents from a real-time compensation of the noise.

Two-way scheme

The two-way scheme has been proposed for the first time in [107], in analogy to the satellite-based TWSTFT technique. Fig. 1.2 shows a sketch of the experimental setup. Two ultrastable laser sources ($Laser_1$ and $Laser_2$), one at each end of the link, are launched in counter propagating directions along the fibre. At both ends of the fibre, a heterodyne beat note (f_{bn1} and f_{bn2}) between the local and the remote laser is detected with a photodiode (PD_1 and PD_2), filtered and amplified. The AOMs (AOM_1 and AOM_2) are used to distinguish the real signals from the backreflections generated along the fibre.
Differently form the Doppler-noise cancellation scheme, this technique exploits only a single-pass of the lasers along the fibre link. This mitigates all the issues related to signal attenuations and amplifiers noise. Nonetheless, proper filtering and tracking VCOs (VCO_1 and VCO_2) are required for a cycle-slips-free detection of the two heterodyne beat notes. On the other hand, since the RF signals are generated by beating the signals of the two independent laser sources, PMD-related effects are not compensated by Faraday mirrors and a polarization controller is required to optimize the signal power.

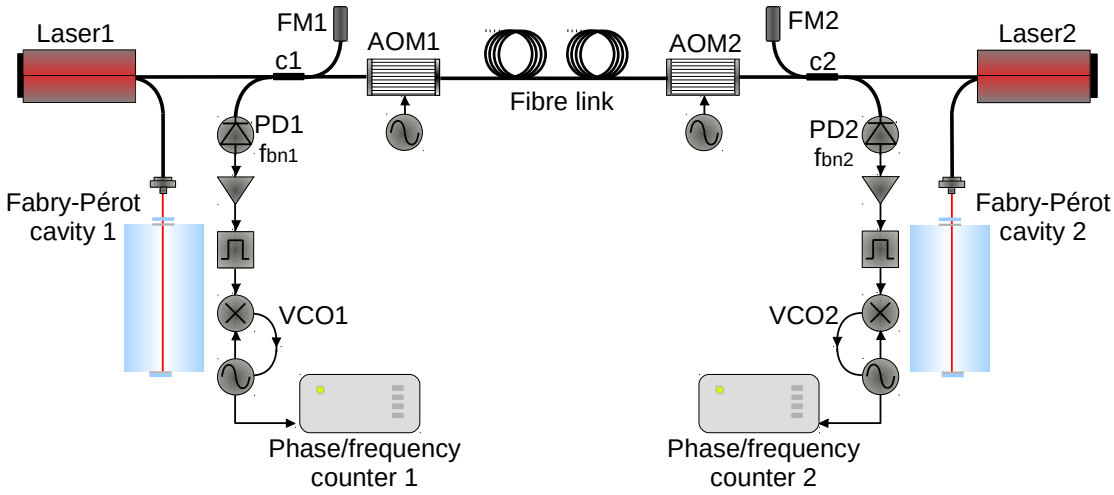

Figure 1.2: Optical and electronic setup for the two-way noise cancellation scheme. Two laser sources ($Laser_1$ and $Laser_2$) are frequency-stabilized against two optical cavities (Fabry-Pérot cavity 1 and 2) and launched in the fibre. c_1 and c_2 are the couplers for the interferometers at the two extremities of the link. AOM_1 and AOM_2 are the two acousto-optic modulators and FM_1 and FM_2 are the Faraday mirrors. At each side of the fibre a beat note (f_{bn1} and f_{bn2}) is detected with a photodiode (PD_1 and PD_2), tracked with a voltage-controlled oscillator (VCO_1 and VCO_2) and acquired by the local frequency counter (Frequency counter 1 and 2).

Post-processing of the data recorded at the two remote ends of the link is required: the noise contribution of the fibre is cancelled out by subtracting the two acquired data series. As a consequence, differently from the Doppler-noise cancellation scheme, this method is unable to provide a real-time noise compensation.
To mathematically derive the residual phase noise contribution of the link on the lasers comparison, we first consider the instantaneous phases of the two laser sources: $\phi_{\mathrm{L1}}(t)$ and $\phi_{\mathrm{L2}}(t)$. The instantaneous phase of f_{bn1} and f_{bn2} can be written as:

$$\phi_{\mathrm{bn1}}(t) = \phi_{\mathrm{L1}}(t) - \left[\phi_{\mathrm{L2}}\left(t - \frac{nL}{c}\right) + \overrightarrow{\phi}(t)\right] \tag{1.19}$$

and

$$\phi_{\mathrm{bn2}}(t) = \phi_{\mathrm{L2}}(t) - \left[\phi_{\mathrm{L1}}\left(t - \frac{nL}{c}\right) + \overleftarrow{\phi}(t)\right], \tag{1.20}$$

where $\overrightarrow{\phi}(t)$ and $\overleftarrow{\phi}(t)$ are the phase noise contributions of the fibre, experienced by the signals travelling in the two directions. The coherence length of the laser sources can be assumed much higher than the link length, thus $\phi_{\mathrm{L1}}(t) \approx \phi_{\mathrm{L1}}\left(t - \frac{nL}{c}\right)$ and $\phi_{\mathrm{L2}}(t) \approx \phi_{\mathrm{L2}}\left(t - \frac{nL}{c}\right)$. The phase comparison between the lasers is obtained by subtracting the two beat notes and dividing by 2.

$$\frac{\phi_{\mathrm{bn1}}(t) - \phi_{\mathrm{bn2}}(t)}{2} = \phi_{\mathrm{L1}}(t) - \phi_{\mathrm{L2}}(t) - \frac{\left(\overrightarrow{\phi}(t) - \overleftarrow{\phi}(t)\right)}{2}. \tag{1.21}$$

The term $\phi_{\text{fibre,DIFF}} = \frac{1}{2}\left(\overrightarrow{\phi}(t) - \overleftarrow{\phi}(t)\right)$ is the ultimate limit of the noise rejection set by the uncorrelated part of the noise affecting the two signals. This depends on the fact that the two signals travel along each portion of the fibre at different times. The residual phase noise perturbation can be evaluated as follows [107]:

$$\delta\phi_{\text{fibre,DIFF}}(t) = \frac{1}{2}\int_0^L \delta\phi_z\left(t - \tau + \frac{nz}{c}\right)dz - \int_0^L \delta\phi_z\left(t - \frac{nz}{c}\right)dz, \tag{1.22}$$

where $\delta\phi_z$ is the phase perturbation experienced by the counter propagating signals, at a z distance from extremity 1 of the fibre. By using the standard relations of the Fourier algebra, the PSD can be computed:

$$S_{\text{fibre,DIFF}}(f) = \frac{1}{12}(2\pi f\tau)^2 S_{\text{fibre}}(f). \tag{1.23}$$

This holds in the assumption that the PSD of the one-way noise $S_{\text{fibre}}(f)$ is uncorrelated with position. This technique has an additional rejection factor of $\frac{1}{4}$ with respect than the Doppler-noise cancellation.
A good synchronization between the remote acquisition systems (phase/frequency counter 1 and 2 in fig. 1.2) is required to obtain the highest noise rejection. Chapter 3 describes the implementation of the two-way technique on a testbed of 294 km of fibre and the analysis of the effects of possible timebase mismatches.
A variation of this two-way scheme is called "local" or "real-time" two-way and is presented in [80]. It combines the two-way with the Doppler-noise scheme. In each laboratory the laser is split into two: part is sent to the remote laboratory, while part, after a round-trip returns in the original one. The noise cancellation can be computed in real-time in both laboratories, by comparing the round-trip signal of the local laser and the one-way signal of the remote laser. The same rejection level of the standard two-way is achieved, avoiding the need of exchanging data between remote laboratories and relaxing the requirements on time synchronization. On the other hand, it does not benefit from the advantages of single-pass transmission as the standard two-way.
As for the Doppler-noise scheme, the performance of the two-way noise cancellation is deteriorated in case of a unidirectional infrastructure due to the uncorrelated part of the noise affecting adjacent fibres. [80] shows a noise rejection below 10^{-15} on 100 km fibre link.

1.2.3 Amplification and repeater laser stations

Considering P_0 the input power of a signal along a fibre, the transmitted power P_{T} is attenuated according to the law [108]:

$$P_{\text{T}} = P_0 e^{-\alpha L}, \tag{1.24}$$

where L is the link length and α is a measure of the total fibre loss usually expressed in dB/km as:

$$\alpha_{\mathrm{dB}} = -\frac{10}{L}\log\left(\frac{P_{\mathrm{T}}}{P_0}\right). \tag{1.25}$$

The main sources of losses are the medium absorption and the Rayleigh scattering. The first depends on the transmission wavelength: the electronic resonances of the glass of the fibre are in the ultra violet and far infrared spectral region, thus in the C band the absorption is mainly due to glass impurities. The Rayleigh scattering arises from density fluctuations in the fused silica, which result in fluctuations of the refractive index, scattering light in all directions. Since this effect is intrinsic to the fibre, it sets the ultimate limit on the fibre loss. Last generation fibres exhibit a minimum loss of $\alpha_{\mathrm{dB}} = 0.2\,\mathrm{dB/km}$, although in practical situations higher losses are introduced by fibre splicing and connections.
To recover for optical losses on long fibre links the following optical amplification techniques have been exploited.

Erbium Doped fibre Amplifier (EDFA). It is a concentrated amplification technique. The amplifier is based on a fibre patch, usually tens of metres long and doped with Er^+ ions, exploiting a scheme with three atomic levels, conceptually similar to a laser without feedback [109]. Stimulated emission at 1542 nm is obtained by pumping at 980 nm or 1450 nm, often using semiconductor lasers. The device is compact and agile, it is therefore widely used in telecommunications and by far the most exploited amplification technique for coherent fibre links [30, 41, 92, 110].
In order to meet the conditions of full reciprocity of propagation path, bidirectional EDFAs have been implemented. In these devices no component, such as isolators and circulators, is incorporated to separate the two propagating directions. As a consequence, beside the desired signal, unwanted interfering signals may rise, increasing the noise floor and deteriorating the SNR at the remote end of the link.
The first noise source is generated by the spontaneous emission of the amplifier. Spontaneous photons are amplified by the active fibre, originating the so called Amplified Spontaneous Emission (ASE) which forms a noise pedestal of several nanometres around the coherent signal. Additional noise is introduced by amplified back-reflections, either resulting from Rayleigh backscattering or occurring at the fibre connectors. If the gain is kept equal or slightly lower than the optical losses, the reflections at the connectors act as feedback and laser-like situations may rise. For this reason, the gain must be kept lower than in unidirectional amplifiers and it usually cannot exceed 20 dB. This allows to recover the loss of 60-80 km of in-field fibre, where the overall losses are usually higher than expected due to several splicing and connectors.
In case of fibre links longer than 100 km, cascaded bidirectional EDFA are employed.

In these conditions the consequences of back-reflections and ASE become more severe. The most detrimental effect is the amplification of stray signals generated by upstream amplifiers, which significantly reduces the optical SNR. A detailed calculation of the build-up of noise in a chain of bidirectional EDFAs can be found in [111]. For each specific link a careful tuning of the amplifiers gain is required in order to maximize the SNR. The most satisfactory conditions are generally achieved by reducing the gain of the single amplifiers and increasing the number of amplifiers along the chain [110].

Fibre Brillouin Amplifier (FBA). The Brillouin scattering arises from the non-linear interaction between a light wave and the acoustic phonons in the fibre, generating a back-scattered Stokes light-wave down-shifted by approximately 11 GHz. If the acoustic wave is generated via electrostriction, the process is referred to as Stimulated Brillouin Scattering (SBS) and is the base of the FBA [108].
An external diode laser is used as pump. If the signal to be amplified is at the same frequency as the Stokes light-wave, the pump is scattered coherently to the incoming signal, giving rise to a distributed amplification.
The threshold pump for activating the Brillouin amplification is few milliwatts. By increasing the pump, a logarithmic growth of the gain is observed up to a saturation point below 100 mW. The achievable gain is higher for decreasing signal power values, up to 60 dB amplification can be achieved for a signal of 1 nW. On the other hand, lower SNR are obtained for higher gains, e.g. for 60 dB gain a SNR = 20 dB is obtained on a bandwidth of 100 kHz [112]; thus such a high gain cannot be exploited in practice: for example with a pump power of 30 mW a SNR of 30 dB and a gain of 45 dB are achievable [112].
Such high gain values allow a smaller number of amplification stages with respect to infrastructures based only on EDFAs. In addition, the distributed nature of this type of amplification reduces all the issues related to amplified backreflections.
In comparison to EDFAs, FBAs require a much elaborated design. Two pump diodes are required, one for each propagating direction. The spectrum of the amplifier gain has a Lorentzian profile with a linewidth of 10 MHz, therefore the detuning frequency between the pump laser and the incoming signal needs to be stabilized to keep the amplification level constant. This requires to phase-lock the pump laser, which significantly increases the complexity of the system. In addition, to achieve the maximum gain, the polarization axes of signal and pump need to be aligned using a polarization control. If a dark channel infrastructure is exploited, the high power of the laser pump may cause some disturbances to data transmission on nearby channels, especially in case of unlocked pump; the detailed issues are described in appendix A.
FBA have been employed, as unique amplification technique, for a fibre link of 1400 km [113].

Distributed Raman Amplifier (DRA). This amplification technique is widely used in telecommunications, in particular for very long distances where EDFAs cannot be easily installed (i.e. submarine fibres). It is based on the Stimulated Raman Scattering, which consists in a transfer of power from a pump laser to the signal laser through the scattering of optical phonons. In order to obtain the maximum transfer of power at 1542 nm, the pump frequency has to be 13.7 THz higher than the signal [108]. Similarly to the FBA, the gain is polarization-sensitive, thus an automatic control is required to keep the polarization axes of pump and signal aligned. On the other hand, it is characterized by a bandwidth of several terahertz and no phase-lock is required allowing a simpler system. In addition, since the Raman scattering occurs in both directions, this technique is intrinsically bidirectional.
The Raman amplification for metrological dissemination has been tested on a fibre link of 180 km in dark channel configuration [114].

Repeater Laser Stations (RLS). Although the described amplification techniques can recover the optical losses on fibre links up to several hundreds of kilometres, some issues rise on ultra long-haul links, related to the noise introduced by cascaded amplifiers and to the length of the link itself. The latter increases the integrated phase noise of the free running fibre and reduces the compensation bandwidth.
For these reasons repetition laser stations have been introduced [105] (fig. 1.3). In

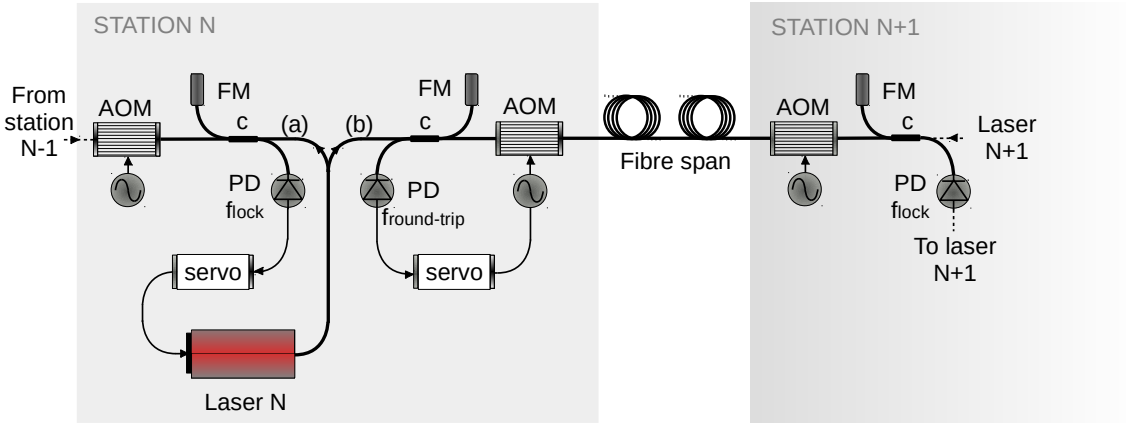

Figure 1.3: Optical and electronic apparatus of the N^{th} repetition station of cascaded links. A diode laser (Laser N) is phase-locked (f_{lock} to the incoming signal from the previous station (from station $N-1$). Part (a) is sent backwards to generate a round-trip signal in the previous station, while part (b) is sent forward to the next station. $f_{\text{round-trip}}$ is the beat note between local and round-trip signal to compensate for the noise of the following fibre span.

this configuration the link is divided into cascaded spans, and the intermediate stations are conceived to regenerate and disseminate the optical signal from one span to the next. Each station is equipped with a narrow linewidth diode laser (*Laser N*) which is phase-locked to the incoming signal. This results in a coherent regeneration of the signal.
In the N^{th} station of the chain, part of the regenerating laser is sent back to the preceding station $(N-1)$, where it is used to compensate for the noise of the link span between stations $N-1$ and N. The remainder is injected towards the next station $(N+1)$. The round-trip signal ($f_{\text{round-trip}}$) of the following span (between stations N and $N+1$) is also detected in station N, in order to correct the phase noise of the following fibre span.
This segmentation results in an improvement of the noise compensation since the control bandwidth decreases with the propagation delay. In particular, following the assumption that the noise of the free running fibre scales as the length of the fibre, the relative frequency stability of a cascaded link, divided into N segments, is expected to improve by a factor of $\sqrt{N}$ and the correction bandwidth is increased by a factor N [78], as compared to that of a single-span link. A fibre link infrastructure of 1100 km has been demonstrated in [78] using this approach. It achieved a noise rejection at the level of 5×10^{-20} level after 60 000 s measurements.
Moreover, cascaded links with RLS are useful in case of networks with a complex topology, enabling intermediate signal dropping. At each repetition station, part of the regenerated signal may be kept as absolute frequency reference for a local user.

1.2.4 The optical frequency comb

In order to distribute an absolute frequency reference via fibre link, the transfer laser has to be measured or frequency-locked to a frequency standard. Nowadays optical frequency combs [76] are used to bridge the gap between the microwave and optical domain, avoiding complex conversion chains. An optical comb consists in a mode-locked laser, i.e. a train of pulses whose repetition-rate is determined by the round-trip time of the light into the laser cavity.
Regarding the representation of the pulse train in the frequency domain, the comb spectrum is obtained (fig. 1.4); exploiting the non-linear effects of micro-structured optical fibres, it is broadened to a span of an octave [115]. Each line composing the spectrum can be expressed as:

$$\nu_m = m f_{\text{rep}} + f_0, \tag{1.26}$$

whose spacing is usually referred to as the repetition rate of the comb f_{rep}. Since the laser cavity is a dispersive medium, the group velocity of the pulse does not coincide with the phase velocity; as a consequence, a phase shift between the optical carrier and the envelop peak is generated, which is the reason why comb modes are

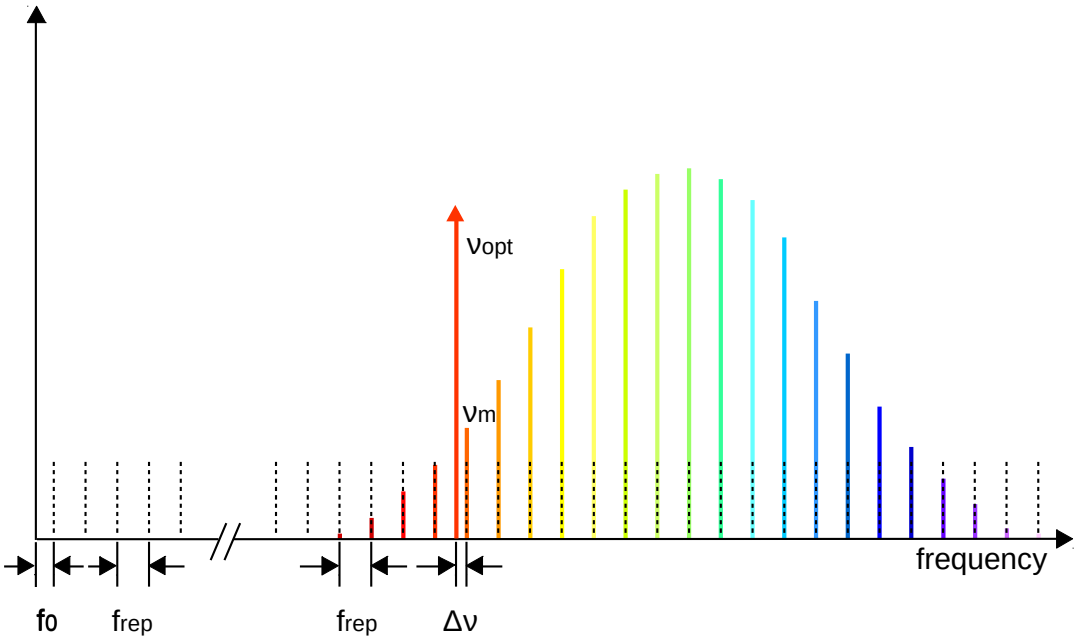

Figure 1.4: Frequency spectrum of the frequency comb. The repetition rate f_{rep} is the spacing between the comb "teeth", f_0 is the frequency offset of the comb spectrum, ν_{m} is the frequency of the m^{th} "tooth" of the comb. ν_{opt} is the optical frequency to be measured and $\Delta\nu$ is the frequency difference between ν_{opt} and the closest comb "tooth".

not integer of the repetition rate and are offset by f_0.
In principle, the measure of every optical frequency could be performed as:

$$\nu_{\mathrm{opt}} = m f_{\mathrm{rep}} + f_0 + \Delta\nu, \tag{1.27}$$

by determining $\Delta\nu$, m, f_0 and f_{rep}, as shown in fig. 1.4.
$\Delta\nu$ represents the beat note of the optical signal with the closest comb mode and is easily measured in the RF domain while m can be determined by a rough measurement of the unknown optical signal wavelength with a wavemeter having a resolution of 100 MHz.
f_0 is detected through the $f-2f$ interferometer. It is based on a second-harmonic-generator crystal which is used to frequency double each comb line obtaining $2f$. The frequency-doubled comb spectrum and the comb spectrum are then compared:

$$\delta\nu = 2\left(f_{\mathrm{rep}} + f_0\right) - \left(n f_{\mathrm{rep}} + f_0\right), \tag{1.28}$$

and f_0 is derived as the lowest order beat note between all comb lines: for each $n = 2m$, $\delta\nu = f_0$. It is stabilized against an RF reference by acting on the laser

pump power modes. This operation slightly modifies the refractive index of the active medium inside the cavity and in turns the dispersion.
The determination of the repetition rate is the most critical part. According to eq. (1.27), its uncertainty contribution is multiplied by the mode number, which is usually in the order of 10^6, limiting the overall measurement.
f_{rep} is detected by sending the comb to a fast photodiode and stabilized by changing the cavity length using piezo-mounted cavity mirrors. When f_0 and f_{rep} are stabilised to stable RF references and $\Delta\nu$ is measured on a frequency counter, the unknown laser frequency can be determined according to eq. (1.27).
The comb can also be used to perform relative frequency measurements between optical signals. In this case, the comb acts as a spectral bridge between the two optical frequencies ν_1 and ν_2 to be compared. The two optical frequencies can be written as follows, according to eq. (1.27):

$$\nu_1 = m_1 f_{\mathrm{rep}} + f_0 + \Delta\nu_1 \tag{1.29}$$

and

$$\nu_2 = m_2 f_{\mathrm{rep}} + f_0 + \Delta\nu_2. \tag{1.30}$$

The direct measure of the two optical signals would be limited by the accuracy of f_{rep} multiplied by the mode numbers m_1 and m_2. Whereas, through a proper manipulations of eq. (1.29) and (1.30) the ratio between ν_1 and ν_2 is obtained, which is independent from f_{rep} [116]:

$$\frac{\nu_2}{\nu_1} = \frac{m_2}{m_1}\left(1 - \frac{\nu_{\mathrm{c}}}{\nu_1}\right), \tag{1.31}$$

with:

$$\nu_c = \nu_1 - \nu 2 \times \frac{m_1}{m_2}. \tag{1.32}$$

Chapter 2

The Italian fibre link

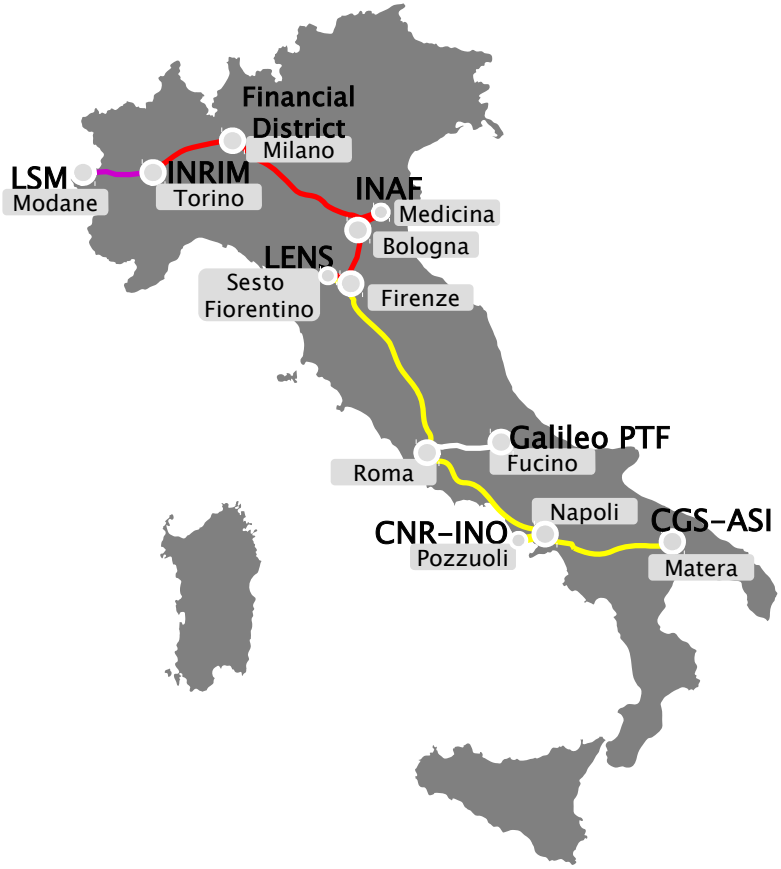

Figure 2.1: The Italian fibre link. Red line: link span under operation since 2014. Yellow line: extension in 2018. Purple line: link span connecting the INRIM to the French border, for a future connection to the European network.

In Italy in 2014 a coherent optical fibre connecting INRIM to the National

Institute for Astrophysics (INAF) in Medicina (near Bologna) and to the European Laboratory for Non-Linear Spectroscopy (LENS) in Sesto Fiorentino (near Firenze) was completed [30]. Since then, diverse experiments were carried out in collaboration with these institutes: high precision atom spectroscopy [50, 56] and absolute molecular spectroscopy in the mid infra-red [57] with LENS, and VLBI experiments [31] with INAF. On the same infrastructure a time dissemination over fibre is under development [117] exploiting the White Rabbit technique [53, 118]. A high precision time reference will be provided in 2019 to the financial district in Milano and to the other terminals of the backbone already receiving the frequency reference.
Another section of the link connects INRIM to LSM at the French border, and will allow a connection to the National Metrology Institute in France. This will also give access to the European network for more fibre-based comparisons of remote atomic clocks.
The extension of the fibre backbone towards the laboratories of the Space Geodesy Center (CGS) of the Italian Space Agency (ASI) in Matera was completed in November 2018. It has received funding from the Italian Ministry of Research and Education (MIUR) through Progetti Premiali ("Metrology for Geodesy and Space" - MetGeSp project) and is part of the OFTEN project. It is of particular interest, since it will provide the same frequency reference to two VLBI radio telescopes, Medicina and Matera, allowing common-clock VLBI observations with the two Italian antennas.
The link extension also provides an absolute frequency reference to the National Institute of Optics (INO) of the National Research Council (CNR) in Pozzuoli, near Napoli, for high resolution spectroscopy experiments. A further extension is planned from Roma towards the Galileo Precise Time Facility near Fucino.

2.1 The link infrastructure

2.1.1 The first link span: Torino-Medicina

The first span of the link between INRIM and Medicina is described here. A sketch of the metrological chain developed for the atomic clock dissemination and for the synthesis of the RF reference required by the radio observatory in Medicina is shown in fig. 2.2.
The frequency dissemination is based on the Doppler-noise cancellation technique. The ultrastable laser exhibits a linewidth below 10 Hz and the thermal control of the Fabry-Pérot cavity ensures a short-term stability at the level of 2×10^{-15} at 1 s and a residual drift of $< 1 \times 10^{-15}$ /s. To disseminate the reference of a frequency standard, the laser is frequency-locked laser to $\mathrm{HM}_{\mathrm{INRIM}}$, which in turn is regularly measured against the primary frequency standard ITCsF2, developed and

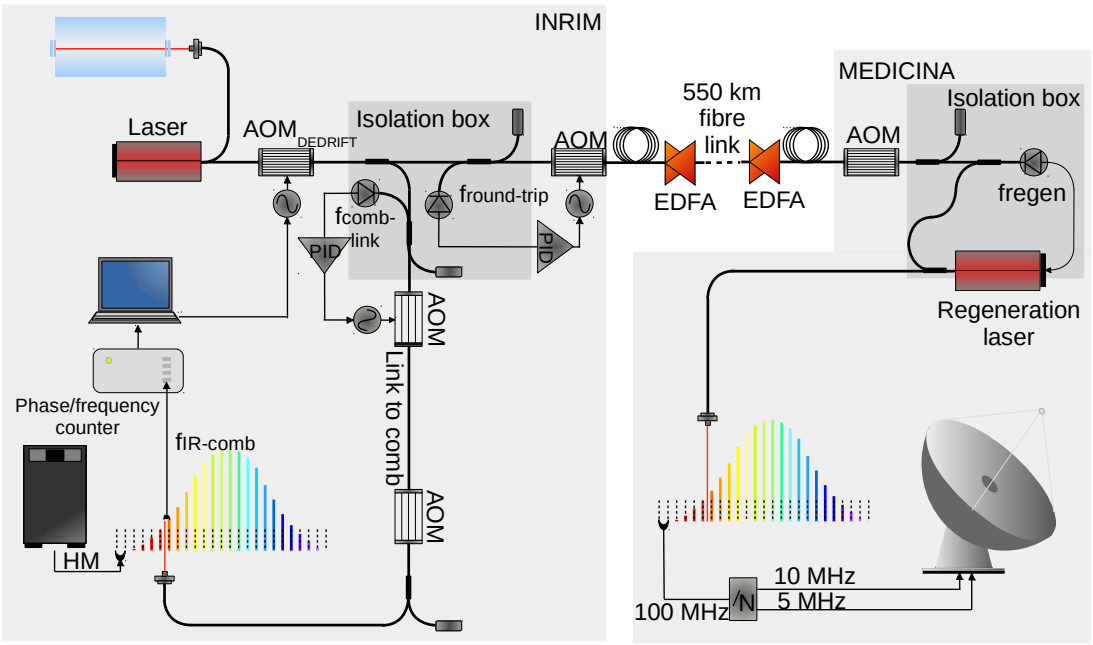

Figure 2.2: Metrological chain for optical reference dissemination and RF synthesis. The infrared laser is frequency-stabilized with a Fabry-Pérot cavity on the short term and frequency-locked to the Hydrogen Maser reference on the long term. This is done by stabilizing the beat note between laser and comb to a fixed frequency: the beat note is counted with a dead-time-free phase/frequency counter and a correction is digitally elaborated and fed to an acousto-optic modulator (AOM_{DEDRIFT}). The noise of the short link connecting the laser laboratory to the comb laboratory is phase-stabilized with the Doppler-noise compensation ($f_{\mathrm{comb\text{-}link}}$). The referenced laser is sent to Medicina along a 535-km-long link, provided with 9 bidirectional EDFAs for loss compensation. At the remote end the signal is regenerated by phase-locking a diode laser (regeneration laser) to the link signal. This is used to frequency-stabilize an optical comb, whose microwave spectrum is used to synthesize a 100 MHz reference for the radio antenna.

maintained at INRIM. The laser stabilization to the HM is done by extracting part of the laser and measuring it against the frequency comb. Both the comb repetition rate and f_0 are stabilized to the $\mathrm{HM}_{\mathrm{INRIM}}$ reference. The beat note between the IR laser and the closest mode of the comb is acquired with a dead-time-free phase/frequency counter [119] operated in "averaging mode". This amounts to a first order filter on the acquired signal, which ensures a sufficient rejection of the high frequency noise of the HM. The beat note is stabilized via software to a fixed value ($f_{\mathrm{IR,COMB}}$) using an AOM (AOM_{DEDRIFT} in fig. 2.2) as actuator. The locking bandwidth is 0.025 Hz, which is a compromise between a tight lock and a good rejection of the HM high-frequency noise. Since the laser stabilization system and the optical comb are placed in different laboratories, the fibre between the two

is actively stabilized. In addition, all couplers employed for the IR laser branching and as interferometers for the noise cancellations are housed in an isolation wood box and further shielded by insulating foam, to keep the noise contribution of uncompensated fibre branches at the 10^{-19} instability level. The resulting laser stability coincides with that of the HM, i.e. 1.5×10^{-14} at 10 s and 1.2×10^{-15} at 1000 s on a measurement bandwidth of 1 Hz. The residual drift has been evaluated $< 1 \times 10^{-19}$ /s and, after performing an independent measurement with another comb stabilized against the same reference, no frequency bias has been observed above 3×10^{-16}, limited by statistics (averaging time). This ensures an optical reference reproducing the frequency instability of the $\mathrm{HM}_{\mathrm{INRIM}}$ to be available at the remote end of the link as absolute reference.
The fibre link connecting INRIM to the observatory in Medicina is 535 km long, exploiting a dark fibre infrastructure, except for the last 21 km which are based on the dark channel transmission. The total loss has been evaluated ~ 150 dB. Eight bidirectional EDFAs are installed in intermediate telecom shelters and a ninth is installed in Medicina at the remote end of the link. The fibre phase noise is actively compensated for through the Doppler-noise cancellation scheme. The SNR obtained on the round-trip signal is 32 dB on 100 kHz resolution bandwidth. This ensures a low rate of cycle slips, i.e. sudden relocks of the PLL in different working points, that cause a loss of coherence on the delivered frequency signal. The cycle slips detection is performed by splitting into two the round-trip beat note after the photodiode. Each of the two signals is independently amplified, filtered and tracked with a VCO. All the data that deviate by more than half a cycle are discarded, which corresponds to a 0.5 Hz outlier for an acquisition at 1 s.
In Medicina the coherent signal is regenerated with a diode laser, whose free running frequency noise is $S_\nu(f) = \frac{A}{f}$, with $A = 4 \times 10^6\ \mathrm{Hz}^2$ and a linewidth of several kilohertz [120]. The regeneration is performed by phase-locking this diode laser to the incoming signal with a bandwidth of 50 kHz. The regenerated radiation is used as reference for the local optical comb. The closest comb mode is phase-locked to the diode laser with a bandwidth of ~ 200 kHz exploiting an intra-cavity electro-optic modulator and a piezo stretcher as actuator. The 100 MHz comb reference is generated by extracting the 40^{th} harmonic of the repetition rate and by dividing it by 100.
To match the range of input signals required for the VLBI synthesis chain in Medicina, the 100 MHz reference is sent to a low-noise frequency divider, which generates two signals at 10 MHz and 5 MHz and a Pulse per Second (PPS) used to trigger the timestamping of the data sampling. It exhibits the same stability of the comb-generated RF source but requires to be synchronized to a GPS-received PPS for the absolute timing.
The first characterization of the system performed by Clivati et al. in [121] showed that the stability of $\mathrm{HM}_{\mathrm{INRIM}}$-$\mathrm{HM}_{\mathrm{MEDICINA}}$ was limited at every averaging time by the instability of the HMs, specifically by $\mathrm{HM}_{\mathrm{MEDICINA}}$, 8×10^{-14} at 1 s and

2×10^{-15} at 1000 s on a 1 Hz measurement bandwidth. No frequency offset was detected within the HMs accuracy which is routinely evaluated via GPS.

2.1.2 The backbone extension: Medicina-Matera

Figure 2.3: Italian fibre link divided into four cascaded spans. At the four terminals the signal is regenerated and the noise of the following span is compensated.

From:	To:	Length (km)	EDFAs
Torino	Medicina	535	10
Medicina	Sesto Fiorentino	149	3
Sesto Fiorentino	Pozzuoli	668	11
Pozzuoli	Matera	387	6

Table 2.1: Terminals, length and number of amplification stages of the four link spans.

The extension of the Italian link has been planned as shown in fig. 2.3. The total

link length from Torino to Matera is 1739 km. To ensure a higher phase noise rejection the link has been divided into four cascaded spans (tab. 2.1). Moreover, since EDFAs are employed along the entire backbone to recover for optical losses, regenerating the signal at each terminal allows to interrupt the amplifier chain, reducing the build-up of ASE and amplitude noise. The terminals of the link host diverse physical experiments: atomic and molecular spectroscopy in Sesto Fiorentino and molecular spectroscopy in Pozzuoli. Such experiments have already experienced (as in Sesto Fiorentino, [50, 56, 57]) or will experience (as in Pozzuoli) an improvement in the measurement capability thanks to the high-stability frequency reference provided by the optical link.
The first span is described in the previous section and is routinely operated. A connection between INRIM and LENS already existed, although it did not allow the simultaneous dissemination to Medicina and Sesto Fiorentino. Hence the second span of the link has been implemented to allow the cascaded dissemination to the two laboratories. The third and fourth span were completely to be set up and characterized. This new section extends from LENS to Matera on a pair of dark fibres for a total length of 1055 km. The extension required the staging of 15 amplification stations (two more EDFAs are at the link ends in Pozzuoli and Matera) equipped with dedicated bidirectional EDFAs and telecontrol devices.

Amplification stations

Fig. 2.4 shows a map with the path of the link split into multiple spans by the cascaded EDFAs. Tab. 2.2 summarizes the length and optical losses for each span. A mapping of the phase noise along the whole fibre is shown in the plot of fig. 2.5. The characterization of the noise distribution from INRIM to Sesto F.no-LENS can be found in [30].
The phase noise of the link from LENS to intermediate shelters has been measured adopting the scheme shown in fig. 2.6. The light coming from LENS is frequency shifted by an AOM driven by a VCO. It is back-reflected with a Faraday mirror towards LENS, where the round-trip phase noise is recorded ($f_{\text{round-trip}}$). A complete characterization of the whole link was not possible for time and logistic reasons (not every intermediate shelter, housing the apparatuses, is accessible 24/7 and in some cases special permissions are required). The Firenze-Pozzuoli span is almost fully characterized, which allows us a study of the noise distribution along the fibre span. The spectra related to San Giovanni V.d.A., Lucignano and Città della Pieve have been taken with a free running diode laser. The contribution arising from the loss of coherence of the laser, as shown in eq. (1.13), is clearly evident for Fourier frequencies > 100 Hz. It is noted that the noise bump around 12 Hz has a significant increase in the second and fourth span. We attribute the acoustic noise bump to man-made activities, especially road traffic. Therefore, although the exact path of the fibre is not known, we can assume that the increase of noise is due to the

Figure 2.4: The map shows the position of the EDFAs installed along the link backbone. The orange EDFA were installed back in 2014, while the green EDFAs have been installed last year for the link extension. All the amplifiers are housed in telecom shelters except for the dark-orange and dark-green EDFAs which are placed in the laboratories at the span terminals.

From:	To:	Length (km)	Loss (dB)
Torino-INRIM	Torino	25	9
Torino	Santhià	67	18
Santhià	Novara	77	18
Novara	Lainate	50	15
Lainate	Rogoredo	60	18
Rogoredo	Piacenza	67	16
Piacenza	Reggio Emilia	94	23
Reggio Emilia	Bologna	74	19
Bologna	**Medicina INAF**	21	16
Medicina INAF	Bologna	21	17
Bologna	Rioveggio	38	10
Rioveggio	Firenze	72	18
Firenze	**Sesto Fiorentino LENS**	18	7
Sesto Fiorentino LENS	San Giovanni V.d.A.	64	20
San Giovanni V.d.A.	Lucignano	54	14
Lucignano	Città della Pieve	59	13
Città della Pieve	Giove	73	17
Giove	Capena	66	15
Capena	Roma	52	18
Roma	Pomezia	48	18
Pomezia	Latina	49	14
Latina	Riva Gaia	57	16
Riva Gaia	Minturno	57	16
Minturno	Napoli	81	21
Napoli	**Pozzuoli INO**	8	10
Pozzuoli INO	Napoli	8	9
Napoli	Salerno	87	24
Salerno	Sicignano	56	15
Sicignano	Trivigno	81	24
Trivigno	Macchia di Ferrandina	85	21
Macchia di Ferrandina	**Matera ASI**	70	19
		1739	508

Table 2.2: Summary of the length and optical losses of the link spans between Sesto Fiorentino and Matera separated by EDFAs

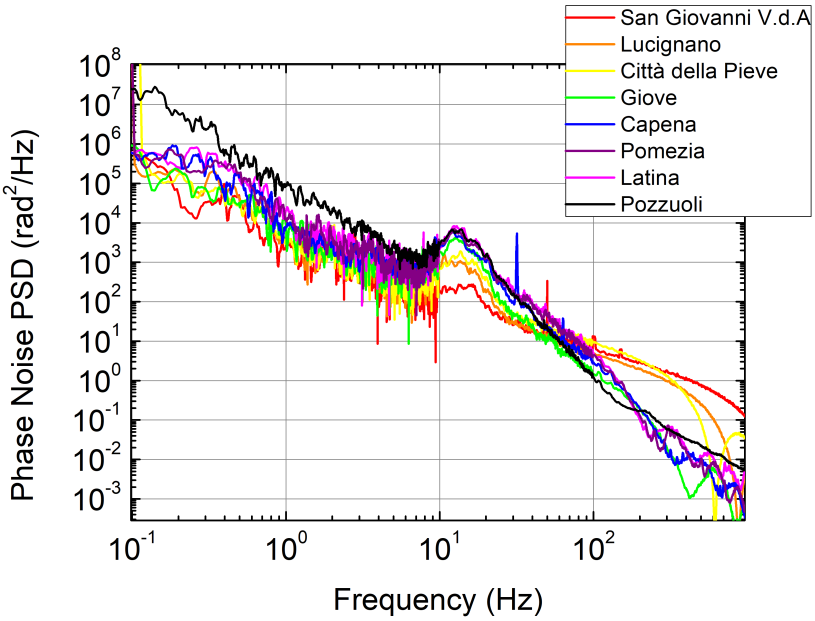

Figure 2.5: Phase noise PSDs of the fibre spans between some of the amplifier stations and LENS.

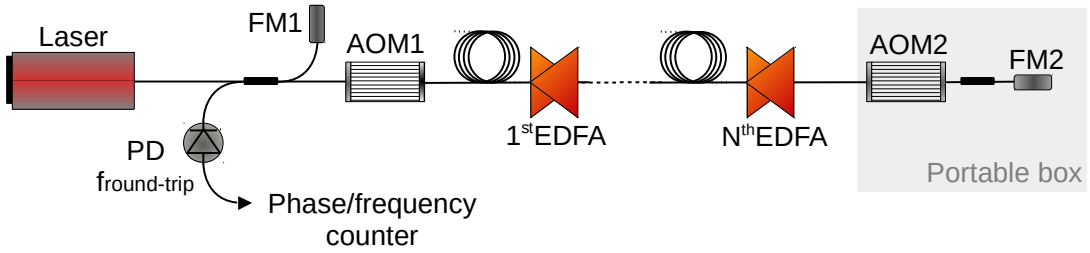

Figure 2.6: Optical and electronic apparatus for the fibre phase noise evaluation between LENS and intermediate amplification stations. The portable box contains an acousto-optic modulator (AOM), driven by a voltage-controlled oscillator (VCO), and a Faraday mirror (FM) to back-reflect the light and generate the round-trip signal.

proximity to main traffic arteries.
This effect can be seen also in fig. 2.7, which shows the phase noise PSD per-unit-length for fixed Fourier frequencies, namely 1 Hz and 12 Hz, vs the link length. $f = 12$ Hz has been chosen as representative of the acoustic peak. The first four graphs are related to the four link spans of the Torino-Matera backbone. The noise is almost uniformly distributed along the first and third span. The only exception can be seen on the first span at $\sim$ 300 km, where the fibre crosses the densely populated city of Milano and hence a higher noise contribution is observed. Particularly high is the noise at 1 Hz and 12 Hz on the Medicina-Sesto F.no span. To

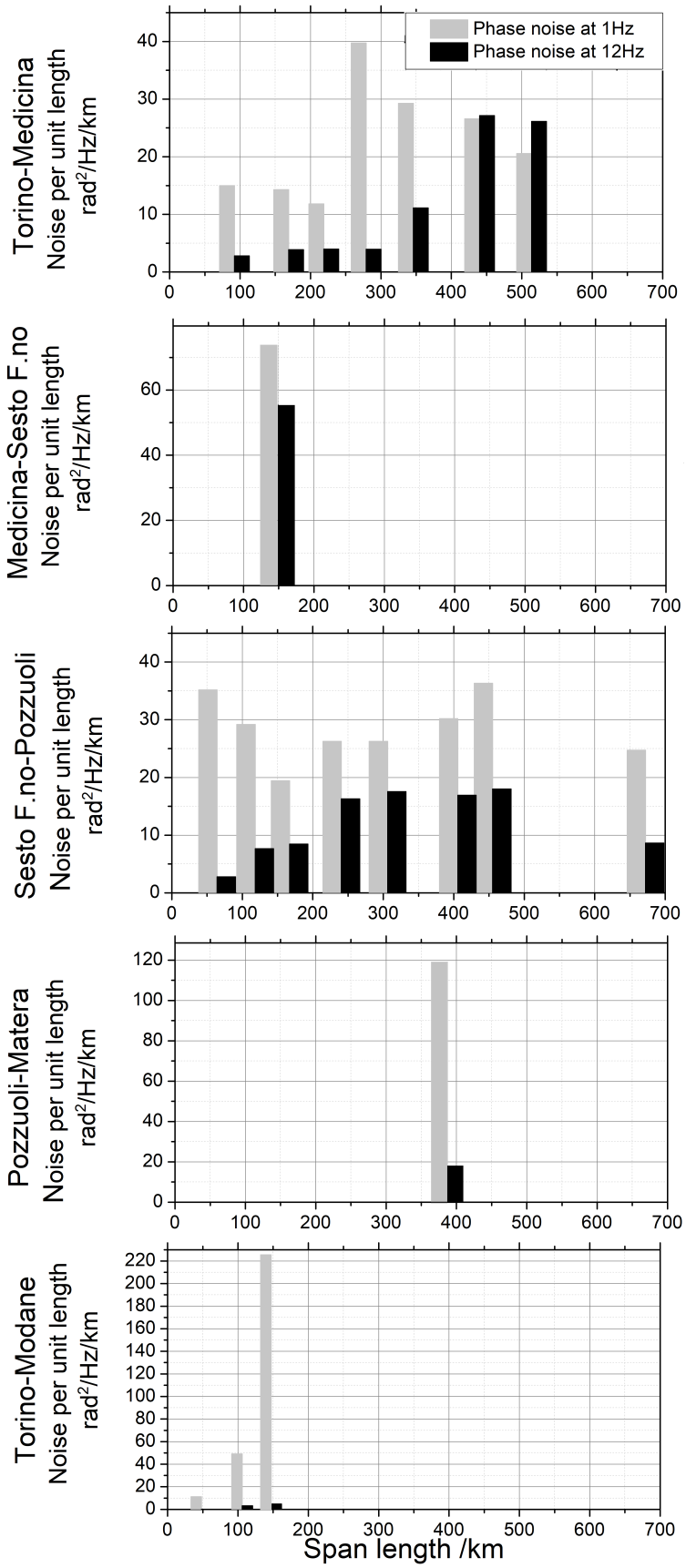

Figure 2.7: Phase noise PSD per-unit-length calculated at 1 Hz, grey bars, and 12 Hz (acoustic peak), black bars. The values are extracted from the noise spectra measured at intermediate stations of five link spans, form the top: Torino-Medicina, Medicina-Sesto Fiorentino, Sesto Fiorentino-Pozzuoli, Pozzuoli-Matera and Torino-Modane.

our knowledge the fibres of the Torino-Medicina and Medicina-Sesto F.no spans are running for a large part along the highway. However, since the precise fibre path is not available, no assumption can be made for the high noise exhibited by the Medicina-Sesto F.no fibres.
Particularly high is also the 3 Hz noise on the Pozzuoli-Matera span, which is probably due to aerial fibres. The entire fibre backbone is based on buried fibres except for the last span between Macchia di Ferrandina and Matera where ~ 5 km of fibre are suspended between poles. Unfortunately no intermediate noise measure is available for this last span to further investigate this aspect.
The fifth plot refers to the section of the Italian link connecting INRIM to LSM (see fig. 2.1) and is reported here for comparison. We know that the first span of this link is running in the metropolitan area of Torino, while the last section is entirely deployed next to the busy highway that runs from Torino to the Fréjus tunnel at the French border. The high environmental noise introduced along the highway may be attributed to the presence of trucks for commercial activities. However, no further information about the fibres sheathing and isolation is available.

Regeneration terminals

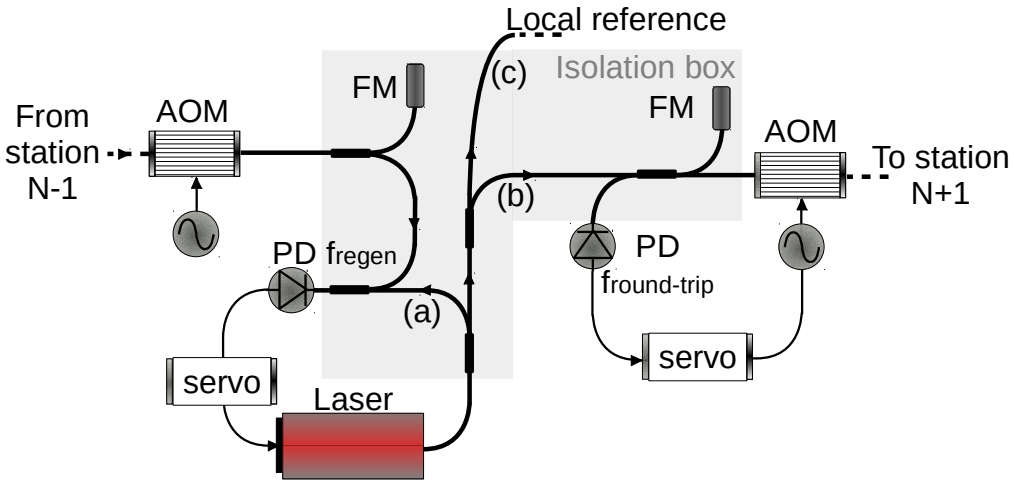

Figure 2.8: Optical and electronic apparatus of the regeneration stations at the link terminals. The regeneration laser is split into three branches: branch (a) is used to heterodyne mixing with the incoming signal to phase-lock the laser, branch (b) is injected into the next link span and (c) is kept as absolute frequency reference at the link terminal. Differently from the repetition stations presented in [78] and described in section 1.2.3, in this case the power of the incoming signal is high enough to be used as reference for regeneration phase-lock and to be backreflected for the round-trip signal generation.

The four regeneration terminals are located in Medicina (INAF), Sesto Fiorentino (LENS), Pozzuoli (CNR-INO) and Matera (ASI), with the same structure as that in

Medicina. Fig. 2.8 shows a complete sketch of one link terminal, including both the regeneration and the noise compensation setups. The electronic apparatus is provided with an automatic relock system, based on a single-board microcontroller, which allows remote operation of the regeneration stations. In particular this is required for VCOs and regeneration PLLs. The latter is fully automated at the LENS terminal, while a manual version has been temporarily installed in Pozzuoli and Matera. These devices will be upgraded in February 2019.
Each terminal is equipped with a router VPN, to which a public ip address has been assigned. In this way, both the instrumentation at the terminals and the link amplifiers can be accessed by any other device connected to the public network and provided with the VPN credentials. This ensures that each amplification station can be reached from the northern and the southern link terminals. This redundancy ensures higher immunity to fibre cuts and devices breakdowns. In addition, it allows a faster localization of possible failures or interruptions

Characterization

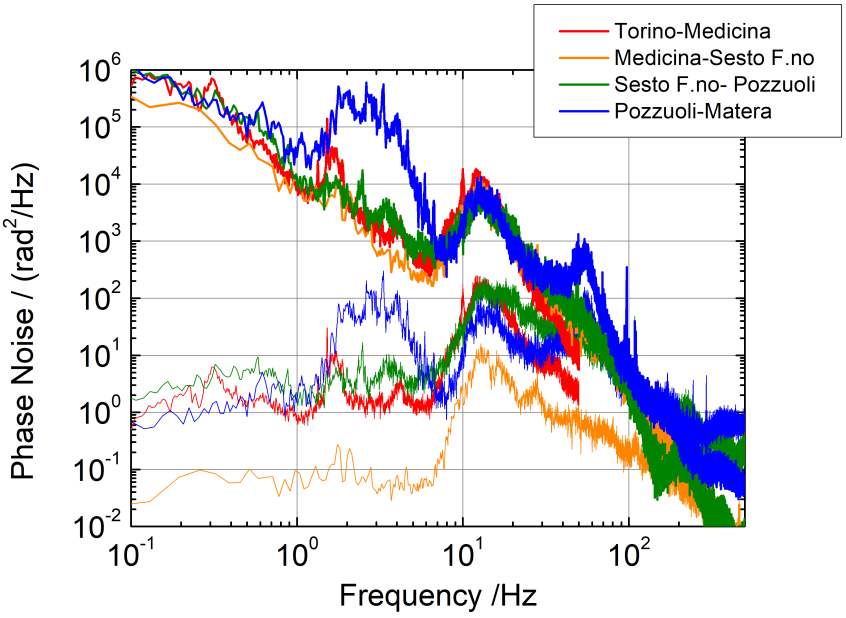

Figure 2.9: Phase noise PSDs of the four cascaded links. Red: Torino-Medicina. Yellow: Medicina-Sesto Fiorentino. Green: Sesto Fiorentino-Pozzuoli. Blue: Pozzuoli-Matera.

In fig. 2.9 the phase noise PSD of the four cascaded links is plotted (thick lines). In each spectrum is present a noise bump around 12 Hz due to acoustic noise. The noise bump around 3 Hz in the Pozzuoli-Matera link is attributed to the aerial fibres and may vary significantly, up to 20 dB, between different measurements. This can be explained since the noise on aerial fibres strongly depends on the weather

conditions, in particular to the wind speed.
Before installation, the performances of the loop control circuits have been tested in the INRIM laboratories, and no unexpected noise contribution has been observed. At every terminal the occurrence of cycle slips on the PLL for the link noise cancellation is monitored by redundantly tracking and counting the round-trip signals. The local oscillators of the intermediate stations in Matera and Medicina are referenced to the local HMs, which are GPS-disciplined, while the RF reference in Pozzuoli is provided by a GPS-disciplined Rubidium clock. Thus, the reference relative instability is expected to be at the 10^{-13} level at 1 s for the HMs and at the 10^{-11} level at 1 s for the Rubidium clock. This means an absolute uncertainty contribution of 10^{-4} Hz, which corresponds to a relative uncertainty at the 5×10^{-19} level on the optical signal, below the expected stability contribution of the compensated link noise. On the other hand, the RF reference currently employed at LENS is a free running oven-controlled quartz oscillator, whose relative uncertainty is estimated at the 10^{-8} level. It results in a relative uncertainty at the 10^{-15} level on the optical signal, which is comparable to the stability of the ultrastable laser delivered from INRIM when locked to the HM after 24 hours measurements. Therefore, undesired frequency shifts may be introduced to the disseminated signal, setting an ultimate limit to the uncertainty of the delivered frequency reference. This will be taken into account when analysing the first remote HMs comparisons (chapter 5) and a GPS-calibrated reference will be exploited in the future.
The residual phase noise at each span end has not been characterized yet, since it would require to double each link span as performed in [30]. However, an estimation of the expected delay-limited noise can be performed. The PSDs of the compensated fibre noise at the four span ends are estimated according to eq. (1.11) and are represented by the thinner-line spectra in fig. 2.9. By summing the contributions of the four spans, an instability of $\sim 4 \times 10^{-15}\tau^{-1}$ is calculated, which is more than enough to meet the requirements of our experiments. Indeed, the instability achieved by the masers comparison after 24 hours measurement is expected at the 10^{-15} level, while for the experiment of molecular spectroscopy with CNR-INO the stability requirements are even less stringent, since the expected uncertainties are at the 10^{-13} level.

2.2 Improvements in reliability

All the experiments performed in the intermediate stations of the link backbone require the fibre link to run for several hours without interruption. In particular the VLBI observations (see section 5.1) last 24 hours. A limited number of failures of the frequency synthesis chain is tolerated by routine analysis software, and any failure affects the overall result. So, guaranteeing the highest possible uptime at each of the network nodes is mandatory. In previous experiments [31] an uptime

of more than 90% has been achieved. The interruption in the dissemination is due to unlocks of some components of the metrological chain described above.
A technical upgrade of the setup has been planned with the goal of a 100% uptime of the link infrastructure; its implementation and results on the Torino-Medicina span are described hereafter.

2.2.1 Automatic control of the optical amplifiers

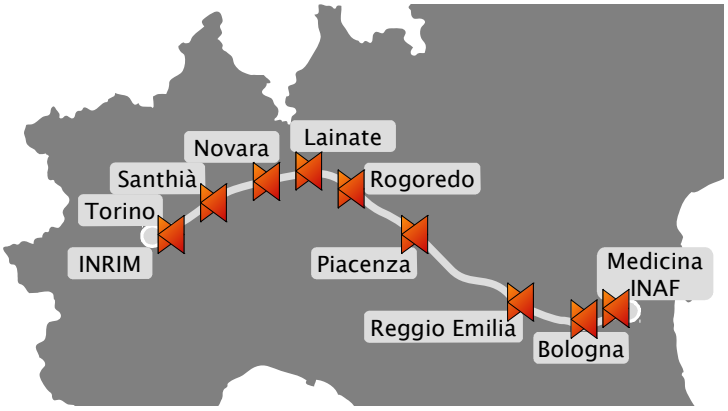

Figure 2.10: Amplification stations of the link Torino-Medicina. Each station is equipped with a bidirectional EDFA and system for the remote control.

The first critical aspect of this chain is represented by the nine optical bidirectional amplifiers, installed in intermediate telecom shelters along the 535 km link (fig. 2.10). During the installation the working point of each amplifier was carefully tuned, increasing the pump power up to the level where cycle slips started to be detected on the round-trip beat note.
Damages and cuts repairing may change the configuration of the fibres in terms of splicing and connections, increasing the total loss of the link. Moreover, the amplifiers are hosted in environments which are not intended for scientific applications: the room temperature is not always controlled and, even when an air conditioning system is present, this does not guarantee a good room temperature stabilization. This generates variations of several dBs over a day on the amplifiers gain. Due to all these factors the amplifiers setpoint need to be routinely adjusted.
Fig. 2.11 shows the gain variations of four amplifiers of the chain over 24 hours, starting from Monday 5 June 2017 at 9.30 am. The strong gain oscillations on the Santhià amplifier can be attributed to the cycles of the air conditioning system installed in the amplifier housing room. The same cause, although not verified,

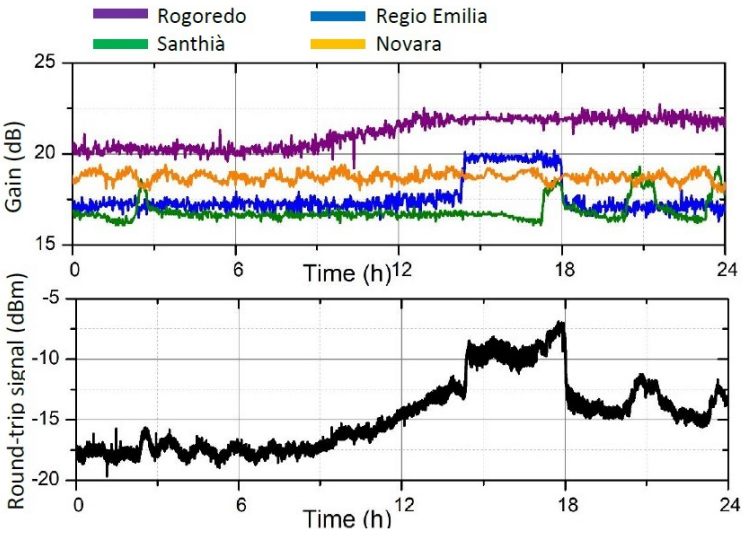

Figure 2.11: Upper graph: variation of the gain of four bidirectional EDFAs. Green: Santihià. Yellow: Novara. Red: Rogoredo. Blue: Reggio Emilia. Lower graph: variation of the amplitude of the round-trip signal over 24 hours, starting from Monday 5 June 2017 at 9.30 am (black line).

can be presumed for the oscillation on the Novara amplifier. On the Reggio Emilia amplifier the gain rises by almost 3 dB for more than three hours with a steep step, which can be traced back to a power surge, while the slow increment of 2 dB on the Rogoredo amplifier can be due to a thermal effect; however, a practical verification would be very difficult to perform and not particularly useful as these sources of gain variation could not be overcome.
The consequent amplitude variations on the round-trip signal exceed 10 dB on a daily basis. Such a high change prevents from a clean signal detection, causing a strong increment of cycle slips together with numerous unlocks of the tracking VCOs, as the RF power is directly proportional to the VCO locking bandwidth.
A real-time remote control of the gain of the installed amplifiers was implemented. Our devices were equipped with a GSM-based control, which however proved to be insufficient in terms of response time and reliability.

Remote control system

The new remote control system is based on the standard scheme employed in telecommunications for internet data transmission which exploits a fibre pair transmitting data in opposite directions. The setup has been designed in collaboration with one of our fibre providers, TOP-IX consortium.
In fig. 2.12 a sketch of the telecontrol devices installed in every amplification stage is shown. Each of the four incoming fibres is connected to a Dense Wavelength Division Multiplexer (DWDM). This is a 3-port device acting as a filter and wavelength separator: when the signal is sent to the Common port, light at a specific

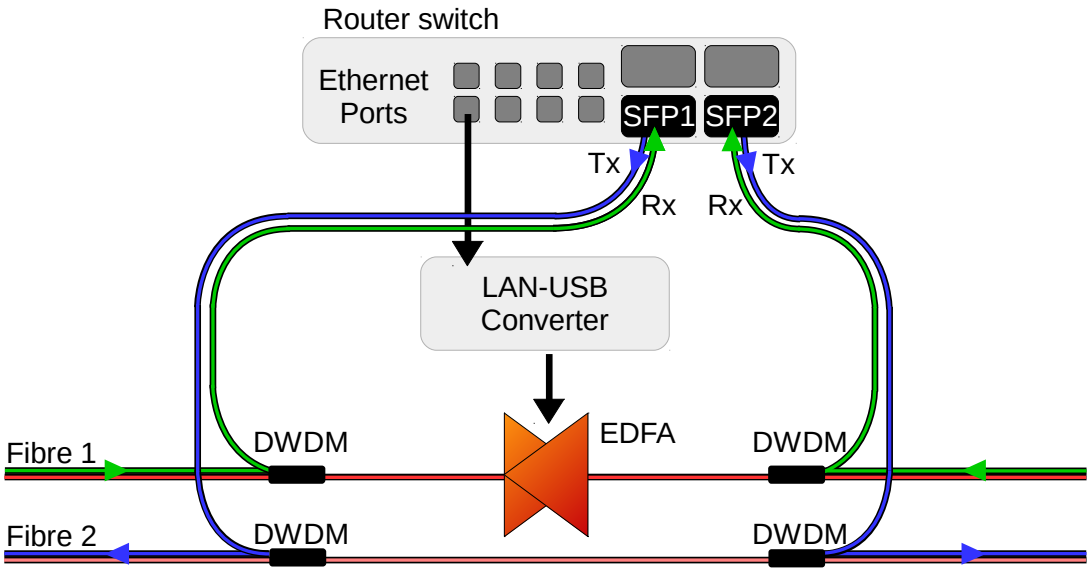

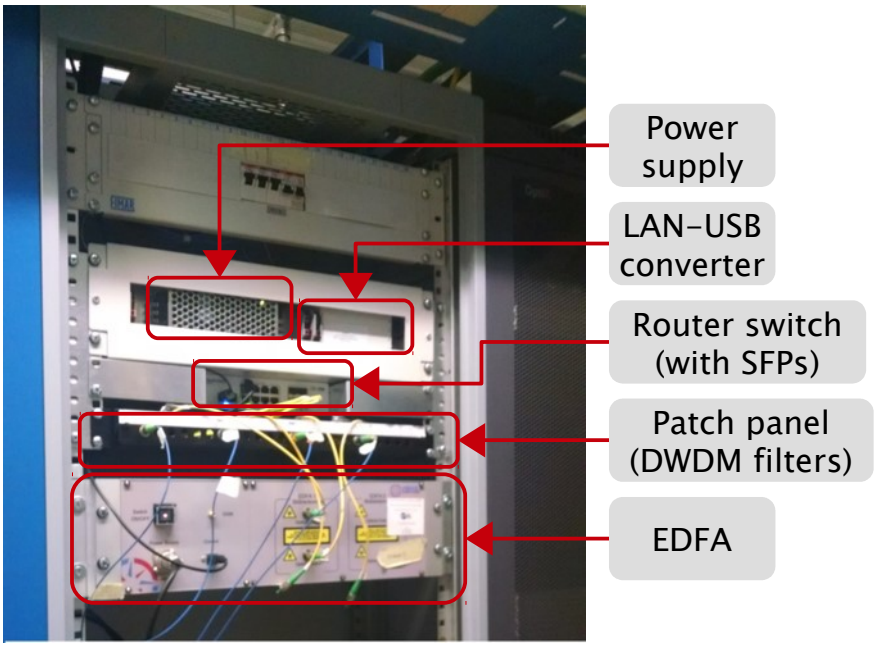

Figure 2.12: Scheme of the remote control system of one station. Fibre 1 carries the metrological signal on ITU channel 44 and the data signal at 1610 nm, Fibre 2 carries the data signal in the opposite direction. The DWDM filters are used to extract the metrological signal from the data. SFP1 and SFP2 are used to transduce the optical data packets (received, Rx, and transmitted, Tx) to electronics, which in turn are managed with a router switch. The commands are sent from the switch to the amplifier via ethernet and subsequently converted into USB (LAN-USB converter).

wavelength is extracted to the Signal port, while all other signals are sent to the Reflection port. Vice versa, the DWDM act as a wavelength combiner for light coupled into the Signal and Reflection port. Our devices separate light at 194.4 GHz or 1542.14 nm, which corresponds to the channel 44 of the ITU grid. This has a twofold purpose: on one hand it is used to filter out the broad-band ASE noise generated by the EDFA, avoiding gain saturation and reducing multiple ASE back-reflections along the link. On the other hand it allows to separate the metrological signal, which is sent to the EDFA for amplification, from the data used for the EDFA remote control. In our infrastructure one fibre (Fibre 1 in fig. 2.12) carries both data and metrological signal, while the other fibre (Fibre 2 in fig. 2.12) is solely employed for data transmission in the other direction. This approach allows easy reconfiguration if data transmission on other channels is required (e.g. for the White Rabbit implementation). In fact, multiple DWDM operating at different wavelengths can be cascaded.
The data signal for the telecontrol is transmitted on the ITU channel at 1610 nm of the Coarse Wavelength Division Multiplexing (CWDM) technology. It is deviated to the DWDM Reflection port and sent to a commercial router switch manufactured by Mikrotik. Each switch is provided with eight Gigabit Ethernet ports (one in use) and four Small Form-factor Pluggable (SFP) cages (two in use). Each SFP transceiver is used to convert the received optic signal into electric and vice versa. It consists in a laser emitting in the C-band (at 1610 nm in our case), which is amplitude-modulated to encode the signal to be transmitted (Tx), while a fast photodiode is used to detect the incoming signal (Rx) and convert it into electric. Each SFP is connected to a pair of fibres, one used in Receiving, the other in Transmission.
The ethernet outputs are used to control local devices, in this case the bidirectional EDFA. Since the installed amplifiers do not have any ethernet port available, a LAN-USB converter is used to translate the ethernet data into usb commands.
To ensure the security of the system and to protect it from external cyber-attacks, all devices are running inside a virtual private network (VPN). A VPN router is installed at INRIM, allowing a direct access to all the devices while any external user can log into the VPN if provided with credentials. The system is based on a cascaded connection, if a breakdown occurs at one station the following amplifiers of the chain are automatically out of connection. For this reason, more routers VPN are installed in each intermediate link terminal and connected to the public internet network. In this way, each amplifier of the link can be accessed both from the North and South sides, ensuring higher robustness to the system against fibre cuts.

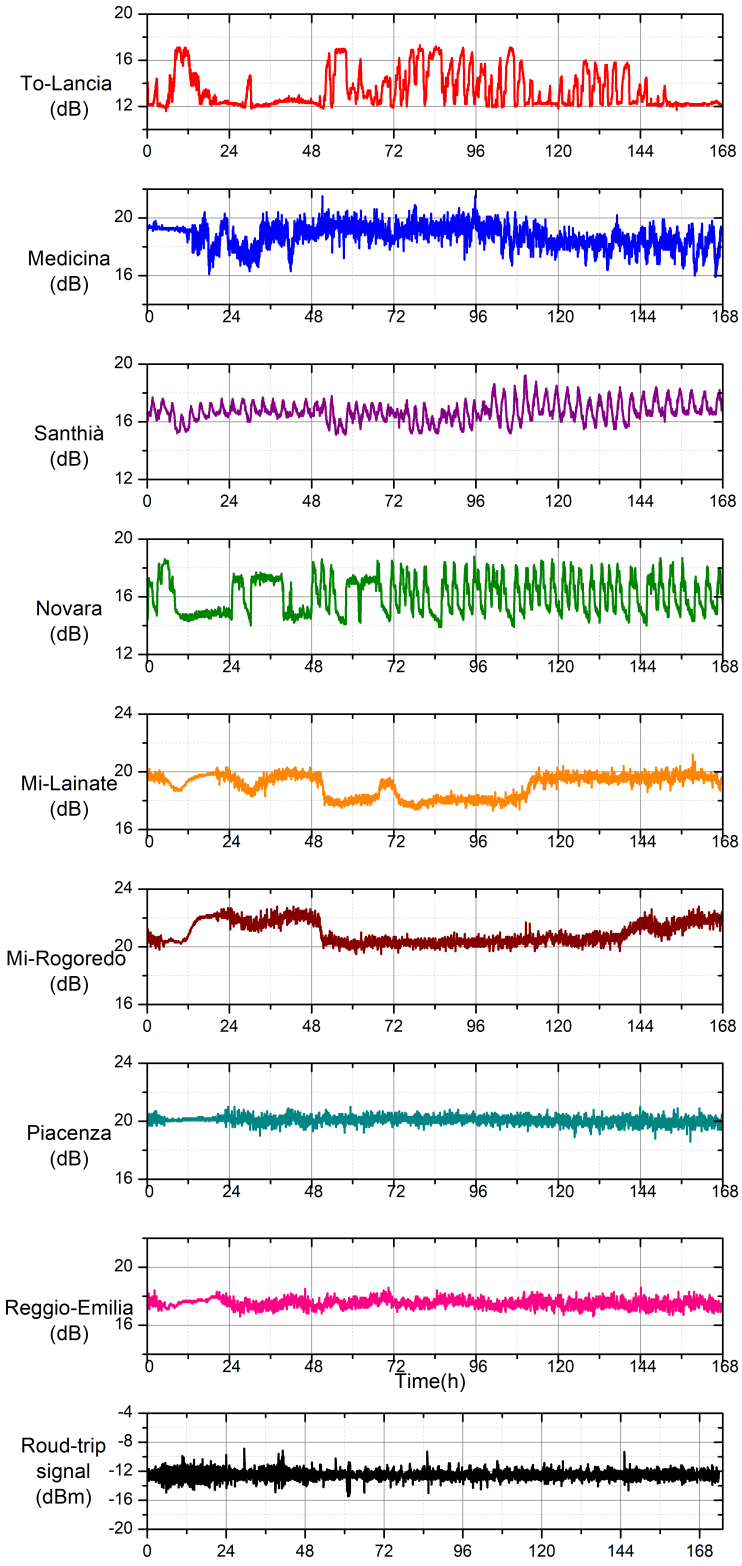

Figure 2.13: Amplitude and gain variation over 7 days, starting from Monday 21 October 2018 at 12 am. Black line: peak amplitude of the round-trip signal in Torino. Red and Blue lines: gain of the two bidirectional EDFAs used as actuators. The other traces refer to the gain of the remaining amplifiers of the chain.

Amplifier gain control

This telecontrol system allows a real-time adjustment of the amplifiers set-point and a monitor of their functionalities. In addition, we can read the input and output signal power levels, through the EDFA-embedded photodiodes. From these readings the gain variations over time of each EDFA are calculated and plotted in fig. 2.13. The gain of the Bologna amplifier is not shown, since it is a different EDFA model, not provided with photodiodes. In order to ensure the overall gain of the amplifiers chain to remain constant over time an automatic control-system has been implemented. It relies on the detection of the round-trip beat note with a spectrum analyser, the peak value is acquired by averaging over 300 measurements to reduce the amplitude noise. If the peak value exceeds the chosen thresholds, a correction is digitally calculated and applied to a selected amplifier of the chain used as actuator. The Lancia amplifier (red line) has been chosen to this scope, since its working point is preset at half of the available range for the pump current, differently from the other amplifiers which are working at the higher limit of the dynamic range. It is straightforward to notice on the red trace the compensation of the temperature oscillations of the amplifiers in Santhià and Novara. The increase of the Lancia gain from $\sim 12\,\mathrm{dB}$ to $\sim 16\,\mathrm{dB}$ after hour 48 can be attributed to the gain reduction in Lainate and Rogoredo.
Since the dynamic of the Lancia amplifier is not enough to compensate for the overall variation of the amplifiers chain, the amplifier in Medicina has been chosen as second actuator. The correction signal is sent to this later amplifier whenever the setpoint of the Lancia amplifier exceeds its dynamic range. From fig. 2.13 it can be easily seen that, once Lancia reaches a 12 dB gain amplification (corresponding to the lowest pump current that can be set without turning the EDFA off), the gain of the Medicina EDFA is also reduced to keep the round-trip signal constant. This is particularly evident at hour 12. Further activations of the Medicina EDFA can be seen between hour 108 and hour 120 and after hour 144. Those last are less evident since the gain corrections are superimposed to the spontaneous gain variations of the amplifier.
Thanks to this automatic control, the amplitude variations of the round-trip signal are kept within 2 dB, allowing an uptime for the noise compensation system of more than seven days, limited by a failure of the pc that caused the interruption of the amplifier control software. In addition, the rate of cycle slips has been strongly reduced as the round-trip beat note power was kept constant over time: below 100 over seven days (fig. 2.14).
This automatic control system is extremely useful also because it returns a real-time monitor of the integrity of the fibres. Any fibre cut or abrupt decrease of the signal is immediately detected.

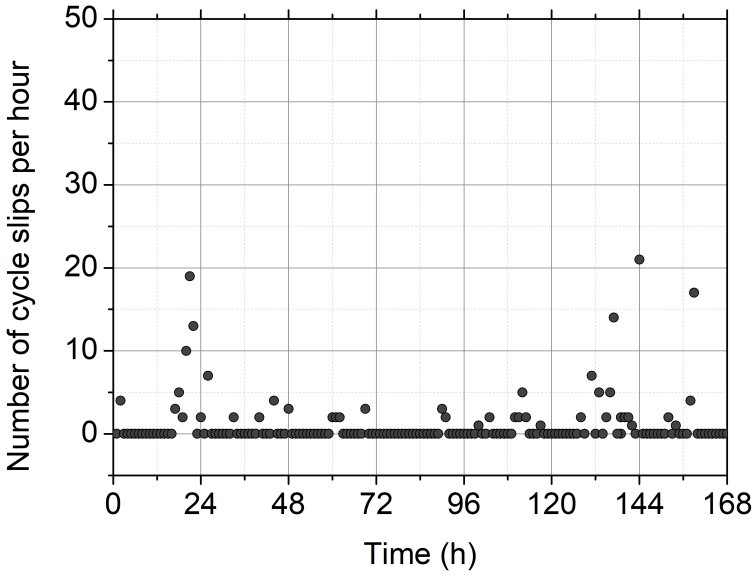

Figure 2.14: Blue dots: number of detected cycle slips per hour, over seven days measurement.

2.2.2 Polarization control

The second critical point of the chain is the signal regeneration at the remote end of the link. For a robust phase-lock the amplitude of the beat note between the incoming signal and the local regeneration laser must be stable over time. In fact, the power variations directly affect the bandwidth of the phase-lock since the phase detector is a mixer used in the phase quadrature condition. In addition, a degradation in the SNR at detection affects cycles slips and in the worst case, a power drop may lead to unlocks of the PLL. Most power variations depend on the drift of the incoming signal polarization plane, due to time-varying birefringence of the optical fibre. To compensate for them an automatic polarization control has been implemented.
It relies on a fibre polarization scrambler placed at the remote end of the fibre link. It converts any input state of polarization to any output state by applying a DC voltage to four independent piezo-actuated fibre squeezers with different orientations. The voltage channels are driven by a microcontroller through four digital-to-analog converters. The voltage levels are calculated following an optimization algorithm, designed to maximize the amplitude of the regeneration beat note. The amplitude level is monitored by acquiring the peak value of the beat note from a spectrum analyser; to overcome the amplitude noise, the acquisition is the result of 300 averaged measurements.
The polarization adjustment is started whenever the signal drops below a certain

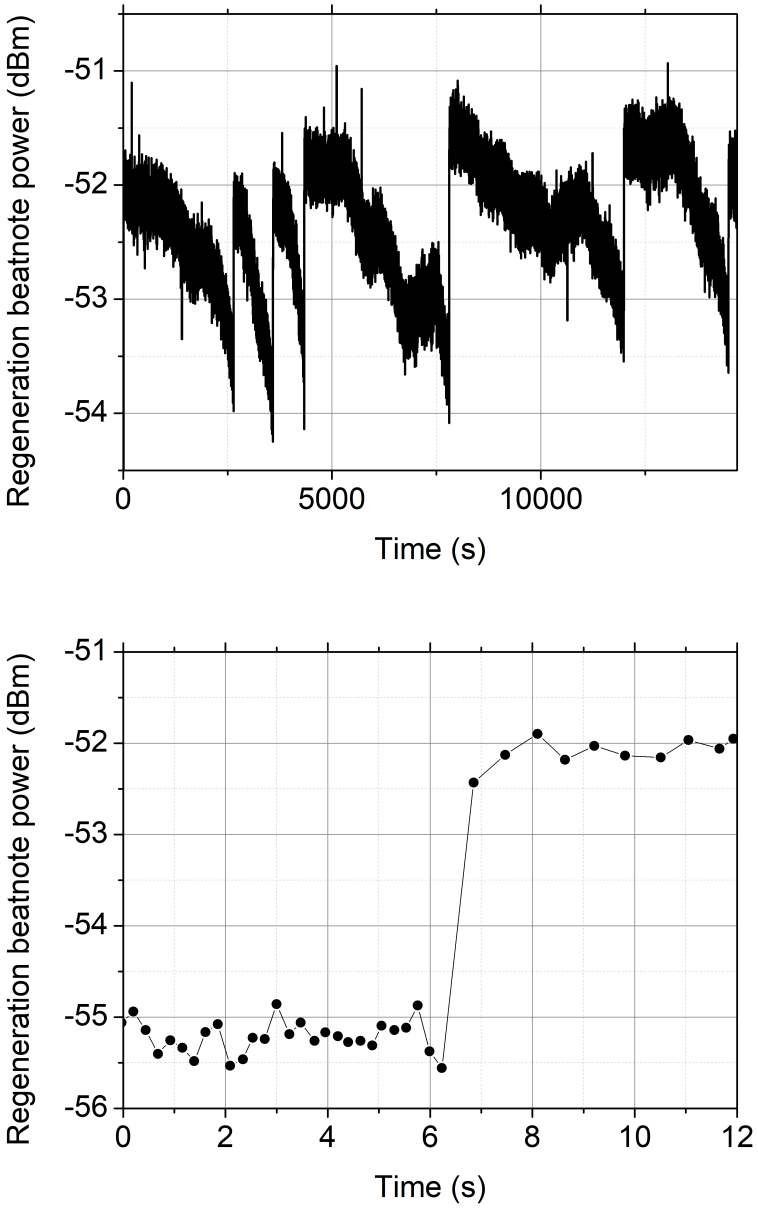

Figure 2.15: Upper plot: peak power level of the regeneration beat note with active polarization control over approximately 3.5 hours. Lower plot: zoom of a situation in which the polarization control is activated and the peak amplitude is recovered.

threshold. The polarization controller has an unpredictable behaviour, which depends on the input polarization state and on the previous squeezers configuration. Hence, the effect of a given voltage on the output polarization state is in principle unknown. Therefore, the algorithm cyclically applies a small perturbation to

each control channel, to detect the direction for which the peak power is increased. Once the sign is determined, the algorithm proceeds with small increments in that direction, until a maximum is reached. The procedure is repeated on the following channels and the complete cycle is repeated until the power increases above the predefined threshold. It is activated between 10 and 20 times a day and the response time of the correction is of $\sim 1\,\mathrm{s}$ (fig. 2.15). It is mainly limited by the response time of the spectrum analyser and by the averaging over 300 acquisitions. Nevertheless, this is enough to compensate for the slow variation of polarization state which is due to environmental effects on the fibre.
With this control system the SNR on the regeneration beat note can be kept at 45 dB in 100 kHz resolution bandwidth. Seven days without unlocks have been achieved and no cycle slips are detected on the regeneration beat note. Still, unexpected fast flips of the polarization state in the link-disseminated signal, with consequent unlocks of the system, can occasionally happen, which have been attributed to human work along the fibre line and cannot be predicted. They currently represent the major weakness of the overall chain and would require a higher correction bandwidth to be compensated for.
The first limit to the correction bandwidth of the system is currently represented by the acquisition time required by the spectrum analyser. By substituting it with a different type of power detector, e.g. an analog RF power detector directly connected to the microcontroller through an analog-to-digital converter, the response time is expected to be reduced up to a factor of 10. However, this would result in a correction bandwidth of $\sim 100\,\mathrm{mHz}$, which is not enough to cope with the fast polarization changes we observed. The second limiting factor is the requirement of averaging over multiple acquisitions to overcome the amplitude noise of the optical signal, which is mainly generated by the cascaded bidirectional EDFAs. Therefore, the number of acquisitions, which is currently set to 300, cannot be significantly reduced with fibre links of hundreds of kilometres. In addition, the unpredictable behaviour of the polarization scrambler in use requires to determine the correction sign before every correction cycle, by probing both signs on each channel. This part of the optimization algorithm increases the computational time and cannot be overcome with similar types of actuators, since it depends on the unpredictable relation between the input polarization state and the squeezers configuration. The number of averages and the optimization algorithm set the ultimate limit to the correction bandwidth.
An alternative approach to overcome the issue of fast polarization variations based on digital signal processing has been proposed in [122] and is still under investigation. It takes advantage of a dual-polarization coherent receiver, currently used in telecommunications, which enables to extract from the optical signals the phase information and perform a digital phase-lock regardless the polarization state. It has been demonstrated to be effective in experimental conditions where the polarization is subjected to fast polarization changes.

Chapter 3

Two-way frequency transfer over fibre

This chapter describes the realization and characterization of a setup for a two-way frequency transfer over fibre link. In comparison with the Doppler-noise cancellation, this technique does not require a round-trip signal, becoming less sensible to power losses and signal deteriorations due to phase noise and ASE, as highlighted in [80, 107]. The residual fibre noise of the two-way difference, is described by the formula:

$$S_{\text{fibre,two-way}}(f) = \frac{1}{3}(2\pi f\tau)^2 S_{\text{fibre}}(f), \tag{3.1}$$

where τ is the one-way travelling time of the light along the fibre and $S_{\text{fibre}}(f)$ is the noise of the uncompensated fibre. It is worth to notice that, in case of a remote clocks or lasers comparison, this contribution is further divided by a factor of two, to retrieve the clocks difference. Thus the PSD of the fibre noise contribution becomes:

$$S_{\text{two-way comparison}}(f) = \frac{1}{12}(2\pi f\tau)^2 S_{\text{fibre}}(f). \tag{3.2}$$

In this chapter, in order to assess the rejection level of fibre noise, we evaluate the noise contribution expressed by eq. (3.1).
We present the realization of two-way frequency dissemination over fibre on a 294 km multiplexed link. In previous works, the two-way scheme has been demonstrated on fibre loop testbeds, with the two ends of the fibre in the same laboratory, allowing to share the same laser for the two propagating directions and to employ one common acquisition system. Here, we realized two completely independent setups at the two link ends, to fully resemble a frequency comparison between remote laboratories. This includes different lasers and separate acquisition systems, allowing to investigate the synchronization requirements and to assess the ultimate limit of the two-way noise cancellation.
The results of this work can be found in [81].

The fibre testbed

Our measurements were performed on a 294 km fibre loop composed of two fibres, 147 km long, deployed between INRIM and the Laboratorie Souterrain de Modane (LSM), in the Fréjus tunnel (fig. 3.1). Part of the link (14 km) is established on a Coarse-wavelength division multiplexing architecture, while the remainder (280 km) is on a Dense-wavelength division multiplexing, where channel 44 (194.4 THz, or 1542.14 nm) is dedicated to the metrological signal.
Two bidirectional EDFAs are placed on each fibre, with an additional EDFA in Modane. Fig. 3.1 shows a map of the fibres split into three spans by the cascaded amplifiers and a summary of the span lengths and optical losses is reported in tab. 3.1. As can be seen, the average loss of the link amounts to 0.34 dB/km, which is significantly higher than expected. This is attributed to the high number of splices and connectors on the loop.

From:	To:	Length (km)	Loss (dB)
INRIM	Torino, metropolitan area (via Piero della Francesca)	48	18
Torino, metropolitan area (via Piero della Francesca)	Susa	58	16
Susa	Modane	41	17

Table 3.1: Summary of the length and optical losses of the link spans between Torino and Modane separated by EDFAs.

The two fibres are joined together at the remote end, in the LSM laboratories, forming a loop of 294 km, with both ends at INRIM. The uncompensated loss is 36 dB, which ensures a SNR of 35 dB on a 100 kHz resolution bandwidth, on the one-way loop signal. This allows a clean signal detection, to perform the two-way cancellation. On the other hand, the active noise compensation scheme could not be implemented in this setup. With such a high amount of losses, the SNR on the round-trip signal would be to low to perform a robust and cycle-slips-free PLL.
Fig. 3.2 shows the phase noise of the link from INRIM to intermediate shelters. The first span of the link, although running in the city centre of Torino, appears to be the less noisy. On the contrary, the noisiest spans are the second and the third, where the fibre is deployed along the highway. This can be attributed to the presence of trucks travelling the highway.

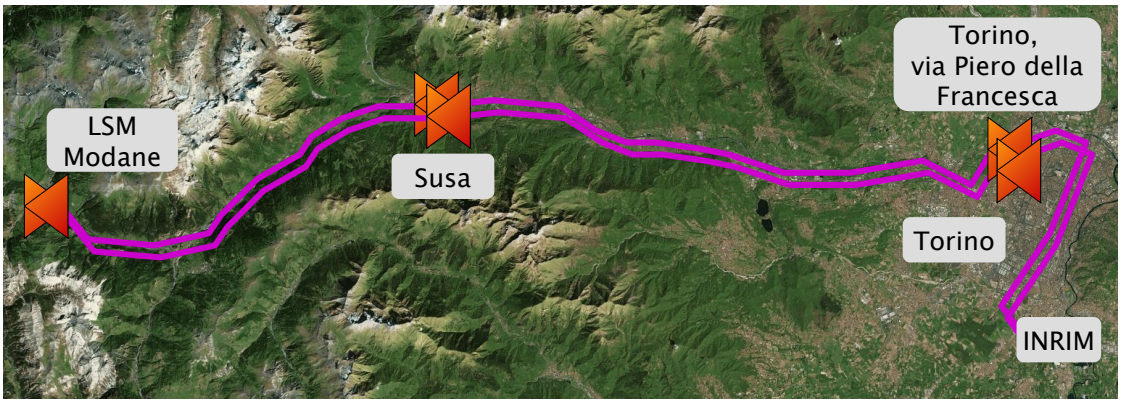

Figure 3.1: Fibre link between INIRM and LSM (Modane). It is based on a pair of multiplexed fibres equipped with bidirectional EDFAs installed in intermediate shelters: Torino, metropolitan area (via Piero della Francesca), Susa and Modane.

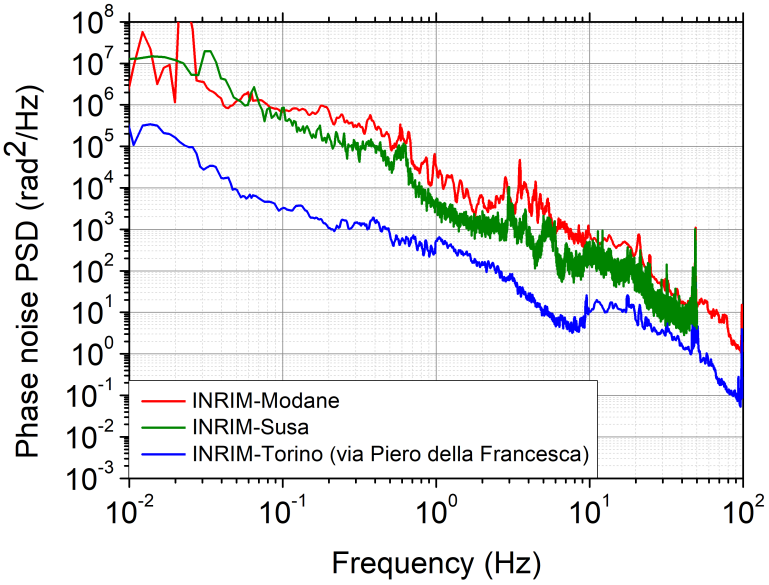

Figure 3.2: Phase noise PSDs of the links from INRIM to intermediate shelters. Red: Modane, green: Susa, blue: Torino, via Piero della Francesca.

The experimental setup

The two-way transmission was characterized with the scheme shown in fig. 3.3 (similar to that described in fig. 1.2).
Two ultrastable lasers are used ($Laser_1$ and $Laser_2$), each one is frequency-stabilized on a high-finesse Fabry-Pérot cavity. The mechanical systems, i.e. vacuum chamber, temperature control and seismic dumping platforms, are independent. To remove the long-term frequency drift, the two lasers are loosely locked to the Hydrogen

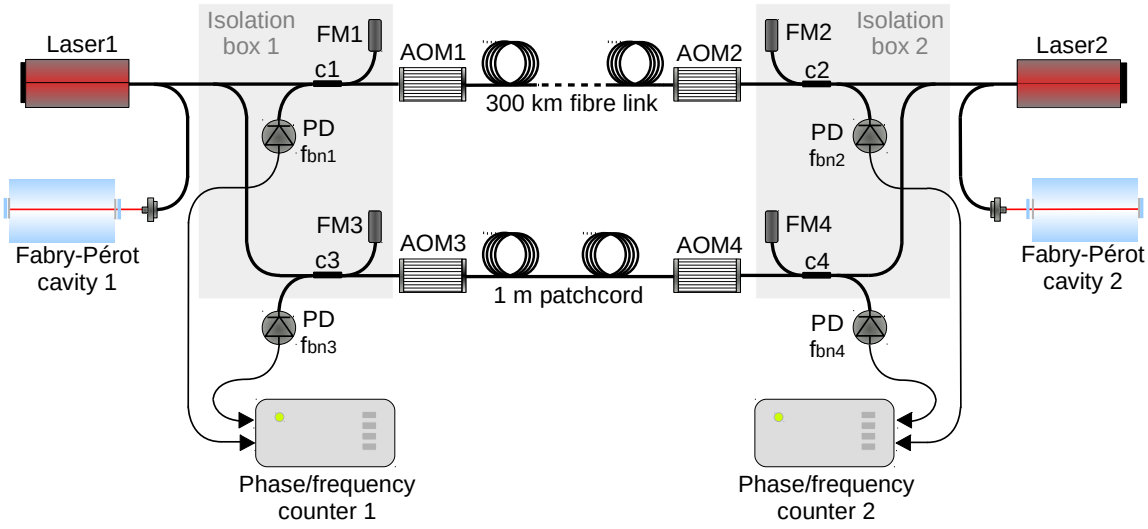

Figure 3.3: Optical and electronic apparatus for the two-way measurement. c, fibre couplers; FM, Faraday mirrors; PD, photodiode; AOM, acousto-optic modulators; EDFA, erbium-doped fibre amplifiers.

maser by means of the frequency comb, ensuring a frequency drift $< 10^{-15}$/day. We note that the frequency-drift removal is a key feature. In fact, if a laser with a relative frequency drift d, is transmitted in a link where the delay is τ, there will be a relative frequency difference $d\tau$ between the transmitted and the launched frequency. For our setup, the drift is roughly 0.1 Hz/s and $\tau = 1.5$ ms and hence a frequency offset at the level of $\sim 10^{-18}$ would be observed without stabilization to the maser. Interestingly, the Doppler-noise cancellation is not affected by this disturbance. In this scheme, the slow frequency drift of the laser is detected and compensated as phase noise by the phase-locked loop.

The lasers are launched in the 294 km link from the two extremities, in opposite directions. The couplers c_1 and c_2 are used to generate the beat notes between local and remote lasers (f_{bn1} and f_{bn2}). The acousto optic modulators (AOM_1 and AOM_2) ensure the frequency of the signals to be shifted at each pass. In this way, the beat note between the local and the remote laser can be distinguished from the beat note between the remote laser and the stray backreflections of the local laser injected into the fibre. In order to minimize the noise introduced by uncommon fibre paths, e.g. the coupler branches representing the short arm of the Michelson interferometers, all the couplers at the same extremity of the link are placed into a single isolation box as shown in fig. 3.3.

The beat notes are collected on two low-noise photodiodes (PD_1 and PD_2) and redundantly tracked with VCOs for cycle slips detection. The link design does not ensure that the incoming light has the same polarization of the local light. To maximize the SNR of the beat note, the polarization is optimized, approximately

once per hour, using a manual polarization controller.
To evaluate the residual link noise of the two-way cancellation we perform the difference (more details are given in eq. (1.21)):

$$\phi_{\mathrm{bn1}} - \phi_{\mathrm{bn2}} = 2\left(\phi_{\mathrm{L1}} - \phi_{\mathrm{L2}}\right) - \phi_{\mathrm{link1}\to 2} + \phi_{\mathrm{link2}\to 1}, \tag{3.3}$$

which is dominated by the relative phase noise of the two independent lasers, ϕ_{L1} and ϕ_{L2}, while $\phi_{\mathrm{link1}\to 2}$ and $\phi_{\mathrm{link2}\to 1}$ are the noise contributions of the fibre travelled in opposite directions. In order to remove the laser contribution, a second branch is added to the setup. A parallel link is implemented, consisting of a 1 metre patchcord terminated by two additional couplers (c_3 and c_4) which are used to generate f_{bn3} and f_{bn4}. Their difference is:

$$\phi_{\mathrm{bn3}} - \phi_{\mathrm{bn4}} = 2\left(\phi_{\mathrm{L1}} - \phi_{\mathrm{L2}}\right), \tag{3.4}$$

where the residual noise of the patchcord has been discarded since it is negligible in comparison to all other noise contributions. By subtracting eq. (3.4) from eq. (3.3), the laser noise is rejected and the residual noise of the long link is retrieved:

$$\phi_{\mathrm{link}} = \left(\phi_{\mathrm{bn1}} - \phi_{\mathrm{bn2}}\right) - \left(\phi_{\mathrm{bn3}} - \phi_{\mathrm{bn4}}\right) = -\phi_{\mathrm{link1}\to 2} + \phi_{\mathrm{link2}\to 1}. \tag{3.5}$$

As previously stated, this is the residual noise contribution of the fibre link, which, in case of a comparison of two optical signals, e.g. two atomic clocks, is further divided by a factor of two.

The interpolation contribution

The data acquisition is based on sampling the heterodyne beat notes with two independent frequency counters. Hence $\phi_{\mathrm{bn1}}(t)$ and $\phi_{\mathrm{bn2}}(t)$ are more correctly written as:

$$\phi_{\mathrm{bn1},k} = \phi_{\mathrm{bn1}}\left(t_0 + k t_{\mathrm{s}}\right) \tag{3.6}$$

and

$$\phi_{\mathrm{bn2},k} = \phi_{\mathrm{bn2}}\left(t_0 + \Delta + k t_{\mathrm{s}}\right), \tag{3.7}$$

where $k \in \mathbb{N}$, t_{s} is the sampling time of the acquisition, t_0 is arbitrary set as the measurement beginning and Δ is the time delay between the two acquisitions, in the general situation where the two counters are not synchronized. As a direct consequence, the subtraction requested by eq. (3.5) cannot be directly performed without previously evaluating the two data series on a common timebase. This is done by performing a linear interpolation of $\phi_{\mathrm{bn1},k}$ and recalculating it on the timebase of $\phi_{\mathrm{bn2},k}$:

$$\phi'_{\mathrm{bn1},k} = \frac{\Delta}{t_{\mathrm{s}}}\phi_{\mathrm{bn1},k+1} + \left(\frac{\Delta}{t_{\mathrm{s}}}\right)\phi_{\mathrm{bn1},k}. \tag{3.8}$$

Substituting eq. (3.7) and (3.8) into eq. (3.5) we obtain:

$$\phi_{\text{link}}\left(t_0+\Delta+kt_\text{s}\right)=\frac{\Delta}{t_\text{s}}\phi_{\text{bn1},k+1}+\left(1-\frac{\Delta}{t_\text{s}}\right)\phi_{\text{bn1},k}-\phi_{\text{bn2},k}. \tag{3.9}$$

ϕ_{bn3} is acquired on the same timebase as ϕ_{bn1} and ϕ_{bn4} on the same base as ϕ_{bn2}. Therefore, they can be subtracted prior to perform the re-interpolation and are neglected here for the sake of clarity. By using the standard rules of the Fourier algebra, the PSD of the two-way difference that undergoes an interpolation process is evaluated from eq. (3.9) as:

$$S_{\text{fibre,interp}}\left(f\right)=\left|\frac{\Delta}{t_\text{s}}\left(e^{-i2\pi f t_\text{s}}-1\right)-\left(e^{-i2\pi f\Delta}-1\right)\right|^2 S_{\text{fibre}}\left(f\right), \tag{3.10}$$

where $S_{\text{fibre}}\left(f\right)$ is the one-way noise of the uncompensated fibre. It can be seen that the residual link noise depends both on the gate time of the data sampling, t_s, and on the temporal mismatch of the acquisitions at the two fibre ends, Δ, which is assumed to be constant over time. In order to evaluate the effects of re-interpolation on the noise cancellation, a comparison between the two-way difference performed in synchronized ($S_{\text{fibre,two-way}}$, eq. (3.1)) and unsynchronized conditions ($S_{\text{fibre,interp}}$, eq. (3.10)) is performed. This is done considering the transfer function in the two cases, defined as:

$$T_{\text{Two-way}}\left(f\right)=\frac{S_{\text{fibre,two-way}}\left(f\right)}{S_{\text{fibre}}\left(f\right)}=\frac{1}{3}\left|e^{-i2\pi f\tau}-1\right|^2 \tag{3.11}$$

and

$$T_{\text{Interp}}\left(f\right)=\frac{S_{\text{fibre,interp}}\left(f\right)}{S_{\text{fibre}}\left(f\right)}=\left|\frac{\Delta}{t_\text{s}}\left(e^{-i2\pi f t_\text{s}}-1\right)-\left(e^{-i2\pi f\Delta}-1\right)\right|^2. \tag{3.12}$$

They are plotted for comparison in fig. 3.4. The gate time has been set at $t_\text{s}=1\,\text{s}$, which is usually a good choice to filter out the high frequency fibre noise, and $\tau=1.5\,\text{ms}$, which is the time delay for 294 km. $T_{\text{Interp}}\left(f\right)$ is plotted for different Δ values, chosen as entire multiples of τ, to show different conditions of timebase delay between remote acquisition systems. It is seen that, already for $\Delta=\tau$, T_{Interp} is higher than $T_{\text{Two-way}}$ and hence the noise rejection is less effective in the case of unsynchronised, re-interpolated measurements.
Fig. 3.5 shows the ratio $T_{\text{Interp}}/T_{\text{Two-way}}$ evaluated at a fixed value of Fourier frequency, 1 Hz, as a function of the timebase mismatch, Δ. The value for which the ratio is equal to 1 is $\Delta=\frac{\tau}{\sqrt{3}}\simeq 0.58\tau$, which for our 294 km-long testbed means $\Delta=0.87\,\text{ms}$. The maximum value of the curve and hence the highest contribution of the interpolation appears to be for $\Delta=\left(\frac{1}{2}+n\right)t_\text{s}$, with $n\in\mathbb{N}$, whereas, when Δ is an entire multiple of t_s, the PSD contribution due to the lack of synchronisation

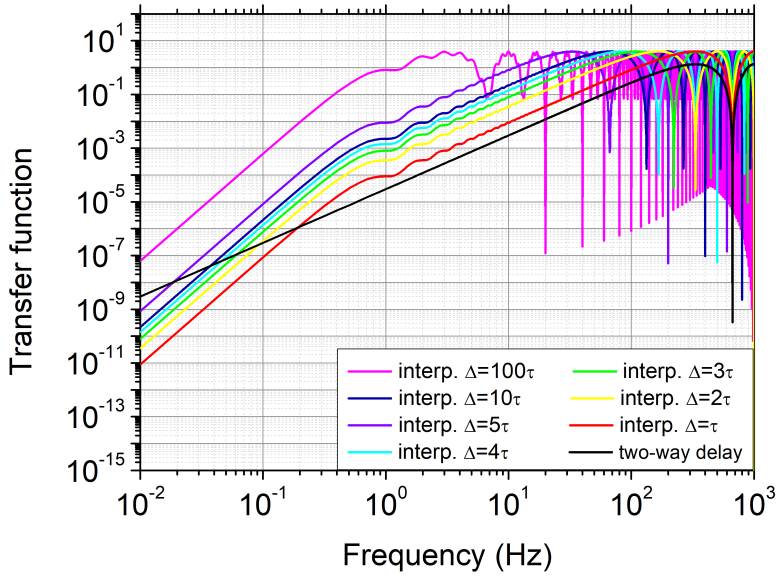

Figure 3.4: Transfer functions of the two-way noise compensation calculated for $t_s = 1\,s$ and $\tau = 1.5\,ms$. Black line: synchronized two-way, coloured lines: unsynchronized two-way with interpolation. The latter are calculated for various values of Δ multiples of τ.

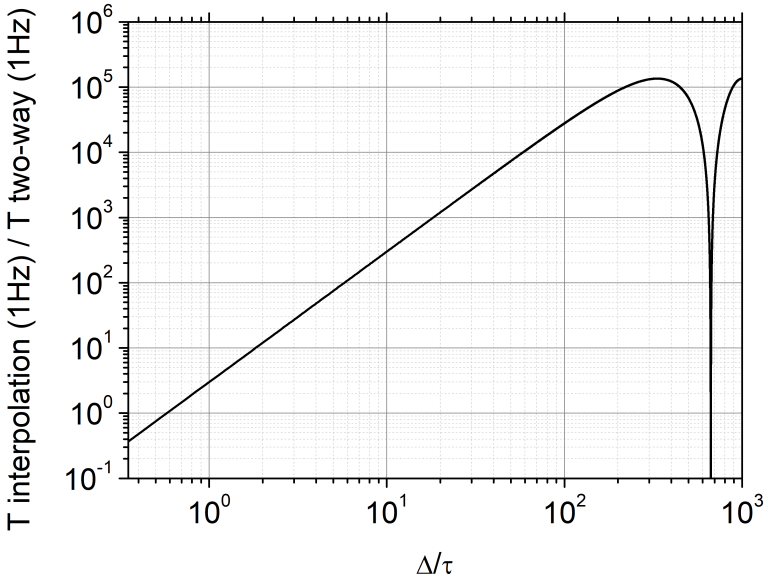

Figure 3.5: Ratio between T_{Interp} and $T_{\mathrm{Two\text{-}way}}$ calculated for $t_s = 1\,s$, $\tau = 1.5\,ms$ and the Fourier frequency of 1 Hz.

becomes negligible again. This is expected, as for such values the re-calculation on a common time scale does not require an interpolation.
Moreover, it has to be considered that, in case of an acquisition time of 1 s, it is likely that $\Delta \gg \tau$, since Δ is usually tens or hundreds of milliseconds. In this case the contribution brought by the interpolation becomes dominant on the Fourier spectrum and it cannot be neglected even if Δ is known precisely. A higher sampling rate, although sometimes unpractical, would mitigate this effect.
A good solution to avoid the interpolation process is to trigger each counter with an external PPS of adequate performances, hence with an ultimate uncertainty lower than τ, as available in most laboratories.
The same analysis has been performed exploiting the sinc function as interpolation algorithm. This resulted in an improvement in stability of $20-30\%$, while the computational time increased by orders of magnitude. As a consequence, we chose the linear interpolation as the best algorithm for our analysis, in terms of performances and efficiency.

The experimental results

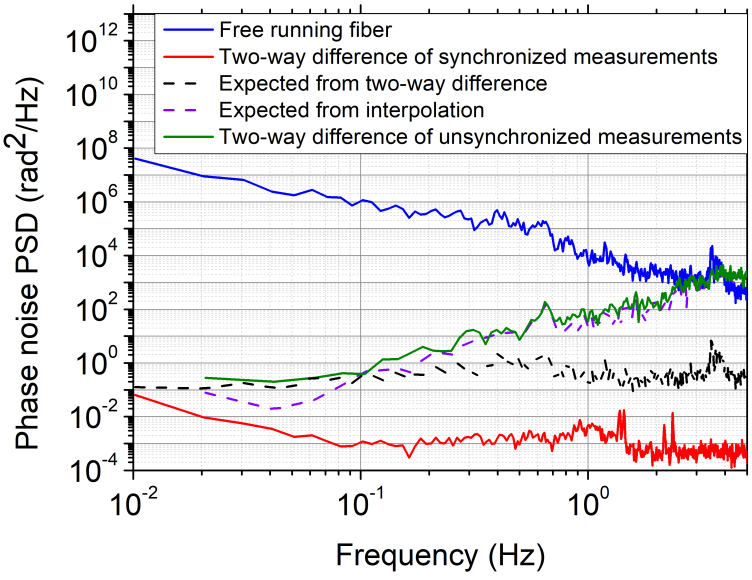

Figure 3.6: Phase noise PSDs measured on the 294 km link. Blue: noise of the uncompensated fibre, red: residual noise after two-way compensation with synchronized measurements and performed on a loop of parallel fibres, black dashed: expected residual noise after two-way compensation with synchronized measurements and uncorrelated noise along the fibre link, green: residual noise after two-way compensation with unsynchronized measurements and purple dashed: expected residual noise after two-way compensation with unsynchronized synchronized measurements, calculated for the Δ value evaluated for the green measurement.

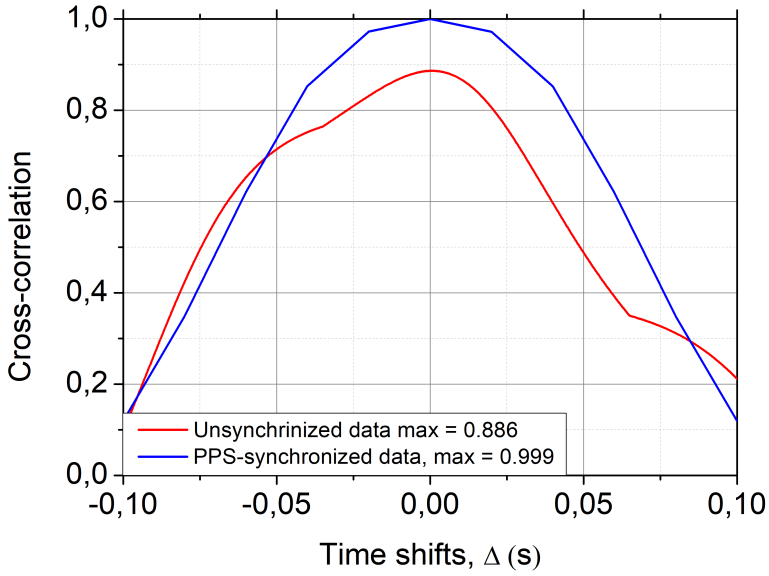

Figure 3.7: Correlation curve between the data series ϕ_{bn1} and ϕ_{bn2}. Blue: data acquired with synchronized counters, the correlation maximum is evaluated at 0.886. Red: data acquired with unsynchronized counters, the correlation maximum is evaluated at 0.999. The timebases of both curves have been rescaled and centred to zero for an easier visualization.

Fig. 3.6 shows the PSD of the uncompensated 294 km fibre (blue spectrum) and the two-way difference obtained from synchronized data (red spectrum). It is almost 20 dB lower than the expected difference evaluated with eq. (3.1), represented by the black dashed line. Such effect can be explained by the high correlation in the noise of the two fibres and was confirmed by independent measurements of the noise spectrum for each of the two 147 km. A more detailed evaluation of the degree of correlation is presented in chapter 4.
The two-way difference between unsynchronized measurements is shown by the green spectrum in fig. 3.6. The data were re-interpolated manually to match timebases. The value of Δ was retrieved by performing the cross-correlation between the data series of ϕ_{bn1} and ϕ_{bn2} and was chosen as the delay that maximised the correlation:

$$R_{\phi bn1,\phi bn2}(\Delta) = \int_{-\infty}^{\infty} \phi^*_{\mathrm{bn1}}(t)\, \phi_{\mathrm{bn2}}(t+\Delta)\, dt \tag{3.13}$$

This operation introduces additional noise to the system, as shown in eq. (3.10). The expected noise is shown by the dashed purple line and is in agreement with experimental results.
We note that, since each point of the correlation curve is determined through a re-interpolation of one data series on the timebase of the other, this introduces a noise contribution according to eq. (3.8) that decreases the level of correlation. For

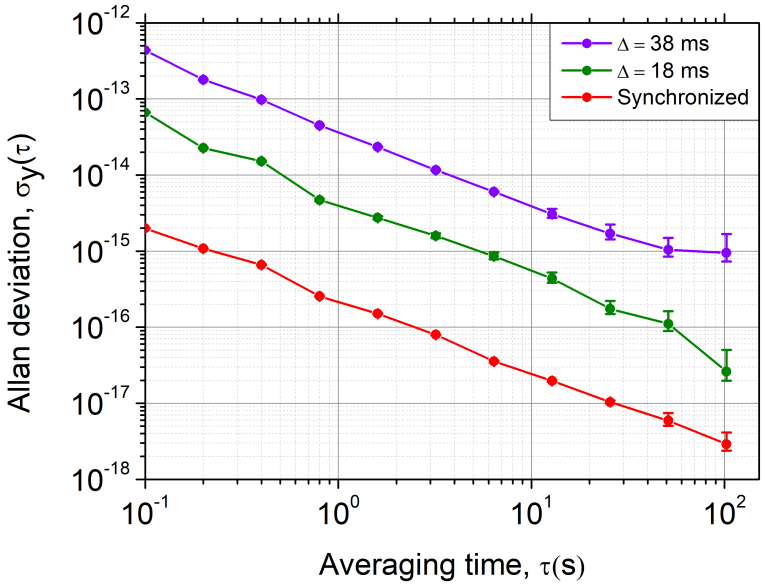

Figure 3.8: Frequency stability in terms of Allan deviation of the residual noise of a two-way compensation. Red: synchronized measurement, green: unsynchronized with $\Delta = 18\,\mathrm{ms}$, purple: unsynchronised with $\Delta = 38\,\mathrm{ms}$.

this reason, comparing the two correlation curves of fig. 3.7, it is noticed that for unsynchronized measurements (red curve) the maximum of the cross-correlation curve is never as high as for synchronized measurements (blue curve).
The noise at high frequencies, introduced by the interpolation process, deteriorates the link instability even at long averaging times. This happens if the Allan deviation is used as estimator, since it cannot average down faster than t_a^{-1}, where t_a is the measurement time [103]. This effect could be reduced by choosing a lower measurement bandwidth. However, this would result in an increase of computational time, since sharp digital filters are required for low sampling rates to avoid aliasing of high-frequency noise. These measurements are performed with a first order averaging filter, obtained by employing the frequency counter in the so-called "averaging mode" or "Λ-mode". Fig. 3.8 shows the stability in terms of Allan deviation of the two-way difference, calculated from multiple data samples with different Δ, and acquired with a gate time of 100 ms. The measurement noise depends on Δ according to eq. (3.10) and it can be calculated for the various acquisitions. The Allan deviation associated to noise of type $S(f) = h_2 f^2$ is:

$$\sigma_\mathrm{y}^2(\tau) = \frac{h_2 f_\mathrm{H}^3}{4\nu_0^2\pi^2} \dot{t}_\mathrm{a}^{-2}, \tag{3.14}$$

where f_H is the measurement bandwidth, ν_0 is the absolute frequency of the laser and t_a is the averaging time. Form eq. (3.10) and eq. (3.14), one obtains $\frac{\sigma_\Delta(t_\mathrm{a})}{\sigma_0(t_\mathrm{a})}$,

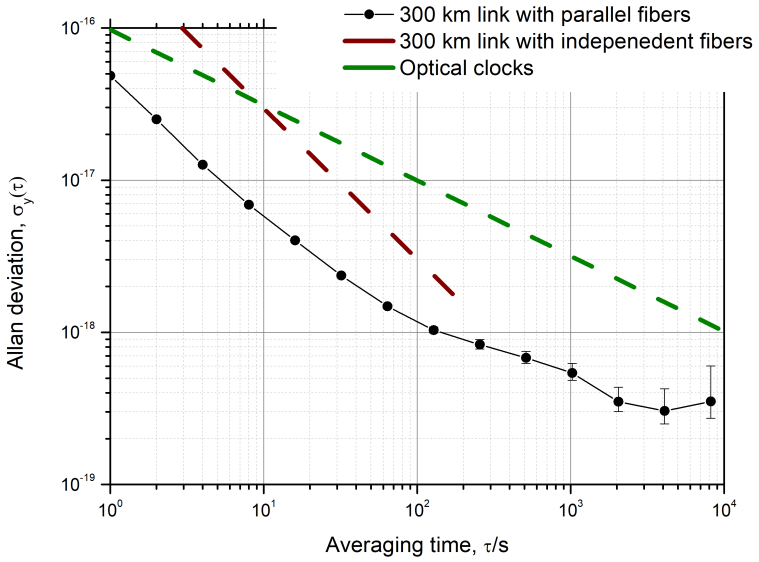

Figure 3.9: Frequency stability in terms of Allan deviation of the residual noise of a two-way compensation. Black: PPS-synchronized measurement on a 294 km link loop generated from parallel fibres, brown dashed: expected link contribution in case of non-correlated fibre noise, green dashed: typical uncertainty of the best optical clocks of new generation.

which represents the noise increase as a function of delta. The results are in agreement with the Allan deviations shown in fig. 3.8.
Fig. 3.9 shows the residual instability of the two-way noise cancellation performed with PPS-synchronized acquisition systems. Two cycles-slips have been detected, by redundantly tracking the beat note signals, and removed. It is observed that for $t_a > 100\,s$ the Allan deviation drops slower than t_a^{-1}, achieving an ultimate stability of 3×10^{-19} in $10^4\,s$. The interferometers noise floor has been evaluated by replacing the 294 km link with a fixed attenuator of equal loss, displaying an instability contribution of 1×10^{-19}. We attribute the ultimate limit of 3×10^{-19} to the polarization mode dispersion along the fibre link. The frequency offset introduced by the fibre noise is zero within this uncertainty level.
The green dashed line is the expected uncertainty for the best optical clocks of new generation and the brown dashed line is the noise contribution expected from the 294 km link in the case of uncorrelated fibre noise, estimated from the black dashed spectrum in fig. 3.6. It is seen that the link contribution would be negligible with respect to the clocks afters 10 s averaging time.

The experimental results demonstrate that the performances of the two-way technique are adequate for the comparison of remote atomic clocks. Therefore, the plan

is to implement the two-way scheme in the forthcoming 1700 km link between INRIM and LNE-SYRTE.
This procedure to evaluate the noise contribution introduced by interpolation processes in unsynchronized datasets can be extended to other related situations, such as multiple comparisons of atomic clocks via fibre link. Indeed, exploiting the European fibre network connecting several NMIs, the comparison between frequency standards which are not directly connected by fibre links can be retrieved by simultaneous pair-wise comparisons which have a clock in common. If no hardware-synchronization is ensured, the unsuppressed noise contribution introduced by the interpolation algorithm may not be negligible with respect to the noise relative uncertainty.

Chapter 4

Frequency dissemination on submarine fibre cables

Fibre-based frequency dissemination techniques have demonstrated to support clocks comparisons at the ultimate clocks uncertainty level on a continental scale. However, to date, satellite techniques remain the only way to compare clocks on transcontinental distances. The establishment of a worldwide network of optical fibres for clock comparisons would represent a breakthrough in frequency metrology. This will require the implementation of phase-stabilized optical links over submarine fibres.
Experiments over submarine fibres are reported in literature, regarding RF dissemination in synchronized networks [123] and time transfer through the passive listening of the data flow [124]. However, in these works, the submarine cables are not considered a subject of study, and no characterization of the link itself is reported.
Part of my research activity was devoted to the characterization of the phase noise in submarine fibres both in terms of spectral and time-domain analysis, focused on the dissemination of ultrastable optical carriers. The research has been performed in collaboration with the University of Malta and the National Physical Laboratory (NPL) in Teddington, UK, exploiting two ∼200-km-long testbeds, with different characteristics, based on fibre cables running on the bottom of the sea and connecting Malta to Sicily. The fibre providers are Melita Limited, which is a telecommunication company that provides cable television, mobile telephone, broadband Internet, and fixed-line telephone services and Enemalta Corporation, which is an electric society and is responsible for the production and supply of electricity and for the importation of petroleum and gas.
Based on the results obtained on such testbeds and in view of future transoceanic atomic clocks comparisons, a quantitative prediction is also performed about the expected level of noise cancellation on intercontinental distances. The results of this work are presented in [64].

4.1 Metrological characterization of submarine fibres

The experimental setup

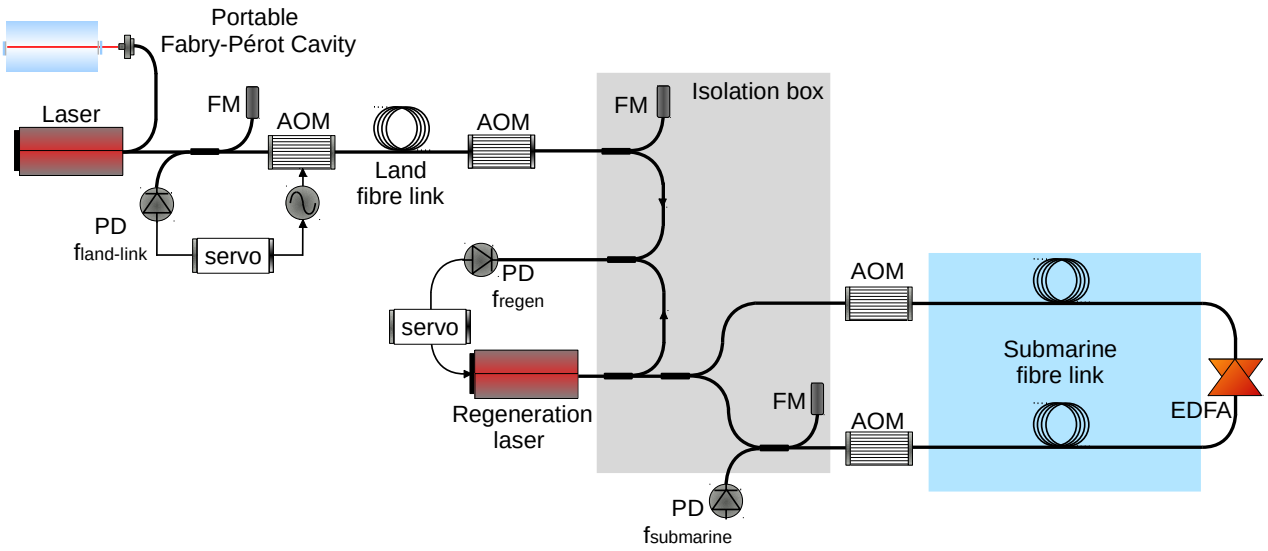

Figure 4.1: Optical and electronic setup for the submarine phase noise measurement.

The phase noise of the two submarine fibre links has been measured adopting the scheme shown in fig. 4.1.
An ultrastable laser is generated by frequency-locking a fibre laser to a high-finesse Fabry-Pérot cavity placed at the University of Malta (fig. 4.2). The design of the transportable system has been performed at NPL. The apparatus has been mounted and characterized at INRIM and afterwards transported to Malta with a van. The cavity has a vertical structure which minimizes the influence of vertical accelerations. It is clamped at its mid-plane inside an aluminium shield, to ensure an adequate robustness for transportation. On the external surface of the aluminium shield two thermistors are glued: one is used as sensor for the temperature control while the second is employed as a monitor of the cavity temperature. Two 14 W peltier thermoelectric coolers are placed on the top and on the bottom of the shield and are used as actuators for the temperature stabilization. To isolate the cavity from external temperature variations, the aluminium shield is placed inside a vacuum chamber. The internal pressure is maintained at 10^{-8} mbar through an ion pump with a pumping speed of 20 l/s, which was battery powered during the transportation.
Before transportation, a compete characterization of the physical package has been

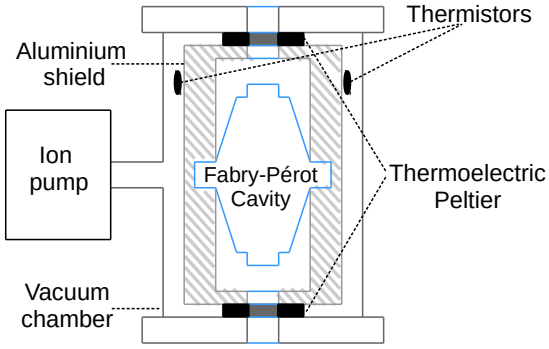

(a) Sketch of the transportable cavity. An ion pump is used to keep the vacuum at 10^{-8} mbar. The cavity is clamped inside an aluminium shield; on its external surface two thermistors are glued to monitor the cavity temperature while two peltier thermoelectric coolers are placed on the top and on the bottom of the shield for temperature stabilization.

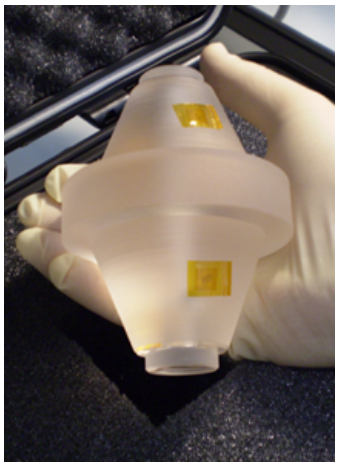

(b) Picture of the Fabry-Pérot optical cavity.

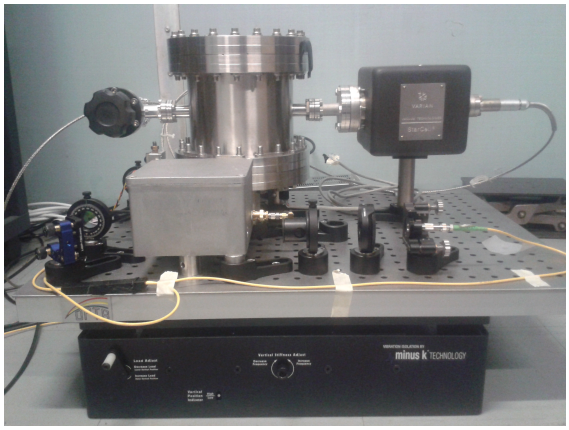

(c) Picture of the portable system: the vacuum chamber with the ion pump is placed in the centre of a 50×65 cm breadboard. On the same board is mounted the optical bench for the laser alignment to the cavity.

Figure 4.2: Transportable optical Fabry-Pérot cavity.

performed. The temperature fluctuations are $\sim 20\,\mu$K on the short-term, while over timescales of several hours they are kept at the millikelvin level through active stabilization, implemented following the active disturbance rejection method [125]. This guarantees that the daily frequency fluctuations remain below 15 kHz. The laser frequency instability, expressed in terms of Allan deviation, is shown in fig. 4.3. It has been evaluated with the three-cornered hat method [126], as we expected it to be the lowest among all the available lasers used for comparison. The ultrastable

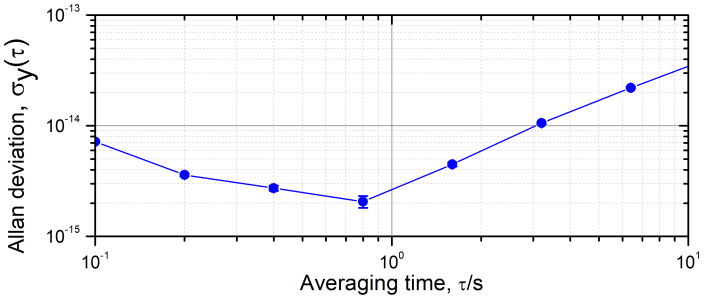

Figure 4.3: Allan deviation of the ultrastable laser frequency-locked to the portable Fabry-Pérot cavity. It has been evaluated at INRIM, after measuring the stability of the beat note between the transportable laser with two different local ultrastable sources and processing the data with the three-cornered hat method.

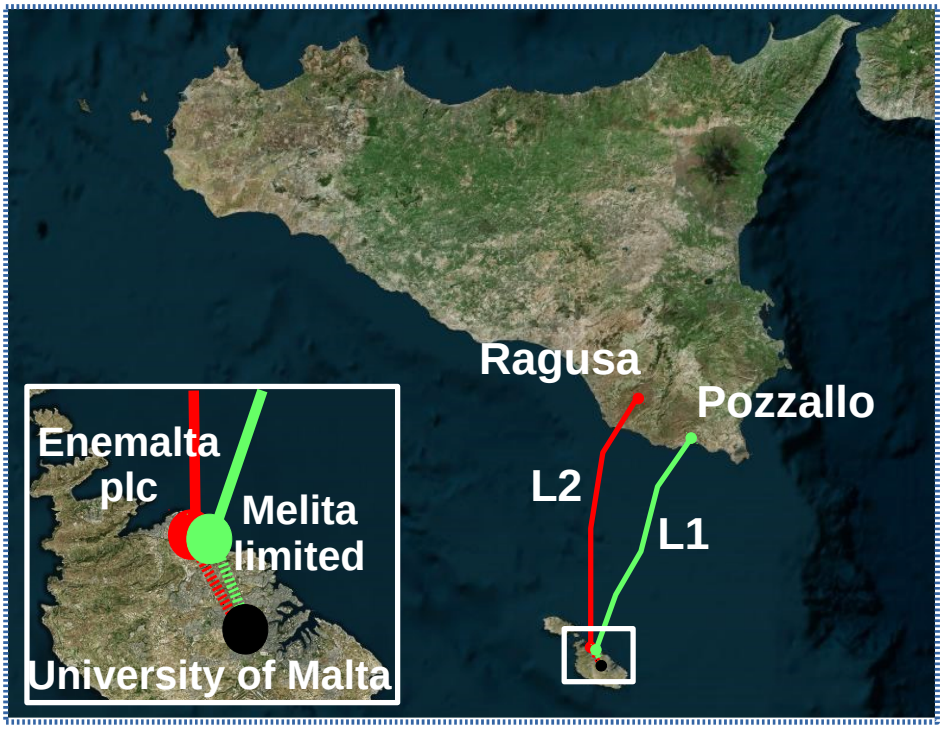

Figure 4.4: Map of the two testbeds employed for the submarine phase noise measurement. L1: green link, 96.4 km, connecting the data centre of Melita Limited to Pozzallo. L2: red link, 98.5 km, connecting the data centre of Enemalta Corporation to Ragusa. The dashed links are the actively stabilized land spans, connecting the University of Malta to the landing stations.

laser based on the transportable cavity was beaten against two independent ultrastable cavities at INRIM. The data have been processed with the three-cornered hat method retrieving the stability of the transportable laser. It has been estimated at the level of 2×10^{-15} at 1 s, with a ~ 0.1 Hz/s frequency drift.

No ultrastable laser source was available in Malta to verify whether the laser spectral purity and stability were maintained after transportation. Therefore, we relied on indirect observables. The Pound-Drever-Hall discriminator has been considered, whose SNR and width have been recovered after transportation. No degradation has been observed on the in-loop noise of the frequency-lock to the cavity, meaning that the environmental noise sources did not change substantially. The readings of the temperature monitor inside the vacuum chamber were comparable to those recorded in the INRIM laboratory. Thus, it could be assumed that the performances observed at INRIM were preserved for the experiment in Malta.
The Malta extremity of both submarine links is located into a landing station, i.e. the access point to the fibres closest to the sea. The measurement setup has been placed here to minimize the contribution of land fibre spans, which are expected to be noisier than the submarine cables, albeit much shorter. However, the ultrastable laser source, could not be operated in the landing stations, where only little room was available for this experiment. Therefore, the laser has been placed in a dedicated laboratory at the University of Malta, which ensures a much quieter environment from the point of view of temperature variations and acoustic vibrations. As a consequence, two additional land links, of 18 km and 8 km for the two setups respectively, delivered the cavity-stabilised optical carrier from the university to the landing stations. To reduce the spectral purity degradation of the optical carrier due to the path in the land fibre span, these links have been phase-stabilized with the Doppler-noise cancellation technique (round-trip signal in fig. 4.1: $f_{\text{land-link}}$).
At the landing station the ultrastable signal is regenerated to recover for optical losses, by phase locking a diode laser to the incoming signal (f_{regen}). The light of the diode laser is launched in the submarine fibre. The light travelling the submarine link is compared to the local laser after a round-trip, generating the beat note $f_{\text{submarine}}$, that carries the information about the phase variations experienced by the light along the submarine fibre.
A map with the two testbeds ($L1$ and $L2$) is shown in fig. 4.4. The first link ($L1$) relies on a 96.4-km-long fibre cable, buried 1 m below the sea floor for the largest part of its length, with less than 2 km on land. The second link ($L2$) is composed by a first 98.5-km-long submarine cable and a second 19-km-long land cable running on the Sicilian land. In this second testbed, the submarine fibres are installed inside a three-core copper cable used for the high voltage (HV) electricity distribution. $L1$ and $L2$ were installed in 2009 and 2014, respectively. Thus, the residual mechanical stresses which are introduced by the settling of recently installed fibres can be considered extinguished.
In both cases the fibres have been joined at the far end, in Sicily, such that a 192.8-km and a 235-km-long loop were generated. The overall loss of both links amounts to 44 dB. $L2$ includes a bidirectional EDFA with $\sim$ 15 dB gain, placed at the far end in Sicily.
All the fibre couplers and Faraday mirrors (FM) employed for the phase-lock and

the loop signal detection are carefully isolated into a wooden box filled with foam to reduce the effect of environmental noise. Two 25 m patchcords are employed to merge the distance between the isolated interferometers and the submarine fibre input.
Two acousto-optic modulators (AOMs) are employed to frequency shift the signal and generate the heterodyne round-trip beat note ($f_{\text{submarine}}$). After being filtered and amplified, it is tracked with a VCO and sampled with a dead-time-free phase/frequency counter. The detection of cycle slips is performed by redundantly tracking the beat note with a second VCO. A low-noise, oven-controlled quartz oscillator is used to provide an adequate frequency reference to the AOMs, to the phase-locked loops local oscillators and to the frequency counter. A manual polarization controller is used to maximize the SNR of the submarine loop beat note; however, no polarization adjustment has been required over the whole measuring time, in contrast to what happens with signals running over land-based links.

Phase noise in submarine fibre cables

Both $L1$ and $L2$ are based on a dark fibre infrastructure, with fibres buried 1 m under the seafloor. This is typically done in shallow water seas (the Sicily-Malta channel is characterized by an extremely flat floor with a maximum depth of 200 m) to reduce the risk of damage by boat anchors and trawling by fishing vessels. In deeper waters the cables are installed both on or below the seafloor, depending on the seafloor surface.

Link1

Fig. 4.5 shows the PSD of the phase noise of the 2×96.4-km-long $L1$ (red spectrum) compared to land fibres of similar length, which are part of the Italian fibre network: the blue spectrum represents the noise of a round-trip link between INRIM and Modane, 2×147 km, and the black spectrum corresponds to a span of the INRIM-Medicina where the fibre terminations have been joined to form a loop of length 2×92 km. Both land links run for a large part along the highway. The phase noise of the submarine link is considerably lower in comparison to the land ones. The difference is particularly relevant in the acoustic region, since it is mainly generated by man-made activities which are almost absent on the bottom of the sea [128]. The grey spectrum represents the noise floor of our measurement setup in Malta. It has been measured excluding the submarine fibres and joining together the two 25 m patchcords with a fixed 44 dB attenuator, that simulates the losses of the $L1$ link. The 25 m fibres were suspended on the ceiling of the landing station, which for $L1$ is an air-conditioned server room housing instrumentations with embedded cooling fans. This affects the noise floor in the acoustic region, while at lower Fourier frequencies it is limited by temperature effects on the fibres. It

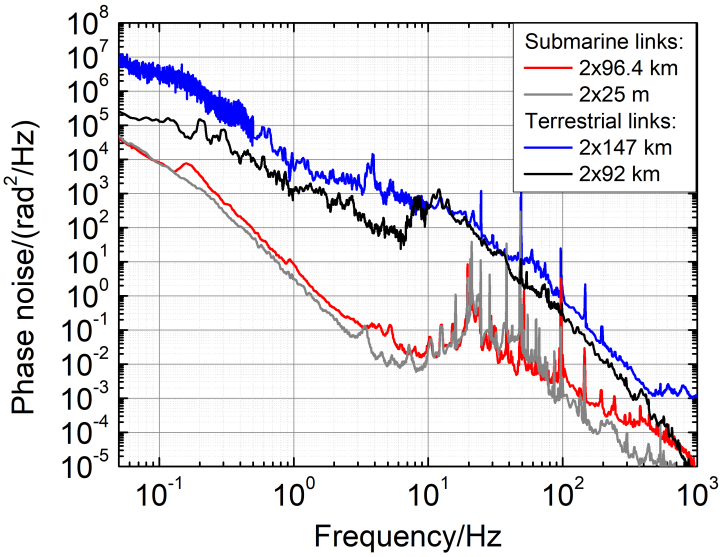

Figure 4.5: Phase noise of free running fibre links. Red: submarine fibre of L1, 2×96.4 km; grey: 2×25 m fibre patches used in the landing station of L1; black: 2×92 km land link between INRIM and Novara; blue 2×147 km land link between INRIM and Modane.

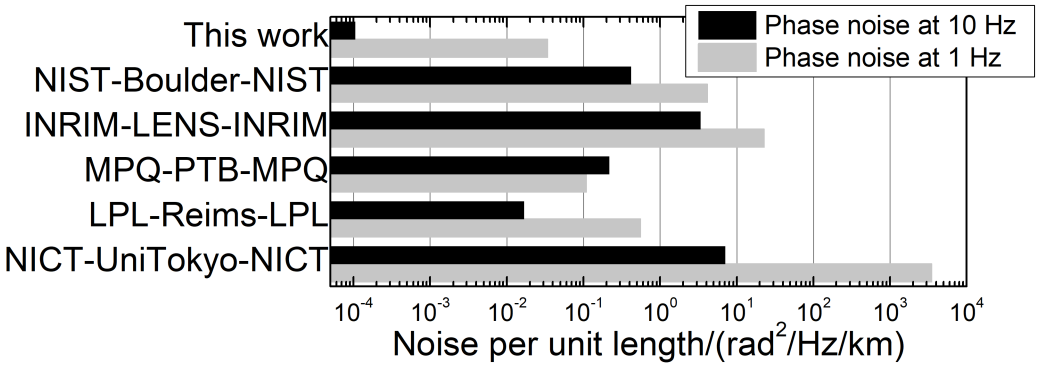

Figure 4.6: Phase noise per-unit-length at 1 Hz and 10 Hz. NIST-Boulder- NIST: US, 76 km [39]; INRIM-LENS-INRIM: Italy, 1284 km [30]; MPQ-PTB-MPQ: Germany, 1840 km [79]; LPL-Remis-LPL: France, 540 km [127]; NICT-UniTokyo-NICT: Japan, partly aerial fibres, 114 km [99].

represents the upper limit to the noise of submarine fibres. A peak at ~ 0.15 Hz is observed on the submarine spectrum. It is due to microseismic noise on the sea floor originated by the wind-sea interaction. Further details are given in chapter 5.

A more extensive comparison between submarine and land links is reported in fig. 4.6 in terms of noise per-unit-length evaluated at 1 Hz and 10 Hz. It confirms that a difference of more than two orders of magnitude is observed in the acoustic

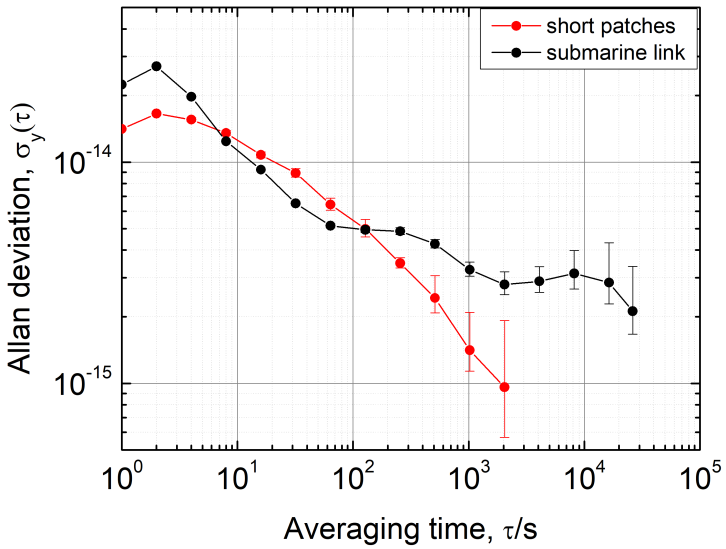

Figure 4.7: Frequency stability in terms of Allan deviation along the submarine link. Black: L1 submarine fibre; red: 2×25 m fibre patches.

region, where the noise is mainly caused by human activities. High variability is observed also on the noise of the various land links. We attribute it to the influence of the fibres location: the US link, NIST-Boulder-NIST, runs around the town of Boulder [39], it is characterized by repeated excursions above ground and thus benefits from a lower insulation with respect to buried links; the Italian link, INRIM-LENS-INRIM, runs for a large part along a busy highway [30]; the German link, MPQ-PTB-MPQ, runs next to a gas pipeline [79], which ensures a higher insulation from environmental noise sources with respect to fibres along the highway; the French link, LPL-Reims-LPL, runs between Paris and the town of Reims [127] and is composed for a large part by more quiet intercity fibres; the Japanese link, NICT-UniTokyo-NICT, runs in the densely populated metropolitan area of Tokyo, the significant high noise at 1 Hz may be attributed to the fact that part of the link is established on aerial fibres [99].

The long-term stability of the submarine link, expressed in terms of Allan deviation, is reported in fig. 4.7 (black data). It is compared to the noise of the link composed by the short 25 m patches only (red data). The Allan deviation has been calculated from phase data acquired with an equivalent measurement bandwidth of 0.5 Hz. The excess of noise on the short term is attributed to the 0.15 Hz peak. Thanks to the good temperature stability of the server room on the long term, guaranteed by the air conditioning system, the frequency stability of the setup noise floor averages down for long integration times, while the slow temperature variations of the submarine environment emerge at averaging times larger than

1000 s, showing an ultimate instability at 2×10^{-15}. No frequency offset has been observed within this uncertainty. This is a relevant result from the metrological point of view, since such a low instability level achievable on uncompensated fibres is already adequate for many metrological applications.

Link2

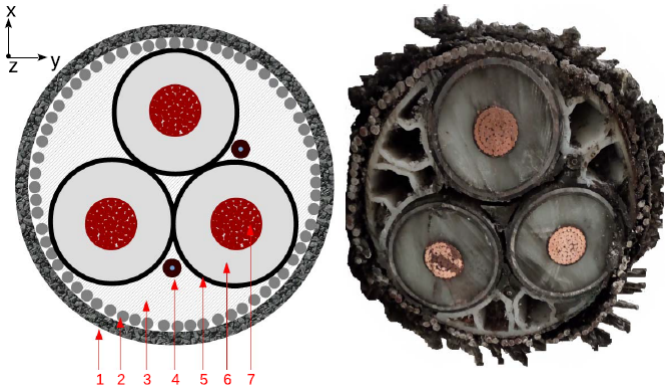

Figure 4.8: Left: simplified sketch of the cable. 1: external protection, 2: steel-wire armour, 3: filler, 4: optical cables, 5: lead-alloy sheath, 6: cross-linked polyethylene (XLPE) dielectric insulation, 7: copper conductors. Right: picture of the cable cross-section housing the fibres of L2.

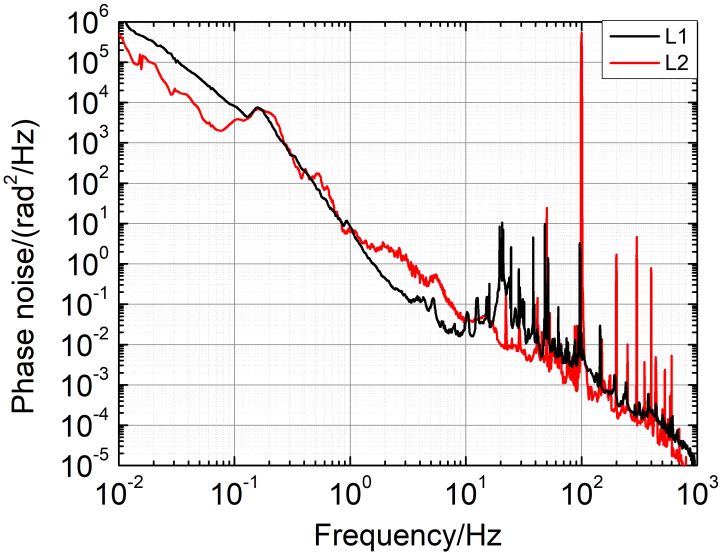

Figure 4.9: Phase noise of the two free running submarine links. Black: L1, red: L2.

The second testbed is based on fibres running into a duct of HV-alternating current (HV-AC). The alternate triphase transmission is usually employed for short-distance lines, while in case of high-capacity long distances ($\sim$ 1000 km) the HV-direct current (HV-DC) is usually preferred [129]. The used cable is designed for 245 kV-50 Hz voltage and rated for 655 A. A picture of the submarine cable with a sketch of its cross-section is shown in fig. 4.8. The three copper HV cables are insulated with cross-linked polyethylene (XLPE) and further sheathed by a lead alloy [130]. The entire structure is externally protected by a single-layer steel-wire armour. Two fibre cables, housing 36 fibres each, are placed in the interstitial spaced of the HV cable.
Fig. 4.9 shows the noise spectrum of the free running fibre of $L2$ compared to that of $L1$. As for $L1$, the acoustic noise (between 10 Hz and 100 Hz) is limited by the noise floor set by the two 25-m-long fibre patches employed in the landing station. The noise floor measured for $L2$ is lower than $L1$, since in this case the 25 m fibre patches are placed for a large part in the empty basement of a data centre where no other instrumentation is present. A lower noise is also observed between 10 mHz and 100 mHz. In this spectral region the noise of $L1$ is limited by the thermal cycles of the air-conditioning in the server room, which is not present in the landing station of $L2$. On the other hand, the excess of noise between 1 Hz and 10 Hz on $L2$ may be attributed to the 20 km of land fibre running on the Sicilian soil. A strong modulation at 100 Hz is observed on the PSD of $L2$ and is discussed below.

Interaction with the electromagnetic field

The interaction between the electromagnetic field generated by the HV-cables and the fibre signal may in principle deteriorate both the phase and the polarization state of the optical carrier. This may occur through Kerr effect, elctrostriction and Faraday effect [131, 132]. Before properly quantifying their impact on the measurement taken on $L2$, the three effects are briefly revised hereafter.
The Kerr effect is a change in the refractive index n of a material in response to an applied electric field [133, 134]. The effect is maximum if the electric field ($\mathbf{E}$) direction is parallel to the optical field polarization axis, while it is reduced, although non-null, for orthogonal polarization states. The phases variations of the optical field components parallel ($\Delta\phi_{\mathrm{k},\parallel}$) and orthogonal ($\Delta\phi_{\mathrm{k},\perp}$) to the electric field are:

$$\Delta\phi_{\mathrm{k},\parallel} = 2\pi\frac{L}{\lambda}\frac{n}{Z_0}n_{\mathrm{k}}|\mathbf{E}|^2 \tag{4.1}$$

and

$$\Delta\phi_{\mathrm{k},\perp} = \frac{2}{3}\pi\frac{L}{\lambda}\frac{n}{Z_0}n_{\mathrm{k}}|\mathbf{E}|^2, \tag{4.2}$$

where λ is the optical wavelength, L is the link length, $Z_0 \simeq 377\,\Omega$ is the vacuum impedance and $n_{\mathrm{k}} = 2.3 \times 10^{-20}\,\mathrm{m^2/W}$ is the second-order non-linear index of

refraction coefficient due to the Kerr effect [131]. In case of an optical fibre this induces birefringence, which affects both the phase and the polarization of the optical field.
Electrostriction is a property of all dielectrics that causes an isotropic change of the refractive index under the application of an external electric field. This in turn generates a phase variation $\Delta\phi_{\mathrm{es}}$:

$$\Delta\phi_{\mathrm{es}} = -2\pi\frac{L}{\lambda}\frac{n}{Z_0}n_{\mathrm{es}}|\mathbf{E}|^2, \tag{4.3}$$

where $n_{\mathrm{es}} = 0.52 \times 10^{-20}\,\mathrm{m}^2/\mathrm{W}$ [131]. The minus sign in front of the expression accounts for a decrease of the index of refraction, i.e. electrostriction has on the phase an opposite effect as compared to the Kerr effect.
Lastly, the presence of an external magnetic field induces a rotation of the polarization plane by an angle $\Delta\theta_{\mathrm{F}}$. Due to the Faraday effect the angle of rotation is linearly proportional to the component of the magnetic field in the direction of propagation ($\mathrm{B}_{\parallel}$):

$$\Delta\theta_{\mathrm{F}} = \mathcal{V}\mathrm{B}_{\parallel}L, \tag{4.4}$$

where $\mathcal{V}$ is the Verdet constant, which for single mode optical fibres and at a wavelength of 1542 nm is $\sim 0.53\,\mathrm{rad}/(\mathrm{Tm})$ [132].
An analytical evaluation of these effects on the cables of $L2$ is not straightforward, since it requires specific information about the HV-AC cables geometry and the electro and magnetic field distribution. Nevertheless, it can be shown, according to the standard electro-magnetic theory [135], that the presence of lead alloy sheaths confines the electric field into the three cores. Thus, both Kerr effect and electrostriction can be considered negligible [136]. On the other hand, the sheath is not able to isolate the fibre cable from the magnetic field generated by the alternating current [136]. The magnetic field propagates outside the conductors through closed loops on the xy-plane (see the reference frame in fig. 4.8), orthogonal to the direction of the optical field which propagates along the z-axis [135]. Thus, the Faraday effect can be considered negligible as well.
As a further confirmation that no polarization modulation is induced on the optical signal, the power of the beat note $f_{\mathrm{submarine}}$ (fig. 4.1) has been monitored over time. The measurement is performed with a sampling rate of 50 kHz, both for $L2$ and for the interferometer configuration (in which the submarine fibre is replaced by an optical attenuator). A variation of 0.1 dB is observed at 50 Hz and 100 Hz on root-mean-square power of the submarine signal and a similar value is measured for the interferometer. Thus, any polarization effect can be excluded.
For completeness it is worth to mention that a different situation occurs in optical fibres travelling along with aerial HV lines [137, 138]. Aerial cables hanging between poles are often placed in the interior of twisted ground wires to protect them from lightning strikes. The OPGW twisting causes a non-perfect parallelism

between optical fibres and HV-cables. As a consequence, any time-varying current, e.g. due to the line cycle or to occasional events like lightning strikes [137, 138], can induce a magnetic field in the axial direction. This results in rotations of the polarization plane of the light due to the Faraday effect.

Although all the possible effects related to the interaction with the HV-electromagnetic field have been excluded, a strong modulation on the optical phase at 100 Hz has been observed (fig. 4.9). We exclude it to be an artefact of the experimental setup settled in the landing station, since a similar modulation is not observed when the submarine fibre is replaced with a short patchcord. A similar effect is described in [139], which reports the observation of an acoustic tonal noise at twice the line frequency, emerging by more than 20 dB over the background at the distance of 100 m from a submarine HV cable. This is due to the force generated between the current-carrying wires which induces a vibration at twice the line frequency, hence 100 Hz. Although a quantitative estimation for $L2$ is difficult to perform, assuming a cylindrical propagation for the sound wave, the magnitude of the line-synchronous component close to the source is expected to be 20 dB higher at 1 m from the source than at 100 m. Hence, we believe that closer to the cable, the vibration peak could emerge by more than 40 dB from the floor. From the spectrum in fig. 4.9, the 100 Hz modulation seems to be even higher in comparison to the noise background. This can be explained considering that in $L2$ the cable is buried under the ground, which further isolates the cable from the external acoustic noise.
In practice, this strong modulation does not limit the measurement presented here, since its frequency is well within the VCOs tracking bandwidth. However, it may be an issue for some metrological applications, since the limited bandwidth of the active compensation loop does not allow its complete suppression. Indeed, for long links the compensation bandwidth may be narrower than 100 Hz, e.g. a bandwidth of $f_{\mathrm{bw}} = 100$ Hz is achieved for a link of 500 km. Moreover, even though a broader compensation bandwidth is allowed, the transfer function of the noise compensation loop increases as $T(f) \sim f^2$ within the bandwidth and $T(f_{\mathrm{bw}}) = 1$. Considering that the 100 Hz modulation is more than 70 dB over the noise background, it would be only partially suppressed even on short links. A better suppression could be achieved by applying steep digital filters on the recorded data, which considerably increases the computational time.

High-current-induced temperature chances

A second effect that has to be taken into account when fibres run into electric ducts is related to the strong temperature variations induced by the change of the electric current flowing in the HV cables. Fig. 4.10a (black line) shows the temperature variation ΔT experienced by the submarine fibres of $L2$ over almost 72 hours. It has been estimated from the phase variation $\Delta\phi$ measured over the

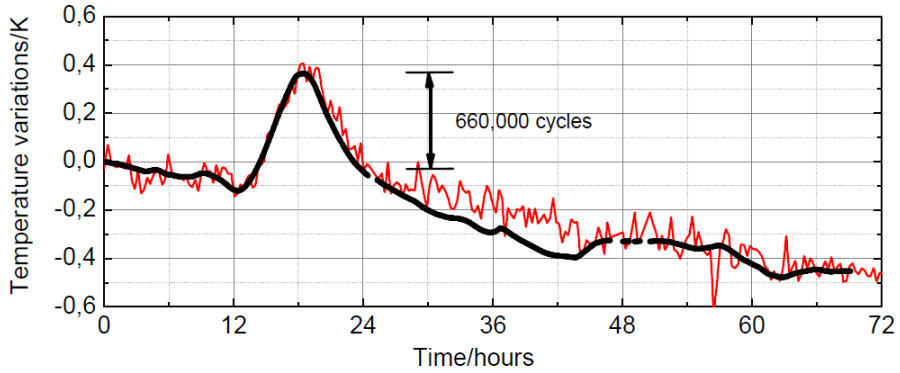

(a) Temperature variations estimated from the optical phase evolution (black line) and measured by a distributed Brillouin sensor placed along the cable (red line).

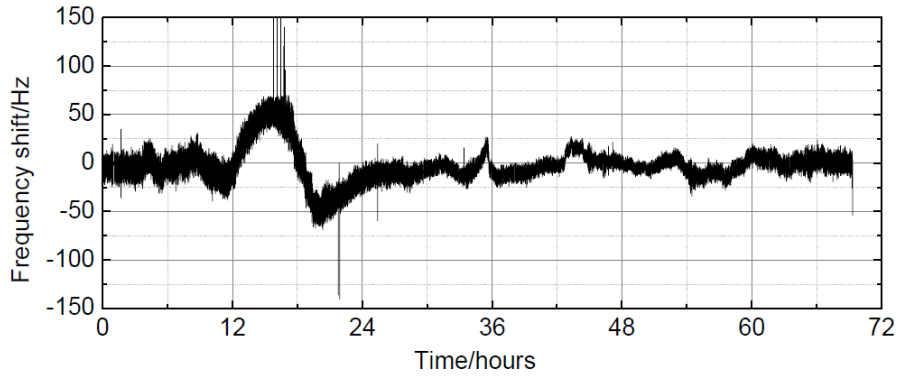

(b) Frequency shift induced by the temperature variations.

Figure 4.10: Temperature variations on $L2$.

round-trip, according to the relation:

$$\Delta T = \Delta\phi / \left(2\pi\nu \frac{2L}{c} \frac{\partial n}{\partial T} \right), \tag{4.5}$$

where ν and c stand for the optical frequency and speed of light in vacuum, L is the link length, and $\frac{\partial n}{\partial T} = 10^{-5}\,/\mathrm{K}$ is the thermooptic coefficient [140].
It is compared to the fibre temperature measured by a distributed Brillouin sensor, which is installed for commercial purposes along the HV-cable. The sensor is designed for space-resolved temperature measurements, with a 2 m resolution. Temperature readings are integrated over the fibre length (red trace), and compared to the temperature derived from the integrated optical phase (black trace). A variation of 0.8 K over 72 hours is observed, which is much larger than expected in a submarine environment. Indeed, considering the long-term phase variation of $L1$ and assuming that it is entirely attributable to temperature, a daily variation < 14 mK is calculated. For a further comparison, in the link connecting INRIM to

LSM (2×147 km, blue trace in fig. 4.5), which is fully established on land and with several access points to the network which are not buried, variations of ~ 1.4 K have been calculated with daily periodicity.
Such high variations experienced by the submarine cables are attributed to changes on the load current carried by the adjacent electric cable. A phase variation as large as 6×10^5 cycles is induced in few hours. Fig. 4.10b shows the corresponding frequency variations: frequency shifts as high as 60 Hz are observed, or 3×10^{-13} in relative terms.
This noise source has to be taken into account and carefully assessed before implementing links where fibres are housed in HV cables. Similar effects may appear also in gas and oil pipelines where the temperature is continuously adapted to regulate the flux. Furthermore, in such infrastructures as well, additional issues related to the presence of electric and magnetic fields may rise, since the fluid temperature is controlled by electric heating and induction.

4.2 Towards transoceanic clocks comparisons

From the noise measurements on the two ~ 200 km submarine links, an extrapolation of the expected noise on transoceanic fibres is derived; in particular, in this case, a fibre link of 7000 km is considered, which is approximately the length of a fibre crossing the Atlantic Ocean, i.e. from UK to the US east coast. This allows an estimation of a possible comparison of atomic clocks across the ocean.
We evaluated the expected transfer stability achievable with a two-way noise cancellation. We will consider the two cases when a single fibre is adopted for both directions of propagation, or two separate fibres are used. The first scheme is performed when the infrastructure allows the propagation of the optical signal in both directions on the same fibre. This requires substituting the unidirectional devices employed on standard telecom infrastructures, e.g. optical amplifiers, with bidirectional ones. Since this operation on a submarine environment may be difficult and costly, the unidirectional transmission scheme may be adopted, which is based on a pair of adjacent fibres, one for each propagating direction.
To estimate the noise of the free running fibre on a transcontinental distance, the following relation is considered:

$$S_L(f) = \frac{L}{L_0} S_{L_0}(f), \tag{4.6}$$

where $S_{L_0}(f)$ is the noise of a fibre link of length L_0. This holds under the assumption that the noise is uncorrelated with position. Such condition is met if the perturbations have a correlation length much shorter than the link length [39]. On the long term the noise is dominated by temperature variations. Due to the lack of information in literature, it is difficult to obtain a proper estimation of the

temperature variations on the sea floor on timescales of hours and days. However, studies are reported on the impact of temperature changes on the sea floors on seasonal and annual scales. From such studies it emerges that temperature fluctuations are strongly reduced with depth [141] and variations of few tens of millikelvin have been registered on the oceans floor, at depths of about 3000 m, on a monthly scale [142]. By consequence, on hourly scales, the temperature excursions can be assumed significantly lower in the oceans than in the Sicilia-Malta links. On shorter timescales, the noise is mainly due to sea currents and weathering effects such as wind and rain, which act on a local scale. Therefore, their noise contribution can be considered uncorrelated with position when integrated over the transoceanic link length [143]. In contrast, our measurements are most probably affected by the acoustic noise due to the heavy ship traffic and coastal activities, which is not significantly extinguished at the sea floor in such shallow waters (< 200 m) and in proximity of coastal areas. As a consequence, we believe that the extrapolation based on these measurements is conservative, since the impact of man-made noise is expected to be much lower on the deep oceans floor.
Our measurements were performed on a looped link, based on two 100-km-long adjacent fibres. To derive the noise of the one-way fibre, the round-trip noise has to be divided by a factor of 4, as shown in [39]. This holds for Fourier frequencies $f \ll \frac{c}{nL}$ and is a consequence of the high correlation of the noise between the two fibres.
The noise of a 7000 km fibre is extrapolated from that of a $\sim$ 100 km link using eq. (4.6). We will proceed by considering the residual noise when the passive fibre noise rejection technique presented in chapter 1 is adopted. Albeit a similar estimation could be performed also for active noise cancellation, we believe that the two-way cancellation scheme is more suited for transoceanic comparisons, since it suffers less from optical losses, which is a critical aspect on fibres of thousands of kilometres. Moreover, it ensures an improvement of 6 dB on the noise rejection with respect to the active compensation scheme.

To mathematically derive the expected residual phase noise in the unidirectional configuration, it is necessary to consider that the noise affecting adjacent fibres is not totally correlated. We assume it to be composed by a correlated part which is equal in amplitude and phase between the two fibres plus an uncorrelated part. The PSD of the uncorrelated component can be related to the total fibre noise as:

$$S_\delta(f) = (1-k)^2 S_\phi(f), \tag{4.7}$$

with $0 \leq k \leq 1$. Since the value of k depends on the structure and on the insulation of the cable containing the fibres, it may vary for different infrastructures. It is usually close to 1, therefore we will assume $S_\delta(f) \ll S_\phi(f)$.
To evaluate the PSD of the residual noise in a two-way comparison on a fibre pair, we indicate the noise of the two fibres, travelled in opposite directions, with $\overrightarrow{\phi}(t)$

and $\overleftarrow{\phi}(t)$:

$$\begin{aligned}\overrightarrow{\phi}(t) &= \phi(t) + \delta_1(t)\\ \overleftarrow{\phi}(t) &= \phi(t) + \delta_2(t),\end{aligned} \tag{4.8}$$

where $\phi(t)$ is the phase noise that acts equally on the two fibres, while $\delta_1(t)$ and $\delta_2(t)$ are the independent contributions. In the phase comparison between the lasers at the two ends (see section 1.2.2), the residual fibre noise can be expressed as the sum of these terms, integrated over the fibre path:

$$\begin{aligned}&\frac{1}{2}\left(\overrightarrow{\phi}(t) - \overleftarrow{\phi}(t)\right) =\\ &+\frac{1}{2}\int_0^L \left[\phi\left(t + \frac{n(z-L)}{c}\right) + \delta_1\left(t + \frac{n(z-L)}{c}\right)\right] dz\\ &-\frac{1}{2}\int_0^L \left[\phi\left(t - \frac{nz}{c}\right) + \delta_2\left(t - \frac{nz}{c}\right)\right] dz.\end{aligned} \tag{4.9}$$

The evaluation of residual phase fluctuations of the link is first performed in the frequency domain for each elementary segment of the fibre, whose noise is assumed uncorrelated with others, then integrated over the full length. The PSD of the phase noise in each segment ($S(z,f)$) is calculated by performing the Fourier transform ($F\{\cdot\}$, eq. (1.10)) of the autocorrelation function ($R(\mathrm{T})$, eq. (1.9)) of the segment noise. Exploiting the property of the Fourier transform for a time translation, $F\{R(\mathrm{T})\} = F\{R(\mathrm{T'})\}e^{2\pi f(\mathrm{T}-\mathrm{T'})}$, the PSD is written as:

$$\begin{aligned}&S(z,f) = \frac{1}{4}\{\\ &F\{R_\phi(\mathrm{T})\}\left[2 - \left(e^{i2\pi f(L-2z)n/c} + e^{-i2\pi f(L-2z)n/c}\right)\right]\\ &+F\{R_{\phi\delta_1}(\mathrm{T})\}\left[1 - e^{i2\pi f(2z-L)n/c}\right]\\ &+F\{R_{\phi\delta_2}(\mathrm{T})\}\left[1 - e^{i2\pi f(L-2z)n/c}\right]\\ &+F\{R_{\delta_1\phi}(\mathrm{T})\}\left[1 - e^{i2\pi f(L-2z)n/c}\right]\\ &+F\{R_{\delta_2\phi}(\mathrm{T})\}\left[1 - e^{i2\pi f(2z-L)n/c}\right]\\ &+F\{R_{\delta_1}(\mathrm{T})\} + F\{R_{\delta_2}(\mathrm{T})\},\end{aligned} \tag{4.10}$$

where $R_x(\mathrm{T})$ is the autocorrelation function of the x variable and $R_{xy}(\mathrm{T})$ is the cross-correlation function between variables x and y. The mixed products of δ_1 and δ_2 have been neglected since they are uncorrelated by definition. Again, following the assumption that the noise of each fibre segment is independent, the Fourier

transforms can be renamed as:

$$\begin{aligned} F\{R_{\phi}\} &= \frac{S_{\phi}(f)}{L}, \\ F\{R_{\phi\delta_i}\} &= \frac{S_{\phi\delta_i}(f)}{L}, \\ F\{R_{\delta_i\phi}\} &= \frac{S_{\delta_i\phi}(f)}{L}, \\ \sum_{i=1}^{2} F\{R_{\delta_i}\} &= \frac{(1-k)^2 S_{\phi}(f)}{L}, \end{aligned} \tag{4.11}$$

with i = 1,2. The cross-spectral terms can be neglected considering that $S_{\phi\delta_i}(f), S_{\delta_i\phi}(f) \ll S_{\phi}(f)$.
Integrating eq. (4.11) over the fibre length, the PSD becomes:

$$S_{\text{pair,tw}}(f) = \frac{1}{4}\left[(1-k)^2 + \frac{1}{3}\left(2\pi f \frac{nL}{c}\right)^2\right] S_{\phi}(f). \tag{4.12}$$

It is important to stress that this relation holds for $f \ll \frac{c}{nL}$. For $k = 1$, i.e. totally correlated fibres, it reduces to eq. (1.23), i.e. to the case in which a single fibre is used in the two directions. A comparison of two-way measurements performed both in bidirectional and unidirectional configuration on the same infrastructure can be found in [80], whose results confirm the relation obtained in eq. (4.12).

An estimation of k can be derived from the results presented in [80] by Bercy et al., on the French fibre network. By comparing the phase of the free running fibre with that of the two-way comparison over a fibre pair, a noise rejection of 27 dB can be estimated for $f > 0.1$ Hz. Considering eq. (4.12), this implies $k = 0.91$. On timescales of hours, an improvement of 2 orders of magnitude in the link instability is observed. From that we infer a rejection of 40 dB at low frequencies, which corresponds to $k = 0.98$.

Another estimation can be retrieved from the two-way measurement presented in chapter 3. As explained, in this case two parallel fibres ($Fibre_1$ and $Fibre_2$ in fig. 4.11) have been joined at the remote end to obtain a loop with both ends in the same laboratory. This scheme did not allow a direct evaluation of the degree of correlation between the noise of the two fibres. Nevertheless, due to the peculiarity of the fibre link setup, it is still possible to perform an estimation of k. A scheme of the looped link is shown in fig. 4.11. Since $Fibre_1$ and $Fibre_2$ are adjacent, the environmental noise affecting the signal travelling the loop is partially correlated. Thus, $\overrightarrow{\phi}(t)$ e $\overleftarrow{\phi}(t)$, which are the phase perturbations on the signals travelling the link loop in opposite directions, can be written as:

$$\begin{aligned} \overrightarrow{\phi}(t) &= \overrightarrow{\varphi}(t) + \overrightarrow{\delta}(t) \\ \overleftarrow{\phi}(t) &= \overleftarrow{\varphi}(t) + \overleftarrow{\delta}(t), \end{aligned} \tag{4.13}$$

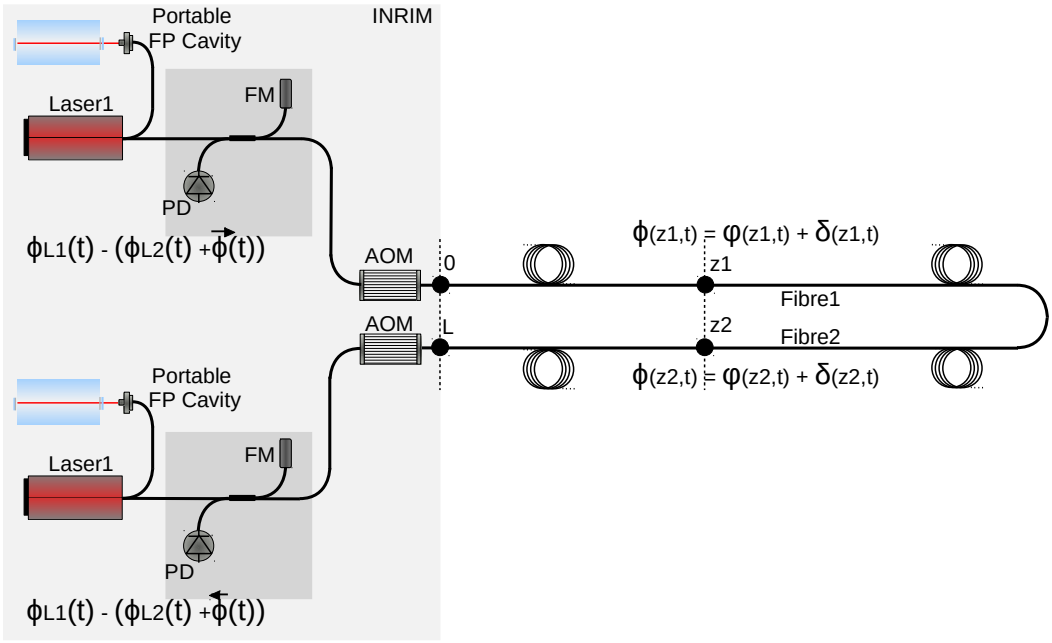

Figure 4.11: Sketch of the testbed based on a fibre pair between INRIM and Modane, employed for the evaluation of k using the two-way cancellation scheme. It shows that the fibre link consists on two adjacent fibres, $Fibre_1$ and $Fibre_2$, looped together at the end. The vertical dashed lines show the elementary segments of the two fibres which are located in the same position along the fibre bundle, i.e. 0 and L (the two link extremities), $z1$ and $z2$.

where $\varphi(t)$ is the environmental noise component that affects the two fibres equally, while $\delta(t)$ is the uncorrelated part of the noise.
Considering the phase fluctuations per fibre segment, we can assume that $\overrightarrow{\varphi}(t, z_1) = \overleftarrow{\varphi}(t, z_2)$, since z_1 and z_2 are located in the same physical position along the fibre bundle. Integrating over the fibre length we obtain $\overrightarrow{\varphi}(t) = \overleftarrow{\varphi}(t)$ and thus the two-way difference becomes:

$$\overrightarrow{\phi}(t) - \overleftarrow{\phi}(t) = \overrightarrow{\delta}(t) - \overleftarrow{\delta}(t), \tag{4.14}$$

where $\overrightarrow{\delta}(t)$ and $\overleftarrow{\delta}(t)$ can be related to the overall fibre noise $\overrightarrow{\phi}(t)$ and $\overleftarrow{\phi}(t)$ according to eq. (4.7). In this case the $\frac{1}{2}$ factor in front of $\overrightarrow{\phi}(t) - \overleftarrow{\phi}(t)$ is omitted since the measurement we are considering (reported in chapter 3) are related to the measure of the residual fibre noise described by eq. (3.1).
To calculate the expected noise PSD, the same procedure used for eq. (4.12) is followed. The two-way difference expressed as the integral of the phase variations per fibre segment is:

$$\overrightarrow{\phi}(t) - \overleftarrow{\phi}(t) = \int_0^L \delta\left(t + \frac{n(z-L)}{c}\right) dz - \int_0^L \delta\left(t - \frac{nz}{c}\right) dz. \tag{4.15}$$

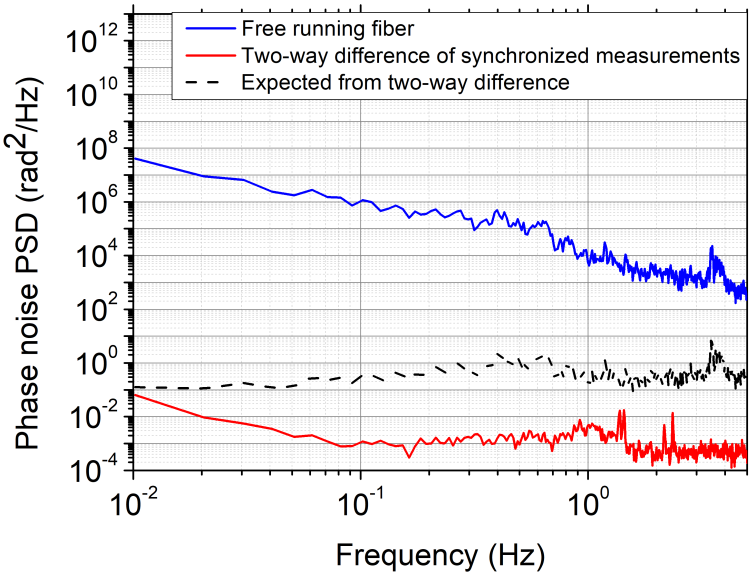

Figure 4.12: Phase noise of the $2 \times 147\,\mathrm{km}$ link between INRIM and Modane. Blue: noise of the free running fibre link; black: expected residual noise after two-way noise cancellation on a bidirectional fibre; red: residual noise after two-way noise cancellation on the bidirectional link based on a loop of two adjacent fibres.

The Fourier transform of the autocorrelation function per fibre segment contains a single term:

$$S\left(z,f\right) = F\{R_{\delta}\left(\mathrm{T}\right)\}\left[2 - \left(e^{i2\pi f(L-2z)n/c} + e^{-i2\pi f(L-2z)n/c}\right)\right], \tag{4.16}$$

and $F\{R_{\delta}\left(\mathrm{T}\right)\}$ can be written as $\frac{(1-k)^2 S_{\phi}(f)}{L}$. Integrating eq. (4.16) over the fibre length the PSD becomes:

$$S_{\text{adjacent,tw}}\left(f\right) = \frac{1}{3}\left(2\pi f\frac{nL}{c}\right)^2 (1-k)^2\, S_{\phi}\left(f\right) = (1-k)^2\, S_{\text{two-way}}\left(f\right), \tag{4.17}$$

where $S_{\text{two-way}}\left(f\right)$ is the residual fibre noise of a two-way difference expressed by eq. (3.1). The blue spectrum in fig. 4.12 represents the noise of the free running fibre. The noise spectrum related to the two-way noise measured on the looped testbed ($S_{\text{adjacent,tw}}\left(f\right)$) is shown by the red line, while the noise expected from uncorrelated fibres ($S_{\text{two-way}}\left(f\right)$) can be derived from the free running fibre noise and is shown by the black dashed line. For $f > 0.1\,\mathrm{Hz}$, a difference of 26 dB is observed between the two cases. This corresponds to a configuration where $k = 0.95$. In this case it would be useless to consider the long-term noise rejection to evaluate k, since, as discussed in the previous chapter, our measurement is probably limited by other effects, such as the polarization mode dispersion.

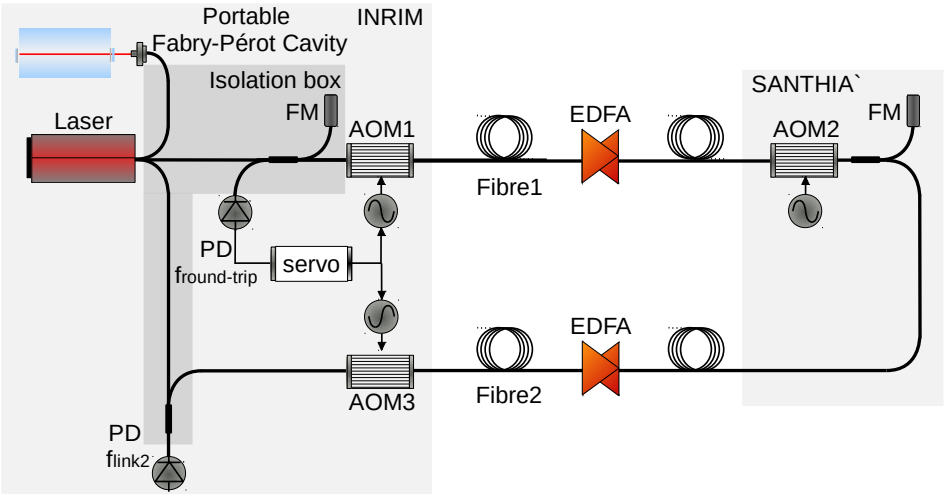

Figure 4.13: Sketch of the testbed based on a fibre pair between INRIM and Santhià, employed for the evaluation of k using the Doppler-noise cancellation scheme.

A further estimation of k is obtained from a measurement performed on a span of the Italian link between Torino and the town of Santhià, of length 92 km.
The setup scheme is shown in fig. 4.13. The signal of the ultrastable laser is launched in $Fibre_1$. At the remote end of $Fibre_1$ the signal is split into two. Part is reflected with a Faraday mirror (FM) towards INRIM, where it is compared to a local reference ($f_{round-trip}$) and used to actively compensate the noise of $Fibre_1$. The second part is sent back to INRIM along $Fibre_2$ (adjacent to $Fibre_1$). To detect the phase noise accumulated along $Fibre_2$, this signal is also compared to the local reference in the laboratory (f_{link2}). The correction signal fed to AOM_1 to compensate for the phase noise of $Fibre_1$ is also fed to AOM_3. This enables to compensate the phase noise component of $Fibre_2$ which is correlated to the noise of $Fibre_1$, while the uncorrelated part remains uncompensated. By comparing the residual noise of the active cancellation of $Fibre_2$ with its free running noise, we can retrieve an estimation of k. It can be shown that eq. (4.12) for the Doppler-noise scheme becomes:

$$S_{\mathrm{pair,Doppler}}(f) = \left[(1-k)^2 + \frac{1}{3}\left(2\pi f \frac{nL}{c}\right)^2\right] S_\phi(f)\,, \tag{4.18}$$

differing by a factor $\frac{1}{4}$ from the two-way scheme. Fig. 4.14 shows the phase noise spectra of the free running $Fibre_2$ (blue) and of the actively compensated $Fibre_2$ (green). In this case, the spectra have to be considered for $f < 10$ Hz, since for higher frequencies they could be affected by bandwidth-limitation artefacts introduced by the active noise compensation. A rejection of 40 dB is observed in this spectral region between the blue and the green spectra, which, according to eq. (4.18), corresponds to $k = 0.98$. From the stability plot, a value for the long

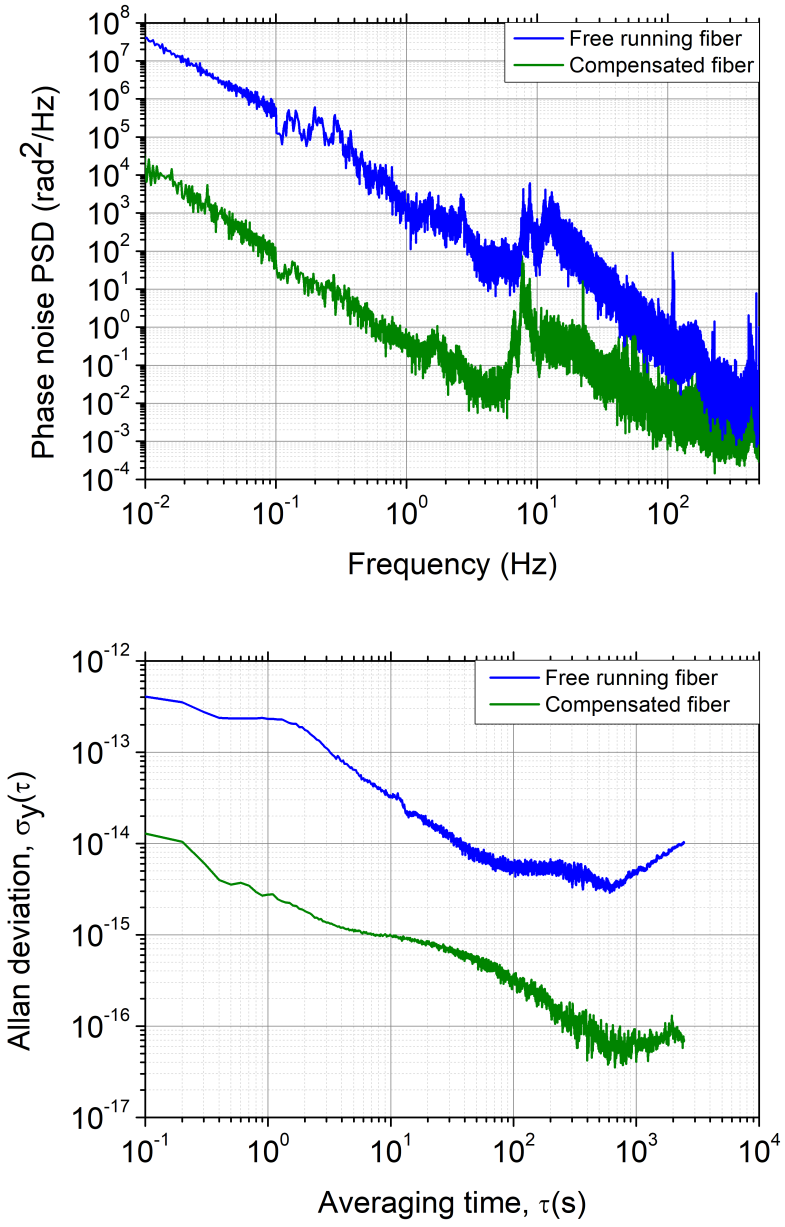

Figure 4.14: Phase noise and frequency stability of the 92 km link between INRIM and Santhià . Blue: noise of the free running fibre link; green: residual noise after a Doppler-noise cancellation on a unidirectional fibre pair; yellow: residual noise after Doppler-noise cancellation on a bidirectional fibre.

term can be retrieved. At $\tau = 10^3$ s a noise rejection of 13 dB is observed. This results in 26 dB on the noise PSD and $k = 0.95$.
The results obtained from the three infrastructures are summarized in tab. 4.1. For

the following estimation we chose the value $k = 0.91$, which is the worst observed condition, to keep the evaluation as conservative as possible.

Testbed	Length (km)	Fourier frequency (Hz)	k
French link	92	10^{-1}	0.91
		10^{-3}	0.98
INRIM-Modane	294	10^{-1}	0.95
INRIM-Santhià	92	10^{-1}	0.99
		10^{-3}	0.95

Table 4.1: Correlation level (k) between the phase noise affecting the signals running on a pair of adjacent fibres, evaluated for three different testbeds.

Noise evaluation of a transcontinental link

The noise of a transoceanic link where passive noise rejection is implemented is now evaluated considering a link length of $L = 7000\,\mathrm{km}$. The results are shown in terms of PSD (fig. 4.15a) and Allan deviation (fig. 4.15b). The grey traces correspond to the noise measured on L1 while the light grey refers to L2. The black line in fig. 4.15a is the best approximation of the L2 spectrum, according to the model: $S_\phi(f) = \frac{h_{-2}}{f^2} + \frac{h_{-3}}{f^3}$, with $h_{-2} = 4\,\mathrm{rad^2Hz}$ and $h_{-3} = 0.18\,\mathrm{rad^2Hz^2}$. The corresponding Allan variation is calculated with the following relation [103]:

$$\sigma_y^2(\tau) = \frac{1}{2}\frac{h_{-2}}{\nu_0^2}\tau^{-1} + 2\ln 2\frac{h_{-3}}{\nu_0^2}, \tag{4.19}$$

where ν_0 is the absolute frequency of the optical carrier. The resulting Allan deviation is shown in fig. 4.15b for the two links. An inconsistency between model and experimental results of $L1$ is observed on short timescales, which can be attributed to the acoustic noise of the server room. The discrepancy on the long term with $L2$ is due to the strong temperature excursion generated by the high currents flowing in the HV cables.
This model is used to extrapolate the noise of the transoceanic fibre using eq. (4.6). The latter is shown by the green lines. The performance achievable by the two-way noise cancellation both with unidirectional and bidirectional fibres is estimated from the transoceanic spectrum, using eq. (4.12) and (1.23) respectively. The result in the former case is shown by the orange trace. As previously mentioned, this evaluation holds for $f \ll \frac{c}{nL}$ which for 7000 km means $f \ll 30\,\mathrm{Hz}$. For this reason, the spectra are shown for $f < 3\,\mathrm{Hz}$.
It is seen that the long-term stability when bidirectional fibres are used achieves the 1×10^{-19} level, which in principle makes this technique suitable for clocks comparisons across the ocean. However, the infrastructure of submarine fibres may not be

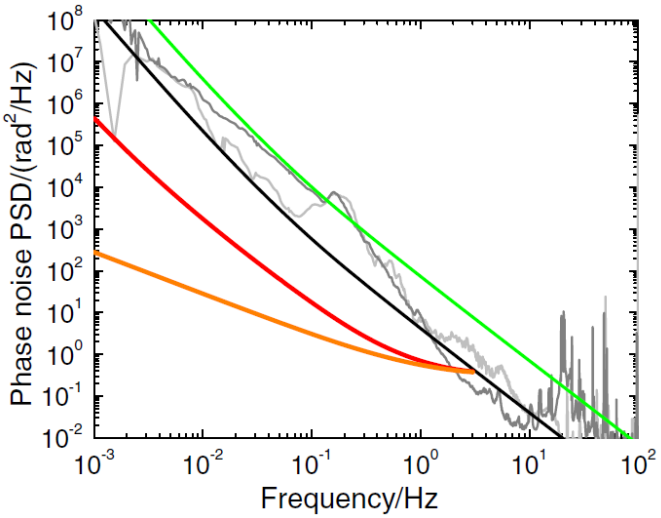

(a) PSDs, the orange and red spectra are plotted only for Fourier frequency $f < 3\,\mathrm{Hz}$, where the low-frequency approximation for noise compensation is valid.

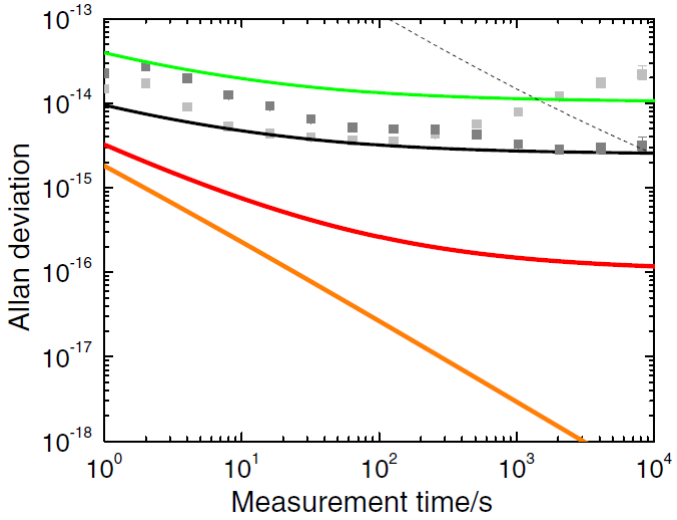

(b) Allan deviation.

Figure 4.15: PSDs and Allan deviation for submarine fibre links. Gray and light gray: measured values for the L1 and L2 testbeds, established over a $\sim$ 100 km looped fibre; black: mathematical model for the observed noise; green: extrapolated noise of a free-running 7000 km transoceanic fibre; orange and red: expected behaviour of a two-way frequency comparison over a 7000 km transoceanic fibre, established over a single fibre and a fibre pair, respectively.

able to sustain a bidirectional communication, requiring the transmission scheme on a fibre pair. The expected residual noise for unidirectional frequency transfer, evaluated with eq. (4.12), is shown by the red lines; again, the spectrum is plotted for $f < 3\,\mathrm{Hz}$. In this second case the stability does not drop below the 1×10^{-16}

level on the long term, limited by the uncorrelated noise of the fibres which cannot be rejected. This uncertainty is not enough to perform a comparison of optical clocks at their level of accuracy.
Even though the long-term stability estimated here is comparable to that exhibited by satellites, it is achieved after less than one-hour measurement, while satellites require several days of averaging to achieve the same performance (dashed grey line in fig. 4.15b). Therefore, fibre-based frequency transfer across the ocean may allow a much faster comparison of primary standards, which could lead to a significant improvement in the computation of the International Atomic Time.
In addition, the presented estimation is conservative, as submarine fibres deployed on the bottom of the ocean are expected to exhibit a lower noise than fibres buried in the Sicily-Malta channel.
A possible limitation may be introduced by the cascaded EDFAs installed along transoceanic fibres to recover for optical losses. As explained in chapter 1, the amplified spontaneous emissions generated in a chain of amplifiers affects the transmitted signal, deteriorating the optical signal-to-noise ratio. This may result in an increase of cycle-slips on the signal detection which introduces undesired frequency offsets on the disseminated frequency reference. Therefore, this effect has to be carefully investigated for transoceanic distances, where a chain of cascaded EDFAs of unprecedented length is employed.

Chapter 5

Optical link applications: radio astronomy, geodesy and seismology

Optical fibre links have demonstrated to sustain the remote comparisons of optical clocks of new generation at their intrinsic level of accuracy. The capability of disseminating high-stability frequency references opens the possibility of a number of exploitations in applied science. Prominent examples which were investigated by INRIM are applications in radio astronomy and geodesy based on Very-Long-Baseline-Interferometry (VLBI), relativistic geodesy and monitoring of seismic events.
The benefits that frequency metrology can bring to VLBI are under evaluation in collaboration with the National Institute for Astrophysics (INAF) and the Italian Space Agency (ASI), exploiting the fibre connection between Torino, Medicina and Matera.
An experiment of chronometric geodesy was performed in collaboration with the Physikalisch-Technische Bundesanstalt (PTB) and the National Physical Laboratory (NPL) on the fibre link between Torino and the Laboratoire Souterrain de Modane (LSM).
The use of optical fibres as distributed sensors for the detection of seismic events has been investigated with NPL, the University of Malta and the British Geological Survey, exploiting different testbeds based both on submarine and land fibres.
These applications are described in the following sections.

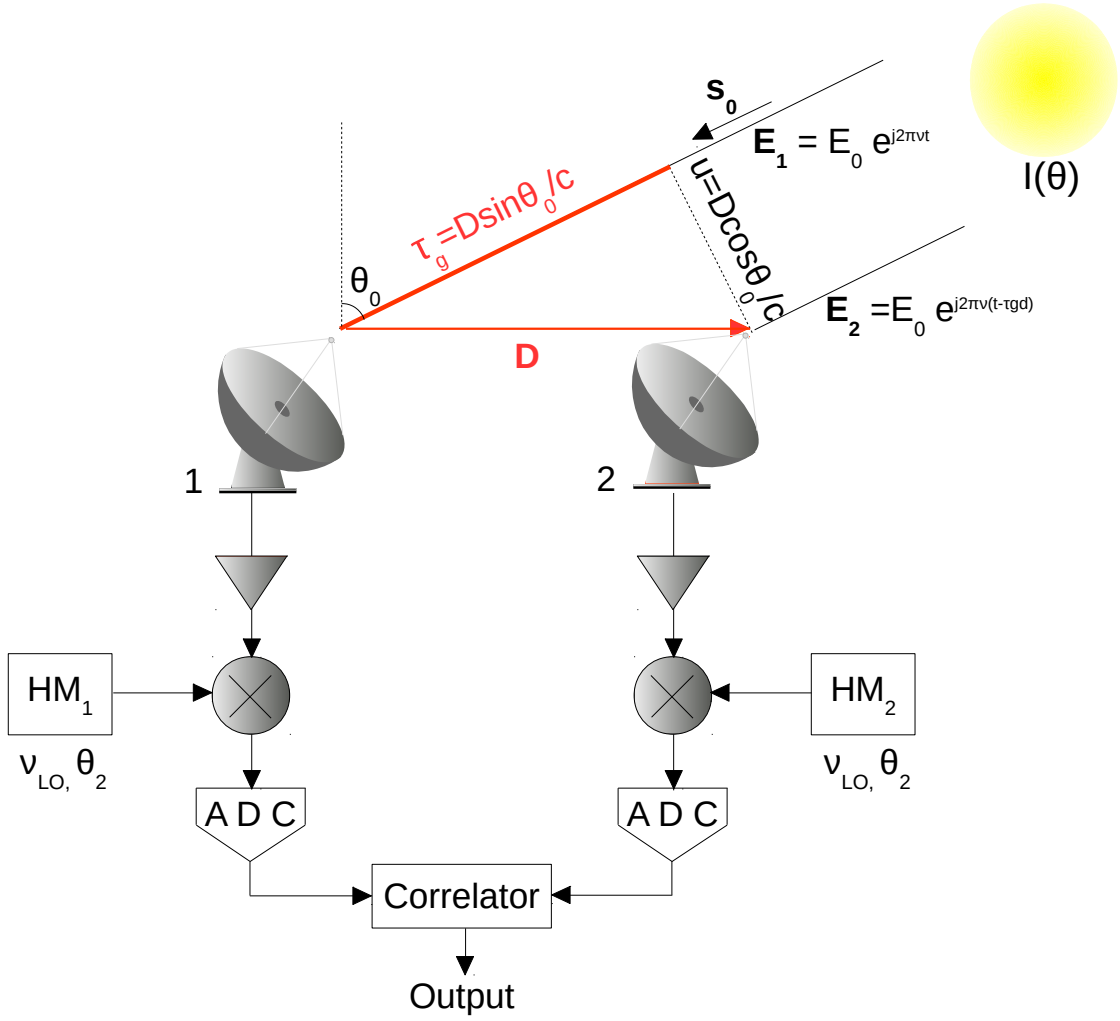

Figure 5.1: Scheme of a VLBI observation with two radio telescopes. $\boldsymbol{E_1}$ and $\boldsymbol{E_2}$ are the planar waves received by the two antennas and $I(\theta)$ is the intensity distribution of the radio source. Each signal is amplified and down-converted using an Hydrogen Maser (HM_1 and HM_2) as local oscillator whose nominal frequency is ν_{LO}, θ_1 and θ_2 are the phase noise attributed to each Maser. The down-converted signals are digitalized (ADC) and correlated.

5.1 Very Long Baseline Interferometry

5.1.1 Basic principles of VLBI

VLBI is an interferometric technique, based on the simultaneous observation of a radio astronomical source by an array of radio telescopes spread all over the Earth. By correlating the data acquired by each antenna, the resolution of the observation is improved with respect to a single telescope observation by orders

of magnitude. Fig. 5.1 shows a basic configuration with only two antennas. $\boldsymbol{D}$ is the baseline, i.e. the geometrical distance between the two telescopes. $I(\theta)$ is the intensity distribution of the radio source, the direction of the incoming radiation is shown by the vector $\boldsymbol{s_0}$ and θ_0 expresses the source elevation. The incoming radiation can be approximated to a planar wave, thus the electric fields $\boldsymbol{E_1}$ and $\boldsymbol{E_2}$ received by two antennas are:

$$\boldsymbol{E_1} = E_0 e^{j2\pi\nu t} \tag{5.1}$$

and

$$\boldsymbol{E_2} = E_0 e^{j2\pi\nu\left(t-\tau_{\mathrm{gd}}\right)}. \tag{5.2}$$

ν is the absolute frequency of the radiation and τ_{gd} is the difference in arrival times of the signal at the two antennas. In literature it is usually referred to as group delay and represents the fundamental observable of VLBI. It consists on several terms:

$$\tau_{\mathrm{gd}} = \tau_{\mathrm{g}} + \tau_{\mathrm{sou}} + \tau_{\mathrm{iono}} + \tau_{\mathrm{trop}} + \tau_{\mathrm{ab}} + \tau_{\mathrm{rel}} + \tau_{\mathrm{str}}, \tag{5.3}$$

where: τ_{g} is the geometric delay, τ_{sou} is the phase-delay term introduced by the spatial extension of the source, τ_{iono} is the delay introduced by the propagation through the ionized portion of the atmosphere, τ_{trop} is due to the propagation through non-ionized atmosphere, τ_{ab} is the contribution of diurnal aberration, i.e. the apparent motion of celestial objects depending on the velocity of the observer, τ_{rel} stands for special and general relativistic corrections and τ_{str} is the instrumental delay.
The biggest contribution is τ_{g}, which depends on the scalar product of the baseline $\boldsymbol{D}$ and the unit vector of the radio source $\boldsymbol{s_0}$ [144]:

$$\tau_{\mathrm{g}} = \frac{\boldsymbol{D}\cdot\boldsymbol{s_0}}{c} = \frac{D\sin\theta_0}{c}. \tag{5.4}$$

A measure of τ_{gd} is obtained by cross-correlating the signals received by each antenna. Since the frequency of the radiation may range from 300 MHz up to 100 GHz, at the receiver the signal is down-converted with a local oscillator (ν_{LO}) to the RF domain. In this way the signal processing can be performed at intermediate frequencies, facilitating amplification, filtering and recording. To this purpose, hydrogen masers (HMs) are used; their absolute frequency and the long-term drift are periodically calibrated via GPS.
Considering an observation performed by two telescopes, the voltage signals generated by the two antennas are $V_1 = V_{10}e^{j\phi_1}$ and $V_2 = V_{20}e^{j\phi_2}$. The useful information is contained in the phase terms, which after down-conversion are digitally sampled as:

$$\begin{aligned}\phi_1(t,\nu) &= 2\pi\left(\nu-\nu_{\mathrm{LO}}\right)\left(t-\tau_1\right)-\theta_1\\ \phi_2(t,\nu) &= 2\pi\left(\nu-\nu_{\mathrm{LO}}\right)\left(t-\tau_2\right)-2\pi\nu\tau_{\mathrm{gd}}-\theta_2.\end{aligned} \tag{5.5}$$

θ_1 and θ_2 are the phase contributions introduced by the frequency standards used for down-conversion, while τ_1 and τ_2 are related to different timescales at the two telescopes.
During data processing, the phase series sampled by antenna 2 is advanced in time by τ'_{gd}, which is the best estimation of τ_{gd}, obtained from the computation of known physics, least square estimations, theoretical models derived from locally measured parameters and dual-frequency observations. Thus:

$$\phi_2(t,\nu) = 2\pi(\nu - \nu_{\mathrm{LO}})\left(t - \tau_2 + \tau'_{\mathrm{gd}}\right) - 2\pi\nu\tau_{\mathrm{gd}} - \theta_2. \tag{5.6}$$

The cross-correlation function is computed through a digital multi-delay correlator, which applies a variable delay to the ϕ_2 phase series. This is equivalent to scanning τ'_{gd} around the nominal value $\tau'_{\mathrm{gd}} \simeq \tau_{\mathrm{gd}}$. The correlator inputs are V_1 and V_2 and the output is:

$$r(\tau) = \int_{-\infty}^{\infty} V_1(t)\, V_2(t-\tau)\, dt. \tag{5.7}$$

The interference fringes depend on the phase difference:

$$\phi_{1,2}(t,\nu) = \phi_1 - \phi_2 = 2\pi\nu'(\tau + \tau_{\mathrm{e}}) + 2\pi\nu_{\mathrm{LO}}\tau_{\mathrm{gd}} + \theta_{21}, \tag{5.8}$$

where $\nu' = \nu - \nu_{\mathrm{LO}}$, $\tau = \tau_{\mathrm{gd}} - \tau'_{\mathrm{gd}}$, $\tau_{\mathrm{e}} = \tau_2 - \tau_1$ and $\theta_{21} = \theta_2 - \theta_1$. It is worth to notice that this is the phase of the fringes obtained for the lower-side bandwidth $(\nu - \nu_{\mathrm{LO}})$, the same calculation can be performed for the upper-side bandwidth $(\nu + \nu_{\mathrm{LO}})$. In a double-sideband system the data are retrieved from both sidebands, by separately applying appropriated processing. The output of the correlator is [55]:

$$r(\tau) = |V_0|^2 \cos\left[2\pi\left(\nu'\tau + \nu'\tau_{\mathrm{e}} + \nu_{\mathrm{LO}}\tau_{\mathrm{gd}}\right) + \theta_{21}\right]. \tag{5.9}$$

A point source has been considered so far, whose signal is received by the antenna along the θ_0 direction, i.e. the phase reference position. In radio astronomy extended sources are observed, whose intensity profile is $I(\theta)$ (a one-dimensional profile is considered here for simplicity). Therefore, the antenna receives radiations from directions $\theta_0 + \Delta\theta$, where $\Delta\theta$ may vary in a range of few degrees, while the applied correction for τ_{gd} is $\tau'_{\mathrm{gd}} = \frac{D\sin\theta_0}{c}$, i.e. the estimated delay for the direction θ_0. For a radiation arriving from a $\theta_0 + \Delta\theta$ direction, the fringe response term of eq. (5.9) becomes:

$$\begin{aligned} \cos(2\pi\nu'\tau) &= \cos\left\{2\pi\nu'\left[\frac{D}{c}\sin(\theta_0 + \Delta\theta) - \tau'_{\mathrm{gd}}\right]\right\} \\ &\simeq \cos\left[2\pi\nu'\frac{D}{c}\sin\Delta\theta\cos\theta_0\right], \end{aligned} \tag{5.10}$$

for $\Delta\theta \ll \theta_0$. The quantity:

$$u = \frac{\nu' D\cos\theta_0}{c} \tag{5.11}$$

is equal to the component of the antenna baseline normal to the direction of the reference position θ_0. It determines the angular resolution of the interference fringes and can be interpreted as spatial frequency, measured in cycles per radians, since the spatial variable $l = \sin \Delta\theta$, being small, can be expressed in radians. Eq. (5.10) becomes:

$$F(l) = \cos(2\pi u l). \tag{5.12}$$

It may be seen as the array response to a point source from a certain l direction. By varying l over the extended source, i.e. by tracking, for instance, the source during its apparent motion in the sky, the interference fringes are observed.
In addition, the received intensity distribution is modified by the reception pattern of the antenna, $A(l)$, which is a plot of the effective area of the antenna, as a function of the angle from the centre of the telescope dish. Moreover, since the incoming radiation has a broad spectrum, the frequency response of the antenna conversion chain has to be taken into account. The bandwidth pattern, $F_{\mathrm{B}}(l)$, is an envelope function whose shape and width depend on the passband filters of the antenna.
The fringe pattern $F(l)$, the reception pattern $A(l)$ and the bandwidth pattern $F_{\mathrm{B}}(l)$ represent the power reception pattern of the antenna. For an extended source, the correlator output of eq. (5.9) becomes the convolution integral of the power reception pattern with the source intensity distribution:

$$R(l) = |V_0|^2 \cos[2\pi u l + 2\pi\nu'\tau_{\mathrm{e}} + 2\pi\nu_{\mathrm{LO}}\tau_{\mathrm{gd}} + \theta_{21}] * A(l) F_{\mathrm{B}}(l) I(l), \tag{5.13}$$

where $I(l)$ is the intensity profile expressed as function of the spatial variable l and the $*$ symbol denotes the convolution.
The Fourier transform of $I(l)$ is defined as the visibility of the radio source:

$$\mathcal{V}(u) = |\mathcal{V}_0| e^{j\phi_u}. \tag{5.14}$$

It represents the amplitude and phase of the sinusoidal component of the intensity profile with spatial frequency u. In the case of a point-like source $|\mathcal{V}_0| = 1$ and $\phi_u = 0$.
$\mathcal{V}$ can be retrieved from the Fourier transform of $R(l)$ as defined in eq. (5.13). By evaluating it for different u values, i.e. performing observations at different times of the day (different θ_0 values) and with different baselines, a full sampling of $\mathcal{V}(u)$ is obtained. From the anti-transform of $\mathcal{V}(u)$, $I(l)$ is retrieved, which is the observable of a VLBI radio astronomical observation.
On the other hand, if a geodetic observation is performed, a point-like source is used and the information about the baseline displacement is retrieved from the cosine phase of eq. (5.9), in particular from the geometrical component τ_{g}.
It is straightforward to see that the final resolution of a VLBI observation, both for geodesy and radio astronomy, has many contributions (eq. (5.3)). Beside the instrumental uncertainty, which is reduced with proper calibration, the dominant

contributions are the uncertainties introduced by the theoretical models of the various delay components of τ_{gd}, in particular the troposphere delay and the noise of the reference clocks employed as local oscillators for down-conversion and for timestamping.
The troposphere introduces a time-varying delay, which is mainly due to inhomogeneities in the water vapour concentration, whose instability ranges from 10^{-13} to 10^{-14} at 1 s depending on the weather conditions, reaching the 10^{-16} level after 10 000 s measurement.
On the other hand, HMs ensure an uncertainty contribution as low as 6×10^{-14} at one second. This instability becomes a dominant noise source when the HM reference is multiplied to down-convert radiations in the order of ~ 100 GHz, since in multiplication chains the noise increases as the square of the multiplication factor. In addition, HMs are affected by a linear drift that ranges between $10^{-15}\,\mathrm{d}^{-1}$ and $10^{-16}\,\mathrm{d}^{-1}$, while geodetic observations aim at a positioning resolution of 1 mm which is achievable if the uncertainty of the reference clock is at the 10^{-16} level [145].
As a consequence, an improvement of the reference clocks would be crucial to preserve the coherence of the sky signal during down-conversion at different telescopes. To this purpose, a proposed solution is to upgrade the local clocks. This is done with Cryogenic Sapphire Oscillators [146], while in the future optical clocks of new generation could bring significant improvements. An alternative solution is to exploit the dissemination of the high accuracy frequency standards developed by NMIs. Satellite systems, which are currently used for the calibration of the local HMs, are able to achieve the 10^{-14} to 10^{-15} level of uncertainty after one day averaging, which does not cope with the VLBI requirements. On the other hand, optical links guarantee the 10^{-14} level of uncertainty at 1 s, being able to disseminate the frequency references of atomic clocks at their level of accuracy after few hours measurement. The use of a fibre link for VLBI observation has been proposed for the first time in [121]. The RF reference required by the VLBI processing system can be provided by direct RF dissemination (section 1.1.2) [51, 52] or by delivering an optical carrier and generating a stable RF by means of an optical comb.
The latter technique is exploited since 2015 for the fibre-based dissemination between INRIM and the Medicina radiotelescopes in central Italy. In [31] is reported a proof-of-principle measurement campaign during which the reference of the INRIM HM was delivered to Medicina via optical link. Currently, an HM is disseminated. The system will be upgraded, transferring the frequency references of the optical standards developed and maintained at INRIM (Yb under operation [22] and Sr under development [147]). This will guarantee an effective improvement in the disseminated clock stability and accuracy.
An alternative to reduce the noise contribution of the reference clock is the common-clock approach, i.e. the dissemination of the same frequency reference to more

radiotelescopes simultaneously. To this scope a theoretical analysis has been performed by the Research Institute of Sweden (RISE) together with the Onsala telescope staff. Simulations predict that the uncertainty in the determination of some parameters of interest (geometrical delays, air turbulence and water vapour content, tides and variations of telescopes position) is reduced between 20 and 35 % when all stations share one single clock. As expected, the improvement is reduced if only two stations of the radiotelescopes network share a common clock, as the results depend on the global analysis of the full network. The extension of the Italian link to the Matera radiotelescope in south Italy allows the simultaneous dissemination of the INRIM frequency standards to the INAF and ASI VLBI antennas, enabling to perform the first of common-clock VLBI observations.

5.1.2 The Italian project for VLBI

In 2015 the fibre infrastructure connecting INRIM to the INAF radiotelescope in Medicina has been completed within the LIFT (Italian Link for Frequency and Time) project [121]. The first VLBI observation exploiting the remote link reference [31] was performed in September 2015 demonstrating satisfactory results. Interleaved VLBI observations were performed using the local and the link-disseminated clocks. In this latter configuration it was possible to retrieve the fringe pattern over the whole 24-hour session and the group delay residuals showed a good agreement with those obtained with the local clock.
The aim of the MetGeSp project (Metrology for Geodesy and Space), started in 2015, is to create a fibre network for the simultaneous frequency dissemination to the radiotelescopes located in Medicina and Matera, in view of common-clock VLBI observations. To this scope, the Italian fibre link infrastructure has been extended from Medicina to Matera (see section 2.1.2). The upgrades described in section 2.2 have been implemented to guarantee several days of continuous operation.
In preparation to the first common-clock VLBI observation planned for 2019, several preliminary tests have been performed in order to assess the compatibility of the new infrastructure with existing systems, required adaptations, reliability and achievable performances. A real-time phase comparison of local and remote HMs has been performed. It serves as inspection tool for timely detection of failures and performances monitoring of the recently implemented fibre link and synthesis chain. In addition, the software, which is routinely used for standard VLBI analysis, does not give access to the parameters of interest for our analysis and some bugs were identified. Therefore, a dedicated software was designed by the staff of the Italian Institute of Radioastronomy, to extract the phase information at all stages of the analysis. To test and refine the new software, dedicated VLBI observations have been performed, involving the Italian radio telescopes in Medicina, Matera and Noto, with the Medicina radio telescope exploiting the link reference.

Hydrogen Masers comparisons

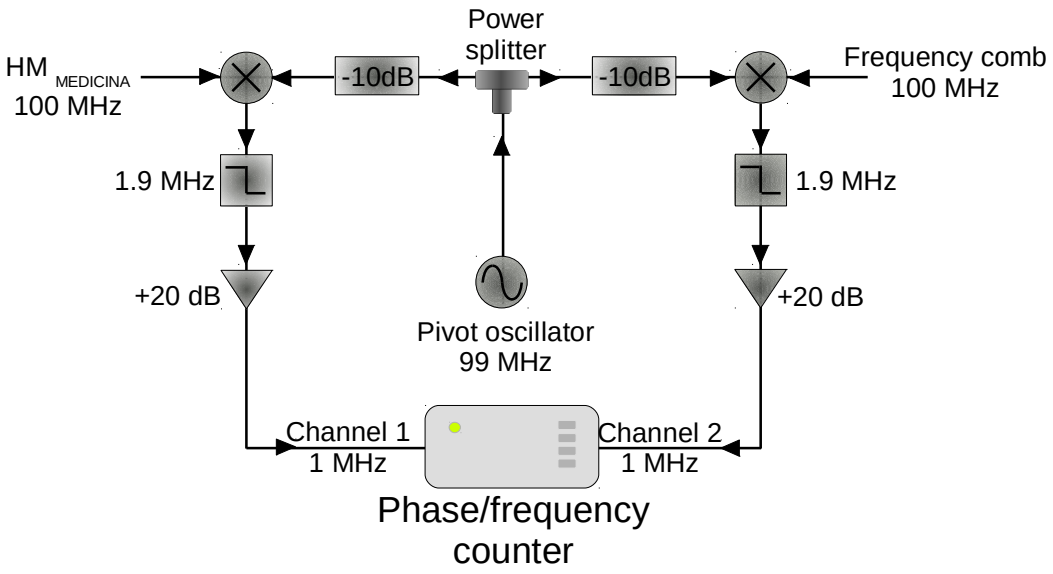

Figure 5.2: Electrical chain for the comparison of $HM_{MEDICINA}$ and HM_{INRIM} delivered with the fibre link.

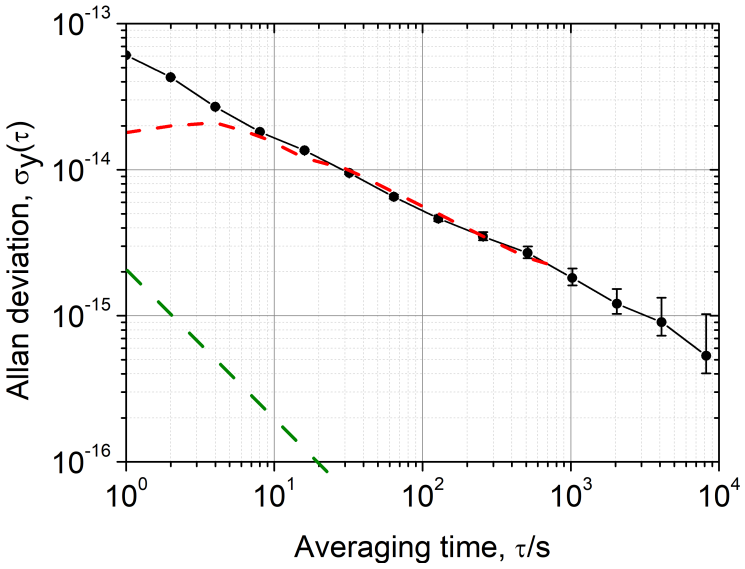

Figure 5.3: Allan deviation of the HMs comparison. Black dots: HMs comparison, $HM_{MEDICINA}$ vs HM_{INRIM}. Red dashed line: instability of the 1542 nm laser when locked to HM_{INRIM}. Green dashed line: expected contribution from the fibre link.

Torino-Medicina. The metrological chain used to deliver the frequency reference from Torino to Medicina (first span of the Italian link) and synthesize the RF reference for the radio telescope is described in section 2.1.1. A real-time comparison between the HM_{INRIM} and the $HM_{MEDICINA}$ is performed. It ensures a constant calibration of $HM_{MEDICINA}$ and a monitor of the system reliability. In addition, this may serve for VLBI observations in which the link reference is not directly used as reference for the antenna. The post process of VLBI data with the $HM_{MEDICINA}$ vs HM_{INRIM} phase comparison allows to remove the noise contribution of $HM_{MEDICINA}$, retrieving the VLBI observation referred to HM_{INRIM}.
To this purpose the scheme shown in fig. 5.2 has been adopted. The 100 MHz references generated with the frequency comb and by the local HM are down-mixed to 1 MHz by means of a pivot oscillator to increase the measurement resolution. The acquisition is performed with a dead-time-free phase/frequency counter operating in averaging mode at 1 s gate time with a fixed phase resolution. The instrumental noise floor has been evaluated at the $2 \times 10^{-14}/\sqrt{\tau}$ level, with τ averaging time, which is enough to compare the HMs at their uncertainty level. The RF fixed attenuators have been introduced to reduce impact of RF mixers and splitters leakage, as well as the reflections along the RF cables due to impedance mismatch and cross-talks between the two down-conversion chains. All these effects were observed to degrade the system noise floor to several parts in 10^{-14}. The HMs comparison is retrieved from the phase difference between the two channels of the counter.
The frequency instability of $HM_{MEDICINA}$ vs HM_{INRIM} is shown in fig. 5.3. At low averaging times it is dominated by the intrinsic instability of $HM_{MEDICINA}$, i.e. 6×10^{-14} at 1 s on a 0.5 Hz measurement bandwidth, in agreement with the specifications. On the long term, it is limited by the instability of the fibre-disseminated signal, which is shown by the red dashed line. At 1 s it is dominated by the laser instability, which is 2×10^{-14} on a 0.5 Hz measurement bandwidth. This is one order of magnitude worse than the frequency instability of the cavity-stabilized laser, because of non-complete rejection of the HM noise from the lock (see section 2.1.1). On the long term the fibre disseminated signal is dominated by HM_{INRIM}, i.e. 2×10^{-15} at 1000 s. The noise contribution of the fibre link is represented by the green dashed line and is negligible at every measurement time.

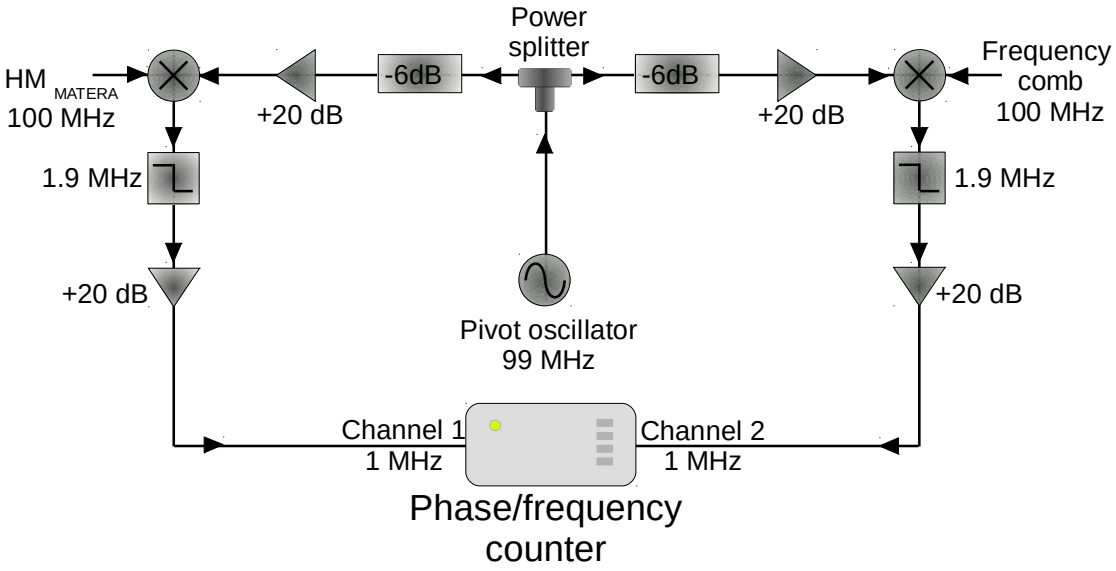

Figure 5.4: Electrical chain for the comparison of HM_{MATERA} and HM_{INRIM} delivered with the fibre link.

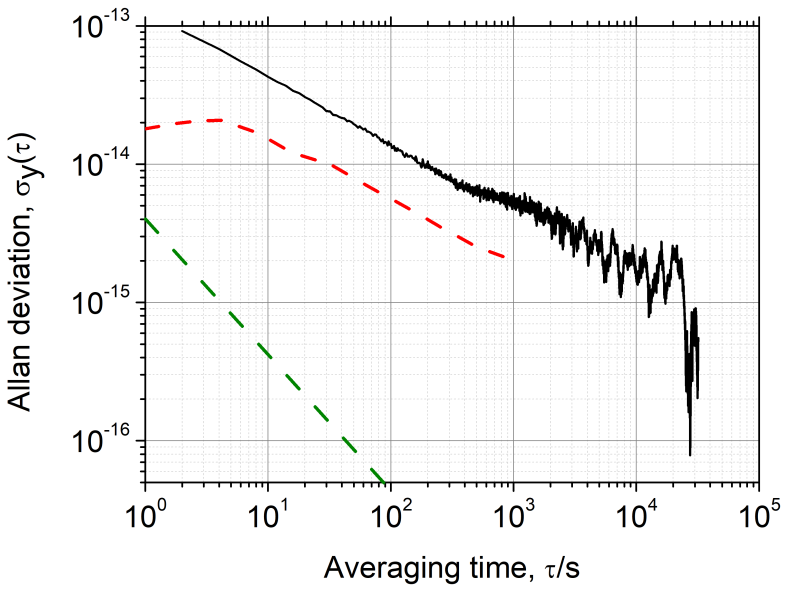

Figure 5.5: Allan deviation of the HMs comparison. Black dots: HMs comparison, HM_{MATERA} vs HM_{INRIM}. Red dashed line: instability of the 1542 nm laser when locked to HM_{INRIM}. Green dashed line: expected contribution from the fibre link.

Torino-Matera. In Matera, a conversion chain similar to that in Medicina has been implemented (fig. 2.1.1) to generate the 100 MHz reference from the link signal. The scheme shown in fig. 5.4 is employed to measure the phase difference between $\mathrm{HM}_{\mathrm{MATERA}}$ and $\mathrm{HM}_{\mathrm{INRIM}}$. It is substantially similar to that employed in Medicina. Additional RF amplifiers are used here to further reduce the crosstalk between the two down-conversion chains.
Fig. 5.5 shows the Allan deviation of $\mathrm{HM}_{\mathrm{MATERA}}$ vs $\mathrm{HM}_{\mathrm{INRIM}}$. The linear drift of the HMs has been manually removed from the raw data. The comparison is clearly limited by $\mathrm{HM}_{\mathrm{MATERA}}$ since the instability of the laser locked to $\mathrm{HM}_{\mathrm{INRIM}}$ is almost one order of magnitude lower (red dashed line). This is in agreement with the specification of $\mathrm{HM}_{\mathrm{MATERA}}$. The expected contribution of the link noise is represented by the green dashed line and is negligible at every averaging time.

Medicina-Matera. Fig. 5.6 shows the Allan deviation of $\mathrm{HM}_{\mathrm{MEDICINA}}$ vs $\mathrm{HM}_{\mathrm{INRIM}}$ (green) and $\mathrm{HM}_{\mathrm{MATERA}}$ vs $\mathrm{HM}_{\mathrm{INRIM}}$ (red), the HMs drift has been removed from both data series. Since the HMs comparisons at the two antennas are performed simultaneously, the direct difference between $\mathrm{HM}_{\mathrm{MEDICINA}}$ and $\mathrm{HM}_{\mathrm{MATERA}}$ is obtained by performing the phase difference:

$$\phi_{\mathrm{MEDICINA}} - \phi_{\mathrm{MATERA}} = (\phi_{\mathrm{MEDICINA}} - \phi_{\mathrm{INRIM}}) - (\phi_{\mathrm{MATERA}} - \phi_{\mathrm{INRIM}})\,. \quad (5.15)$$

It is shown in fig. 5.6 by the blue line. The stability is clearly limited by $\mathrm{HM}_{\mathrm{MATERA}}$ as it overlaps with the stability of $\mathrm{HM}_{\mathrm{MATERA}}$ vs $\mathrm{HM}_{\mathrm{INRIM}}$.
The data obtained from the fibre-based measurements have been compared with the measurement performed with the GPS PPP technique. The latter is performed employing the geodetic receivers INR6, MEDI and MATE, which are directly connected to the three HMs. This serves as a cross-check to verify that no frequency shift is introduced along the fibre link and on the synthesis chains within the GPS uncertainty. The relative instability of the GPS PPP $\mathrm{HM}_{\mathrm{MEDICINA}}$ vs $\mathrm{HM}_{\mathrm{MATERA}}$ comparison is shown by the grey trace in fig. 5.6.
The correlation between the data measured with the two transfer techniques is considered negligible. The comparison is performed in terms of frequency average, also known as "clock rate" (CR) in radio astronomy, and frequency drift, known as "quadratic term" (QT). The results are reported in tab. 5.1. The values obtained from the fibre and GPS PPP-based comparisons are in agreement within the GPS uncertainty. Therefore, no unexpected frequency shift is introduced on the fibre-based dissemination at the $\sim 10^{-14}$ level.

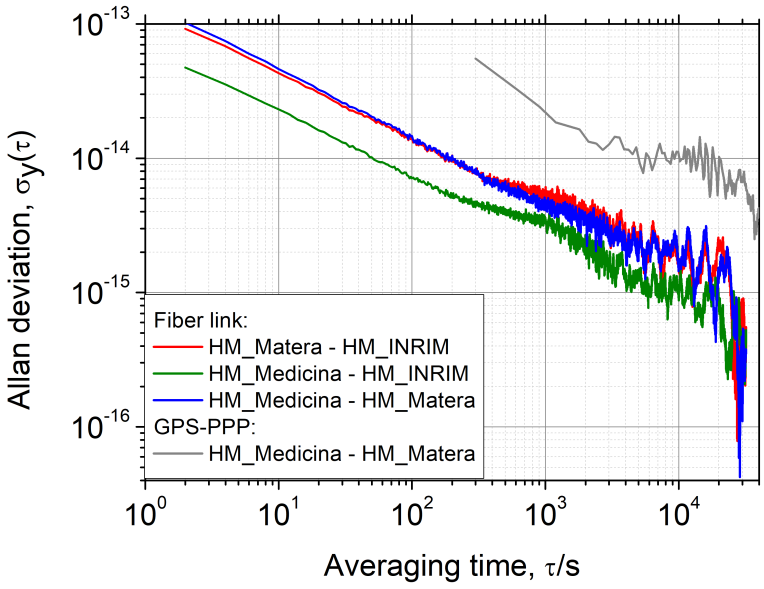

Figure 5.6: Allan deviation of the HMs comparisons. Red: $\mathrm{HM_{MEDICINA}}$ vs $\mathrm{HM_{INRIM}}$. Blue: $\mathrm{HM_{MATERA}}$ vs $\mathrm{HM_{INRIM}}$. Green: $\mathrm{HM_{MEDICINA}}$ vs $\mathrm{HM_{MATERA}}$. Grey: $\mathrm{HM_{MEDICINA}}$ vs $\mathrm{HM_{MATERA}}$ via GPS PPP.

		fibre	GPS PPP
$\mathrm{HM_{MATERA}}$ vs $\mathrm{HM_{INRIM}}$	CR	$736.25(40) \times 10^{-15}$	$741(6) \times 10^{-15}$
	QT	$-5.8(72) \times 10^{-16}\,\mathrm{s}^{-1}$	$3(9) \times 10^{-15}\,\mathrm{s}^{-1}$
$\mathrm{HM_{MEDICINA}}$ vs $\mathrm{HM_{INRIM}}$	CR	$721.05(20) \times 10^{-15}$	$721(8) \times 10^{-15}$
	QT	$1.4(4) \times 10^{-15}\,\mathrm{s}^{-1}$	$0(1) \times 10^{-14}\,\mathrm{s}^{-1}$
$\mathrm{HM_{MATERA}}$ vs $\mathrm{HM_{MEDICINA}}$	CR	$-15.2(5) \times 10^{-15}$	$-20(7) \times 10^{-15}$
	QT	$2.0(8) \times 10^{-15}\,\mathrm{s}^{-1}$	$0.2(10) \times 10^{-14}\,\mathrm{s}^{-1}$

Table 5.1: Results of the HMs comparison performed with fibre link and GPS PPP. The comparison is expressed in terms of frequency average or "clock rate" (CR) and frequency drift or "quadratic term" (QT).

VLBI observations

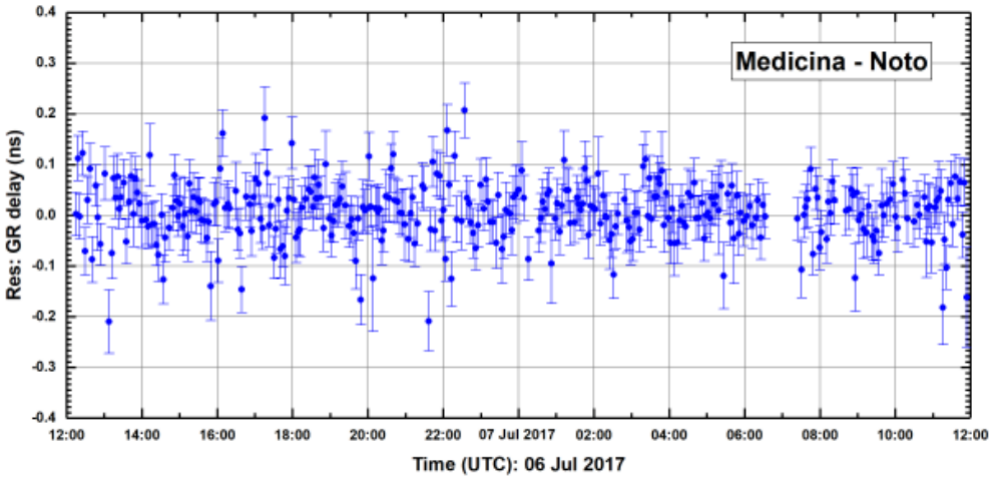

Figure 5.7: Group delay residuals vs observing time of the VLBI observation of July $6^{\text{th}} - 7^{\text{th}}$ 2017.

Dedicated VLBI campaigns have been scheduled to test the new software, implemented for the analysis of VLBI data obtained with the fibre link reference. Two geodetic observations have been performed involving the three Italian telescopes maintained by INAF and ASI: Medicina, Noto, and Matera, with the Medicina telescope using the link reference. The first observation was performed on July $6^{\text{th}} - 7^{\text{th}}$ 2017. Fig. 5.7 shows the results in terms of group delay residuals, retrieved with the new software. An unlock was induced by fast flips of polarization state in the link-disseminated signal. It occurred at ~ 7 UTC, and it is attributed to human work on the fibres. The problems introduced by this loss of coherence were fixed at the data analysis stage, such that the residuals have been retrieved for the whole uptime of the metrological chain, i.e. 97% of the 24 hours observation. The test was repeated on April $3^{\text{rd}} - 4^{\text{th}}$ 2018 and during this campaign no unlock occurred from the link.
In addition, a series of VLBI experiments were performed during the months of January and February 2018. They consisted in four short observations of three hours each, involving the telescopes in Medicina, Matera and Noto together with other European antennas. The fourth of these observations was performed using the link reference in Medicina.

5.1.3 VLBI for remote clocks comparisons

An alternative exploitation of eq. (5.9) is the comparison of remote atomic clocks, retrieving the information about the clocks phase difference from θ_{12}. For such measurements point-like sources are employed and τ_{gd} (eq. (5.3)) is estimated

from previous observations and theoretical models. Preliminary studies have been performed to investigate the potential of VLBI for time and frequency transfer compared to GPS-based techniques [148], showing a similar performance of the two approaches in terms of long-term stability. Moreover, a combined solution of VLBI and GNSS has been proposed, which benefits from the strengths of both techniques with an improvement of 10% in uncertainty [149].
A measurement campaign started in July 2018, conducted by INRIM, INAF and the Japanese NMI, NICT, is under way. The aim is to further investigate the capabilities of VLBI for frequency transfer, by comparing the INRIM Yb optical clock and the NICT Sr clock via VLBI and GPS. To this scope two transportable antennas developed by NICT are used. They have a 2.4 m-diameter dish and are designed for broadband observations, $3 - 14$ GHz, which are expected to bring an enhanced sensitivity. One of the portable antennas is installed in Medicina, close to the INAF radio telescope, and is provided with the reference of $\mathrm{HM}_{\mathrm{MEDICINA}}$. The VLBI data are post-processed and combined with the measure of $\mathrm{HM}_{\mathrm{MEDICINA}}$ against the frequency reference of the INRIM atomic clocks delivered through the optical fibre link. This allows to remove the $\mathrm{HM}_{\mathrm{MEDICINA}}$ noise contribution and to compare through VLBI the INRIM Yb optical clock. The second antenna is in the NICT headquarters in Koganei (Japan), enabling the comparison of the Yb clock with the local Sr clock. In addition, the Kashima (Japan) 34 m radio telescope is involved, generating a three antennas network for the VLBI observations. To test the capability of these broad band antennas, a series of geodetic VLBI observations has been scheduled between September 2018 and February 2019. The antennas are directly provided with the frequency reference of hydrogen masers, which in turn are calibrated against the optical clocks. The results of the VLBI clocks measurement will be compared with those retrieved by simultaneous GPS-based measurement, to verify possible improvements brought by the broadband antennas.

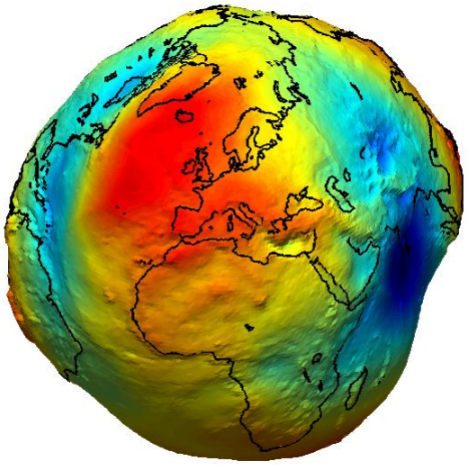

Figure 5.8: A representation of the Earth geoid as it is obtained from satellite measurements Source: European Space Agency (ESA)

5.2 Chronometric geodesy

The geoid determination. In a first approximation the equipotential surface of the Earth gravitational field can be described as a sphere distorted into an ellipsoid by the Earth rotation. In this approximation the direction of the gravity vector, i.e. the vertical direction measured with a plumb line, is orthogonal to the ellipsoid surface. Due to inhomogeneities in the density distribution of the Earth interior, the actual equipotential surface is a geoid (fig. 5.8). It coincides by definition with the mean sea level and it may differ from the ellipsoid by up to 100 m. As a consequence, the direction of the actual gravity vector differs from the vertical direction coming from the ellipsoid model. Similarly, two different definitions of height are introduced. The orthometric height is defined as the distance from the geoid calculated along the local vertical direction (plumb line). The ellipsoid height is calculated as the distance from the ellipsoid along the direction perpendicular to the ellipsoid itself. The height difference between the two is the so-called geoid separation.
The determination of the geoid is one of the main targets of geodesy and the measure of the orthometric height is currently performed through terrestrial and satellites gravity measurements. The first approach exploits levelling instruments, such as spirit levels, which enable a precision at the submillimetre level. However, to determine the absolute height of a point with respect to the geoid, the measure must be referred to the mean sea level. For distances larger than 1 km the propagation introduces systematic errors, which may deteriorate the final uncertainty up to some decimetres. To determine the difference in height between two distant points the coordinate system of the GNSS is used. However, this provides a measure of

the ellipsoid height and has to be corrected for the geoid separation, which is determined by local gravity field models retrieved from terrestrial and satellites data. By combining the GNSS system approach with terrestrial techniques an ultimate uncertainty at the decimetre level is obtained [150, 151]. The main limitations are the so called "vertical datum problem" [152], i.e. different determinations of heights between countries, and the fact that the results obtained by the two techniques may differ by up to 50 cm [153].

Relativistic geodesy. It is well-known that, as a result of the gravitational redshift, the time measured by a clock depends on its velocity and position in the gravity field. Considering two clocks at rest placed in different locations, their frequency difference can be expressed as [151]:

$$\Delta\nu = \nu_0 \frac{g\,(h_1 - h_2)}{c^2} = \nu_0 \frac{\Delta U}{c^2}, \tag{5.16}$$

where ν_0 is the clock transition at rest at the height reference surface (usually the geoid), g is the gravity acceleration, h_1 and h_2 are the orthometric heights of the two clocks with respect to the geoid and ΔU is the gravity potential difference.
This effect has been verified in 1977 with an experiment conducted by Briatore and Leschiutta [154], comparing a Cs beam clock at the Istituto Elettrotecnico Nazionale Galileo Ferraris in Torino, 250 m above the sea level, with a second Cs beam clock placed at the CNR cosmic-ray laboratory on the Italian Alps, 3500 m above the sea level. The time-delay measured between the two clocks after 66 days was in agreement with the prediction within the measurement uncertainty.
By reversing eq. (5.16), it is noted that atomic clocks can be used as probing tools for the gravity potential. This is a cross-disciplinary research field which belongs to the relativistic geodesy and is more specifically referred to as chronometric levelling. This term was introduced in the early 80's by Vermeer and Bjerhammar [58, 59], who proposed for the first time the use of clocks to determine gravity equipotential surfaces.
A number of tests has been performed in recent years [33, 48, 60] pushed by the rapid development of optical clocks. In particular, to resolve a difference of gravity potential corresponding to 1 cm, it is necessary to determine the redshift between the clocks frequency with a relative uncertainty of 10^{-18}, which is the ultimate uncertainty of the best optical clocks of new generation [16, 18–20]. Therefore, chronometric levelling could be a complementary method to traditional geodetic techniques to measure potential differences over long distances, improving the current definition of the geoid and the spatial determination of the geopotential [155, 156]. In addition, the exploitation of optical clocks allows to achieve the centimetre level after few hours measurement while traditional techniques require days to obtain the same uncertainty level. This enables to study the variation of the gravity potential over timescales of hours.

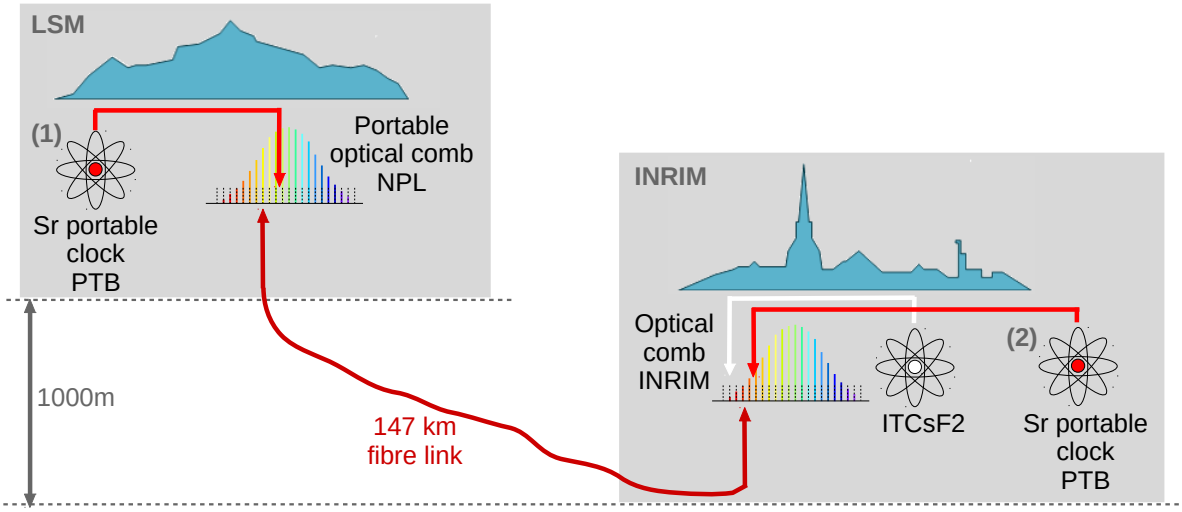

Figure 5.9: Sketch of the chronometric levelling experiment performed between INRIM and LSM. For the first part of the experiment the Sr portable clock is placed at LSM (1) and then moved to INRIM (2).

5.2.1 The chronometric levelling campaign at INRIM

A proof-of-principle chronometric levelling experiment was performed in the frame of the European Metrology Research Programme (EMRP) project "International Timescales with Optical Clocks" (ITOC) [32]. It involved three National Metrology Institutes, INRIM, PTB and NPL, and the Laboratoire Souterrain de Modane (LSM). The latter is a particle physics laboratory, located 1700 m underground, in the middle of the Fréjus tunnel, connecting Italy to France. The purpose of the experiment was to measure the gravity potential difference between INRIM and LSM, by comparing clocks located in the two laboratories. LSM is ~ 1000 m higher than Torino which leads to a fractional frequency difference of 10^{-13}.
A sketch of the experimental setup is shown in fig. 5.9. The Cs fountain ITCsF2 located at INRIM is compared to the portable Sr clock developed and operated by PTB, placed in the LSM subterranean laboratory, through a 147-km-long fibre link. This is done by locking an ultrastable 1542 nm laser to $\mathrm{HM}_{\mathrm{INRIM}}$ through the optical comb at INRIM (see the scheme described in section 2.1.1 and fig. 2.2). The HM is in turn regularly steered with respect to the ITCsF2. The 1542 nm laser is disseminated to LSM and the fibre noise is compensated with the Doppler-noise compensation scheme. At the remote link end, the signal is compared to the Sr portable clock using a portable optical comb developed at NPL and transported to LSM. The comparison of the link signal and the Sr clock is performed using the optical comb as transfer oscillator, i.e. as a spectral bridge between the two optical frequencies, as described in section 1.2.4. This prevents the measurement to be limited by the uncertainty of the comb reference and allows to perform the comparison

between the link laser and the clock laser at their intrinsic level of uncertainty.
The peculiarity of this test with respect to previous experiments is the use of a portable clock, transported into a dedicated van. This allowed, after the first part of the experiment at LSM, to move the Sr clock to INRIM and to directly calibrate it against ITCsF2. This enabled to perform a pure chronometric levelling measurement: from the difference between the measurements taken at LSM and at INRIM, the variation of the gravity potential is retrieved, independently from the uncertainty budget of the two clocks. Moreover, this experiment demonstrated for the first time the portable clock operation on a realistic test site. The portable clock was placed in an uncommon environment for an atomic clock: a storage area with no specific isolation from temperature variations and environmental noise. This introduced several complications that allowed an unprecedented stress test for the reliability of the transportable optical lattice clock.
In the following section the fibre link setup employed for the experiment is described.

Fibre link implementation and characterization

The fibre link employed for the Cs fountain dissemination from INRIM to LSM is based on the same fibre pair used for the experiment described in chapter 3. The link is 147 km long, with a mixed dense- and coarse-wavelength division multiplexing transmission. A sketch is shown in fig. 5.10, two bidirectional EDFAs are installed on each fibre to recover for optical losses. The first fibre is used for the dissemination of the coherent optical carrier, while the second is used to provide an RF frequency reference to the clock setup and optical comb at LSM, since a GNSS dissemination would be impracticable in the underground laboratory.

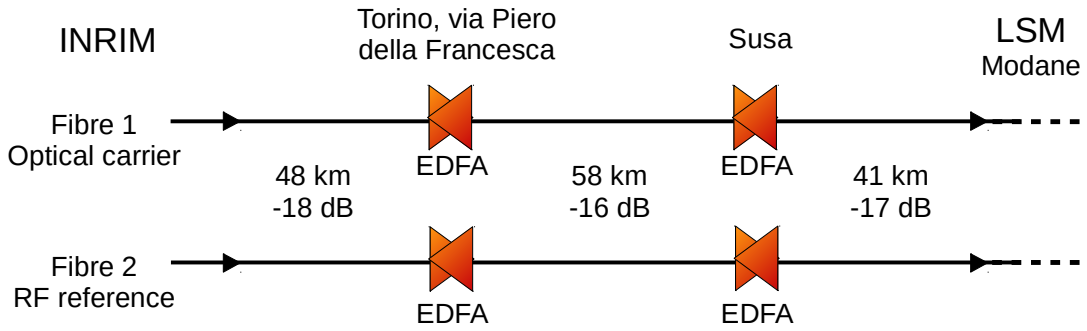

Figure 5.10: Sketch of the fibre link implemented between INRIM and LSM with a summary of length and optical losses of the fibre spans between the amplification stations.

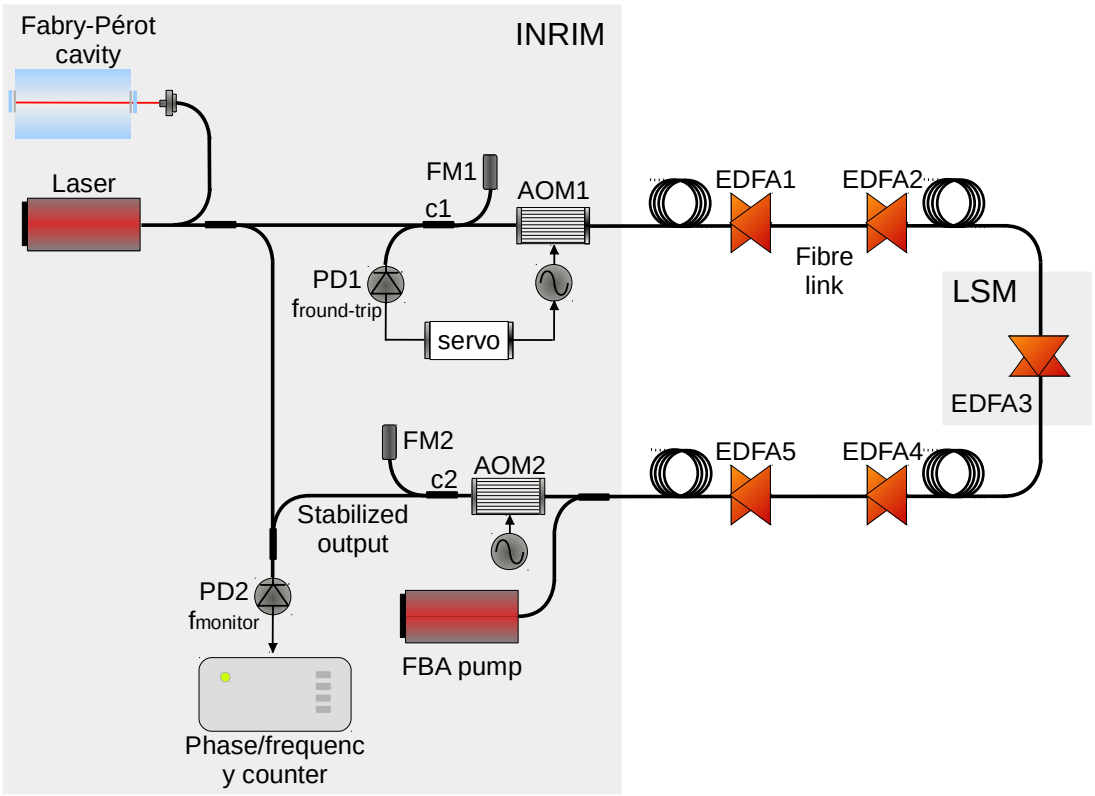

Figure 5.11: Optical and electronic apparatus for the characterization of the optical carrier frequency dissemination over the INRIM-LSM fibre link.

Coherent dissemination. To characterize the fibre link in preparation to the campaign, the scheme depicted in fig. 5.11 has been implemented. The two fibres are looped at the remote end and one additional EDFA is installed at LSM. To minimize the stray backreflections, the EDFA gain is always kept $< 18\,\mathrm{dB}$ and is remotely adjusted with the telecontrol system described in section 2.2.1. To guarantee a sufficient SNR on the round-trip signal an additional FBA is employed at the remote end of the link, prior to the Faraday mirror (FM_2). Due to the low injection losses of the DWDM network, the Brillouin pump is limited to 2.5 mW, which enables an amplification of 10 dB. The combined use of EDFAs and FBA allows losses reduction from 102 dB to 30 dB.
The phase-noise compensation is based on the Doppler-noise cancellation scheme. The first fibre coupler (c_1) is used to detect the round-trip signal and generate the beat note ($f_{\text{round-trip}}$) for the link stabilization. To detect the occurrence of cycle slips and remove them from the clocks comparison, the round-trip beat note is redundantly tracked with two VCOs.

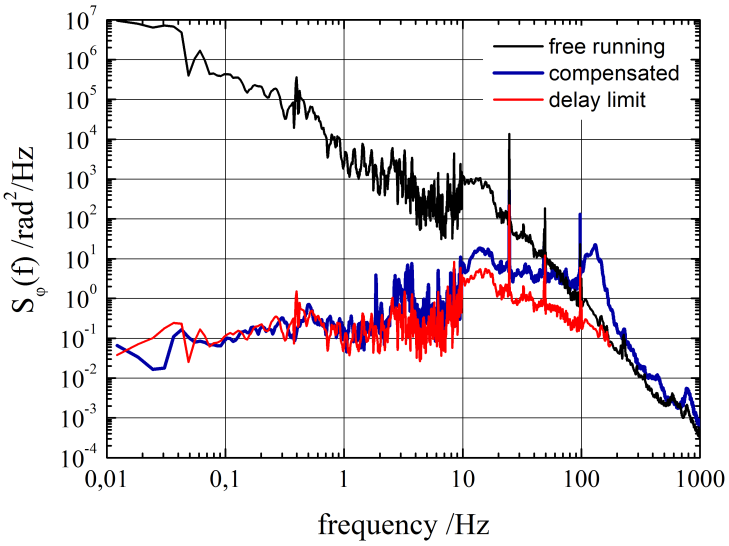

Figure 5.12: PSD of the fibre phase noise. Black: free-running fibre. Blue: residual noise of the compensated fibre. Red: expected residual noise of a Doppler-noise cancellation on a 294 km link.

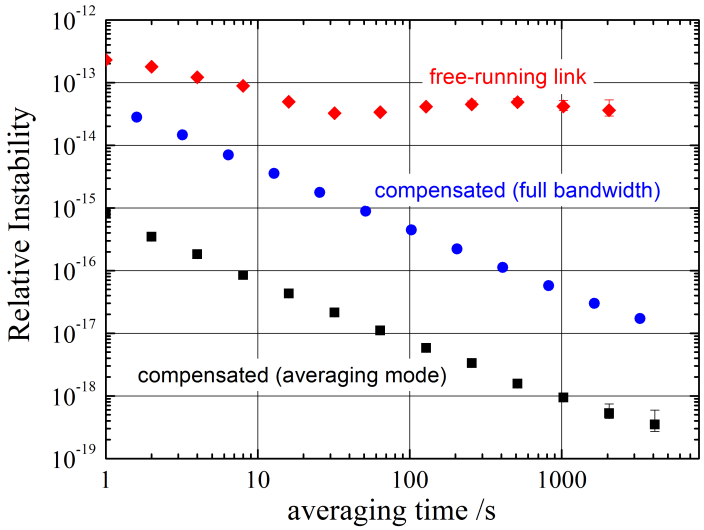

Figure 5.13: Stability in terms of Allan deviation of the fibre phase noise. Red: free-running fibre. Blue: residual noise after phase-stabilization calculated from data acquired with a dead-time-free phase/frequency counter operated in full-bandwidth mode. Black: residual noise calculated from data acquired in averaging mode.

In this configuration both the local and remote end of the link are placed in the same laboratory, which enables to characterize the fibre noise just by comparing the loop signal, i.e. the signal which has travelled the link loop, with the local one. To this purpose the second coupler (c_2) is used, generating f_{monitor}. The PSD of the fibre phase noise is shown in fig. 5.12. The black spectrum represents the uncompensated fibre noise. The noise bump between 10 Hz and 20 Hz is attributed to the traffic noise, considering that the fibres are deployed for a large part along the highway. The blue spectrum represents the residual noise when the noise compensation is engaged and is compared to the expected residual noise (red spectrum) evaluated with eq. (1.11) for a 294 km link. The expected compensation bandwidth is about 170 Hz which is consistent with the servo-bump observed in fig. 5.12.
f_{monitor} has been sampled with a dead-time-free phase/frequency counter, operating at 1 s gate time. The stability of the compensated link has been evaluated both operating the counter in full-bandwidth mode (blue circles) and in averaging-mode (black squares). The latter is equivalent to a low-pass Lorentzian filter of bandwidth 0.5 Hz, which rejects most of the delay-unsuppressed wide-band noise of the fibre, ensuring an improvement in stability of more than one order of magnitude as compared to those observed in the full-bandwidth mode (fig. 5.13). A stability of 3×10^{-19} is obtained after few hours measurement and no frequency offset has been observed within this uncertainty. Therefore, no instability contribution is added by the fibre link on the clock comparison after 10 s measurements.

RF dissemination. The RF dissemination is performed through a free-running fibre laser, which is amplitude modulated at 100 MHz with a Mach-Zehnder electro-optical modulator and transmitted through the fibre.
No compensation of the fibre noise is implemented, since the stability requirements are less stringent on the RF reference with respect to the optical carrier. In fact, none of the referenced instruments has a direct contribution to the clocks comparison uncertainty. The repetition rate, f_{rep}, of the portable optical comb is referenced to the disseminated RF, however it does not contribute to the lasers comparison since the comb is used as transfer oscillator. The RF link signal is also employed for the reference of the AOMs, the frequency counters and f_0 of the frequency comb. Their uncertainty contribution is negligible as well, since the absolute RF uncertainty, which is at the millihertz level, is directly summed to the absolute uncertainties of the link and clock lasers, which are at the Hertz level.
To characterize the stability of the disseminated RF reference, the link loop has been exploited as depicted in fig. 5.14. The modulated laser is launched into the fibre and, at the far end, the modulation is detected with a fast photodiode, amplified and compared to the output of a commercial synthesizer. The 10 MHz reference of the synthesizer is generated by an Oven-Controlled Quartz oscillator (OCXO). The phase error retrieved from the comparison is fed to the OCXO to lock it to the fibre signal. A bandwidth of 0.1 Hz has been chosen as a compromise between

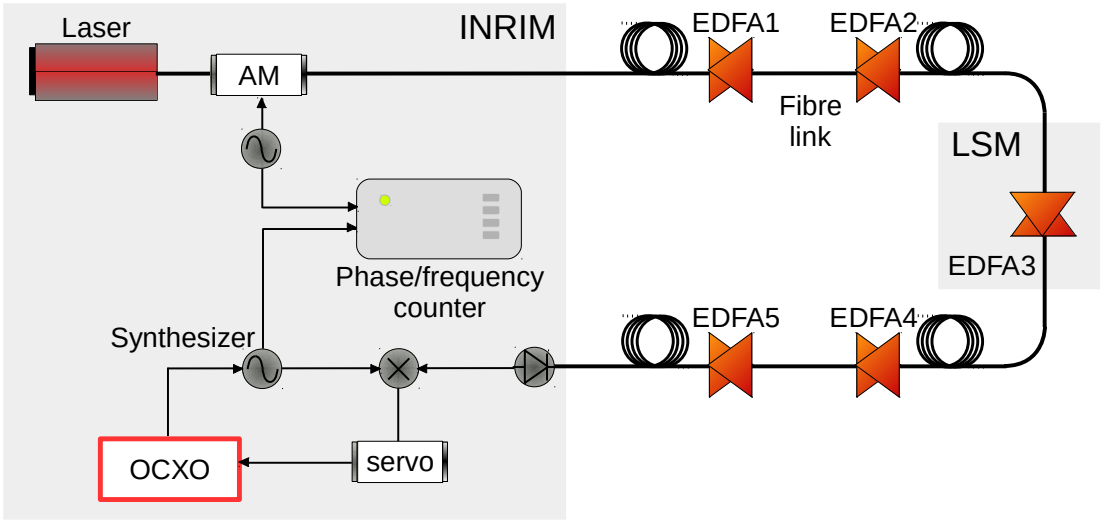

Figure 5.14: Optical and electronic apparatus for the characterization of the RF frequency dissemination over the INRIM-LSM fibre link. AM is the amplitude modulation applied to the free-running 1542 nm laser exploiting an electro-optic modulator and OCXO is the Oven-Controlled Quartz oscillator.

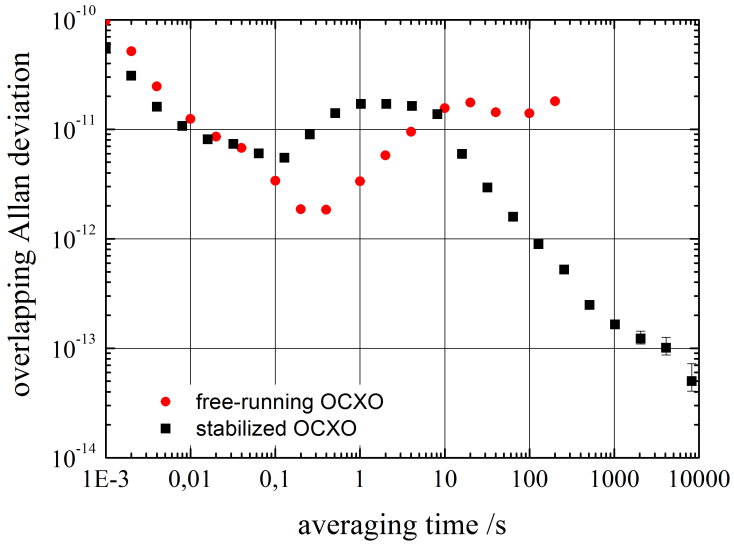

Figure 5.15: Stability in terms of Allan deviation of the OCXO noise. Red: free-running mode. Black: stability of the OCXO when locked to the optically-delivered RF signal, acquired in full bandwidth mode.

obtaining a tight lock and sufficiently rejecting the fibre noise.
The data are acquired with a dead-time-free phase/frequency counter operating

in full bandwidth mode. Fig. 5.15 shows the stability of the free running OCXO (black squares) compared to the stability of the OCXO locked to the fibre signal (red circles). On the short term, it is limited by the OCXO noise, while for averaging times between 0.1 s and 1000 s the stability is dominated by the noise of the optically-delivered signal, i.e. the intrinsic instability of the 100 MHz reference. For longer measurement times, the stability is limited by the uncompensated fibre length variations due to environmental effects. No frequency offset has been observed at the 10^{-13} stability level. The stability level at every averaging time meets the requirements for the RF references in this experiment.

Results

The campaign consisted of two weeks of experiment with the Sr clock placed at LSM followed by two weeks with the Sr clock placed at INRIM. In both cases a large part of the time was spent in recovering the operating conditions for the Sr clock after transportation.
The measurement uptime of the Sr clock at LSM was as low as 2.8 hours. This was mainly due to the small number of working hours allowed into the tunnel laboratory and to the frequent interruptions caused by the blasts generated by the construction of an emergency gallery near the laboratory. For these reasons, the first comparison is limited by the Cs fountain instability of $10^{-13}\,\tau^{-1/2}$. To reduce the final uncertainty of the measurement, the $\mathrm{HM}_{\mathrm{INRIM}}$ has been used as flywheel: the HM is continuously steered with respect to the Cs fountain and, at the same time, the link laser is frequency locked to $\mathrm{HM}_{\mathrm{INRIM}}$. Taking advantage of the HM high stability, the averaging time of the Sr clock vs link laser measurement has been extended to 48 hours [157], for an uncertainty of 17×10^{-16}. The systematic uncertainties of Sr and Cs clocks have been evaluated at 2.6×10^{-16} and 3×10^{-16} respectively.
The second part of the campaign performed at INRIM allowed a longer measurement time, leading to a lower uncertainty on the Sr accuracy budget, 1.8×10^{-16}, and to a total comparison uncertainty of 9×10^{-16}.
A relativistic redshift of 47.92(83) Hz has been evaluated for the Sr clock between the measurements at LSM and at INRIM (the uncertainty in brackets corresponds to $1\,\sigma$, and is associated to the last digit of the result). The corresponding difference of gravity potential is $10\,034(174)\,\mathrm{m^2 s^{-2}}$. This result is in agreement with the value of $10\,032.1(16)\,\mathrm{m^2 s^{-2}}$, which has been previously determined by combining GNSS-based measurements of the ellipsoid heights at INRIM and LSM with local gravity measurements.
Although this chronometric levelling result is not competitive with those obtained with standard geodetic methods, it is particularly relevant as the first experiment of chronometric levelling performed with a transportable atomic clock.

5.3 Seismology

In the previous sections, optical fibres have been considered as a tool for frequency dissemination and attention has been paid in compensating for the environmental noise affecting the fibre. In reverse, fibres can be used as sensors of the environmental effects perturbing the optical path. With the interferometric scheme employed for frequency dissemination, it is possible to detect changes in the propagation delay at the femtosecond level. Optical fibres can thus be used as distributed sensors of seismic and micro-seismic events.

5.3.1 Earthquakes detection

The study of seismic events is crucial for the understanding of the Earth interior dynamics [61], from changes in volcanic structures [158] to magma generation and mid-ocean ridge development [159]. The detection of earthquakes is currently performed by seismic stations spread all over the dry land and by a small number of underwater stations, equipped with ocean bottom seismometers (OBS). Due to the high costs of installation and operation, these are installed in restricted areas for a limited period of time [160–162]. Only a small number of OBS is permanently deployed close to the seismic areas for research purposes and tsunami alert [163–166]. This is far from being sufficient for an exhaustive monitoring of the submarine seismic activity. Earthquakes generated on the oceans floor remain largely undetected, since most of them are too weak (magnitude < 4) to reach the land stations with sufficient intensity to be detected.
On the other hand more than 100 000 km of fibres are deployed on the bottom of the seas, employed for telecommunication purposes (fig. 5.16) and the installation of further 200 000 km is planned for the forthcoming years [167]. The possibility of using fibres as distributed seismic sensors appears therefore as a promising alternative to complement the existing OBS network. Distributed acoustic sensing techniques (DAS) have already been developed [62, 168, 169]. They use light which is backscattered along the fibre to retrieve the information about the perturbations affecting the optical cable. This technique is limited by the optical losses experienced by the signal travelling the fibre. In order to obtain a sufficient signal-to-noise ratio on the returning signal, this technique is currently implemented on fibre spans shorter than 100 km. This is extremely useful for some applications in the field of oil and gas industries, to monitor the noise disturbance along the cables. However, a range of 100 km far from the coast is not enough to significantly increase the capability of earthquakes detection.
We demonstrated in [63] the possibility of using optical fibres for earthquakes detection exploiting the interferometric techniques employed for frequency metrology. We detected seismic events with different magnitudes, e.g. from teleseismic events of magnitude 7.9 to small earthquakes of magnitude 3.4, at distances from the

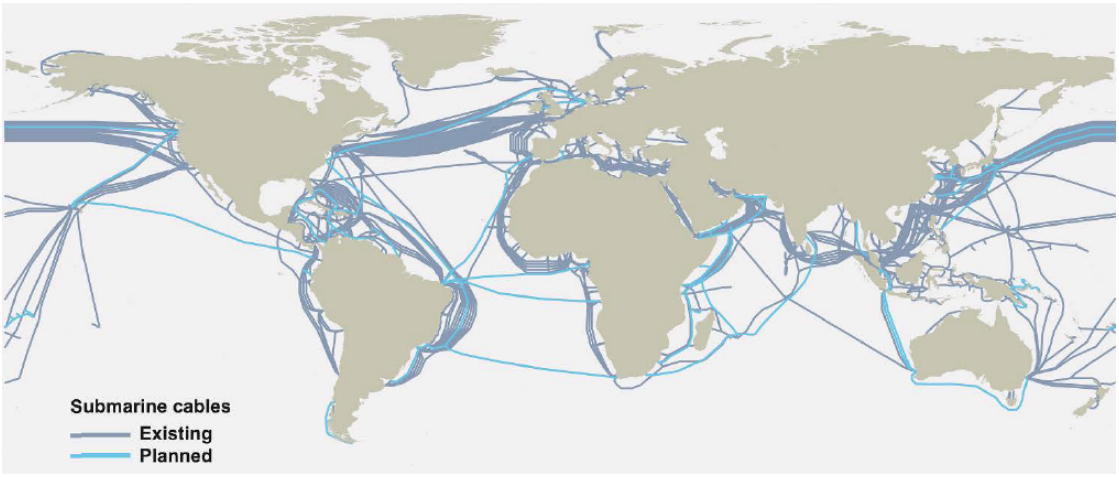

Figure 5.16: Map of the submarine telecommunication fibres. Violet: existing infrastructure. Blue: planned extensions. Map data © OpenStreetMap contributors; Cable data: TeleGeography's Telecom Resources licensed under Creative Commons Share alike.

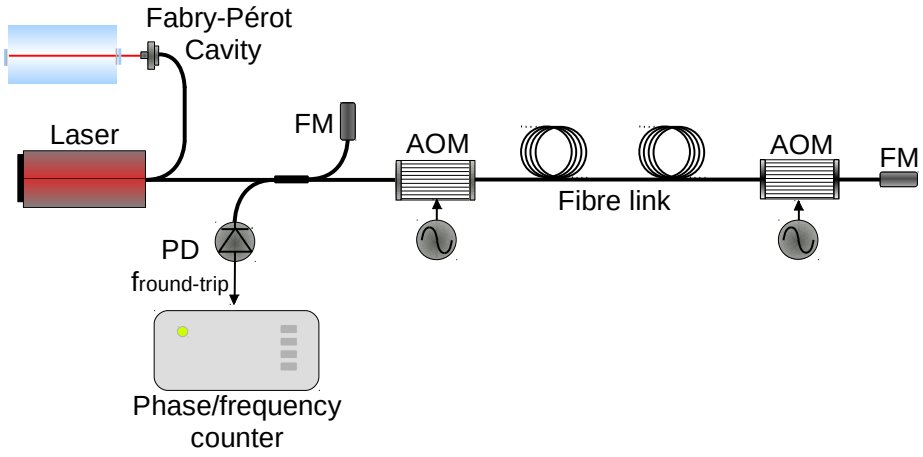

Figure 5.17: Optical and electronic apparatus employed for the earthquakes detection. FM: Faraday mirror, AOM: acousto-optic modulator, PD: photodiode.

epicentre ranging from 25 km to 18 000 km. Based on such results, we predict the possibility of using submarine transcontinental fibres to detect small earthquakes generated on the bottom of the oceans, making this technique a promising complement to the standard detection methods. This experiment has been jointly executed by INRIM, NPL, the British Geological Survey and the University of Malta.

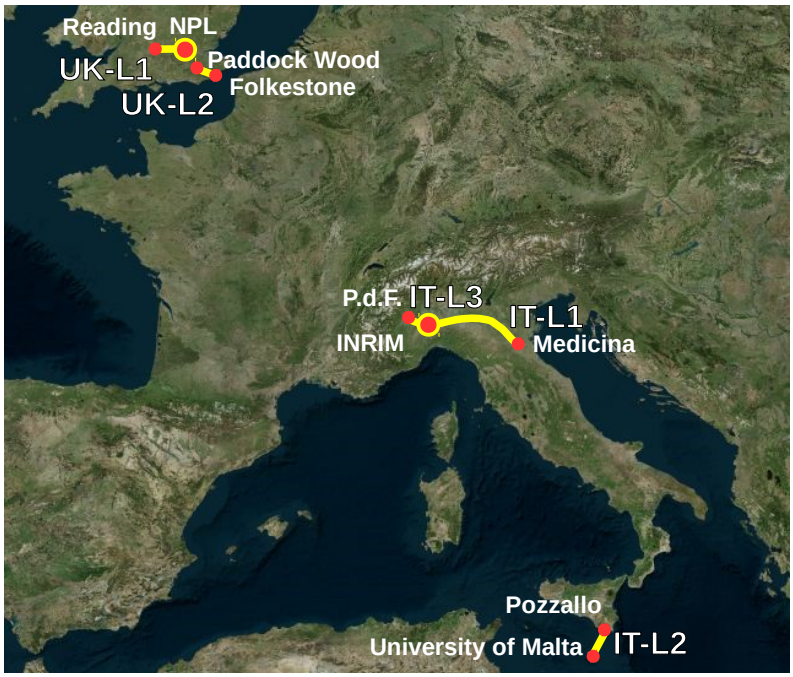

Figure 5.18: Map of the five testbeds employed for earthquakes detection. IT-L1: 535 km, connecting INRIM to Medicina. ITL2: 96.4 km, connecting Malta to Pozzallo (Sicily). IT-L3: 43 km, connecting INRIM to the amplification station of Torino via Piero della Francesca. UK-L1: 79 km, connecting NPL to the data centre in Reading. UK-L2: 75 km, connecting two amplification stations, in Paddock Wood and in Folkestone.

Detection scheme

The setup employed for earthquakes detection is depicted in fig. 5.17. The light of an ultrastable laser is injected into a fibre link. At the remote end it is back reflected by means of a Faraday mirror. In the original laboratory it is compared to the local signal to detect the optical phase variations generated along the fibre path. The two AOMs are used to distinguish the round-trip signal from stray back-eflections and to generate a self-heterodyne beat note between the original and the round-trip signal.
The beat note is detected with a photodiode and, after filtering and amplification, it is sampled with a dead-time-free phase/frequency counter. The interesting frequency range for earthquakes detection is 0.1-20 Hz. For this reason, a high sampling rate is chosen, i.e. 100 samples/s, and a digital filter is applied afterwards to select the Fourier region of interest.
For this experiment different fibre links have been used (fig. 5.18). The first testbed is the span of the Italian link connecting INRIM to Medicina, it is 535 km long and is for a large part deployed along the highway (hereafter referred to as IT-L1). The

Location	Date dd-mm-yy	Time UTC	Magnitude	Testbed	Epicentre distance (km)
Central Italy	24-08-16	01:36:32	Mw 6.0	UK-L1	1400
Central Italy	26-10-16	19:18:05	Mw 5.9	UK-L1	1380
Central Italy	30-10-16	06:40:17	Mw 6.5	UK-L1	1390
New Zealand	13-11-16	11:02:56	Mw 5.9	UK-L1	18 900
Japan	21-11-16	20:59:49	Mw 7.9	UK-L1	9300
Greece [Sea]	01-09-17	16:48:33	mb 5.1	IT-L2	1219
Malta [Sea]	02-09-17	00:45:31	ML 3.4	IT-L2	86
Iran	12-11-17	18:18:17	Mw 7.2	IT-L1,UK-L2	3094
Parma	19-11-17	12:37:44	Mw 4.4	IT-L1	25
Mexico [Sea]	19-01-18	16:17:46	Mw 6.3	IT-L3	9906
Alaska [Sea]	23-01-18	09:31:43	Mw 7.6	IT-L3	8563

Table 5.2: The information about date, time and epicentre location of the earthquakes are available on the web site of the Istituto Nazionale di Geofisica e Vulcanologia (INGV) which is in charge of the monitoring of the national networks for seismic and volcanic phenomena in Italy, http://cnt.rm.ingv.it/.

second tesbed is the 96.4-km-long submarine link, introduced in chapter 4, connecting Malta to Pozzallo in Sicily (IT-L2). A third testbed, IT-L3, has been introduced during the last part of the detection campaign and is a part of the INRIM-Modane link, introduced in chapter 3. This fibre link is 43 km long, running entirely in the urban area of Torino and is characterized by a noise spectrum which is two orders of magnitude lower than that of IT-L1, especially in the Fourier region of interest. Other two testbeds, operated by NPL in UK, have been used: UK-L1 is 79 km long and runs from NPL (Teddington) to a data centre in Reading, UK-L2 is a short-cut of the NPL-SYRTE fibre link, connecting two intermediate stations, in Paddock Wood and Flokestone, it is 75 km long and runs almost entirely in non-metropolitan areas, thus showing a lower noise floor than the Italian links. The availability of five testbeds is crucial to have an almost constant monitor of the occurrence of seismic events, since continuous uptime could not be reached on any of the testbeds. In addition, this allows us to demonstrate the detection of the same seismic events with more fibre links, which is important since the localization of an earthquake in space and time is performed by combining the data of more seismic sensors.
A list of the detected seismic events is reported in tab. 5.2. The magnitude of an earthquake is, by definition, the released energy during the earthquake, and is retrieved from the amplitude of the soil oscillations measured by seismometers. To express magnitude values three scales are used: momentum magnitude M_w, local magnitude ML and body-wave magnitude mb. All the three are logarithmic and are

scaled to have roughly comparable numeric values. The difference depends on the instrument employed for detection, the distance and the energy of the earthquake. An earthquake is generally composed by a sequence of seismic waves with different properties, which vary from the point of view of propagating directions (body and surface waves) and from the point of view of wave type (compressional or shear waves). This results in different propagation velocities and arrival times. The waves which are the most relevant to localize a seismic event in space and time are the primary and secondary waves. Both of them are body waves travelling through the Earth's interior and are the first reaching the seismometer, as they travel at the highest velocity [170]. The primary waves, or P-waves, are compressional and longitude waves that arrive at the seismic station first (hence the name primary). The secondary waves, or S-waves, are shear and transverse waves that are slower than P-waves, being the second waves reaching the seismometer. P- and S- waves are usually the smallest in amplitude and hence the most difficult to be detected. An earthquake can be localized, whenever P- and S- waves are detected by at least three seismic stations with synchronized timebases. Being able to detect primary and secondary waves on the optical phase of the fibre signal is crucial to demonstrate the validity of fibre-based earthquakes detection.
The traces of some of the detected seismic events are shown hereafter. They have been selected as the most representative to describe the feasibility of optical fibres for earthquakes detection.

IRAN - $M_w = 7.3$. This teleseismic event has been detected both with IT-L1 and UK-L2, which are located at a distance from the earthquake epicentre of 3100 km and 4100 km, respectively. Fig. 5.19a shows the phase variations of the two links (orange) compared with the traces of two seismometers (blue), namely MN.MTRZ close to IT-L1 and GB.HMNX close to UK-L2.
The P-wave and the S-wave are marked on the seismograms and on the optical phase trace from UK-L2. This is done by applying a digital FIR pass-band filter to the phase data which have been acquired at a rate of 100 samples/s. The same filter is applied to the seismograms for a better comparison. The frequency spectrum of a seismic wave may vary for different seismic events, depending on magnitude, distance from epicentre, and density of the traversed material. Therefore, the cut-off frequencies have to be chosen for every data set as the best compromise to maximize the signal-to-noise ratio. In this case, the applied pass-band filter is $f_{\mathrm{LOW}} = 0.05$ Hz and $f_{\mathrm{HIGH}} = 0.5$ Hz. The S-wave is clearly visible also on IT-L1, although in this case the noise floor is significantly higher due to the longer link. In addition, the detection of the P-wave has been further complicated by a periodic environmental perturbation.

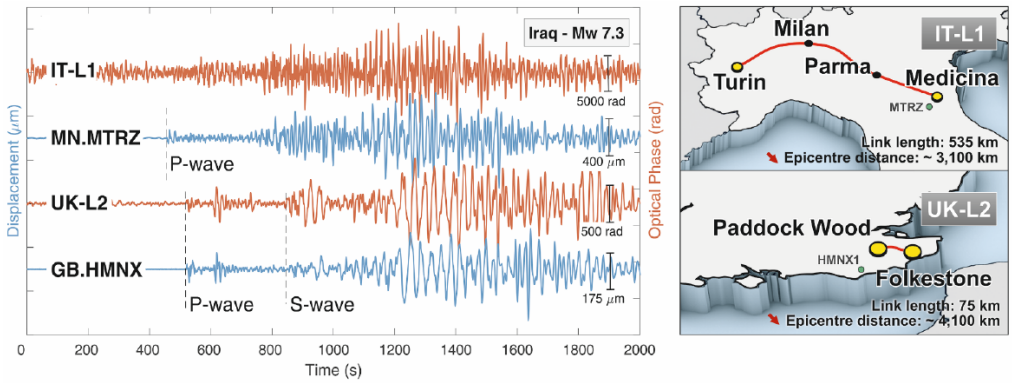

(a) Iran earthquake on 12$^{\text{th}}$ November 2017. Orange: phase traces of IT-L1 and UK-L2 link. Blue: seismograms from Monterenzio (MN.MTRZ) and Herstmonceux (GB.HMNX). The north-south component has been used for all seismic station data.

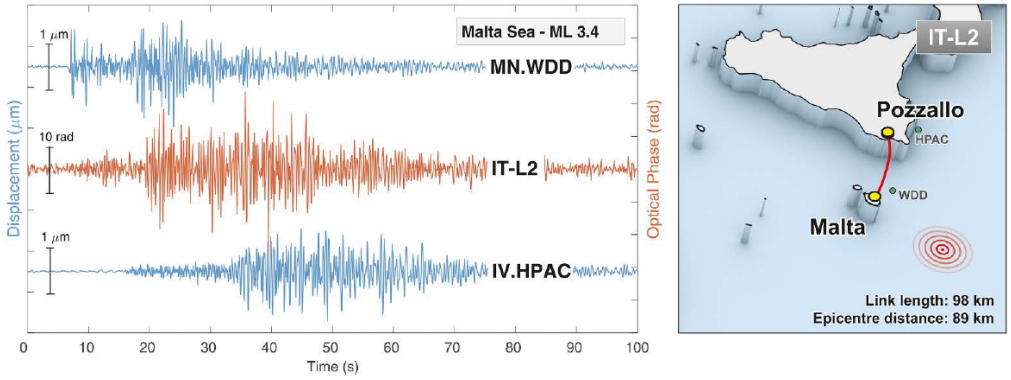

(b) Malta sea earthquake on 2$^{\text{nd}}$ September 2017. Orange: phase traces of IT-L2 link. Blue: seismograms from Malta (MN.WDD) and from Pachino, Sicily (IV.HPAC). The north-south component has been used for all seismic station data.

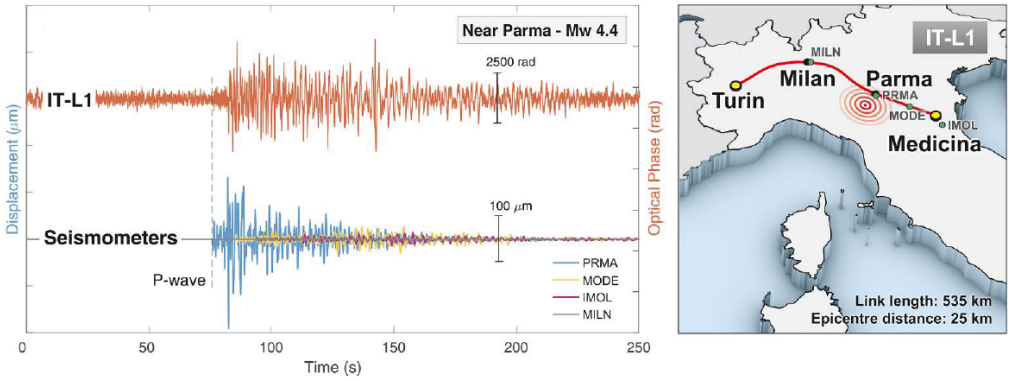

(c) Parma earthquake on 19$^{\text{th}}$ November 2017. Orange: phase traces of IT-L1 link. Blue: seismograms from Parma (PRMA), Modena (MODE), Imola (IMOL) and Milano (MILN). The north-south component has been used for all seismic station data.

Figure 5.19: Optical phase and seismograms of the detected earthquakes.

Malta Sea - ML = 3.4. This earthquake of small magnitude is one of the two events detected with the submarine IT-L2 link. Fig. 5.19b shows the comparison of the fibre phase trace with the traces of two seismometers located in Malta (MN.WDD) and in Pachino, Sicily (IV.HPAC). In this case, the epicentre is located in the Malta sea, 89 km away from the fibre link. The cut-off frequencies of the digital band-pass filter are $f_{\mathrm{LOW}} = 1.5\,\mathrm{Hz}$ and $f_{\mathrm{HIGH}} = 5\,\mathrm{Hz}$. Both P-wave and S-wave are clearly identified, thanks to the low environmental noise floor of submarine fibre cables. A delay of approximately 2 s between the P-wave detected by the fibre and by MN.WDD is observed. This delay corresponds to a propagation speed of 5 km/s between the seismometer and the Malta end of the fibre, i.e. the closest fibre point to the epicentre. This value is in agreement with the speed calculated from the delay observed between the MN.WDD and the IV.HPAC seismograms.

Parma - $M_w = 4.4$. The Parma earthquake was detected with IT-L1. The epicentre is 25 km away from the nearest section of the fibre link, which is much shorter than the actual link length (535 km). This is useful to verify whether the detection is affected by the distributed nature of the fibre sensor.
Fig. 5.19c shows the optical phase of the fibre signal compared to the traces of four seismometers, close to the fibre and at different distances from the epicentre.
The time of arrival identified on the fibre trace corresponds to the smaller distance between the epicentre and the fibre link. It is also associated to the highest amplitude of the detected signal, as confirmed by the seismometer traces. Sections of the link far from the first point of contact of the seismic wave with the link do not contribute significantly, due to the attenuation of the seismic wave with distance. Moreover, it is seen that the arrival time of the P-wave corresponds to that of the Parma seismometer and is substantially unaffected by the distributed detection.
This configuration reproduces, in a smaller scale, the detection of small submarine earthquakes with transcontinental fibres. A large number of earthquakes is generated in seismic areas crossed by submarine fibres, such as the North and Mid-Atlantic ridge, the South American, North American, and African Plates triple junction. In these situations, the distance between the fibre and the epicentre would be much shorter than the fibre length itself and hence the earthquake would affect only a relatively small fraction of the link.

Towards transoceanic fibres

As shown in chapter 4, the noise of a submarine fibre is up to 20 dB lower than that of a terrestrial fibre of the same length, in the frequency range of interest for earthquakes, 0.1 to 20 Hz (see fig. 4.5 and 4.6). Since the perturbations on submarine fibres may be considered uncorrelated with length (as discussed in chapter 4), the following relation holds:

$$S_{\phi,\mathrm{fibre}}(f, L) \propto L. \tag{5.17}$$

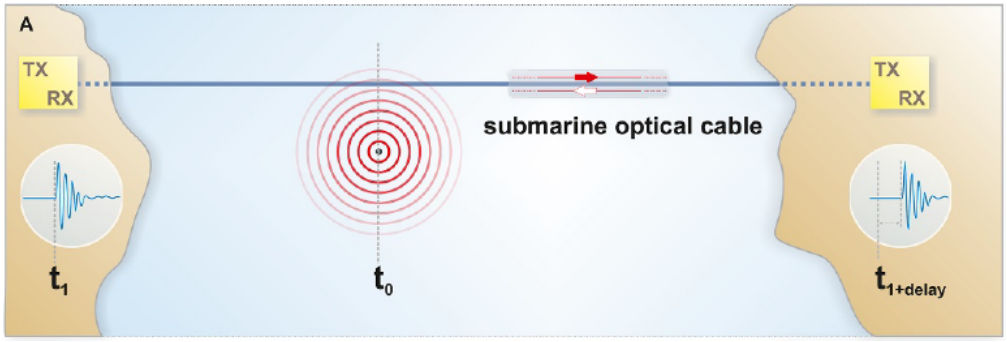

Figure 5.20: Optical scheme for the localization of the epicentre direction. TX is an ultrastable laser source injected into the fibre, RX is the signal of an ultrastable laser source received from the opposite fibre terminal.

Therefore, the noise of a transoceanic fibre of $\sim$ 7000 km is expected to be comparable to that of UK-L1 and lower than that of IT-L1, where we were able to detect earthquakes of small magnitude (see the Parma earthquake). In addition, the acoustic noise on submarine fibres is primarily generated by surface wind-sea and wave-wave interaction [171] and commercial shipping [172]. Such effects are expected to be strongly attenuated with depth ad to play a more marginal role on oceanic floors than on the shallow Malta channel. Thus the prediction performed with eq. (5.17) may be conservative and the noise level on oceans floor could be even lower. As a consequence, small earthquakes are expected to be detected on transcontinental fibres with sufficient SNR.

Earthquakes localization

A crucial step to demonstrate the feasibility of using fibres for seismic study is the epicentre determination. This can be done by using the detection scheme of fig. 5.20. Differently from fig. 5.17, it is based on a two-way scheme: two ultrastable lasers are injected into the fibre in counter propagating directions and at each fibre end the beat note between local and remote laser is acquired. By cross-correlating the two data series, it is possible to retrieve the delay between the arrival times of the perturbed signal at the two fibre terminals (a similar correlation procedure is used in chapter 3). From the relative delay and the fibre length, one can determine the geographical coordinates where the perturbation has reached the fibre.
To verify this localization procedure a proof-of-principle test has been performed in the laboratory, using the setup of fig. 5.21. A single ultrastable laser is used, which is split into two parts and injected into the opposite directions of a 101-km-long fibre loop. The loop is composed by two 50 km and one 1 km fibre spools. The two AOMs are used to shift the signal by 40 MHz each, such that a 80 MHz beat note is detected at each side of the loop between the local and remote laser, f_{bn1} and f_{bn2}. These are down-converted by means of a local oscillator to 100 kHz and sampled

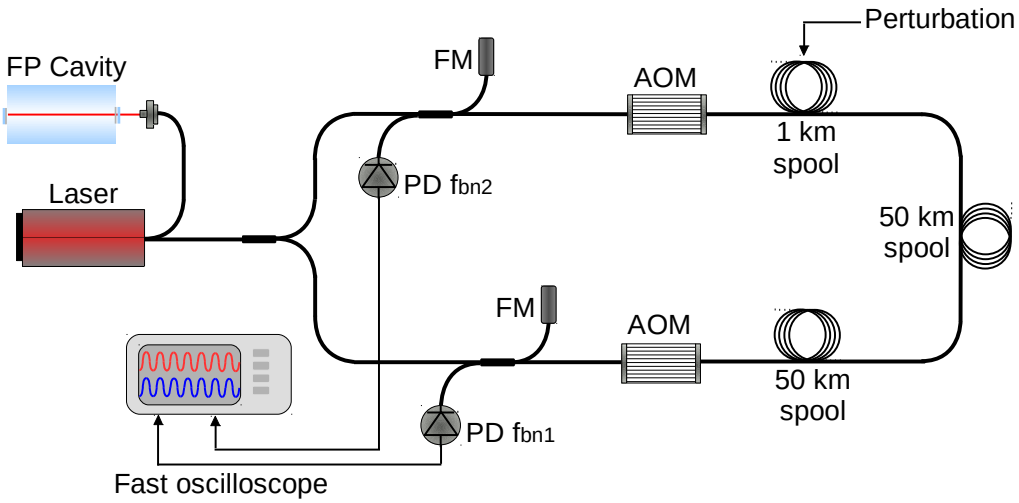

Figure 5.21: Optical and electronic apparatus for the earthquakes localization employed for a proof-of-principle test based on fibre spools in the laboratory.

with a fast oscilloscope at 2.5 Msamples/s. The phase is retrieved performing a I/Q demodulation. Such a high sampling rate is required to maximize the sensitivity in the determination of the time delay; considering the speed of light in the fibre to be $\sim 2 \times 10^{-8}$ m/s, 1 km of fibre is travelled in 5 µs. A sampling rate of 2.5 Msamples/s guarantees a resolution of 400 ns, which corresponds to a lower limit of 80 m for the localization set by the acquisition system.
A perturbation is generated by tapping on the 1 km fibre spool, to simulate the effect of an earthquake. This spool is placed at one end of the link, after 100 km of fibre, thus the expected relative delay is 500 µs. Since the perturbation is generated on a spooled fibre, the tapping point uncertainty is limited to the spool length, i.e. 1 km. This is also the uncertainty with which the submarine fibre is known. Fig. 5.22a shows the two data series (blue and green lines) acquired at the two ends of the link. Two induced perturbations are observed with a peak-to-peak amplitude of ~ 140 rad. A SNR ≈ 10 is observed in the spectral region of seismic noise, which is comparable to that of the seismic perturbation on fibre traces. It is limited by the strong oscillations on the noise floor, due to the vibration at ~ 20 Hz of the laboratory walls generated by the air-conditioning system. Fig. 5.22b shows a zoom of the signal around the perturbation where the two signals appear clearly delayed. The cross-correlation curve is shown in fig. 5.23. The localization of the perturbation is obtained by multiplying the time delay corresponding to the maximum correlation by the speed of light. The latter is $v = \frac{c}{n}$ with $n = 1.4862$, which is the index of refraction of standard telecommunication fibres. The retrieved delay is in agreement with predictions within a 1 km uncertainty.
In our detection system a single oscilloscope has been used to acquire the two data

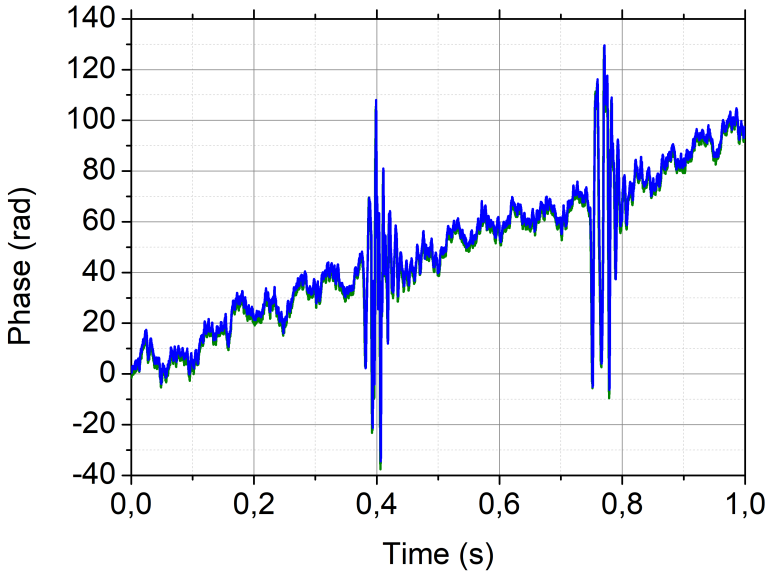

(a) Optical phase showing two perturbations induce by tapping on the 1-km-long fibre spool.

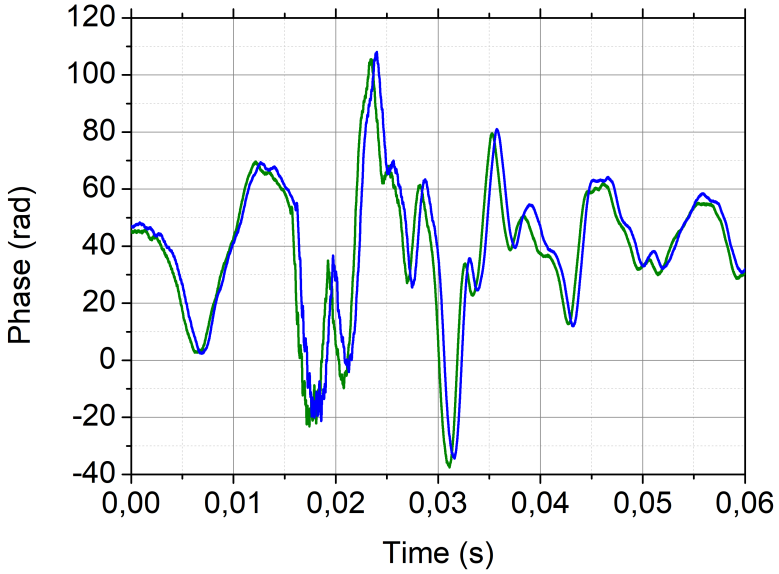

(b) Zoom of the optical phase perturbation, showing the delay in the detection of the seismic perturbation for the signal travelling in opposite directions.

Figure 5.22: Optical phase of the spooled fibre link with external perturbation obtained by tapping on the 1 km spool. The green and blue signals correspond to the phase of the beat notes acquired at the two ends of the link.

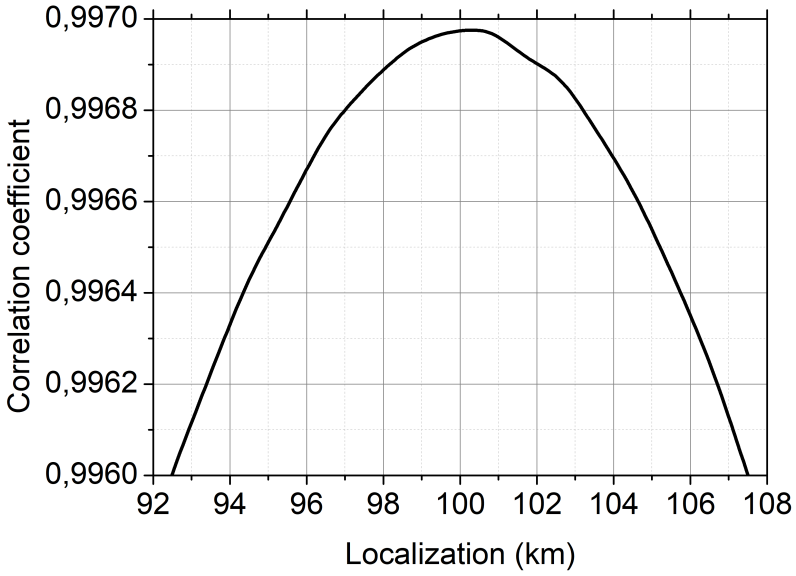

Figure 5.23: Correlation curve of the phase signal acquired at the two link ends. The maximum is between 100 km and 101 km corresponding to the position of the 1 km fibre spool.

series to avoid issues related to synchronization. In a real testbed, the remote acquisition systems require a synchronization at the microsecond level to ensure a localization at the kilometre level. This is easily achieved exploiting two GPS-disciplined receivers, which guarantee a synchronization to UTC at the 10 ns level. Alternatively, a single GPS receiver can be used at one end of the fibre and the UTC time can be transferred to the other end using fibre-based time transfer techniques [118].
While the cross-correlation on a single fibre allows the determination of the epicentre direction, at least two fibres are needed to locate the epicentre. The coordinates of the epicentre are obtained from the point of first contact of the seismic wave along two fibres, exploiting simple geometric rules, fig. 5.24. It is interesting to notice that, due to the distributed fibre detection, only two fibres are necessary to determine the epicentre position, differently to the point-like sensors which have to be a minimum number of three.

With this work we demonstrated the possibility of detecting seismic events exploiting optical fibre cables. These could complement the existing network of seismic stations, in geographical areas where the latter are difficult to be installed and operated. Indeed, the fibre coverage of sea floors is already considerable and is increasing over time. Moreover, it is important to stress that no change in the underwater infrastructure would be required to implement this detection method.

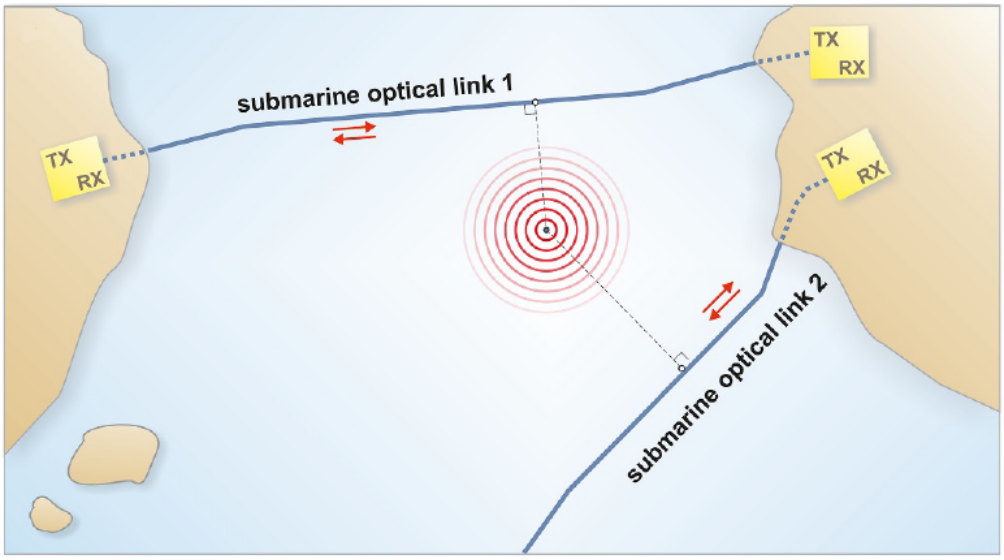

Figure 5.24: Optical scheme for the epicentre localization using two fibre links.

We demonstrated that the key data to localize a seismic event in time and space can be retrieved from the fibre trace. Nevertheless, the fibre is a distributed sensor, which requires specific deconvolution techniques to be developed. In addition, it is characterized by an overlapped sensitivity to all axes of motion. A model that predicts the response to a seismic wave in consideration of its strength, direction, and distance from epicentre needs to be formulated.

5.3.2 Microseismic noise

In addition to the earthquakes detection, the extremely low noise of submarine fibres opens the possibility of other sensing applications. An example is the study of phenomena related to waves formation and propagation, which is currently performed in coastal areas by sensing buoys. In open seas, where the latter are not available, OBS or satellite techniques are used, although they allow a coarse spatial coverage and a poor spectral response. The use of fibres would represent a cost-effective complementary tool.
Among the detectable effects is the microseismicity originated by the wind-sea interaction almost ubiquitously [173]. This generates trains of counter-propagating waves, which in turn are transmitted to the bottom of the sea, causing a vertical motion of the sea floor with a micrometre amplitude at twice the wave frequency, i.e. around 0.1 to 0.2 Hz. During the experiment described in chapter 4, a peak at ~ 0.15 Hz has been observed on the noise spectra of both testbeds.
Its power and frequency slightly vary over timescales of few hours. Fig. 5.25 shows the PSD of the optical phase recorded at different moments during $\sim$ 6 days of

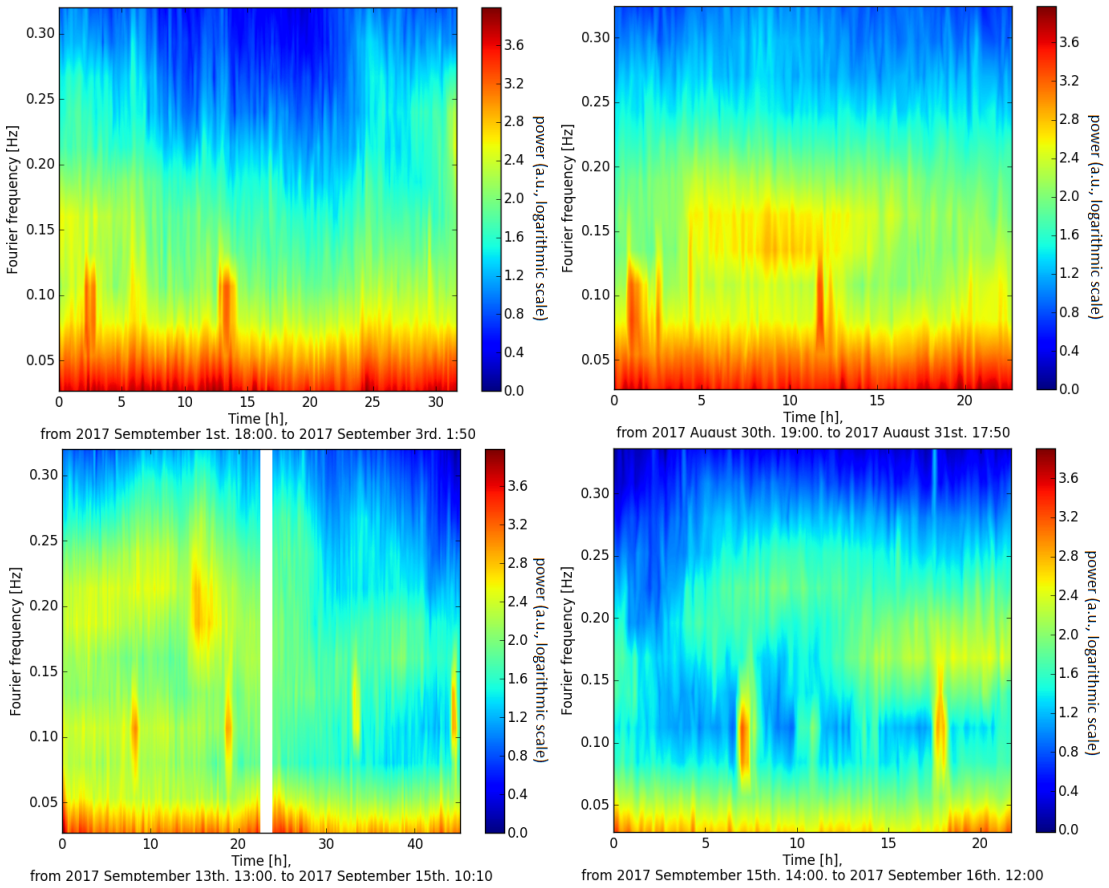

Figure 5.25: The PSD of the fibre optical phase. The colour scale represents the magnitude of the PSD in arbitrary units on a logarithmic scale (red: highest values, blue: lowest values). Each spectrum was calculated over 10 minutes. Upper plots: fibre link L1 from Malta to Pozzallo. Lower plots: fibre link L2 from Malta to Ragusa.

measurement. Each spectrum is calculated over 10 minutes and the colour scale represents the magnitude of the PSD in arbitrary units on a logarithmic scale (red: highest values, blue: lowest values). No periodicity is observed on an hourly or daily scale.

Fig. 5.26 shows the spectrum of the phase noise of L1 (Malta-Pozzallo link) compared to that of two seismometers, close to the link ends in Sicily, IV.HPAC, and in Malta, MN.WDD. The spectra are calculated from data acquired in the same time window, which have been re-normalized for an easier comparison. The 0.15 Hz peak is present in all spectra. However, no correlation has been observed between the variation of the microseismic peak on the optical signal and the variation on seismograms. This is explained by the local nature of these perturbations, which may vary significantly over distances of kilometres, e.g. the distance between the fibre and the seismometers [174]. In addition, the perturbation detected by the

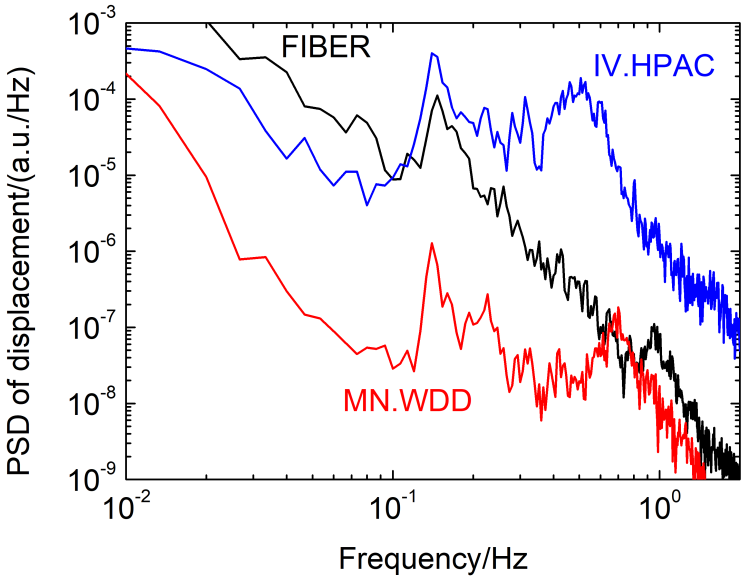

Figure 5.26: Spectra of submarine fibre noise, calculated in a common time window and renormalized for better visualization. Black: PSD of the fibre optical phase. Blue: seismogram from Pachino, Sicily (IV.HPAC). Red seismogram from Malta (MN.WDD).

fibre is the result of an integration all along the fibre path, thus different from the point-like seismometers.
Another fascinating study is related to the Earth's background seismic oscillations, known as *hum* [175]. Such oscillation is in the frequency range of millihertz and is observed also in absence of earthquakes. The origin of this effect is not completely understood and the study is still under way, performed mainly with OBS. The main limitation is the background noise affecting the OBSs, which is due to wave loads and seafloor currents. It can be partially removed with post-processing techniques [176]. However, optical fibres, which are deployed on the bottom of the sea or buried in ground, are expected to be less affected by this noise sources, offering a valid alternative to pursue this study.

Chapter 6

Conclusion and outlooks

This thesis reports on the work done in the years 2015-2018 in the laboratories of the Quantum Metrology and Nanotechnology division of INRIM. It describes the extension of the Italian fibre link for frequency dissemination from Medicina, near Bologna, to Matera. With the realization of this span, the Italian optical link now achieves a length of about 2000 km. Some upgrades have been implemented on the existing infrastructure, aimed at improving the reliability and guaranteeing the uninterrupted operation of the link for several days. Exploiting this fibre, experiments of geodesy, radio astronomy and seismology have been performed and more experiments are planned for the incoming years. The main results achieved during this research project are here summarized.

Optical link applications. The Italian fibre link currently connects INRIM to the radiotelescopes for Very Long Baseline Interferometry in Medicina and Matera. In this thesis I presented the preliminary tests performed to characterize and validate the infrastructure for the dissemination and synthesis of the reference signal. The first common-clock VLBI observation is planned for May 2019. Rejecting the noise contribution of the reference clocks allows a more detailed analysis of the ultimate VLBI resolution and leads to improved models of the troposphere. This is particularly interesting for VLBI as well as for applications in the field of satellite navigation, such as environmental studies, GNSS positioning, time and frequency and aerospace
The Italian link also provides high-quality frequency references to the laboratories of LENS in Sesto Fiorentino (Firenze) and CNR-INO in Pozzuoli (Napoli) for experiments of high precision spectroscopy on cold atoms and molecules. An experiment of spectroscopy on cold acetylene molecules with buffer gas beam cooling is planned with CNR-INO. An uncertainty at the sub-kHz level is expected for the measurement of the molecular transition frequency. This can be achieved with the fibre-disseminated frequency reference, with an improvement of more than two orders of magnitude with respect to the GPS-calibrated rubidium clock which is

currently employed.
We are currently disseminating the INRIM Hydrogen maser. A further improvement to the above-mentioned experiments will be achieved by disseminating the Yb optical clock developed at INRIM, whose reliability over time is currently limited by uptimes of few hours. The Yb clock will bring an improvement of two orders of magnitude to the uncertainty of the disseminated signal.

Exploiting the phase-stabilized link between INRIM and the laboratory of LSM in the Fréjus tunnel, an experiment of chronometric geodesy was performed in collaboration with PTB and NPL. This was a proof-of-principle test of chronometric levelling which demonstrated good agreement with the results obtained by traditional gravimetry techniques. It was limited by the short measurement times allowed by the portable Sr clock placed at LSM and by the use of ITCsF2 for the comparison. Future experiments may benefit from optical clocks with improved performances: a relative uncertainty at the 10^{-18} level would allow a resolution of 1 cm after few hours measurement, outperforming traditional techniques. This paves the way for future campaigns, exploiting the European fibre network, for the realization of an improved mapping of the gravity potential and the investigation of its variations over time.

Finally, I showed the results of seismology experiments with fibre links performed in collaboration with NPL, the University of Malta and the British Geological Survey. We demonstrated the detection of small earthquakes and high-magnitude teleseismic events at a geometrical distance from the epicentre ranging from 25 to 18 000 km, exploiting both terrestrial and submarines optical fibres with lengths from 75 to 535 km. Considering the expected noise level of transoceanic fibres, we predicted the possibility of detecting earthquakes originated on the bottom of the oceans, exploiting the network of submarine optical fibres deployed for telecommunication purposes. This could provide a cost-effective complement to the existing network of seismic sensors and enable the detection of small magnitude earthquakes generated on the oceans floor, which remain currently undetected due to the small number of submarine seismic sensors. This may lead to important contributions to Earth science in the study of the Earth interior dynamic.

The remote comparison of atomic clocks. I described the implementation of the two-way noise cancellation technique for the comparison of remote frequency references on a 294 km fibre link showing that it is suitable for the validation of remote optical frequency standards at their intrinsic level of accuracy. Such technique will be exploited on the fibre link under development between INRIM and LNE-SYRTE for the comparison of the atomic clocks developed by the two institutes, planned for the end of 2019. Once completed the link will be more than 1000 km long and for this reason the use of the two-way scheme will be crucial to reduce the amount of fibre phase noise and optical losses on the delivered signal.

In addition, I presented the phase noise measurements performed on 200 km of

submarine fibre, which demonstrated a noise level orders of magnitude lower than land links of same length. I show an extrapolation of the expected phase noise on transoceanic fibres as well as the expected noise achievable on a transoceanic link with the two-way noise cancellation scheme. Simulations show that a comparison performed on a single bidirectional fibre allows to compare optical clocks at their level of uncertainty. Whereas, if a pair of bidirectional fibres is used, which is the most immediate and cost-effective solution for the submarine environment, an ultimate stability at the 10^{-16} level is achieved on timescales of hours. This may allow the transcontinental comparison of primary standards at their intrinsic level of uncertainty on shorter timescales than satellite-based techniques, which require days of measurement to achieve the same stability level. Therefore, transoceanic fibre links could improve the generation of the International Atomic Time (TAI).

Appendix A

Compatibility test of Brillouin amplification in a dark channel infrastructure

Although the metrological transmission is in principle compatible with the dark channel architecture, some specific configurations need to be investigated. The maximum allowed power levels for the transmitted signals are set by the telecom companies. This may be an issue for distributed amplifiers which require high power pump lasers. The pump power of DRAs is usually hundreds of milliwatts and for this reason they have to be installed by the provider itself. In case of FBAs, a lower pump power of tens of milliwatts is used. However, even though DWDM filters are used, this does not guarantee the required level of isolation among channels and the effective absence of cross-talk between metrological and data channels needs to be verified.
Exploiting the telecontrol devices employed for the amplifiers, a test of data transmission in presence of a Brillouin pump laser, has been performed. This allowed to investigate the compatibility of the Brillouin amplification technique with the dark channel transmission.

Test setup

Our test setup exploits fibre spools, commercial routers and data transmission devices operating on the ITU 43 channel, which has the minimum available spectral separation (100 GHz) from the metrological signal in the ITU 44 channel.
We studied the failures in communication due to the presence of coherent transmission with FBA amplification on the nearby channel. The failures in communication are quantified by measuring the following quantities:

- the number of lost data packets per second. This gives an absolute indication on the rate of lost packets because of errors occurred at detection.

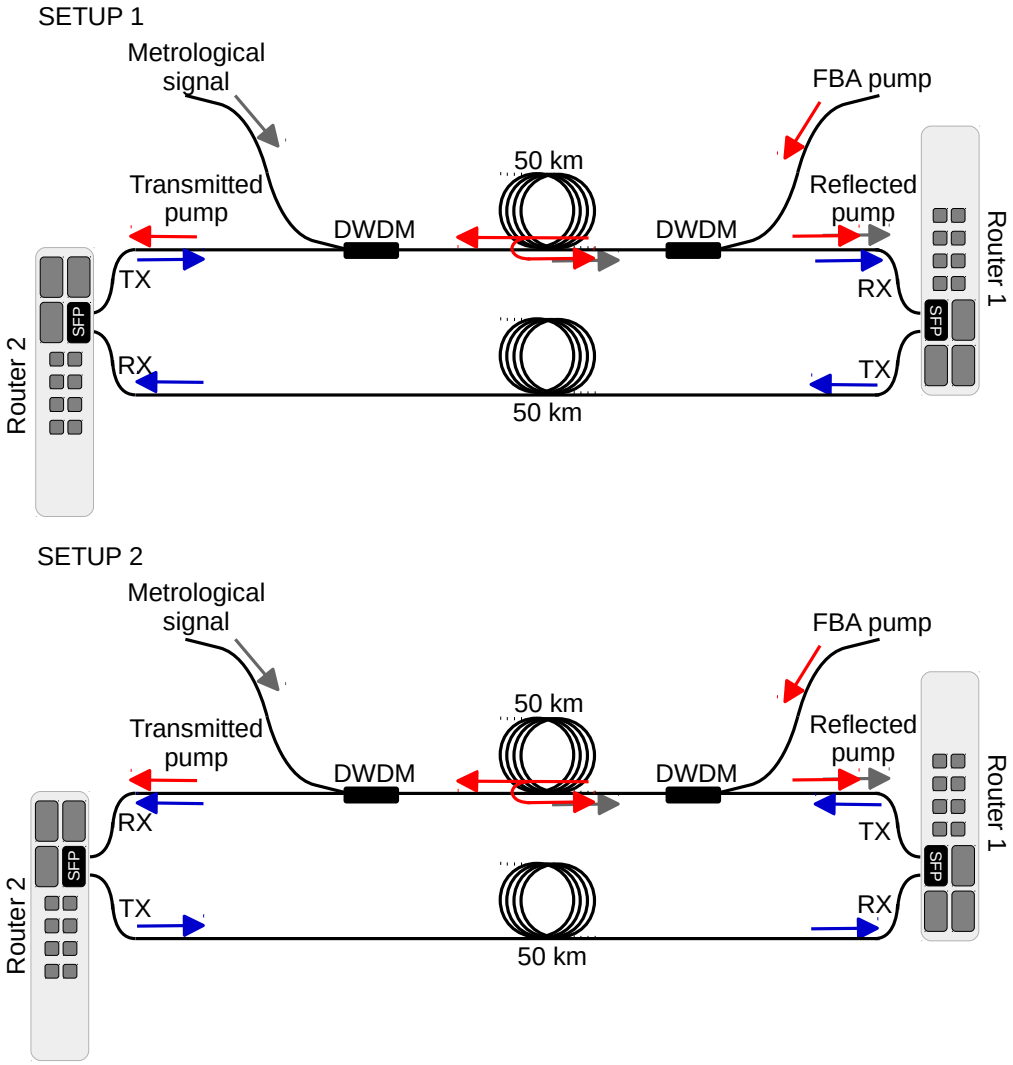

Figure A.1: Setup for the test of data transmission in presence of Brillouin amplification. The communication is preformed between *router*1 and *router*2 over two fibre spools. In *setup*1 the amplified metrological signal is propagating in the same direction as the data, while in *setup*2 amplified signal and data are counterpropagating.

- the rate of lost Megabits per second (Mbps). This parameter allows a more complete information as it quantifies the lost Mbps instead of packets and can be readily weighted by the traffic flow, to quantify the impact of lost information.

For the test, two of the commercial routers switch employed for the amplifiers control have been used, communicating over TCP/IP, which is the main protocol of the Internet Protocol suite. A packet flow of random data is generated at the rate of 50 Mbps, which is the maximum allowed by our devices, to simulate the network

traffic.
The experiment is performed over a fibre pair. One of the fibres is used in bidirectional configuration for standard metrological transmission. Here, an ultrastable laser signal at 1542.14 nm or 194.4 THz (corresponding to the central frequency of ITU44 channel) is injected at one end, while the FBA pump laser, at a wavelength of 1542.05 nm or 194.41 THz is injected at the other end, in counterpropagating direction. Its frequency is blue-detuned by $\sim$ 11 GHz to match the pump/signal shift that maximizes the FBA gain.
The injected metrological signal power is -20 dBm; at the far link end, about -30 dBm are amplified by the FBA pump. The FBA gain is varied between 45 dB and 48 dB, which are obtained with 30 mW and 60 mW of pump power respectively.
In addition, standard data traffic is added to the link: it exploits two separate fibres for transmission (Tx) and receiving (Rx). One of these fibres is necessarily shared with the metrological signal, while the other is fully dedicated to communication. Two representative test cases have been considered. In the first setup (setup 1) the metrological signal shares the fibre with the data transmission (Tx) channel, which is then co-propagating with the amplified metrological signal at the far end. In a second test (setup 2) the metrological signal shares the fibre with the data receiving (Rx) channel and hence the amplified metrological signal and data flow are counter-propagating. On the shared fibre, the metrological and data signals are combined/separated through a DWDM filter entered on the ITU channel 44. These setups are shown in fig. A.1.

Results

The number of lost packets and the lost bitrate appears to be severely affected by the FBA pump only in setup 1. We attribute this to the inter-channel interference between the backscattered FBA pump and the Rx detector internal to the router: in fact, even if the two are in separate channels, the power suppression between the Common and Reflection ports in the DWDM is only $\sim$ 24 dB. As a result, in the test setup, up to -14 dBm of optical power from the ITU44 can impinge the router photodiode, burying the RX signal.
As expected, the effect on the number of lost packets and lost bitrate is more severe as the TX power decreases or as the FBA pump power increases; these aspects are illustrated in fig. A.2.
It is important to highlight that when the FBA pump is not locked to the metrological signal, the lost packet and Mbps rates further increase. This situation is of particular concern as it can happen in case of accidental unlock of the FBA pump and signal. In our setup, we had 3000 lost packets per second and 40 Mbps lost still in the configuration in which the FBA pump was 30 mW and the data signal at the Rx port was -10 dBm. This is attributed to the fact that the FBA pump signal is not subject to coherent scatter in absence of a signal, or when their detuning

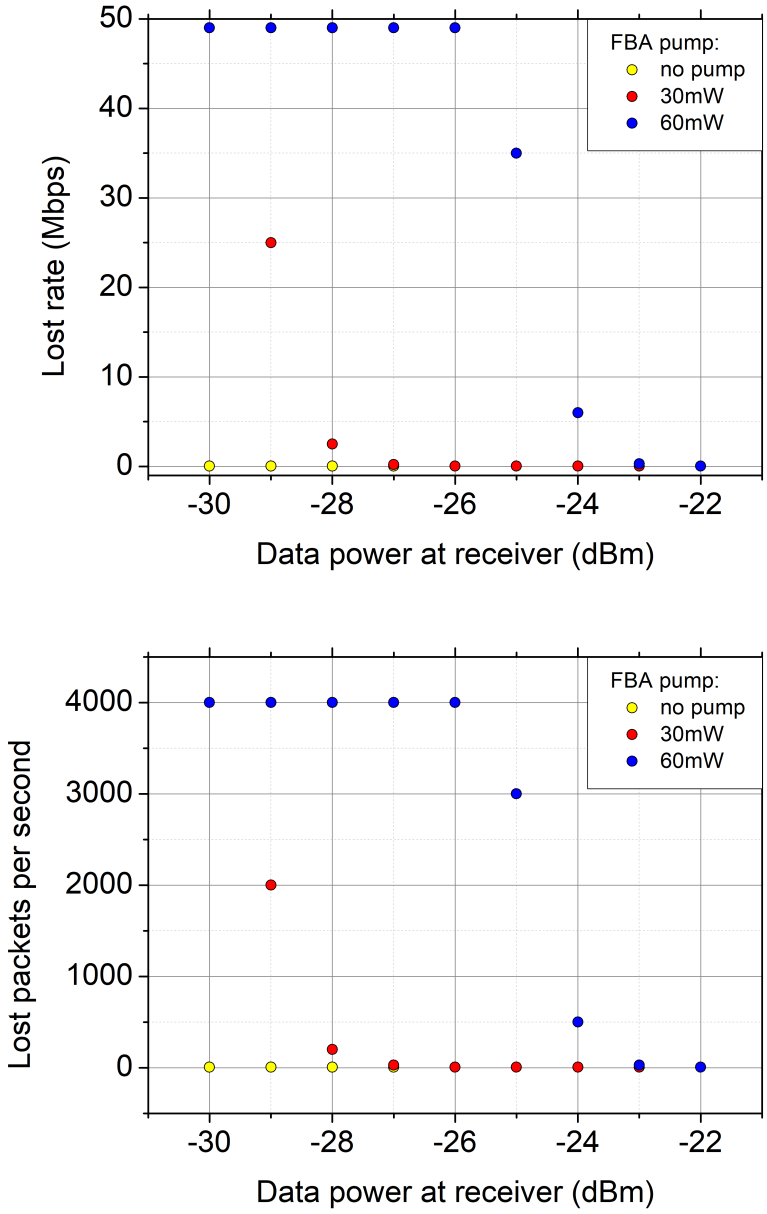

Figure A.2: Lost data rate and lost packets per second for various power levels of the data signal at the receiver, for *setup*1; yellow dots: without Brillouin pump, red dots: with a FBA pump at 30 mW and blue dots: with a FBA pump at 60 mW.

does not match with the optimal one. Hence, most of it undergoes spontaneous Brillouin scatter which introduces a significant amplitude noise in the forward direction. As mentioned, this also affects the signal at the Rx port of the transceiver, even if a DWDM filter is present. This is clearly observed displaying the Rx signal

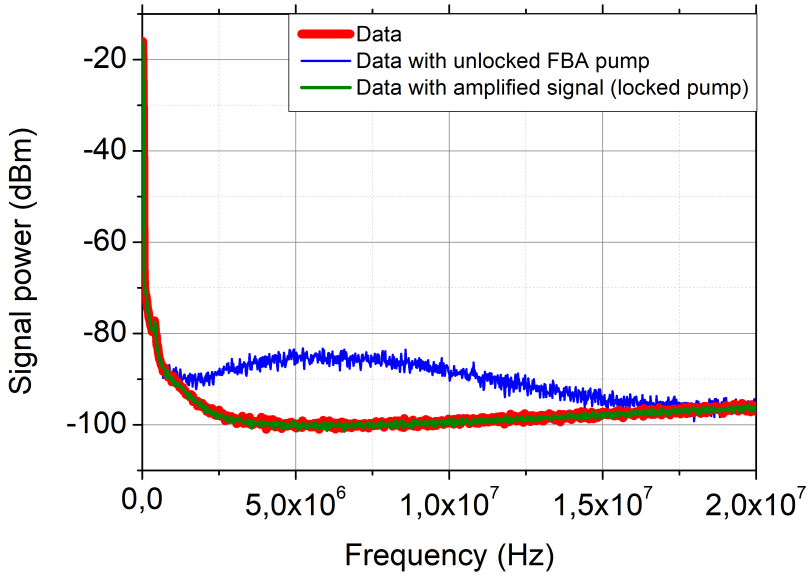

Figure A.3: RF spectrum of the Rx signal detected by *router*1 in *setup*1; red: in presence of data only, green: in presence of data and filtered amplified metrological signal, i.e. FBA pump locked, blue: in presence of data and unlocked FBA pump.

on an oscilloscope and on the RF spectrum analyser (fig. A.3). The noise floor is increased by more than 10 dB in case of unlocked FBA pump with respect to the case of coherent backscattering up to 1.5 GHz Fourier frequency.
In all cases, the degradation on the data transfer can be avoided by adding a further filter in front of the router photodiode on the Rx channel. In this configuration, the rejection improves to $\sim$ 48 dB, thus making the crosstalk between adjacent channels negligible.
No impairments were observed in setup 2, as in this configuration the power leakage from the metrological signal to nearby channels affects the Tx devices and not the photodiode on the Rx channel.
The tests were repeated after shifting the data communication to distant channels, namely in the ITU22 channel (192.2 THz, 1559.79 nm). No change from the reported tests was observed
As a general rule, impairments in data transmission are observed, in case of locked pump, if the Rx power is 10 dB lower than the amplified signal after DWDM filter, while, in case of unlocked pump, a significant deterioration arises whenever the power of the filtered unlocked pump and Rx signal are at the same level.
It is important to stress that the effect of inter-channel crosstalk has to be checked in-field, as it is strongly dependent on several parameters such as:

- The fibre span attenuation, which sets the power of the metrological signal

after amplification, hence the leakage to nearby channels as well.

- The metrological link architecture and the fibre quality (absence of bad splices, connections, backreflections...) which determine the FBA gain affordable for each shelter
- The power provided by transmission devices for ordinary data communication, which has to be compared to the leakage from the metrological signal into the receiving channel.

Bibliography

[1] J. V. L. Parry L. Essen. "An Atomic Standard of Frequency and Time Interval: A Caesium Resonator". In: *Nature* 176.4476 (Aug. 1955), pp. 280–282. DOI: 10.1038/176280a0 (cit. on p. 1).

[2] *Comptes Rendus des Séances e la Trezième Conférence Général des Poids et Measures (1967-68)*. URL: https://www.bipm.org/utils/common/pdf/CGPM/CGPM13.pdf (cit. on p. 1).

[3] R. Wynands and S. Weyers. "Atomic fountain clocks". In: *Metrologia* 42.3 (June 2005), S64–S79. DOI: 10.1088/0026-1394/42/3/S08 (cit. on p. 1).

[4] F. Levi et al. "Accuracy evaluation of ITCsF2: a nitrogen cooled caesium fountain". In: *Metrologia* 51.3 (May 2014), pp. 270–284. DOI: 10.1088/0026-1394/51/3/270 (cit. on pp. 1, 2).

[5] A. Clairon et al. "Ramsey Resonance in a Zacharias Fountain". In: *Europhysics Letters* 16.2 (Sept. 1991), pp. 165–170. DOI: 10.1209/0295-5075/16/2/008 (cit. on p. 1).

[6] N. F. Ramsey. "The method of successive oscillatory fields". In: *Physics Today* 66.1 (Jan. 2013), pp. 36–41. DOI: 10.1063/PT.3.1857 (cit. on p. 1).

[7] *Resolutions adopted - 26th meeting of the CGPM (13-16 November 2018)*. URL: https://www.bipm.org/utils/common/pdf/CGPM-2018/26th-CGPM-Resolutions.pdf (cit. on p. 1).

[8] *SI Brochure: The International System of Units (SI), 9th edition*. 2019. URL: https://www.bipm.org/utils/common/pdf/si-brochure/SI-Brochure-9.pdf (cit. on p. 1).

[9] *Evaluation of measurement data - Guide to the expression of uncertainty measurement*. JCGM, 2008. URL: https://www.bipm.org/utils/common/documents/jcgm/JCGM_100_2008_E.pdf (cit. on p. 2).

[10] D. W. Allan. "Statistics of atomic frequency standards". In: *Proceedings of the IEEE* 54.2 (1966), pp. 221–230. DOI: 10.1109/PROC.1966.4634 (cit. on p. 2).

[11] J. Rutman. "Characterization of phase and frequency instabilities in precision frequency sources: Fifteen years of progress". In: *Proceedings of the IEEE* 66.9 (1978), pp. 1048–1075. DOI: 10.1109/PROC.1978.11080 (cit. on p. 2).

[12] G. Santarelli et al. "Quantum Projection Noise in an Atomic Fountain: A High Stability Cesium Frequency Standard". In: *Physical Review Letters* 82.23 (June 1999), pp. 4619–4622. DOI: 10.1103/PhysRevLett.82.4619 (cit. on p. 2).

[13] N. Huntemann et al. "Single-Ion Atomic Clock with 3×10^{-18} Systematic Uncertainty". In: *Physical Review Letters* 116.6 (Feb. 2016). DOI: 10.1103/PhysRevLett.116.063001 (cit. on p. 2).

[14] P. Dubé et al. "High-Accuracy Measurement of the Differential Scalar Polarizability of a $^{88}Sr^{+}$ Clock Using the Time-Dilation Effect". In: *Physical Review Letters* 112.17 (Apr. 2014). DOI: 10.1103/PhysRevLett.112.173002 (cit. on p. 2).

[15] C. Chou et al. "Frequency Comparison of Two High-Accuracy Al^{+} Optical Clocks". In: *Physical Review Letters* 104.7 (Feb. 2010). DOI: 10.1103/PhysRevLett.104.070802 (cit. on p. 2).

[16] S. M. Brewer et al. "Measurements of $^{27}Al^{+}$ and $^{25}Mg^{+}$ magnetic constants for improved ion clock accuracy". In: (Mar. 11, 2019). arXiv: http://arxiv.org/abs/1903.04661v2 [physics.atom-ph] (cit. on pp. 2, 106).

[17] W. H. Oskay et al. "Single-Atom Optical Clock with High Accuracy". In: *Physical Review Letters* 97.2 (July 2006). DOI: 10.1103/PhysRevLett.97.020801 (cit. on p. 2).

[18] T. L. Nicholson et al. "Systematic evaluation of an atomic clock at 2×10^{-18} total uncertainty". In: *Nature Communications* 6.1 (Apr. 2015). DOI: 10.1038/ncomms7896 (cit. on pp. 2, 106).

[19] I. Ushijima et al. "Cryogenic optical lattice clocks". In: *Nature Photonics* 9.3 (Feb. 2015), pp. 185–189. DOI: 10.1038/nphoton.2015.5 (cit. on pp. 2, 106).

[20] W. F. McGrew et al. "Atomic clock performance enabling geodesy below the centimetre level". In: *Nature* (Nov. 2018). DOI: 10.1038/s41586-018-0738-2 (cit. on pp. 2, 106).

[21] N. Nemitz et al. "Frequency ratio of Yb and Sr clocks with 5×10^{-17} uncertainty at 150 seconds averaging time". In: *Nature Photonics* 10.4 (Feb. 2016), pp. 258–261. DOI: 10.1038/nphoton.2016.20 (cit. on p. 2).

[22] M. Pizzocaro et al. "Absolute frequency measurement of the $^{1}S_{0}$-$^{3}P_{0}$ transition of ^{171}Yb". In: *Metrologia* 54.1 (Jan. 2017), pp. 102–112. DOI: 10.1088/1681-7575/aa4e62 (cit. on pp. 2, 96).

[23] K. Yamanaka et al. "Frequency Ratio of Hg^{199} and Sr^{87} Optical Lattice Clocks beyond the SI Limit". In: *Physical Review Letters* 114.23 (June 2015). DOI: 10.1103/PhysRevLett.114.230801 (cit. on p. 2).

[24] Fritz Riehle et al. "The CIPM list of recommended frequency standard values: guidelines and procedures". In: *Metrologia* 55.2 (Feb. 2018), pp. 188–200. DOI: 10.1088/1681-7575/aaa302 (cit. on p. 2).

[25] S. Origlia et al. "Towards an optical clock for space: Compact, high-performance optical lattice clock based on bosonic atoms". In: *Physical Review A* 98.5 (Nov. 2018). DOI: 10.1103/physreva.98.053443 (cit. on p. 2).

[26] T. Akatsuka, M. Takamoto, and H. Katori. "Optical lattice clocks with non-interacting bosons and fermions". In: *Nature Physics* 4.12 (Oct. 2008), pp. 954–959. DOI: 10.1038/nphys1108 (cit. on p. 2).

[27] P. Wcisło et al. "Experimental constraint on dark matter detection with optical atomic clocks". In: *Nature Astronomy* 1.1 (Dec. 2016), p. 0009. DOI: 10.1038/s41550-016-0009 (cit. on p. 2).

[28] Cédric Delaunay et al. "Probing atomic Higgs-like forces at the precision frontier". In: *Physical Review D* 96.9 (Nov. 2017). DOI: 10.1103/physrevd.96.093001 (cit. on p. 2).

[29] Christian Sanner et al. "Optical clock comparison for Lorentz symmetry testing". In: *Nature* 567.7747 (2019), pp. 204–208. DOI: 10.1038/s41586-019-0972-2 (cit. on p. 2).

[30] D. Calonico et al. "High-accuracy coherent optical frequency transfer over a doubled 642 km fiber link". In: *Applied Physics B* 117.3 (Sept. 2014), pp. 979–986. DOI: 10.1007/s00340-014-5917-8 (cit. on pp. 3, 4, 15, 17, 23, 26, 34, 38, 45, 73, 74).

[31] C. Clivati et al. "A VLBI experiment using a remote atomic clock via a coherent fibre link". In: *Scientific Reports* 7.1 (Feb. 2017). DOI: 10.1038/srep40992 (cit. on pp. 3–5, 34, 45, 96, 97).

[32] J. Grotti et al. "Geodesy and metrology with a transportable optical clock". In: *Nature Physics* 14.5 (Feb. 2018), pp. 437–441. DOI: 10.1038/s41567-017-0042-3 (cit. on pp. 3, 4, 7, 11, 107).

[33] C. Lisdat et al. "A clock network for geodesy and fundamental science". In: *Nature Communications* 7.1 (Aug. 2016). DOI: 10.1038/ncomms12443 (cit. on pp. 3, 4, 7, 106).

[34] P. Delva et al. "Test of Special Relativity Using a Fiber Network of Optical Clocks". In: *Physical Review Letters* 118.22 (June 2017). DOI: 10.1103/PhysRevLett.118.221102 (cit. on pp. 3, 4).

[35] Ł. Śliwczyński et al. “Frequency distribution in delay-stabilized optical DWDM network over the distance of 3000 km”. In: *2015 Joint Conference of the IEEE International Frequency Control Symposium & the European Frequency and Time Forum*. IEEE, Apr. 2015. DOI: 10.1109/fcs.2015.7138841 (cit. on pp. 3, 16).

[36] S. C. Ebenhag et al. “Two-way coherent frequency transfer in a commercial DWDM communication network in Sweden”. In: *2015 Joint Conference of the IEEE International Frequency Control Symposium & the European Frequency and Time Forum*. IEEE, Apr. 2015. DOI: 10.1109/fcs.2015.7138840 (cit. on p. 3).

[37] J. Vojtech et al. “Joint accurate time and stable frequency distribution infrastructure sharing fiber footprint with research network”. In: *Optical Engineering* 56.2 (Feb. 2017), p. 027101. DOI: 10.1117/1.OE.56.2.027101 (cit. on p. 3).

[38] J. Ye et al. “Delivery of high-stability optical and microwave frequency standards over an optical fiber network”. In: *Journal of the Optical Society of America B* 20.7 (July 2003), p. 1459. DOI: 10.1364/JOSAB.20.001459 (cit. on pp. 3, 14).

[39] P. A. Williams, W. C. Swann, and N. R. Newbury. “High-stability transfer of an optical frequency over long fiber-optic links”. In: *Journal of the Optical Society of America B* 25.8 (July 2008), p. 1284. DOI: 10.1364/JOSAB.25.001284 (cit. on pp. 4, 19, 21, 22, 73, 74, 80, 81).

[40] F.-L. Hong et al. “Measuring the frequency of a Sr optical lattice clock using a 120 km coherent optical transfer”. In: *Optics Letters* 34.5 (Feb. 2009), p. 692. DOI: 10.1364/OL.34.000692 (cit. on p. 4).

[41] M. Fujieda et al. “All-optical link for direct comparison of distant optical clocks”. In: *Optics Express* 19.17 (Aug. 2011), p. 16498. DOI: 10.1364/OE.19.016498 (cit. on pp. 4, 15, 23, 26).

[42] L. Kun et al. “Status of Time and Frequency Transfer at NIM”. In: *Proceedings of the 47th Annual Precise Time and Time Interval Systems and Applications Meeting*. Institute of Navigation, Feb. 2016. DOI: 10.33012/2016.13143 (cit. on p. 4).

[43] K. G. H. Baldwin et al. “Dissemination of precise radio-frequency references for environmental sensing over long-haul optical-fiber networks”. In: *Light, Energy and the Environment*. OSA, 2016. DOI: 10.1364/ee.2016.etu3a.3 (cit. on pp. 4, 16).

[44] S. W. Schediwy et al. “Stabilized microwave-frequency transfer using optical phase sensing and actuation”. In: *Optics Letters* 42.9 (Apr. 2017), p. 1648. DOI: 10.1364/OL.42.001648 (cit. on pp. 4, 15).

[45] URL: https://www.ptb.de/emrp/neatft_home.html (cit. on p. 4).

[46] URL: https://www.ptb.de/emrp/often_home.html (cit. on p. 4).

[47] J. Guéna et al. "First international comparison of fountain primary frequency standards via a long distance optical fiber link". In: *Metrologia* 54.3 (May 2017), pp. 348–354. DOI: 10.1088/1681-7575/aa65fe (cit. on p. 4).

[48] T. Takano et al. "Geopotential measurements with synchronously linked optical lattice clocks". In: *Nature Photonics* 10.10 (Aug. 2016), pp. 662–666. DOI: 10.1038/nphoton.2016.159 (cit. on pp. 4, 7, 106).

[49] B. Argence et al. "Quantum cascade laser frequency stabilization at the sub-Hz level". In: *Nature Photonics* 9.7 (June 2015), pp. 456–460. DOI: 10.1038/nphoton.2015.93 (cit. on pp. 4, 6).

[50] C. Clivati et al. "Measuring absolute frequencies beyond the GPS limit via long-haul optical frequency dissemination". In: *Optics Express* 24.11 (May 2016), p. 11865. DOI: 10.1364/OE.24.011865 (cit. on pp. 4, 6, 34, 38).

[51] P. Krehlik et al. "Fibre-optic delivery of time and frequency to VLBI station". In: *Astronomy & Astrophysics* 603 (July 2017), A48. DOI: 10.1051/0004-6361/201730615 (cit. on pp. 4, 5, 96).

[52] Yabai He et al. "Long distance telecom fiber transfer of a radio frequency reference for radio astronomy". In: *Optica* 5.2 (Feb. 2018), p. 138. DOI: 10.1364/optica.5.000138 (cit. on pp. 4, 5, 96).

[53] J. Serrano et al. *The White Rabbit project*. 2013. URL: http://cds.cern.ch/record/1743073 (cit. on pp. 4, 34).

[54] A. Creusot. "Calibration, performances and tests of the first detection unit of the KM3NeT neutrino telescope, in proceedings of 34th ICRC". In: *The Hague, The Netherlands, PoS (ICRC2015)* 1154 (2015) (cit. on p. 4).

[55] A. R. Thompson, J. M. Moran, and G. W. Swenson Jr. *Interferometry and Sythesis in Radio Astronomy*. Ed. by Springer Open. Springer International Publishing, 2017. DOI: 10.1007/978-3-319-44431-4 (cit. on pp. 5, 94).

[56] L. F. Livi et al. "Synthetic Dimensions and Spin-Orbit Coupling with an Optical Clock Transition". In: *Physical Review Letters* 117.22 (Nov. 2016). DOI: 10.1103/PhysRevLett.117.220401 (cit. on pp. 6, 34, 38).

[57] G. Insero et al. "Measuring molecular frequencies in the 1-10 μm range at 11-digits accuracy". In: *Scientific Reports* 7.1 (Oct. 2017). DOI: 10.1038/s41598-017-12891-6 (cit. on pp. 6, 34, 38).

[58] M. Vermeer. *Chronometric Levelling*. Geodeettinen Laitos, Geodetiska Institutet, 1983 (cit. on pp. 6, 106).

[59] A. Bjerhammar. "On a relativistic geodesy". In: *Bulletin Géodésique* 59.3 (Sept. 1985), pp. 207–220. DOI: 10.1007/bf02520327 (cit. on pp. 6, 106).

[60] C. W. Chou et al. "Optical Clocks and Relativity". In: *Science* 329.5999 (Sept. 2010), pp. 1630–1633. DOI: 10.1126/science.1192720 (cit. on pp. 7, 106).

[61] Y. Kaneda. "Introduction to ocean floor networks and their scientific application". In: *Marine Geophysical Research* 113.B1 (Jan. 2014), pp. 177–180. DOI: 10.1007/s11001-014-9232-x (cit. on pp. 7, 114).

[62] J. Mestayer et al. "Field trials of distributed acoustic sensing for geophysical monitoring". In: *SEG Technical Program Expanded Abstracts 2011*. Society of Exploration Geophysicists, Jan. 2011. DOI: 10.1190/1.3628095 (cit. on pp. 7, 114).

[63] G. Marra et al. "Ultrastable laser interferometry for earthquake detection with terrestrial and submarine cables". In: *Science* (June 2018), eaat4458. DOI: 10.1126/science.aat4458 (cit. on pp. 7, 114).

[64] C. Clivati et al. "Optical frequency transfer over submarine fiber links". In: *Optica* 5.8 (July 2018), p. 893. DOI: 10.1364/OPTICA.5.000893 (cit. on pp. 7, 67).

[65] M. Chwalla et al. "Absolute frequency measurement of the $^{40}Ca^{+}$ $4s^2S_{1/2}$ - $3d^2D_{5/2}$ clock transition". In: *Physical Review Letters* 102.2 (Jan. 2009). DOI: 10.1103/PhysRevLett.102.023002 (cit. on p. 11).

[66] A. Bauch. "Time and frequency comparisons using radiofrequency signals from satellites". In: *Comptes Rendus Physique* 16.5 (June 2015), pp. 471–479. DOI: 10.1016/j.crhy.2015.02.006 (cit. on p. 11).

[67] URL: https://www.bipm.org/en/bipm/tai/time-transfer/ (cit. on p. 12).

[68] G. Petit et al. "10^{-16} frequency transfer by GPS PPP with integer ambiguity resolution". In: *Metrologia* 52.2 (Mar. 2015), pp. 301–309. DOI: 10.1088/0026-1394/52/2/301 (cit. on p. 12).

[69] H. Hachisu et al. "Direct comparison of optical lattice clocks with an intercontinental baseline of 9000 km". In: *Optics Letters* 39.14 (July 2014), p. 4072. DOI: 10.1364/OL.39.004072 (cit. on p. 12).

[70] H. S. Margolis et al. "International timescales with optical clocks (ITOC)". In: *2013 Joint European Frequency and Time Forum & International Frequency Control Symposium (EFTF/IFC)*. IEEE, July 2013. DOI: 10.1109/eftf-ifc.2013.6702183 (cit. on p. 13).

[71] M. Fujieda et al. "Carrier-phase two-way satellite frequency transfer over a very long baseline". In: *Metrologia* 51.3 (May 2014), pp. 253–262. DOI: 10.1088/0026-1394/51/3/253 (cit. on p. 13).

[72] *Final Publishable JRP Summary for SIB55 ITOC International timescales with optical clocks*. Tech. rep. 2016. URL: http://projects.npl.co.uk/itoc/documents/sib55-itoc-final-publishable-jrp-summary.pdf (cit. on p. 13).

[73] P. Laurent et al. "The ACES/PHARAO space mission". In: *Comptes Rendus Physique* 16.5 (June 2015), pp. 540–552. DOI: 10.1016/j.crhy.2015.05.002 (cit. on p. 13).

[74] L. S. Ma et al. "Delivering the same optical frequency at two places: accurate cancellation of phase noise introduced by an optical fiber or other time-varying path". In: *Optics Letters* 19.21 (Nov. 1994), p. 1777. DOI: 10.1364/OL.19.001777 (cit. on p. 14).

[75] F. Kéfélian et al. "High-resolution optical frequency dissemination on a telecommunications network with data traffic". In: *Optics Letters* 34.10 (May 2009), p. 1573. DOI: 10.1364/OL.34.001573 (cit. on p. 14).

[76] S. A. Diddams et al. "Direct link between Microwave and Optical Frequencies with a 300 THz Femtosecond Laser Comb". In: *Physical Review Letters* 84.22 (May 2000), pp. 5102–5105. DOI: 10.1103/PhysRevLett.84.5102 (cit. on pp. 14, 29).

[77] E. D. Black. "An introduction to Pound Drever Hall laser frequency stabilization". In: *American Journal of Physics* 69.1 (Jan. 2001), pp. 79–87. DOI: 10.1119/1.1286663 (cit. on p. 15).

[78] N. Chiodo et al. "Cascaded optical fiber link using the internet network for remote clocks comparison". In: *Optics Express* 23.26 (Dec. 2015), p. 33927. DOI: 10.1364/OE.23.033927 (cit. on pp. 15, 23, 29, 43).

[79] S. Droste et al. "Optical Frequency Transfer over a Single Span 1840 km Fiber Link". In: *Physical Review Letters* 111.11 (Sept. 2013). DOI: 10.1103/PhysRevLett.111.110801 (cit. on pp. 15, 23, 73, 74).

[80] A. Bercy et al. "Two-way optical frequency comparisons at 5×10^{-21} relative stability over 100 km telecommunication network fibers". In: *Physical Review A* 90.6 (Dec. 2014). DOI: 10.1103/PhysRevA.90.061802 (cit. on pp. 15, 25, 55, 83).

[81] A. Tampellini et al. "Effect of a timebase mismatch in two-way optical frequency transfer". In: *Metrologia* 54.6 (Oct. 2017), pp. 805–809. DOI: 10.1088/1681-7575/aa8a41 (cit. on pp. 15, 55).

[82] O. Lopez et al. "High-resolution microwave frequency dissemination on an 86 km urban optical link". In: *Applied Physics B* 98.4 (Nov. 2009), pp. 723–727. DOI: 10.1007/s00340-009-3832-1 (cit. on p. 15).

[83] P. Krehlik et al. “ELSTAB Fiber Optic Time and Frequency Distribution Technology: A General Characterization and Fundamental Limits”. In: *IEEE Transactions on Ultrasonics, Ferroelectrics, and Frequency Control* 63.7 (July 2016), pp. 993–1004. DOI: 10.1109/TUFFC.2015.2502547 (cit. on p. 16).

[84] P. Krehlik et al. “Multipoint dissemination of RF frequency in fiber optic link with stabilized propagation delay”. In: *IEEE Transactions on Ultrasonics, Ferroelectrics, and Frequency Control* 60.9 (Sept. 2013), pp. 1804–1810. DOI: 10.1109/TUFFC.2013.2766 (cit. on p. 16).

[85] Y. He et al. “Stable radio-frequency transfer over optical fiber by phase-conjugate frequency mixing”. In: *Optics Express* 21.16 (July 2013), p. 18754. DOI: 10.1364/OE.21.018754 (cit. on p. 16).

[86] M. Fujieda et al. “Ultrastable Frequency Dissemination via Optical Fiber at NICT”. In: *IEEE Transactions on Instrumentation and Measurement* 58.4 (Apr. 2009), pp. 1223–1228. DOI: 10.1109/TIM.2008.2008088 (cit. on p. 16).

[87] L. Yu et al. “Stable radio frequency dissemination by simple hybrid frequency modulation scheme”. In: *Optics Letters* 39.18 (Sept. 2014), p. 5255. DOI: 10.1364/OL.39.005255 (cit. on p. 16).

[88] F. Yin et al. “Phase-conjugation-based fast RF phase stabilization for fiber delivery”. In: *Optics Express* 22.1 (Jan. 2014), p. 878. DOI: 10.1364/OE.22.000878 (cit. on p. 16).

[89] B. Wang et al. “Precise and Continuous Time and Frequency Synchronisation at the 5×10^{-19} Accuracy Level”. In: *Scientific Reports* 2.1 (Aug. 2012). DOI: 10.1038/srep00556 (cit. on p. 16).

[90] C. Gao et al. “Dissemination stability and phase noise characteristics in a cascaded, fiber-based long-haul radio frequency dissemination network”. In: *Review of Scientific Instruments* 86.9 (Sept. 2015), p. 093111. DOI: 10.1063/1.4931395 (cit. on p. 16).

[91] G. Marra et al. “High-resolution microwave frequency transfer over an 86-km-long optical fiber network using a mode-locked laser”. In: *Optics Letters* 36.4 (Feb. 2011), p. 511. DOI: 10.1364/OL.36.000511 (cit. on p. 16).

[92] G. Marra, H. S. Margolis, and D. J. Richardson. “Dissemination of an optical frequency comb over fiber with 3×10^{-18} fractional accuracy”. In: *Optics Express* 20.2 (Jan. 2012), p. 1775. DOI: 10.1364/OE.20.001775 (cit. on pp. 16, 26).

[93] L. C. Sinclair et al. “Comparing Optical Oscillators across the Air to Milliradians in Phase and 10^{-17} in Frequency”. In: *Physical Review Letters* 120.5 (Jan. 2018). DOI: 10.1103/PhysRevLett.120.050801 (cit. on p. 17).

[94] Ł. Śliwczyński, P. Krehlik, and M. Lipiński. "Optical fibers in time and frequency transfer". In: *Measurement Science and Technology* 21.7 (May 2010), p. 075302. DOI: 10.1088/0957-0233/21/7/075302 (cit. on p. 17).

[95] T. J. Pinkert et al. "Effect of soil temperature on optical frequency transfer through unidirectional dense-wavelength-division-multiplexing fiber-optic links". In: *Applied Optics* 54.4 (Jan. 2015), p. 728. DOI: 10.1364/AO.54.000728 (cit. on p. 17).

[96] D. R. Gozzard et al. "Characterization of optical frequency transfer over 154 km of aerial fiber". In: *Optics Letters* 42.11 (May 2017), p. 2197. DOI: 10.1364/OL.42.002197 (cit. on p. 17).

[97] Ł. Śliwczyński et al. "Characterization of the frequency transfer over 300 km of aerial suspended fiber". In: *2016 European Frequency and Time Forum (EFTF)*. IEEE, Apr. 2016. DOI: 10.1109/EFTF.2016.7477756 (cit. on p. 17).

[98] S. C. Ebenhag, P. O. Hedekvist, and L. Weddig. "Measurement and Analysis of Polarization Variations in an Optical Coherent Fiber Communication Network Utilized for Time and Frequency Distribution". In: *Proceedings of the 49th Annual Precise Time and Time Interval Systems and Applications Meeting*. Institute of Navigation, Feb. 2018. DOI: 10.33012/2018.15620 (cit. on p. 17).

[99] M. Fujieda, M. Kumagai, and S. Nagano. "Coherent microwave transfer over a 204 km telecom fiber link by a cascaded system". In: *IEEE Transactions on Ultrasonics, Ferroelectrics and Frequency Control* 57.1 (Jan. 2010), pp. 168–174. DOI: 10.1109/TUFFC.2010.1394 (cit. on pp. 17, 73, 74).

[100] F. M. Gardner. *Phaselock Techniques*. Wiley, 1979 (cit. on p. 20).

[101] N. R. Newbury, P. A. Williams, and W. C. Swann. "Coherent transfer of an optical carrier over 251 km". In: *Optics Letters* 32.21 (Oct. 2007), p. 3056. DOI: 10.1364/OL.32.003056 (cit. on pp. 20, 23).

[102] A. Papoulis. *Probability, random variables, and stochastic processes*. McGraw-Hill, 1965 (cit. on p. 21).

[103] C. E. Calosso, C. Clivati, and S. Micalizio. "Avoiding Aliasing in Allan Variance: An Application to Fiber Link Data Analysis". In: *IEEE Transactions on Ultrasonics, Ferroelectrics, and Frequency Control* 63.4 (Apr. 2016), pp. 646–655. DOI: 10.1109/TUFFC.2016.2519265 (cit. on pp. 21, 64, 88).

[104] F. Stefani et al. "Tackling the limits of optical fiber links". In: *Journal of the Optical Society of America B* 32.5 (Apr. 2015), p. 787. DOI: 10.1364/JOSAB.32.000787 (cit. on p. 22).

[105] O. Lopez et al. "Cascaded multiplexed optical link on a telecommunication network for frequency dissemination". In: *Optics Express* 18.16 (July 2010), p. 16849. DOI: 10.1364/OE.18.016849 (cit. on pp. 23, 28).

[106] C. E. Calosso et al. "Doppler-stabilized fiber link with 6 dB noise improvement below the classical limit". In: *Optics Letters* 40.2 (Jan. 2015), p. 131. DOI: 10.1364/ol.40.000131 (cit. on p. 23).

[107] C. E. Calosso et al. "Frequency transfer via a two-way optical phase comparison on a multiplexed fiber network". In: *Optics Letters* 39.5 (Feb. 2014), p. 1177. DOI: 10.1364/OL.39.001177 (cit. on pp. 23, 25, 55).

[108] G. P.Agrawal. *Nonlinear Fiber Optics*. Academic Press, 2001 (cit. on pp. 25, 27, 28).

[109] C. R. Giles and E. Desurvire. "Modeling erbium-doped fiber amplifiers". In: *Journal of Lightwave Technology* 9.2 (1991), pp. 271–283. DOI: 10.1109/50.65886 (cit. on p. 26).

[110] Ł. Śliwczyński and J. Kolodziej. "Bidirectional Optical Amplification in Long-Distance Two-Way Fiber-Optic Time and Frequency Transfer Systems". In: *IEEE Transactions on Instrumentation and Measurement* 62.1 (Jan. 2013), pp. 253–262. DOI: 10.1109/TIM.2012.2212504 (cit. on pp. 26, 27).

[111] C. Delisle and J. Conradi. "Model for bidirectional transmission in an open cascade of optical amplifiers". In: *Journal of Lightwave Technology* 15.5 (May 1997), pp. 749–757. DOI: 10.1109/50.580808 (cit. on p. 27).

[112] O. Terra, G. Grosche, and H. Schnatz. "Brillouin amplification in phase coherent transfer of optical frequencies over 480 km fiber". In: *Optics Express* 18.15 (July 2010), p. 16102. DOI: 10.1364/OE.18.016102 (cit. on p. 27).

[113] S. M. F. Raupach, A. Koczwara, and G. Grosche. "Brillouin amplification supports 1×10^{-20} uncertainty in optical frequency transfer over 1400 km of underground fiber". In: *Physical Review A* 92.2 (Aug. 2015). DOI: 10.1103/PhysRevA.92.021801 (cit. on p. 27).

[114] C. Clivati et al. "In-field Raman amplification on coherent optical fiber links for frequency metrology". In: *Optics Express* 23.8 (Apr. 2015), p. 10604. DOI: 10.1364/OE.23.010604 (cit. on p. 28).

[115] S. Cundiff J. Ye. *Femtosecond Optical Frequency Comb: Principle, Operation and Application*. Springer, 2005 (cit. on p. 29).

[116] J. Stenger et al. "Ultraprecise Measurement of Optical Frequency Ratios". In: *Physical Review Letters* 88.7 (2002). DOI: 10.1103/PhysRevLett.88.073601 (cit. on p. 31).

[117] D. Calonico et al. "Time and Frequency Distribution over fibre for Geodesy, Seismology and Industry". In: *2018 IEEE International Symposium on Precision Clock Synchronization for Measurement, Control, and Communication (ISPCS)*. IEEE, Sept. 2018. DOI: 10.1109/ispcs.2018.8543065 (cit. on p. 34).

[118] E. F. Dierikx et al. "White Rabbit Precision Time Protocol on Long-Distance Fiber Links". In: *IEEE Transactions on Ultrasonics, Ferroelectrics, and Frequency Control* 63.7 (July 2016), pp. 945–952. DOI: 10.1109/TUFFC.2016.2518122 (cit. on pp. 34, 124).

[119] G. Kramer and W. Klische. "Extra high precision digital phase recorder". In: *18th European Frequency and Time Forum (EFTF 2004)*. IEE, 2004. DOI: 10.1049/cp:20040935 (cit. on p. 35).

[120] C. Clivati et al. "Planar-waveguide external cavity laser stabilization for an optical link with 10^{-19} frequency stability". In: *IEEE Transactions on Ultrasonics, Ferroelectrics, and Frequency Control* 58.12 (Dec. 2011), pp. 2582–2587. DOI: 10.1109/TUFFC.2011.2121 (cit. on p. 36).

[121] C. Clivati et al. "A coherent fiber link for very long baseline interferometry". In: *IEEE Transactions on Ultrasonics, Ferroelectrics, and Frequency Control* 62.11 (Nov. 2015), pp. 1907–1912. DOI: 10.1109/TUFFC.2015.007221 (cit. on pp. 36, 96, 97).

[122] A. Tampellini et al. "Introducing DSP-based Coherent Receivers for Wide-area Reference Frequency Distribution in Metrology Applications". In: *2017 European Conference on Optical Communication (ECOC)*. IEEE, 2017. DOI: 10.1109/ecoc.2017.8345945 (cit. on p. 54).

[123] M. Amemiya et al. "Simple Time and Frequency Dissemination Method Using Optical Fiber Network". In: *IEEE Transactions on Instrumentation and Measurement* 57.5 (May 2008), pp. 878–883. DOI: 10.1109/TIM.2007.915126 (cit. on p. 67).

[124] S. C. Ebenhag et al. "Time transfer between UTC (SP) and UTC (MIKE) using frame detection in fiber-optical communication networks". In: *Proceedings 43rd Precise Time and Time Interval Systems and Applications Meeting*. 2011, pp. 431–441 (cit. on p. 67).

[125] M. Pizzocaro et al. "Active disturbance rejection control of temperature for ultrastable optical cavities". In: *IEEE Transactions on Ultrasonics, Ferroelectrics and Frequency Control* 60.2 (Feb. 2013), pp. 273–280. DOI: 10.1109/TUFFC.2013.2563 (cit. on p. 69).

[126] J.E. Gray and D.W. Allan. "A Method for Estimating the Frequency Stability of an Individual Oscillator". In: *28th Annual Symposium on Frequency Control*. IEEE, 1974. DOI: 10.1109/freq.1974.200027 (cit. on p. 69).

[127] Olivier Lopez et al. "Ultra-stable long distance optical frequency distribution using the Internet fiber network". In: *Optics Express* 20.21 (Sept. 2012), p. 23518. DOI: 10.1364/OE.20.023518 (cit. on pp. 73, 74).

[128] Ł. Śliwczyński and P. Krehlik. "Measurement of acoustic noise in field-deployed fiber optic cables". In: (June 2014). DOI: 10.1109/EFTF.2014.7331504 (cit. on p. 72).

[129] K. Meissner et al. *Impacts of submarine cables on the marine environment - a literature review*. Tech. rep. Institute of Applied Ecology (IfAO), 2006. URL: https://tethys.pnnl.gov/sites/default/files/publications/Meissner-et-al-2006.pdf (cit. on p. 76).

[130] S. Lauria and F. Palone. "Operating envelopes of the Malta-Sicily 245 kV-50 Hz cable". In: *2012 IEEE International Energy Conference and Exhibition (ENERGYCON)*. IEEE, Sept. 2012. DOI: 10.1109/energycon.2012.6347769 (cit. on p. 76).

[131] A. Melloni et al. "Direct measurement of electrostriction in optical fibers". In: *Optics Letters* 23.9 (May 1998), p. 691. DOI: 10.1364/OL.23.000691 (cit. on pp. 76, 77).

[132] J. Prat and J. Comellas. "Dispersion-shifted fiber polarization scrambler based on Faraday effect". In: *IEEE Photonics Technology Letters* 11.7 (July 1999), pp. 845–847. DOI: 10.1109/68.769727 (cit. on pp. 76, 77).

[133] E. L. Buckland and R. W. Boyd. "Measurement of the frequency response of the electrostrictive nonlinearity in optical fibers". In: *Optics Letters* 22.10 (May 1997), p. 676. DOI: 10.1364/OL.22.000676 (cit. on p. 76).

[134] E. L. Buckland and R. W. Boyd. "Electrostrictive contribution to the intensity-dependent refractive index of optical fibers". In: *Optics Letters* 21.15 (Aug. 1996), p. 1117. DOI: 10.1364/OL.21.001117 (cit. on p. 76).

[135] C. R. Paul and S. A. Nasar. *Introduction to Electromagnetic Fields. McGraw-Hill series in Electrical Engineering. Electromagnetics*. 1982 (cit. on p. 77).

[136] A baseline assessment of electromagnetic fields generated by offshore wind farm cables. Tech. rep. COWRIE Report EMF-01, 2002. URL: https://www.thecrownestate.co.uk/media/5859/km-ex-pc-emf-072003-a-baslne-assessmentof-electromagnetic-fields-generated-by-offshore-windfarmcales.pdf. (cit. on p. 77).

[137] J. Leeson, X. Bao, and A. Côté. "Polarization dynamics in optical ground wire network". In: *Applied Optics* 48.12 (Apr. 2009), p. 2214. DOI: 10.1364/AO.48.002214 (cit. on pp. 77, 78).

[138] J. Wuttke, P. M. Krummrich, and J. Rosch. "Polarization oscillations in aerial fiber caused by wind and power-line current". In: *IEEE Photonics Technology Letters* 15.6 (June 2003), pp. 882–884. DOI: 10.1109/LPT.2003.811143 (cit. on pp. 77, 78).

[139] *Vancouver Island Transmission Reinforcement Project: Atmospheric and Underwater Acoustics Assessment*. Tech. rep. British Columbia Transmission Corporation, 2006 (cit. on p. 78).

[140] L. G. Cohen and J. W. Fleming. "Effect of Temperature on Transmission in Lightguides". In: *Bell System Technical Journal* 58.4 (Apr. 1979), pp. 945–951. DOI: 10.1002/j.1538-7305.1979.tb03328.x (cit. on p. 79).

[141] W. H. K. Lee and C. S. Cox. "Time variation of ocean temperatures and its relation to internal waves and oceanic heat flow measurements". In: *Journal of Geophysical Research* 71.8 (Apr. 1966), pp. 2101–2111. DOI: 10.1029/JZ071i008p02101 (cit. on p. 81).

[142] H. W. Broek. "Bottom Temperature Fluctuations on the Continental Slope of the Northwest Atlantic Ocean". In: *Journal of Physical Oceanography* 35.3 (Mar. 2005), pp. 388–394. DOI: 10.1175/JPO-2695.1 (cit. on p. 81).

[143] C. Erbe et al. "The marine soundscape of the Perth Canyon". In: *Progress in Oceanography* 137 (Sept. 2015), pp. 38–51. DOI: 10.1016/j.pocean.2015.05.015 (cit. on p. 81).

[144] H. Schuh and D. Behrend. "VLBI: A fascinating technique for geodesy and astrometry". In: *Journal of Geodynamics* 61 (Oct. 2012), pp. 68–80. DOI: 10.1016/j.jog.2012.07.007 (cit. on p. 93).

[145] A. Niell et al. "VLBI2010: current and future requirements for geodetic VLBI systems". In: *Report of Working Group 3 to the IVS Directing Board* (2005) (cit. on p. 96).

[146] J. F. Cliche and B. Shillue. "Applications of control Precision timing control for radioastronomy maintaining femtosecond synchronization in the atacama large millimeter array". In: *IEEE Control Systems* 26.1 (Feb. 2006), pp. 19–26. DOI: 10.1109/MCS.2006.1580149 (cit. on p. 96).

[147] M. G. Tarallo et al. "A strontium optical lattice clock apparatus for precise frequency metrology and beyond". In: *2017 Joint Conference of the European Frequency and Time Forum and IEEE International Frequency Control Symposium (EFTF/IFC)*. IEEE, July 2017. DOI: 10.1109/fcs.2017.8089020 (cit. on p. 96).

[148] C. Rieck et al. "VLBI time transfer using CONT08 data". In: *EFTF 2010 24th European Frequency and Time Forum*. IEEE, Apr. 2010. DOI: 10.1109/eftf.2010.6533654 (cit. on p. 104).

[149] T. Hobiger et al. “Combining GPS and VLBI for intercontinental frequency transfer”. In: *Metrologia* 52.2 (Mar. 2015), pp. 251–261. DOI: 10.1088/0026-1394/52/2/251 (cit. on p. 104).

[150] H. Denker. “Regional Gravity Field Modeling: Theory and Practical Results”. In: *Sciences of Geodesy - II*. Springer Berlin Heidelberg, July 2012, pp. 185–291. DOI: 10.1007/978-3-642-28000-9_5 (cit. on p. 106).

[151] H. Denker et al. “Geodetic methods to determine the relativistic redshift at the level of 10^{-18} in the context of international timescales: a review and practical results”. In: *Journal of Geodesy* 92.5 (Dec. 2017), pp. 487–516. DOI: 10.1007/s00190-017-1075-1 (cit. on p. 106).

[152] B. Heck and R. Rummel. “Strategies for Solving the Vertical Datum Problem Using Terrestrial and Satellite Geodetic Data”. In: *Sea Surface Topography and the Geoid*. Springer New York, 1990, pp. 116–128. DOI: 10.1007/978-1-4684-7098-7_14 (cit. on p. 106).

[153] T. Gruber et al. *Height System Unication with GOCE*. Tech. rep. GO-HSU-PL-0021. ESA, 2014 (cit. on p. 106).

[154] L. Briatore and S. Leschiutta. “Evidence for the Earth gravitational shift by direct atomic timescale comparison”. In: *Il Nuovo Cimento B Series 11* 37.2 (Feb. 1977), pp. 219–231. DOI: 10.1007/bf02726320 (cit. on p. 106).

[155] D. Philipp et al. “Definition of the relativistic geoid in terms of isochronometric surfaces”. In: *Physical Review D* 95.10 (May 2017). DOI: 10.1103/physrevd.95.104037 (cit. on p. 106).

[156] G. Lion et al. “Determination of a high spatial resolution geopotential model using atomic clock comparisons”. In: *Journal of Geodesy* 91.6 (Jan. 2017), pp. 597–611. DOI: 10.1007/s00190-016-0986-6 (cit. on p. 106).

[157] C. Grebing et al. “Realization of a timescale with an accurate optical lattice clock”. In: *Optica* 3.6 (May 2016), p. 563. DOI: 10.1364/optica.3.000563 (cit. on p. 113).

[158] D. Toomey et al. “The Cascadia Initiative: A Sea Change In Seismological Studies of Subduction Zones”. In: *Oceanography* 27.2 (June 2014), pp. 138–150. DOI: 10.5670/oceanog.2014.49 (cit. on p. 114).

[159] T. M. S. Team. “Imaging the Deep Seismic Structure Beneath a Mid-Ocean Ridge: The MELT Experiment”. In: *Science* 280.5367 (May 1998), pp. 1215–1218. DOI: 10.1126/science.280.5367.1215 (cit. on p. 114).

[160] *Ocean Bottom Seismograph Instrument Pool (OBSIP)*. URL: http://www.obsip.org (cit. on p. 114).

[161] H. Nakstad and J. T. Kringlebotn. "Realisation of a full-scale fiber-optic ocean bottom seismic system". In: 19^{th} *International Conference on Optical Fiber Sensors 7004, 700436*. 2008 (cit. on p. 114).

[162] G. A. Cranch, P. J. Nash, and C. K. Kirkendall. "Large-scale remotely interrogated arrays of fiber-optic interferometric sensors for underwater acoustic applications". In: *IEEE Sensors Journal* 3.1 (Feb. 2003), pp. 19–30. DOI: 10.1109/jsen.2003.810102 (cit. on p. 114).

[163] B. Romanowicz et al. "The Monterey bay broadband ocean bottom seismic observatory". In: *Ann. Geophys.* 49 (2006), pp. 2–3 (cit. on p. 114).

[164] *The Ocean Observatories Initiative*. URL: http://oceanobservatories.org/ (cit. on p. 114).

[165] *Dense Oceanfloor Network system for Earthquakes and Tsunamis*. URL: https://www.jamstec.go.jp/donet/e/rd/index.html (cit. on p. 114).

[166] *North East Pacific Time-series Underwater Networked Experiments (NEPTUNE)*. URL: http://www.oceannetworks.ca/observatories/pacific (cit. on p. 114).

[167] *Submarine Telecoms Industry Report*. URL: http://subtelforum.com/Report5/D2C63B44C07ABF9C60E4BE6591014FCE/IndustryReport5.pdf (cit. on p. 114).

[168] N. J. Lindsey et al. "Fiber-Optic Network Observations of Earthquake Wavefields". In: *Geophysical Research Letters* 44.23 (Dec. 2017), pp. 11,792–11,799. DOI: 10.1002/2017gl075722 (cit. on p. 114).

[169] P. Jousset et al. "Dynamic strain determination using fibre-optic cables allows imaging of seismological and structural features". In: *Nature Communications* 9.1 (July 2018). DOI: 10.1038/s41467-018-04860-y (cit. on p. 114).

[170] P. M. Shearer. *Introduction to seismology*. Cambride University Press (cit. on p. 118).

[171] R. J. Urick. *Principles of Underwater Sound*. p. 423. Peninsula, Los Altos, CA, 1983 (cit. on p. 121).

[172] R. K. Andrew et al. "Ocean ambient sound: Comparing the 1960s with the 1990s for a receiver off the California coast". In: *Acoustics Research Letters Online* 3.2 (Apr. 2002), pp. 65–70. DOI: 10.1121/1.1461915 (cit. on p. 121).

[173] K. Hasselmann. "A statistical analysis of the generation of microseisms". In: *Reviews of Geophysics* 1.2 (1963), p. 177. DOI: 10.1029/rg001i002p00177 (cit. on p. 125).

[174] F. Ardhuin et al. “From seismic noise to ocean wave parameters: General methods and validation”. In: *Journal of Geophysical Research: Oceans* 117.C5 (May 2012), n/a–n/a. DOI: 10.1029/2011jc007449 (cit. on p. 126).

[175] K. Nishida. “Resonant Oscillations Between the Solid Earth and the Atmosphere”. In: *Science* 287.5461 (Mar. 2000), pp. 2244–2246. DOI: 10.1126/science.287.5461.2244 (cit. on p. 127).

[176] M. Deen et al. “First Observation of the Earth singles Permanent Free Oscillations on Ocean Bottom Seismometers”. In: *Geophysical Research Letters* 44.21 (Nov. 2017), pp. 10,988–10,996. DOI: 10.1002/2017gl074892 (cit. on p. 127).

This Ph.D. thesis has been typeset by means of the TEX-system facilities. The typesetting engine was pdfLATEX. The document class was `toptesi`, by Claudio Beccari, with option `tipotesi=scudo`. This class is available in every up-to-date and complete TEX-system installation.